ORNL/TM-2015/656

Research and Development of Multiphysics Models in Support of the Conversion of the High Flux Isotope Reactor to Low Enriched Uranium Fuel

Isaac T. Bodey
Franklin G. Curtis
Adam R. Travis
Rao V. Arimilli
Kivanc Ekici
James D. Freels

November 2015

Approved for public release. Distribution is unlimited.

OAK RIDGE NATIONAL LABORATORY
MANAGED BY UT-BATTELLE FOR THE US DEPARTMENT OF ENERGY

DOCUMENT AVAILABILITY

Reports produced after January 1, 1996, are generally available free via US Department of Energy (DOE) SciTech Connect.

Website http://www.osti.gov/scitech/

Reports produced before January 1, 1996, may be purchased by members of the public from the following source:

National Technical Information Service
5285 Port Royal Road
Springfield, VA 22161
Telephone 703-605-6000 (1-800-553-6847)
TDD 703-487-4639
Fax 703-605-6900
E-mail info@ntis.gov
Website http://www.ntis.gov/help/ordermethods.aspx

Reports are available to DOE employees, DOE contractors, Energy Technology Data Exchange representatives, and International Nuclear Information System representatives from the following source:

Office of Scientific and Technical Information
PO Box 62
Oak Ridge, TN 37831
Telephone 865-576-8401
Fax 865-576-5728
E-mail reports@osti.gov
Website http://www.osti.gov/contact.html

This report was prepared as an account of work sponsored by an agency of the United States Government. Neither the United States Government nor any agency thereof, nor any of their employees, makes any warranty, express or implied, or assumes any legal liability or responsibility for the accuracy, completeness, or usefulness of any information, apparatus, product, or process disclosed, or represents that its use would not infringe privately owned rights. Reference herein to any specific commercial product, process, or service by trade name, trademark, manufacturer, or otherwise, does not necessarily constitute or imply its endorsement, recommendation, or favoring by the United States Government or any agency thereof. The views and opinions of authors expressed herein do not necessarily state or reflect those of the United States Government or any agency thereof.

ORNL/TM-2015/656

Research Reactors Division

RESEARCH AND DEVELOPMENT OF MULTIPHYSICS MODELS IN SUPPORT OF THE CONVERSION OF THE HIGH FLUX ISOTOPE REACTOR TO LOW ENRICHED URANIUM FUEL

I. T. Bodey
F. G. Curtis
Adam R. Travis
R. V. Arimilli
K. Ekici
J. D. Freels

November 2015

Prepared by
OAK RIDGE NATIONAL LABORATORY
Oak Ridge, TN 37831-6283
managed by
UT-BATTELLE, LLC
for the
US DEPARTMENT OF ENERGY
under contract DE-AC05-00OR22725

CONTENTS

LIST OF FIGURES v
LIST OF TABLES xi
PREFACE xii
ACKNOWLEDGEMENTS xiv
ABSTRACT xv

1.0 INTRODUCTION 1
1.1 MOTIVATION 1
1.2 HFIR BACKGROUND 2
1.3 COMSOL MULTIPHYSICS SOLVER 8
1.4 ORGANIZATION OF THE REPORT 8

2.0 CONJUGATE HEAT TRANSFER 11
2.1 2D MODELS AND COMPARISON 11
2.1.1 2D Turbulent Conjugate Heat Transfer (TCHT) Model Geometry and Computational Grid Structure 12
2.1.2 2D TCHT Analysis: Constant Heat Flux Case with Constant and Variable Fluid Properties 18
2.1.3 2D TCHT: HFIR Distributed Power Density Case with Constant and Variable Fluid Properties 33
2.1.4 Discussion of the 2D Conjugate Heat Transfer Results 42
2.2 3D MODELS AND COMPARISON 43
2.2.1 ANSR THTL Model Geometry and Boundary Conditions 43
2.2.2 Computational Grid Structure Development 45
2.2.3 Comparison of Model Results with Experimental Data 46
2.2.4 Computational Grid Convergence Index 48
2.2.5 Conclusions for the 3D Modeling Case 49
2.3 TURBULENCE MODEL CLOSURE EFFECTS 49
3.0 FUEL DEFECTS 51
3.1 REVIEW OF FUEL DEFECT MODELING 51
3.2 3D MODEL FOR COMPARISON 53
3.2.1 Plate Geometry and Grid Structure 53
3.2.2 Nominal Plate Case 56
3.2.3 Blister Defect Case 58
3.2.4 Segregation Defect Case 60
4.0 FLUID STRUCTURE INTERACTIONS 65
4.1 OVERVIEW OF PAST FUEL PLATE FSI ANALYSIS 65
4.2 CYLINDER IN CROSS-FLOW 68
4.2.1 Stationary Cylinder 68
4.2.2 Oscillating Cylinder: Prescribed Displacement 79
4.2.3 Hydroelastic Analysis: Free Displacement 83
4.2.4 Stationary Cylinder with Moving Tail 95
4.3 FLOW OVER FLAT PLATE FUELS 99
4.3.1 Single Plate Smissaert Simulations 100
4.4 FLOW OVER CURVED PLATE FUELS 103
4.4.1 Single Plate ANSR Analysis 106
5.0 3D MODEL SIMPLIFICATIONS AND COMPARISONS 113
5.1 OVERVIEW 113
5.2 3D MODEL FOR COMPARISON 113

5.2.1 Construction 113
5.2.2 Inputs 116
5.2.3 Physics 121
5.2.4 Meshing 125
5.3 SIMPLIFIED T-Z PLANE MODEL (COUPLED MODEL) 130
5.3.1 Construction 130
5.3.2 Inputs 130
5.3.3 Interdimensional Model Coupling 135
5.3.4 Physics 141
5.3.5 Meshing 142
5.3.6 Paneling 143
5.4 SIMPLIFIED s-z PLANE MODEL (BULK MODEL) 145
5.4.1 Construction 145
5.4.2 Inputs 146
5.4.3 Physics 146
5.4.4 Meshing 147
5.5 RESULTS 148
5.5.1 Error Evaluation 148
5.5.2 3D Model Mesh Convergence 151
5.5.3 Coupled Model Mesh Convergence 153
5.5.4 Validation of Simplifying Coupled Model Assumptions 162
5.5.5 Paneling 166
5.5.6 Model Comparisons 168
5.5.7 Computational Efficiency 175
5.5.8 Justification of Selected Residual Tolerance 176
6.0 SUPPORTING DEVELOPMENTS 177
6.1 MATERIAL PROPERTY LIBRARIES 177
6.2 MATERIAL PROPERTY LIBRARIES 180
6.2.1 FORTRAN Compilation in MATLAB 180
6.2.2 MATLAB Function Implementation 182
6.3 DERIVATION OF THE INVOLUTE COORDINATE SYSTEM 182
6.3.1 The Basic Involute 182
6.3.2 Select Alterations to the Basic Involute 185
6.4 CONSTRUCTING CAD GEOMETRIES IN SOLIDWORKS 189
6.4.1 Defining the Geometries 189
6.4.2 SolidWorks Construction Techniques 193
7.0 CONCLUSIONS, RECOMMENDATIONS AND LESSONS LEARNED 195
7.1 RESULTS FROM 2-D CONJUGATE HEAT TRANSFER MODELS 195
7.2 RESULTS FROM THE 3-D CONJUGATE HEAT TRANSFER MODELS 196
7.2.1 Advanced Neutron Source Reactor Thermal Hydraulic Test Loop 196
7.2.2 Fuel Defect Analysis 196
7.3 RESULTS FROM FLUID-STRUCTURE INTERACTION MODELS 197
7.4 RESULTS FROM THERMAL-HYDRAULIC INTERDIMENSIONAL COUPLING MODELS 198
8.0 REFERENCES 201

LIST OF FIGURES

1.1 Illustration of the HFIR core and experimental locations. 3
1.2 Cutaway view of the HFIR fuel element. 4
1.3 Two involute curves with a base radius, $r_{_b}$, and a base pitch, $p_{_b}$, separating the two curves for the entire span. 5
1.4 Representative drawing of a single HFIR fuel plate with HEU fuel. Representative drawing of a single HFIR fuel plate with HEU fuel (Note that the figure is not drawn to scale) 6
1.5 The HEU fuel profile for an inner fuel element 7
1.6 The proposed LEU fuel profile for an inner fuel element 7

2.1 2-D Turbulent conjugate heat transfer model geometry. The terminal locations of the active portion of the fuel domain are shown for reference. The flow direction is indicated for reference as well. In order to simplify the analysis, $z = 0.8127m - y$ will be used as the flow direction variable 13
2.2 Turbulent Conjugate Heat Transfer Model Geometry 15
2.3 Grid Structure of Region 2 (the scale represented here has not been modified) 16
2.4 Temperature difference between the clad surface and the bulk fluid for constant fluid properties (CFP) and NIST fluid properties (NFP). One notices that the system becomes fully thermally developed at approximately 20 D_h for the CFP case 21
2.5 Convection coefficient for constant fluid properties (CFP) and NIST fluid properties (NFP). The two outliers occurring at z = 200D_h is due to end effects where the end of the active region resides 22
2.6 Variation in the direction normal to flow direction (x) of the difference between the local fluid temperature [Tf(x,z)] and the inlet bulk fluid temperature (Tin) for the Constant fluid property case at various axial locations along the heated section of the simulation geometry. The x-coordinate begins on the clad surface (i.e., x = 6.35×10-4 m) and extends to the fluid mid-channel (i.e.,, = 12.7×10-4 m). The heating effect of the clad surface reaches mid-channel for $z \geq 5Dh$ 23
2.7 Variation in the direction normal to flow direction (x) of the difference between the local fluid temperature and the inlet bulk fluid temperature for the variable fluid property case (NFP) at various locations along the heated section of the simulation geometry. The x coordinate begins on the clad surface (i.e., x = 6.35×10^{-4}m) and extends to the fluid mid-channel (i.e., x = 12.7×10^{-4}m). The heating effect of the clad surface reaches mid-channel for $z \geq 5Dh$. 24
2.8 The distribution of the Difference between the local fluid temperature for the constant fluid property case (CFP) and the variable NIST fluid property (NFP) case at different axial locations 25
2.9 Clad surface temperatures and bulk fluid temperatures for both for the constant fluid property (CFP) and the variable NIST fluid property (NFP) cases 27
2.10 Comparison of the Nusselt Modulus – Prandtl Number Ratio as a function of the Reynold's Number. To clarify the legend: C ~ COMSOL, G ~ Gnielinski, ST ~ Sieder-Tate, H ~ Hausen 30
2.11 Relative differences of the Gnielinski, Sieder-Tate, and Hausen correlations compared with the (COMSOL) model Nusselt modulus 31
2.12 Difference between the surface temperature and the inlet bulk fluid temperature as derived from the correlations used for the CFP case 32
2.13 Difference Between the surface temperature and the bulk fluid inlet temperature as derived from the Nusselt correlations used for the NFP case 33
2.14 Distributed power density (DPD) input for model 34
2.15 HFIR DPD resultant surface heat flux distribution 35

2.16 Resultant profiles of the difference between the surface temperature and the bulk fluid temperature 36
2.17 Resultant convection coefficient for the CFP case and the NFP case 37
2.18 Nusselt number correlation results compared with the model Nusselt number for the NFP 39
2.19 Relative differences of the Gnielinski, Sieder-Tate, and Hausen correlations compared with the model Nusselt modulus 40
2.20 Diff temperature distribution for the cfp case generated by the Gnielinski (G-CFP), Sieder-Tate (ST-CFP), and the Hausen (H-CFP) correlations compared with the model temperature distribution 41
2.21 Correlation generated temperature distributions compared with the model distribution for the NFP case 42
2.22 ANSR THTL Test Loop Cross Section. The label T/C represents thermocouple locations along the test section. The red dashed lines represent the symmetry boundaries used in the creation of a quarter geometry to simplify the computational effort 44
2.23 Isometric view of the ANSR THTL model 45
2.24 The Effect of Wall-Offset Models with Grid Elements Too Close to the Wall. The cut-line used for this plot was created at $y = 0.3047$ m (i.e., at the exit of the heated section). The first element is located a distance of 1.75×10^{-7}m from the wall for all the three models 50

3.1 Axisymmetric Geometry used for Fuel Defect Simulations[35,44]. The *t* mils measurement indicated for the thickness of the clad plus filler domain is used as an adjustment factor to vary the thickness of this region (i.e., $10mils \leq t \leq 50mils$). This thickness adjustment factor is also used to adjust the heat generation rate for the fuel and segregation domains as indicated in the table 52
3.2 Cross-sectional view of the fuel defect model geometry. The vantage is in the flow direction. The dimensions are given for reference. The model geometry is 1 m long in the flow direction. The contoured side of the fuel meat domain is obvious and will be referenced throughout the chapter 54
3.3 The 3-D Power Density Profile used in the Fuel Meat Domain of the Simulation Geometry 54
3.4 Nominal Case clad surface temperature along the uncontoured side of the fuel plate. The maximum (211.72˚F) and minimum (119.721˚F) surface temperatures are superposed on the image at the location of their occurrence 56
3.5 Nominal case clad surface heat flux along the uncontoured side of the fuel plate. The maximum (3.331×10^{6} W/m^2) and minimum (-9.7152×10^{4} W/m^2) heat flux values are superposed on the image at the location of their occurrence 57
3.6 Blister Defect Geometry Relative to the Surrounding Fuel and Clad. This model does not consider segregation defects. The location of the maximum clad surface temperature, Tmax, from the nominal case is indicated 59
3.7 Blister Case Clad Surface Temperature Along the Uncontoured Side of the Fuel Plate. Maximum (212.92˚F) and minimum (119.72˚F) temperatures and their locations are shown on the image 59
3.8 Blister Case Clad Surface Heat Flux Along the Uncontoured Side of the Fuel Plate. The maximum (3.33518×10^{6} W/m^2) and minimum (-1.5754×10^{5} W/m^2) values of the heat flux are superposed on the image at the location of their occurrence 60
3.9 Segregation defect geometry relative to the surrounding fuel and clad. This model does not consider blister defects. The location of the maximum clad surface temperature, T_{max}, from the nominal case is indicated 61
3.10 Clad surface temperature on the fuel contour side of the fuel plate. The maximum and minimum temperatures are superposed on the image at the location of their occurrence 61

3.11 Clad surface heat flux on the fuel contour side of the fuel plate. The maximum and minimum surface heat flux values have been superposed on the image at the location of their occurrence 62

4.1 The ATR core with its clover-leaf fuel design[52] 65
4.2 Top-down view of the MIT core[53]. The coolant flows into the page 66
4.3 Domain for the 20D cylinder 70
4.4 Mesh comparison for the 2-D cylinder 71
4.5 Initial condition using the steady-state solver for $Re = 100$. The velocity contours are represented in m/s 72
4.6 Set of time-domain solutions for $Re = 100$. Shown are velocity magnitudes 73
4.7 Time accurate C_l for the stationary cylinder 74-75
4.8 FFT of the C_l for the stationary cylinder 76-77
4.9 C_l for the $Re = 150$ case with aliasing present due to large recording intervals 79
4.10 Graphical Representation of the lock-on region 80
4.11 The cylinder lock-on simulations compared to the experiment by Koopman. The plus symbols (+) represent cases in which lock-on was achieved and the cross symbols (×) represent the cases in which no lock-on was present 82
4.12 Spring-mass-damper model used for the hydroelastic simulations 83
4.13 Flow chart for the fully-coupled solver 85
4.14 Flow chart for the segregated solver 86
4.15 Flow chart for the one-way coupled solver 87
4.16 Solution of the fully coupled 2-D free displacement cylinder 88-90
4.17 Mesh for the 3-D cylinder in cross-flow simulation 91
4.18 Solution of the fully coupled 3-D free displacement cylinder. The results are taken at the free end of the cylinder 92-93
4.19 Incorrect displacement of the 2-D cylinder for the condition of $Re = 100$. The dashed line represents the initial position and the displacement should oscillate about it 94
4.20 Domain for the 2-D stationary cylinder with moving tail 95
4.21 Results for the FSI2 test case. The results (red lines with circles) are compared to the data provided by Turek and Hron in black 97-98
4.22 2-D solution for the FSI2 case at 10s 99
4.23 Deflection of a series of plates using periodic boundary conditions. The periodic boundary condition, applied to a single plate, assumes that all of the fuel plates deflect in the same direction 100
4.24 Bending of a series of plates with deflections of adjacent plates going in the opposite direction, which is a more physical assumption 101
4.25 Single plate setup with full channels and wall boundary conditions 102
4.26 Single plate deflection of the Smissaert case for an inlet velocity of 3.087 m/s (1.23 M_c) 103
4.27 Proposed configuration of the ANSR core[109] 105
4.28 One plate ANSR simulation geometry 108
4.29 Mesh at the leading edge of the one-plate ANSR case 109
4.30 Exaggerated deflection for the ANSR single aluminum plate at an inlet speed of 17.35 m/s. The deflection is measured in mm and the deformation is scaled to accurately show the mode shape of the deflection. The red depicts a positive deflection and the blue depicts a negative deflection while the grey is zero deflection 110
4.31 ANSR experimental deflections compared to the COMSOL results for the aluminum plate 111

5.1 Assembled coolant components. Flow direction is in the +z-direction 114

5.2 COMSOL Assemblage Side Profile Diagram. Note that the diagram is not to scale. The coolant channel is shown in blue, the fuel plate in grey, and the fuel meat in orange. While the coolant and fuel plate extend to both side plates, the fuel meat does not 115
5.3 Solid Geometry Assemblage. Flow direction is in the +*z*-direction. The inner side plate is shown on top in this figure. The geometry in between is the fuel plate. Coolant geometry components are not pictured 115
5.4 Initial pressure profile 117
5.5 Initial Temperature profile 117
5.6 Initial velocity profile 118
5.7 MCNP Cells. The inner fuel element cells are boxed in red 119
5.8 MCNP power density profile. The direction of flow is in the +*z*-direction 120
5.9 COMSOL Power Density Profile. The direction of flow is in the +*z*-direction 121
5.10 Law of the wall. The linear relation for u^+, in blue, is valid to the left of the intersection point in the viscous sublayer. The logarithmic relation, in green, is valid to the right in the inner log-law layer. The smooth Spalding approximation, in teal, is valid throughout[43]. The von Kármán constant, κ, equals 0.41. B equals ~5.5 125
5.11 3D Axial Mesh Distributions. The MCNP axial mesh distribution is shown in (A) and the 2X MCNP distribution in (B). The side plates are highlighted in blue. The coolant channel is shown in grey. The fuel plate and fuel meat are obscured behind the coolant channel. Figure is not representative of final mesh as all spanwise (along the length of the involute curve) mesh distributions have been set to 1 for ease of viewing. The final mesh structure would not be discernible at this scale 127
5.12 Mesh Domains. Figure is not to scale 127
5.13 Fueled section cross-sectional mesh. Structured quadrilateral mesh elements in the coolant region have been converted to triangular elements in order to facilitate meshing between axial coolant components 128
5.14 Free-Tetrahedral Mesh Domains. The leading edge coolant cap geometry is shown in (A), the rounded leading edge clad in (B), and the trailing edge coolant cap in (C) 128
5.15 Boundary-layer mesh detail 129
5.16 Coupled Model Coolant Domain. The coolant slice is shown in blue. The obstructions created by the adjacent fuel plates in the coolant channel are marked with dotted lines. Note, however, that the fuel plates are not included in the 2D geometry. The approximate position of the fuel meat within each fuel plate is shown in orange. Flow direction is in the +*z*-direction. Diagram is not to scale 130
5.17 Involute coordinate contour grid points. Each group of colored markers is associated with a constant *t* value in which *t* (in) = -0.12, -0.11, -0.06, -0.01, 0.04, 0.09, 0.14, 0.15. θ = 0.00 to 1.65 by 0.01 radian increments for each group 131
5.18 θ-Coordinate contour map. The involute geometry is shown for reference 132
5.19 *t*-Coordinate Contour Map. The involute geometry is shown for reference 133
5.20 Axially-dependent leading edge widths. r_c is set to 1 and z_o to 0. Flow direction is in the –*z*-direction 134
5.21 Channel width input function. Flow direction is in the +*z*-direction. The *z*-coordinate in the Figure is a localized coordinate system, not the global *s*-*t*-*z* system 135
5.22 3D-to-2D Coupling mechanism flow chart 136
5.23 2D-to-3D coupling mechanism flow chart 138
5.24 Model Coupling Interdependency Loop. Flow is in the +*z*-direction 140
5.25 Coupled Model solution process flow chart 141
5.26 Coupled model coolant mesh comparison 142
5.27 Coupled model converted boundary layer detail 143
5.28 Fuel plate paneling. Depicted is a five-panel decomposition. Figure is not to scale 144
5.29 Fuel plate paneling diagram 145

5.30 Bulk model *t*-*z* plane cross-section. Not to scale 146
5.31 Bulk model widthwise temperature profile..... 147
5.32 Bulk Model fueled section *s*-*t* plane mesh cross section..... 148
5.33 Axial cut line temperature solution..... 152
5.34 Coupled model coolant mesh convergence—coolant channel enthalpy. The normalized nuclear heat generation, 1.00, is marked with a red line to show the coolant channel's convergence towards the correct value 154
5.35 Coupled model coolant mesh convergence—logarithmic coolant error..... 154
5.36 Coupled model coolant mesh convergence—max fuel meat temperature. The 3D model's maximum fuel meat temperature is marked with a red line to demonstrate the offset between the two models' converged states 155
5.37 Coupled model fuel plate mesh convergence—fuel plate error..... 156
5.38 Coupled model fuel plate mesh convergence—global error..... 156
5.39 Coupled model fuel plate mesh convergence—max fuel meat temperature..... 157
5.40 Coupled model fuel plate mesh p1. Fuel plate *s*-*t* face is highlighted in blue, fuel meat face in green..... 158
5.41 Coupled model fuel plate mesh convergence—max fuel meat t error..... 158
5.42 Coupled model alternate coolant mesh study—global error..... 160
5.43 Coupled model alternate coolant mesh study—max fuel meat T 160
5.44 Mesh alt3 distribution comparison..... 162
5.45 3D Model Inner Side Plate Inward Heat Flux. Figure is not to scale. The *t*-direction has been stretched by a factor of 20 for ease of viewing. The fuel plate is outlined in three parts with the coolant channel surrounding it..... 163
5.46 Coupled model hydrodynamic entrance region velocity profiles 164
5.47 Coupled model entrance region Reynolds number profile 165
5.48 Coupled model thermal entrance region temperature profiles..... 165
5.49 Conceptual paneling model diagram..... 166
5.50 Conceptual paneling model bulk temperature projections..... 167
5.51 Conceptual Paneling model surface and midplane temperature profiles. Temperature profiles are not on the same color scale. They are merely intended to provide a qualitative comparison..... 167
5.52 Coupled paneled model concave fuel plate surface temperature profile 168
5.53 Fuel meat concave surface temperature profile comparison..... 168
5.54 Fuel meat concave surface axial 1D temperature profiles 169
5.55 Fuel meat concave surface spanwise 1D temperature profiles 170
5.56 Cross-Sectional Cut-Out Temperature Profile Comparison. The 3D model cross-section is shown with all geometry elements present including the fuel meat, fuel plate, coolant channels, and inner side plate. Given the dimensional disparity across the coupling interface in the coupled model, only the fuel meat and fuel plate are shown..... 171
5.57 Cross-Sectional Cut-Out Widthwise Line 1 1D Temperature Profiles. While the 3D profile is plotted as a single entity, the coupling interface in the coupled model necessitates that the fuel plate and coolant temperature profiles be plotted separately..... 171
5.58 Cross-Sectional Cut-Out Widthwise Line 2 1D Temperature Profiles. While the 3D profile is plotted as a single entity, the coupling interface in the coupled model necessitates that the fuel plate and coolant temperature profiles be plotted separately..... 172
5.59 Coolant Channel Leading Edge Total Velocity Contour Comparison. Note that the coolant domain in each model consists of only a single channel. Three channels are presented side-by-side in order to better show the profile continuity across the periodic boundaries..... 173
5.60 Coolant Channel trailing edge total velocity contour comparison. Note that the coolant domain in each model consists of only a single channel. Three channels are presented side-by-side in order to better show the profile continuity across the periodic boundaries..... 174

5.61 Coupled model non-symmetric trailing edge pressure profile. The trailing edge pressure profile was taken from a widthwise line located at z = 55.78 cm, 0.1 cm above the trailing edge itself 175

6.1 The specific heat capacity as a function of temperature 178
6.2 The thermal expansion coefficient as a function of temperature 178
6.3 The density as a function of temperature 179
6.4 The thermal conductivity as a function of temperature 179
6.5 Basic circular involute. The involute curve is shown along with its base circle. Tangent guidelines are represented by dashed lines. The numbers indicate the direction of progression of the involute in the direction deemed "positive." 183
6.6 Angular parameters. In this example $\alpha = \theta - \pi/4$. Instances in which α does not start at zero are also possible. These will, however, have some angular offset separating them from contact with the base circle 184
6.7 HFIR core inner element fuel plate configuration. Inner element involute fuel plates are shown in grey with inner and outer side plates capping each end. The alternating white spaces between fuel plates are coolant channels 185
6.8 Perpendicular involute offset. The top involute curve has $\theta = \alpha$. The bottom involute curve has $\theta = \alpha + 1$ which corresponds to a θ_o of 1 radian (CW positive) 186
6.9 Out-of-plane involute curve. The z-direction denotes the direction of the axis. As viewed down the axis, the out-of-plane involute has the same footprint as its in-plane involute 189
6.10 Inner element fuel plate dimensions 190
6.11 Linearized HEU fuel thickness profile. The curve fit is generated from 35 unevenly distributed points 190
6.12 Linearized LEU fuel thickness profile. Overall, the LEU fuel profile is thinner than the HEU profile. Even though the LEU fuel has less U^{235} per weight than the HEU fuel, it has a higher density 191
6.13 Linearized LEU Fuel Geometries. The axially-consistent intermediate LEU geometry is shown on the left. The axially-graded LEU geometry is shown on the right. Figures not to scale 192
6.14 Accessing the equation-driven-curve tool in solidworks. SolidWorks refers to the parametric parameter as t. For an involute curve this traditionally represents the angular coordinate θ although any coordinate can be used is the parametric equations are given as a function of it 193
6.15 2D x-y Plane SolidWorks footprint. Only the curves are created in SolidWorks. The shading of specific areas was done purely as a means of orientation. The two full coolant channels are shaded in blue. The fuel plate and both side plates are shaded in grey. The fuel meat contour is not depicted 194

LIST OF TABLES

2.1 Constant fluid properties evaluated at the average bulk fluid temperature, $\overline{T_b}$ = 347.58 K 18
2.2 FE306B03 Experimental data compared with the COMSOL model results 46
2.3 Fine grid structure with discretization error compared with experimental data 49

3.1 Summary of results for the fuel defect analysis 63

4.1 Shedding frequencies of the stationary cylinder in cross-flow compared to experimental results of Williamson [Williamson(1988)] 78
4.2 Results for the 2-D simulation for the free displacement cylinder. The frequencies were obtained using the FFT. The simulations were performed on a 12 core machine with 192GB RAM 90
4.3 Properties of the fluid structure used for the FS1 test cases 96
4.4 Properties of the PVC plate used by Smissaert in his experiment 99
4.5 Inlet velocities for the ANS prototype and model simulations and experiments 106
4.6 Properties used for the ANSR experiments 106

5.1 Coolant components 114
5.2 Fuel plate components 114
5.3 Initial inlet and outlet conditions 116
5.4 k-ε Transport constants 123
5.5 MCNP axial cell distribution 126
5.6 Modified Hausen correlation validation range 139
5.7 3D model mesh convergence study 152
5.8 Coupled model coolant domain mesh convergence study 153
5.9 Coupled model fuel plate domain mesh convergence study 155
5.10 Coupled model alternate coolant mesh study 159
5.11 Mesh alt3 comparison solutions 162
5.12 Propagation of coolant smoothing effect into fuel plate 175
5.13 Coupled vs 3D speed up 175
5.14 Relative tolerance 176

6.1 The updated U-10MO materials library values 177

PREFACE

by James D. Freels

In 2009, the Research Reactors Division (RRD) of the Oak Ridge National Laboratory (ORNL) started a new contract relationship with the Mechanical, Aerospace, and Biomedical Engineering (MABE) department of the University of Tennessee in Knoxville (UTK) to collaborate in using the COMSOL code (FEMLAB v3.5a at that time). Dr. Kirk T. Lowe was our first student to arrive, along with his major professor, Dr. Rao V. Arimilli. Dr. Arimilli, a COMSOL user since v2.0, came with an established expertise in both fluids and heat transfer (i.e., conjugate heat transfer). We knew from the outset that Kirk would not be with us long since his COMSOL-based PhD research was done prior to his arrival. Nevertheless, he helped us to get started and helped establish several fundamental areas such as user-defined LEU material libraries, Solidworks CAD inputs, software quality assurance (SQA) of v3.5a, and most notably, the tradeoffs between extrusion coupling and periodic boundary conditions (BC). Kirk started his professional career with Bettis Atomic Laboratory in Pittsburgh early in 2010.

Early in the summer of 2009, Dr. Isaac T. Bodey joined our group as a PhD researcher, specializing in conjugate heat transfer, also with Dr. Arimilli as his major professor. Isaac initially concentrated on comparing COMSOL to the legacy FORTRAN code that has traditionally supported the operation of HFIR (HFIR steady-state heat transfer code or HSSHTC). After gaining confidence in his ability to perform these comparisons, he moved on to 2D and 3D simulations of the HFIR fuel plate and channel. He compared COMSOL results to existing hot-spot models, and experimental flow and heat transfer data from the Advanced Neutron Source Reactor (ANSR) design tests. He investigated many other details along the way such as different turbulence models, meshing studies, solver settings, and many other aspects of COMSOL. Isaac completed his dissertation after starting fulltime work with the Savannah River project in Aiken, SC in June, 2013, and graduated approximately a year later in the summer of 2014.

The LEU conversion project, on a national level, has identified (and continues to work on now) the fuel-plate deflections as an important area of research for some thinner plate designs expected for US research reactors using LEU fuel. Research into fluid-structure interaction (FSI) with COMSOL was the scope of work for a new student, Franklin G. Curtis, and his major professor, Dr. Kivanc Ekici, as they joined our team in the fall semester of 2010. Dr. Ekici came to us with established expertise in the FSI field, and his expertise in computational fluid dynamics (CFD) brought the project an additional high level of support in many areas. Franklin quickly developed his expertise in using and understanding COMSOL, and he continues to do that today. He also demonstrated a strong interest and brought real benefits to the group on the computational side; both in using COMSOL, and the interfacing operating system. Franklin has clearly shown competence on the platforms of Linux, Apple-OSX, and Microsoft-Windows. Indeed, one area of development attributed to Franklin is the direct coupling of the NIST water property FORTRAN routines into COMSOL through the MATLAB livelink interface. In addition, Franklin has developed an expertise for many COMSOL details and has demonstrated unique results in all aspects of the code operation including geometry, mesh, inputs, solvers, and results. Through the guidance of Dr. Ekici, Franklin has demonstrated the FSI capability of COMSOL on numerous benchmark problems. Indeed, the COMSOL solutions appear to be superior to other approaches taken by other US researchers using coupled separate legacy codes (CFD+structural). Franklin developed unique approaches to the demanding HFIR FSI problem, and has produced realistic simulations of the HFIR fuel-plate deflections, as validated against ANSR flow tests and other flow tests available. This past summer of 2015, with Franklin's help, a DOE visiting faculty intern independently confirmed Franklin's FSI approach.

Franklin accepted employment with another division of ORNL in October 2014 and has been able to use COMSOL in his new job.

One additional student, Adam R. Travis, joined our LEU research group on March, 2012. He was initially separately funded on the UTK campus for about three months, and then joined us at the ORNL campus as a part-time research student starting June, 2012. Adam's initial involvement while on the UTK campus was in the development of Solidworks CAD models of the HFIR fuel plates and flow channels that were eventually imported into COMSOL. We still use these CAD models and many other COMSOL developments from Adam. Adam focused his MS thesis, and COMSOL research, on the development of simplified 2D models of the HFIR fuel-plate and channel(s) and compared against best-estimate 3D models of the same conjugate heat transfer physics. Adam's work required him to dig deep into involute geometry definitions, and his MS-thesis is perhaps the most elegant description of the involute design of the fuel plate that exists. Adam graduated and took full time employment in June, 2014 with Alcoa in Pittsburgh.

As we close out this phase of the HFIR LEU fuel-conversion research, this report has been generated as a summary of all the work these students have done during their time here. Primarily a collection of the student's graduate thesis and/or dissertation manuscript, there is still more to come as one PhD student has yet to graduate. We are most grateful for their help and development as we all learned from each other and became better at our COMSOL modeling capabilities as a result. Most importantly, the HFIR LEU fuel-conversion project has benefitted by their research.

ACKNOWLEDGEMENTS

The authors would like to acknowledge the support for this project provided by the Research Reactors Division (RRD) of the Oak Ridge National Laboratory (ORNL), the Global Threat Reduction Initiative, Reduced Enrichment for Research and Test Reactors program (RERTR), National Nuclear Security Administration, and U. S. Department of Energy (DOE). The ORNL program manager is Mr. David Renfro and the ORNL multiphysics technical leader is Dr. James D. Freels. And finally, the authors would like to acknowledge and thank Mary L. Wells, of RRD safety analysis staff, for her patience and understanding in completing the conversion of this document to meet all the requirements for ORNL/TM formatting.

ABSTRACT

The findings presented in this report are results of a five-year effort led by the Research Reactors Division (RRD) of the Oak Ridge National Laboratory (ORNL), which is focused on research and development toward the conversion of the High Flux Isotope Reactor (HFIR) fuel from high-enriched uranium (HEU) to low-enriched uranium (LEU). This report focuses on the tasks accomplished by the University of Tennessee—Knoxville (UTK) team from the Department of Mechanical, Aerospace, and Biomedical Engineering (MABE) that provided expert support in multiphysics modeling of complex problems associated with the LEU conversion of the HFIR reactor. The COMSOL software was used as the main computational modeling tool, whereas Solidworks was also used in support of computer-aided-design (CAD) modeling of the proposed LEU fuel design. The UTK research has been governed by a statement of work (SOW), which was updated annually to clearly define the specific tasks reported herein. Ph.D. student Isaac T. Bodey has focused on heat transfer and fluid flow modeling issues and has been aided by his major professor Dr. Rao V. Arimilli. Ph.D. student Franklin G. Curtis has been focusing on modeling the fluid-structure interaction (FSI) phenomena caused by the mechanical forces acting on the fuel plates, which in turn affect the fluid flow in between the fuel plates, and ultimately the heat transfer, which is also affected by the FSI changes. Franklin Curtis has been aided by his major professor Dr. Kivanc Ekici. M.Sc. student Adam R. Travis has focused on two major areas of research: (1) accurate CAD modeling of the proposed LEU plate design, and (2) reduction of the model complexity and dimensionality through interdimensional coupling of the fluid flow and heat transfer for the HFIR plate geometry. Adam Travis is also aided by his major professor, Dr. Kivanc Ekici. We must note that the UTK team, and particularly the graduate students, have been in very close collaboration with Dr. James D. Freels (ORNL technical monitor and mentor) and have benefited greatly from his leadership and expertise in COMSOL modeling of complex physical phenomena. Both UTK and ORNL teams have used COMSOL releases 3.4 through 5.0 inclusive (with particular emphasis on 3.5a, 4.3a, 4.3b, and 4.4) for most of the work described in this report, except where stated otherwise. Just as in the performance of the research, each of the respective sections has been originally authored by respective authors. Therefore, the reader will observe a contrast in writing style throughout this document.

1.0 INTRODUCTION

1.1 MOTIVATION

The HFIR is a light water moderated and cooled research reactor located at the ORNL in Oak Ridge, Tennessee. Rated at 100 MW, HFIR currently operates at a reduced power of 85 MW. The reduction in operational power was a result of a necessary decrease in system pressure due to the embrittlement of the pressure vessel that occurred during the initial 20 years of operation of the device. The HFIR had, and continues to have, the highest neutron flux in the western hemisphere[1]. For the rated operational power of 100 MW, the thermal-neutron flux in the flux trap region (i.e., the center of the core) is ~ 5.5×10^{15} neutrons/cm^2/s. For the reduced power of 85 MW, the thermal-neutron flux in the flux trap is ~ 2.6×10^{15} neutrons/cm^2/s. Thermal neutrons are defined as those neutrons that have undergone a sufficient number of collisions with other material particles such that their speeds are comparable to the thermal motion of the atoms in the moderator material (i.e., thermal equilibrium is achieved between the free neutrons and the moderator material with energies of approximately 0.025 eV[2]).

The original purpose of the HFIR system was to produce trans-plutonium isotopes, specifically californium-252. The HFIR has many experimental facilities available for isotope production (e.g., locations within and surrounding the core) such as the already mentioned flux trap, the removable beryllium locations which surround the core, and control rod access plug facilities[1]. The HFIR also has four neutron beam tubes used to direct the neutrons to targets for both elastic and inelastic scattering experiments used in the determination of the structural and excited properties of materials, respectively.

In an effort to reduce the proliferation of nuclear materials, the global threat reduction initiative (GTRI) was implemented with the mission of reducing and protecting nuclear and radiological materials in civilian sites according to the National Nuclear Security Administration (NNSA)[3]. To comply with the GTRI, the Department of Energy (DOE) initiated the Reduced Enrichment for Research and Test Reactors (RERTR) program in 1978[4]. This program develops the technology that allows research and test reactors to convert from a HEU to a LEU fuel (i.e., $\leq$ 19.75 wt. % U-235) in compliance with the GTRI. The reactor conversion program is designed to reduce the use of HEU fuel by converting domestic and international civilian research reactors and isotope production facilities to LEU fuel to protect Americans and the rest of the world from nuclear and radiological threats[5]. Presently, over 40 research reactors have been converted from HEU to LEU fuel with the support of the NNSA and RERTR. There are currently five major High Performance Research Reactors (HPRRs) that still need to be converted in the United States: the Massachusetts Institute of Technology Nuclear Reactor Laboratory (MIT-NRL), the University of Missouri Research Reactor (MURR), the National Institute of Standards and Technology (NIST) Research Reactor, the HFIR at ORNL and the Advanced Test Reactor (ATR) at Idaho National Laboratory (INL)[6].

There are several goals that the GTRI/RERTR program has defined for the replacement of HEU fuels in research reactors. Some of the key points of these goals are to maintain the current scientific missions of the reactors, ensure similar fuel lifetimes, ensure that conversion can be completed without major changes to the structure or equipment, and demonstrate that the reactor can be converted and operated safely after conversion. For the HFIR, the conversion must maintain the high neutron flux for the same cycle length (approximately 25 days)[7] using existing structures, systems and components while incorporating the current fuel geometric envelope. Staff members at ORNL are currently examining the impact upon the current HFIR safety basis and also performing preliminary formal calculations to support a draft safety analysis report for the eventual conversion of the HFIR to LEU fuel.

The design of the current HEU core is based upon early research reactor experience, HFIR-specific experiments, and historical safety and design basis calculations. Today, it is not economically feasible to perform extensive experiments to support the redesign of the fuel to LEU and the use of computational models is becoming increasingly needed. Currently, the HFIR employs numerous safety calculations and codes, based upon empirical data, to assess each cycle of the reactor. Each code and its implementation for the HFIR are described in detail in the Safety Analysis Report (SAR) for the HFIR[7]. The two main codes used for the thermal-hydraulic analysis of the HFIR core and system are the Steady State Heat Transfer Code (SSHTC)[8] and a modified version of RELAP5[9] both of which are one-dimensional analysis codes. As the name implies, the SSHTC is a proprietary, steady-state code designed to analyze the core of the HFIR. Using experimental data and built-in safety margins, the SSHTC is used to verify the conditions of the core based upon inputs from the neutronics code MCNP[10]. RELAP5 is used to determine the transient response of the entire reactor system for events considered in the accident analysis of the SAR. Both SSHTC and RELAP5 are well-established and validated codes, which are still being used today for the thermal-hydraulics analysis of the HFIR.

With the advancement in computing technology in the past few decades, it is now possible to perform higher fidelity simulations with the aim of supplementing these codes with a three-dimensional analysis that incorporates a variety of physics including conjugate heat transfer, fluid-structure interactions and thermal-structure interactions. One such code available today is COMSOL Multiphysics (or simply COMSOL), which offers modeling of multiphysics phenomena including but not limited to conjugate heat transfer, fluid-structure interactions and thermal-structure interactions. Because of its capabilities and ease of use, our team [including students/professors from the Mechanical, Aerospace and Biomedical Engineering (MABE) Department at the University of Tennessee-Knoxville (UTK) as well as researchers from ORNL] has adopted COMSOL for high-fidelity multiphysics modeling of the complicated physical phenomena in HFIR.

1.2 HFIR BACKGROUND

The HFIR was commissioned by the U. S. Atomic Energy Commission (AEC) in November 1958 to meet the anticipated growing need for transuranic isotopes such as plutonium and curium. In June of 1961, construction began on the HFIR site with criticality achieved on August 25, 1965. By September of 1966, the HFIR was running at its designed power of 100 MW_{th}.

The HFIR was designed on the “flux trap” principle in which an unfueled moderator region is surrounded by an annular region of fuel. The unfueled region, also known as an island, allows fast neutrons leaking from the fuel to be moderated and produces a region of very high thermal neutron flux in the island. The thermalized neutrons can be used for isotope production. One significant isotope produced in the reactor is Californium-252 which is used for a variety of nuclear applications such as reactor start up, neutron activation analysis, and as a medical isotope used to treat some forms of cancer. HFIR is the only producer of this isotope in the western world.

In addition to isotope production within the moderator core, it is also possible to tap the high flux of neutrons outside of the fuel and inside the reflector by placing empty beam tubes into the reflector. This allows the neutrons to be `beamed' into the experiments outside of the reactor shielding. Additionally, materials may be placed in holes inside the reflector for irradiation and later retrieval. A top-down view of the HFIR core and various experimental locations is provided in Fig. 1.1.

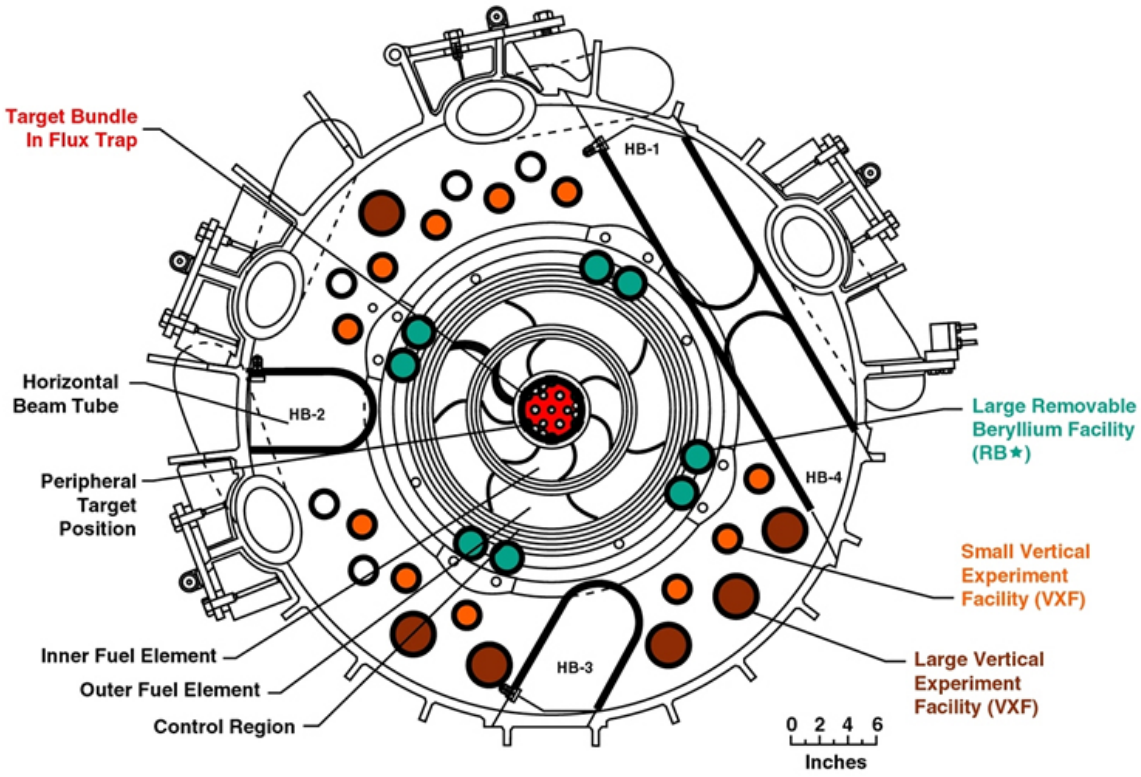

Fig. 1.1. Illustration of the HFIR core and experimental locations.

In November of 1986, tests indicated that the HFIR vessel was being embrittled at a much faster rate than expected and the reactor was shut down to investigate; up until this time, the HFIR was able to achieve a record of operation unsurpassed by any other nuclear reactor in the United States. After careful inspection and reevaluation of the reactor, the HFIR was restarted on May 18, 1990 at a lowered power of 85 MW_{th}. In 2007, the reactor was again shut down but this time to provide users with more experimental capacity. During its one-year shutdown, a variety of new instruments were installed as well as a cold neutron source[11]. The additional instrumentation and upgrading performed during this shutdown has allowed the HFIR to continue to attract leading researchers in the nuclear and related fields.

The construction of the fuel core has some very interesting characteristics designed to facilitate the high performance needed to produce such a high neutron flux. The core consists of two concentric fuel regions containing 171 curved fuel plates in the inner element and 369 fuel plates in the outer element[12]. A cutaway of the fuel assembly is provided in Fig. 1.2.

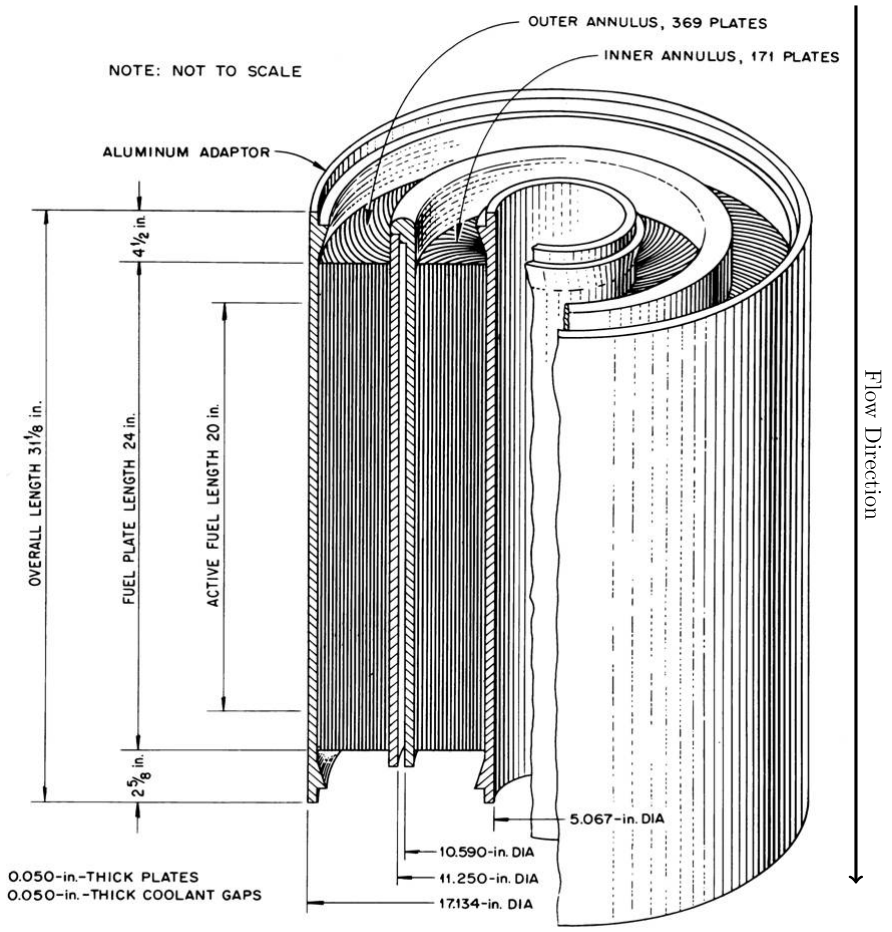

Fig. 1.2. Cutaway view of the HFIR fuel assembly.

The fuel plates are 24 inches long with a 20-inch active fuel region in the middle of the plate. Each fuel plate has a nominal thickness of 50 mils (0.050 inches, 1.27mm) with a coolant gap of 50 mils between each plate. Water is pumped through the core at a rate of 16,800 gallons per minute in order to maintain proper cooling of the reactor[7]. For clarity, the axial direction of the fuel plate refers to the flow direction while the span-wise direction refers to the length along the curved fuel plate, transverse of the flow direction.

Each fuel element follows an involute shape in order to maintain a constant coolant channel gap for the entirety of the fuel plate span. The involute is created by following the path a taut string travels when unwound from a curve. The HFIR fuel plate span is created by using the involute curve of a circle. In parametric form, the path is given by:

$$\mathbf{x} = \boldsymbol{r_b}(\cos\boldsymbol{\theta} + \boldsymbol{\theta}\sin\boldsymbol{\theta}) \quad (1.1)$$

$$\mathbf{y} = \boldsymbol{r_b}(\sin\boldsymbol{\theta} - \boldsymbol{\theta}\cos\boldsymbol{\theta}) \quad (1.2)$$

where $\boldsymbol{r_b}$ is the base radius of the involute circle. The involute has been used extensively in the design and creation of gears as a means to reduce the wear and vibration that occurs when they mesh together[13]. Using the nomenclature from gear theory, the distance between each involute curve is known as the base pitch, $\boldsymbol{p_b}$, and for the HFIR, $\boldsymbol{p_b}$ is the channel thickness of 50 mils. An example of two involute curves separated by a base pitch is provided in Fig. 1.3. Each dashed line in Fig. 1.3 is tangent to the base circle and is perpendicular to the involute curve.

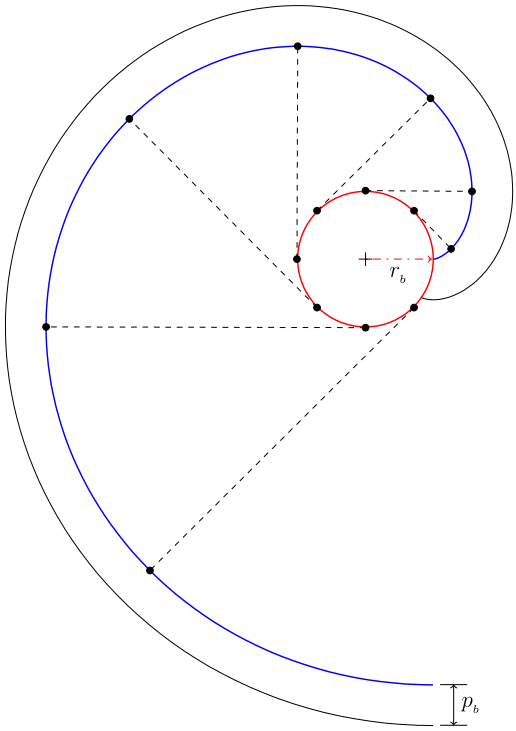

Fig.1.3. Two involute curves with a base radius, r_b, and a base pitch, p_b, separating the two curves for the entire span.

The current fuel used in the HFIR core consists of 93% by weight Uranium-235 (U^{235}) in a dispersion-type fuel pressed between the aluminum cladding along with a filler material consisting of aluminum and, in the inner fuel element, a burnable poison of Boron[14]. A representation of a single fuel plate with HEU fuel is presented in Fig. 1.4.

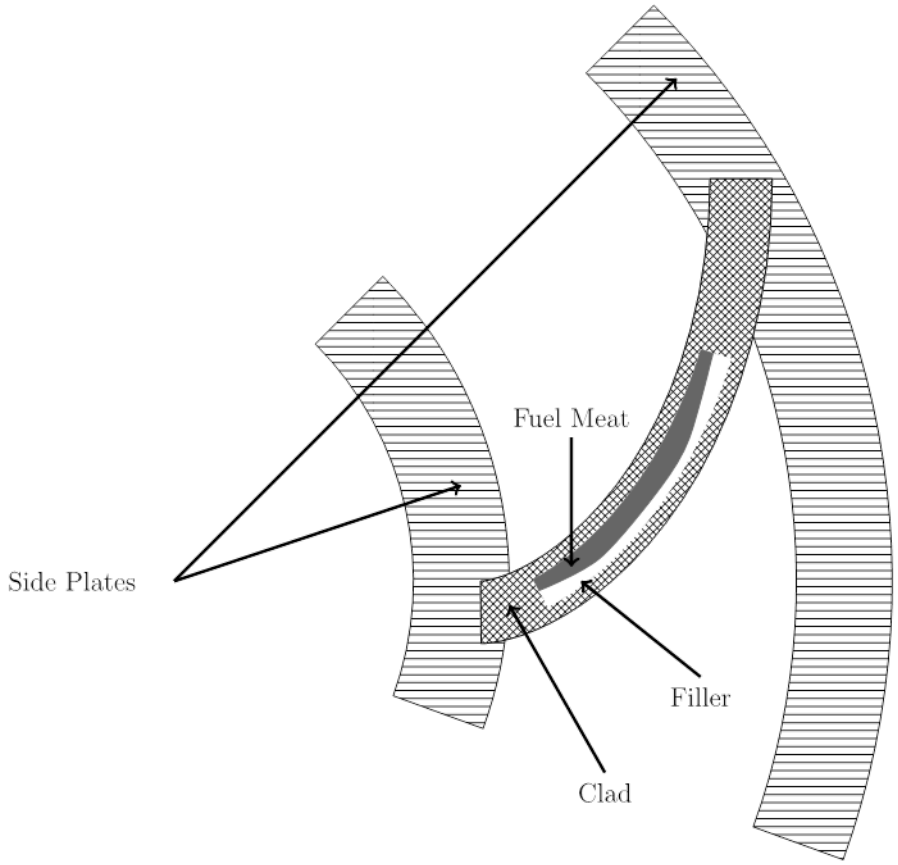

Fig. 1.4. Representative drawing of a single HFIR fuel plate with HEU fuel. (Note that the figure is not drawn to scale).

This fuel profile provides a specific power density profile designed to provide the neutron flux desired within the core and to maintain a safety margin for the entirety of the fuel cycle. The fuel profile for HEU fuel is provided in Fig. 1.5.

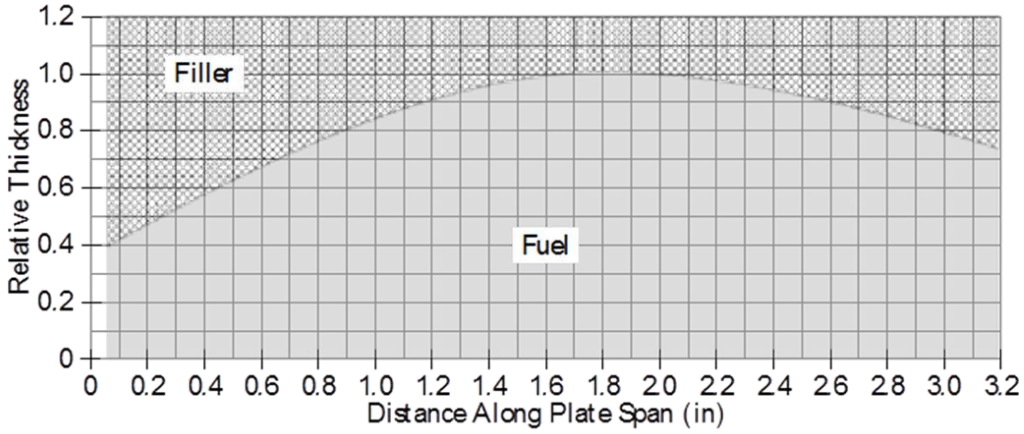

Fig. 1.5. The HEU fuel profile for an inner fuel element.

In order to convert the HFIR to LEU fuel, the internals of the fuel plates must be redesigned and evaluated in order to meet the goals laid out by the GTRI/RERTR. Initial designs have determined that the fuel will be changed from a powdered, dispersion-type fuel to a solid fuel type; the physical properties for the new LEU fuel are described in detail in the INL report by Burkes[15]. A preliminary fuel contour for the LEU fuel proposed for study is provided in Fig. 1.6.

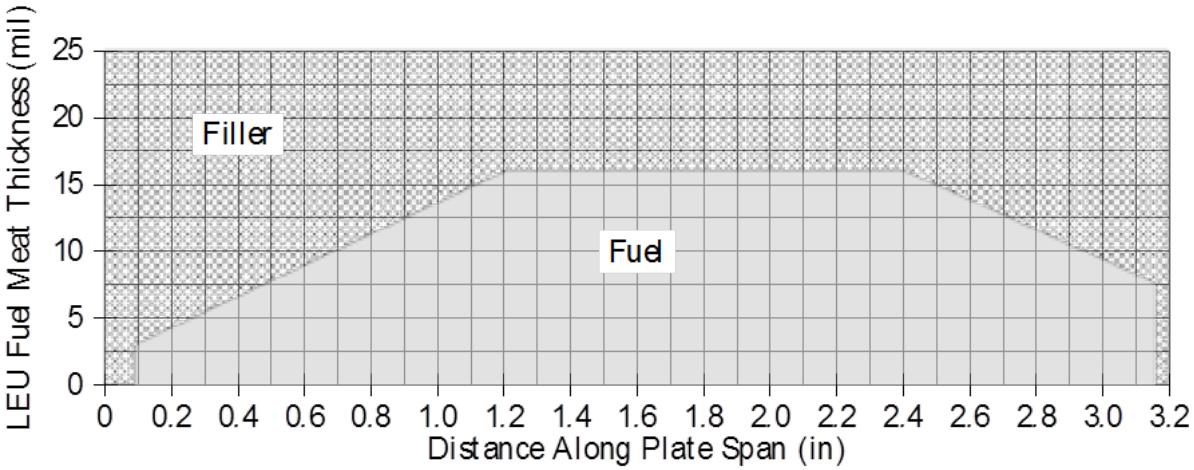

Fig. 1.6. The proposed LEU fuel profile for an inner fuel element.

1.3 COMSOL MULTIPHYSICS SOLVER

As mentioned earlier, in this work, we use COMSOL Multiphysics, which is a finite-element analysis (FEA) commercial software package, to model a number of different coupled physical phenomena relevant to the HFIR. In addition to available built-in solvers such as conjugate heat transfer or fluid-structure interactions, COMSOL [being a generalized partial differential equation (PDE) solver] also allows for the implementation of user-defined physics not provided by its developer. Incorporating the proper boundary conditions between each set of physics allows for the simulation and analysis of very complex systems such as HFIR.

Modern computational fluid dynamic (CFD) simulation, such as that incorporated into COMSOL, in conjunction with conduction modeling in the fuel and cladding, allows coupling of the spatial power distribution in the fuel volume. The multiphysics framework also allows detailed simulation of the impact of fuel manufacturing flaws, fuel cooling channel dimensional variations, and fuel loading uncertainties such that best estimate evaluations of these parameters can be performed.

Past efforts in the analysis of the HFIR core using COMSOL have been mostly limited to thermal-hydraulics[16-25]. More recently, our team has used the solver to model fluid-structure interaction problems[26, 27]. In related work, Jain et al.[28] have simulated coupled thermal-structure interaction phenomena in HFIR. In addition, Chandler[29] incorporated reactor kinetics into the COMSOL code to model the reactions of the LEU fuel for the core.

1.4 ORGANIZATION OF THE REPORT

This report includes continued development of physics, geometric and material models for the COMSOL program. The fuel structure and the coolant are modeled in a computational format allowing coupled solution of the governing thermal-fluid multi-physics equations describing the movement of the nuclear energy from the fuel into the coolant. Also included are the relevant fluid-structure interaction simulation results as well as low-to-high order model coupling studies aimed to improve computing times.

Chapter 2 focuses on two- and three-dimensional conjugate heat transfer modeling of nuclear plates. In addition, predictive capabilities of various turbulent models including the Low-Reynolds number k-ε model (applicable near the solid boundaries), the traditional k-ε model, and the renewed k-ε model are investigated. Three-dimensional single- and multiple-channel models of HFIR fuel plates are developed to evaluate the thermal hydraulic performance.

In Chapter 3, the predictive capabilities of COMSOL in modeling nuclear fuel plate defects including blister and segregation defects are investigated. The work presented in Chapters 2 and 3 constitutes the research carried out Dr. Isaac Bodey (a recent PhD graduate of UTK) for his dissertation[30] under the direction of Prof Rao V. Arimilli.

Chapter 4 reports our team's efforts on modeling fluid-structure interaction phenomena for flat plates as well as more fundamental problems such as elastically mounted circular cylinders in cross flow. The findings presented in this chapter are readily extendible to HFIR plates and will provide useful information for the structural integrity of the future LEU-based fuel plates. Fluid-structure interaction (FSI) model development is still ongoing and will be used to conduct a sensitivity analysis to determine uncertainties associated with mechanical properties, as these are not currently available for the proposed LEU fuel plate designs. Mr. Franklin Curtis, currently a Ph.D. student at UTK, and his advisor Professor Kivanc Ekici are the main contributors to this chapter.

Chapter 5 presents the theory and the numerical results in pairing of two dimensionally inconsistent domains, solid and coolant, through interdimensional model coupling, which was developed in an effort to decrease the computational time of the simulations while ensuring that the accuracy of the simulations are at acceptable levels. Mr. Adam R. Travis, who earned an MS in May 2014, and his advisor Professor Kivanc Ekici are the main contributors to this chapter.

In Chapter 6, additional supporting model/code developments are summarized. In particular, the procedure of importing material properties into COMSOL, parameterization of the HFIR plate involute design, and details about CAD modeling of the proposed LEU plates are reported. The main contributors of these efforts are Mr. Curtis, Mr. Travis and Dr. Bodey.

Finally, Chapter 7 focuses on conclusions, findings and recommendations.

This page intentionally blank.

2.0 CONJUGATE HEAT TRANSFER

Early thermal-hydraulic studies of the HFIR HEU core and its components were carried out using theoretical, numerical, and experimental analysis. These studies were performed for the design power of 100 MW. Many experiments were conducted in order to determine the thermal, hydraulic, and structural safety limits of the HFIR core and core components. Gambill and Bundy[31] performed experiments with diathermic turbulent flows in parallel channels. These experimental results were used to determine friction factors, burnout heat fluxes, and average and local Nusselt number correlations in support of the HFIR program. Cheverton and Sims[32] discuss critical experiments that were used in the design basis of the HFIR core. These experiments were conducted using different material types for the control rods and different core fuel loadings. Cheverton and Kelley[33] performed thermo-structural experiments to determine the expansion characteristics of the fuel plates due to thermal stresses. Data from these and other experimental programs were used in the development of nuclear safety simulations especially those performed by Hilvety and Chapman[34] and McLain[8]. The Steady State Heat Transfer code (SSHTC), developed by Hilvety and Chapman and later modified by McLain was and is still used to determine, numerically, safety limits of the reactor based on both experimental data and theoretical considerations for the original 100MW core and the more recent 85MW core[35]. However, this code does not model the turbulent fluid flow, instead it uses a convection boundary condition with the convection coefficient determined by a modified version of the Hausen correlation for the Nusselt number. Further, the code calculates the change in the bulk fluid temperature, used in the convection boundary condition, by using "suitable heat balances"[8]. A further restriction imposed in the SSHTC is the constraint of diffusion of thermal energy to pass to the fluid in a direction normal to the clad surface only (i.e., thermal energy is not allowed to diffuse in axial and radial directions of the fuel plate).

Modern computational tools allow the user to create more physically accurate models of systems and system components. For example, in the case of the HFIR core, the ability to model the turbulent flow field provides a unique perspective of the thermal hydraulic characteristics of the fuel plate and the flow channels. This unique perspective is discussed in Chapter 3 where fuel defects and their thermal hydraulic consequences are investigated. The proposed conversion of the HFIR to use an LEU fuel provides a unique opportunity to update the computational models used in the analysis of the core and indeed the entire system. As a result, the Research Reactors Division (RRD) of the Oak Ridge National Laboratory (ORNL) decided to use COMSOL for this effort. Version 4.3a of the COMSOL code was used for the computational work found herein. COMSOL provides a suite of finite-element based multiphysics tools for use in the determination of physical quantities in a computational setting.

2.1 2D MODELS AND COMPARISON

The model to be discussed couples the 2-D non-isothermal turbulent flow field with the diffusion of thermal energy within a solid domain. This 2-D modeling analysis was performed to demonstrate, in a relatively simple and controlled way, the influence of variable fluid properties and the influence of distributed thermal energy generation rates on the heat transfer characteristics of the flow field. This portion of the work considers four different situations. First, a constant thermal generation rate is considered with one model employing constant fluid properties and another model using variable fluid properties. Secondly, a distributed thermal generation rate is considered again with two independent models employing constant fluid properties and variable fluid properties.

The plane of interest is that produced by the axial direction and the thickness of the union of one-half of a fuel plate and one-half of a coolant flow channel (i.e., the lateral extent is neglected). The model considers the diffusion of thermal information in the axial direction, however lateral thermal diffusion is inherently prohibited by the dimensionality of the model geometry. Since only two dimensions are represented, the physical processes that would occur in the unrepresented dimension cannot be accounted for in the computational domain (e.g., thermal diffusion) transversal fluid flow, and vortex stretching in this instance. The model results were developed using COMSOL version 4.3a.

2.1.1 2D TCHT Model Geometry and Computational Grid Structure

The simulation geometry for the 2-D TCHT model includes one-half of an inner element fuel plate and one-half of a coolant channel as shown in Fig. 2.1. The fuel plate geometry includes both an active fuel domain and a non-active clad domain. The leading edge of the clad domain has a radius of curvature of 0.025in. (0.635×10^{-4} m), which is consistent with the physical fuel plate of the HFIR. The fluid domain has been extended in both the upstream and downstream directions. The entrance extension in the upstream direction is 0.0267m from the leading edge of the fuel plate. This extension is necessary to allow the flow to adjust to the obstruction presented by the fuel plate. The exit extension in the downstream direction is 0.2539m from the trailing edge of the fuel plate. This extension is necessary to allow the flow to expand and relax the transverse pressure gradient downstream of the fuel plate. This allows one to impose a uniform pressure boundary condition at the global flow outlet of the model.

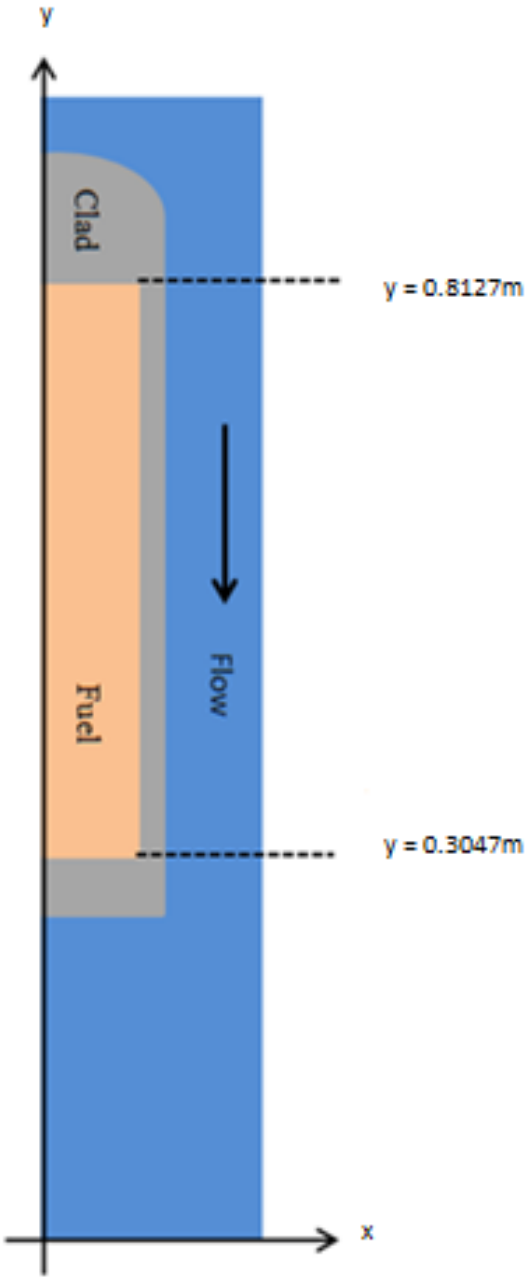

Fig. 2.1. 2-D Turbulent conjugate heat transfer model geometry. The terminal locations of the active portion of the fuel domain are shown for reference. The flow direction is indicated for reference as well. In order to simplify the analysis, $z = 0.8127m - y$ will be used as the flow direction variable.

The inlet boundary condition is set to represent a uniform flow velocity of 7.925 m/s and a uniform temperature of 327 K. Since the model inlet has a larger cross sectional area, the inlet velocity was adjusted to ensure that the nominal flow rate through the core was preserved. The left and right global boundaries are symmetric with respect to flow and heat flux (i.e., the flow velocity vector and the heat flux vector normal to these boundaries are set equal to zero). As stated previously, the global exit boundary is set to a uniform pressure of 377.7 psi (2.606 MPa) which is consistent with the exit pressure of the core system[9]. The global exit boundary is set to a convective outlet for the heat transfer condition. The boundary at the interface between the fuel meat and clad is set with a thermal continuity condition. The boundary at the clad-fluid interface is set with a thermal continuity condition and a no-slip velocity condition. The thermal continuity condition implies that the temperature and heat flux are at least piecewise continuous across the boundary.

The details of the computational grid are associated with the numerically labeled regions of Fig. 2.2. The high aspect ratio of the computational domain prohibits direct visualization of the grid structure. As a result, the grid structure of the different regions indicated in Fig. 2.2 will be discussed in detail so that this structure can be reproduced. It is important to note that there exists a buffer region between Region 2 and Region 3 that is not indicated in Fig.2.2. This buffer region was necessary to consistently connect the grid structure in Region 2 with the grid structure in Region 3. This issue will be discussed shortly. It should be mentioned that the grid structure described below is the product of a significant optimization effort which entailed much trial and error on the part of the author.

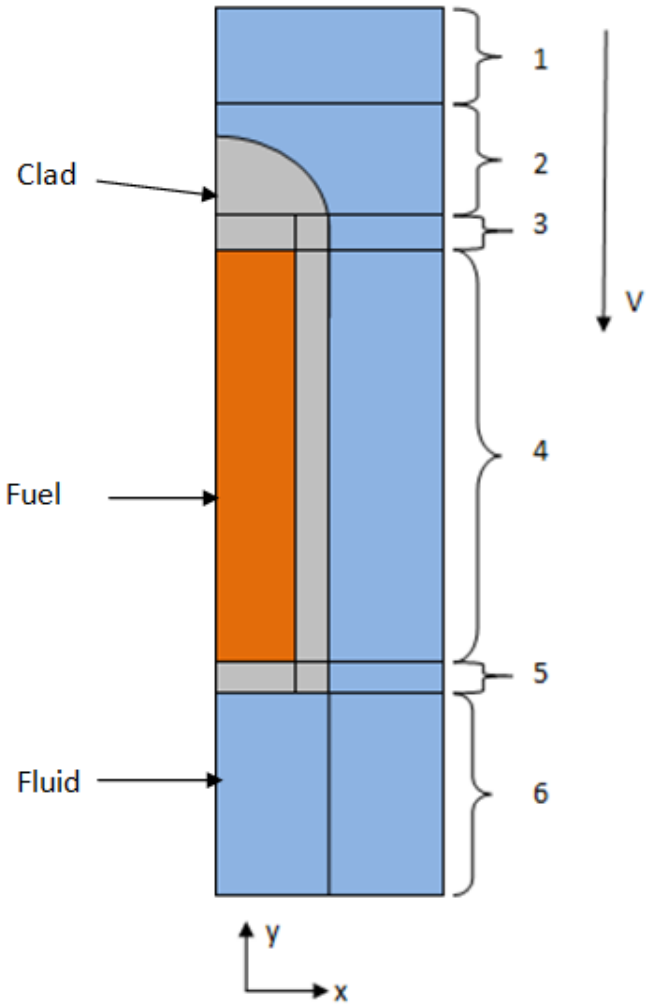

Fig. 2.2. Turbulent conjugate heat transfer model geometry.

The blue domain is the fluid, the grey domain is the clad, and the orange domain is the fuel meat. The boundaries within each individual domain are artificial and used to develop the computational grid. This is not a scale representation of the computational domain. The dimensions have been greatly distorted for visualization purposes since the aspect ratio, axial length/thickness, y/x, is 480.

Region 1 of Fig. 2.2 is discretized using a highly structured quadrilateral mesh (i.e., mapped mesh) with 10 evenly distributed elements in the x-direction and 8 elements in the y-direction distributed with an element ratio of 35. The element ratio prescribes the ratio in size between the last element in a region and the first element in that same region[36]. Therefore, as the element ratio increases the element size decreases from one boundary to the other, e.g. in this instance the last element (i.e., the element closest to the plate within Region 1 of Fig. 2.2) will be 1/35 the size of the first element at the global inlet. This feature is used in Region 1 in anticipation of upstream deviations in the flow field due to the presence of the fuel plate.

The grid in Region 2 of Fig. 2.2 is a composite structure consisting of quadrilateral elements layered along the solid boundary in the fluid domain and triangular elements filling in the remainder of the region,

(i.e., both clad and fluid domains). The triangular grid structure was constructed first to establish the boundary discretization. Then the layered quadrilateral elements (i.e. boundary layer elements) were introduced onto this base structure to capture the development of the boundary layer along the fuel plate. The Region 2 grid structure is shown in Fig. 2.3.

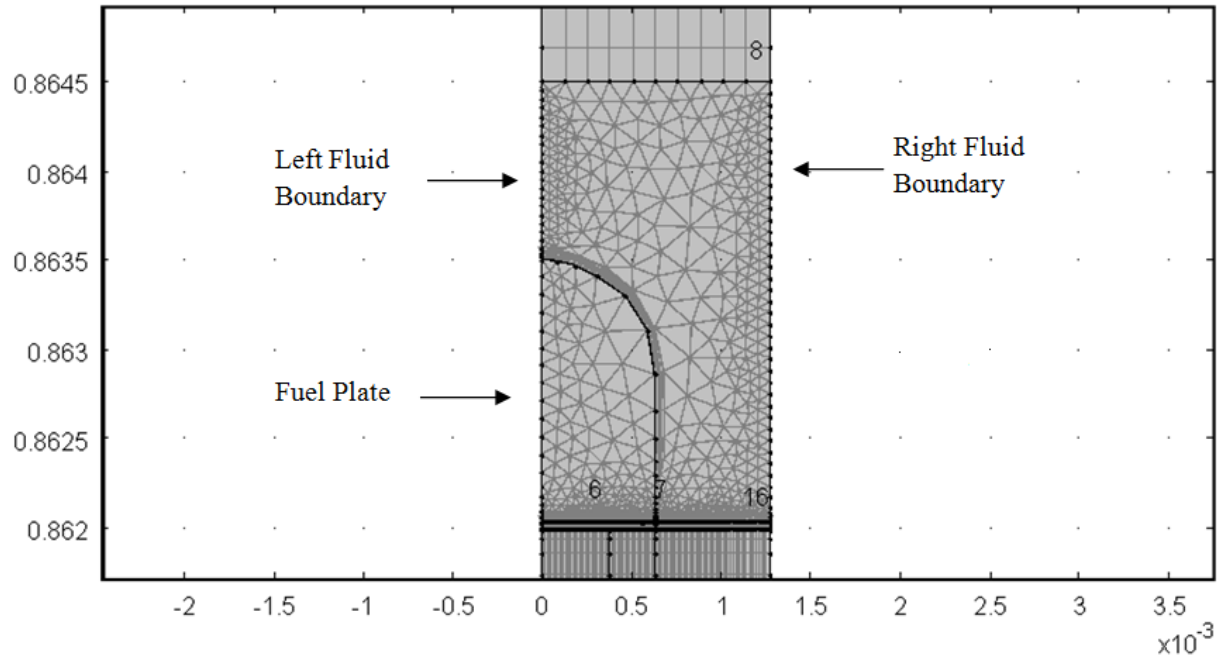

Fig. 2.3. Grid structure of Region 2 (the scale represented here has not been modified).

The Region 1-Region 2 interface has 10 elements which is consistent with the Region 1 distribution. The right fluid boundary of Region 2 has 40 evenly distributed elements, and the left fluid boundary of Region 2 has 20 evenly distributed elements. The higher element density on the left fluid boundary was constructed to provide better resolution for the upstream flow disturbances that would be present due to the fuel plate.

The curved leading edge of the fuel plate (i.e., solid-fluid interface) is discretized with 100 elements. Subsequently, 30 layered quadrilateral elements (i.e., boundary layer elements) are placed along the solid-fluid interface with a stretching factor of 1.1. The stretching factor determines the thickness of each quadrilateral element relative to the previous adjacent element, the succession being in a direction normal to the surface along which the elements are placed[36]. Therefore, a stretching factor of 1.1 adjusts the thickness of elements by 10% relative to the previous element in a direction normal to the solid boundary extending into the fluid domain.

The thickness of the first layer was set to the default value, which is 1/20 of the local domain element height as stated in the COMSOL documentation[36].

There are 80 triangular elements distributed with an element ratio of 15 along the fluid exit boundary of Region 2 (i.e., Region 2-buffer region interface in the fluid domain), which decrease in size as one approaches the fuel plate. This characteristic of the Region 2 grid structure was necessary to remain consistent with the larger mapped structures that exist downstream.

The triangular element structure on the interior of the plate's leading edge does not need to be as dense as the fluid grid structure due to the relatively simple physics to be modeled in that region (i.e., conduction heat transfer). Due to the shared leading edge boundary, the element structure along this boundary is the same as that mentioned previously. The symmetry boundary of the plate in Region 2 has 20 elements. The interface region between Region 2 and the buffer region, however, has a more specific structure due to the downstream mapped grid restrictions. This boundary has 100 evenly distributed elements.

The buffer region contains only triangular elements. The buffer region was constructed due to difficulties matching the different mesh structures in Regions 2 and 3. The element distribution in the x direction of the buffer region is dictated by the Region 2 and Region 3 boundaries. The element distribution in the y direction is governed by the solid-fluid interfacial boundary in the buffer region. This boundary has 40 evenly distributed elements.

Region 3 uses a highly structured quadrilateral grid with high element density at the entrance of the region from the buffer region which decreases into a significantly lower element density at the exit passing into Region 4. Region 3 represents 97 % or 1.94 inches (4.93×10^{-2} m) of the upstream 2 inch (5.08×10^{-2} m) unfueled clad section of the fuel plate and coolant channel.

The solid portion of Region 3 (i.e., the two leftmost artificial domains) has 50 evenly distributed elements in the x direction per domain. The y direction has 50 elements with an element ratio of 355 with element size decreasing in the upstream direction. The distribution in the y direction was chosen to create a smooth transition in the mesh structure from the high element density regions to the reduced element density region of the fueled portion of the fuel plate. Due to the necessity of matching edge discretizations, the fluid domain in this region shares the same distribution in the y direction.

Due to developing velocity boundary layer and thermal boundary layer in Region 4, the mesh structure in the fluid domain of Region 3 is dense at the clad-coolant interface and becomes less dense at the right global boundary of the geometry. The boundary discretization in the x direction in the fluid domain has 80 elements with an element ratio of 15 with size decreasing toward the clad-coolant interface.

The length of the fueled section of the plate is 20 in. (5.08×10^{-1} m). The fueled se
ction is represented by Region 4 in Fig. 2.2. While slight amounts of heat are deposited in the coolant upstream of this region, most of the heat transfer from the nuclear fuel to the coolant occurs in Region 4.

Since the dominant portion of the flow field is in the axial direction, the element density of the flow domain in the axial direction could potentially be significantly reduced. However, there exists a lower limit on the element density which is dictated by the power density profile. The power density profile in the fuel is described in the SSHTC by 27 evenly distributed axial points. The minimum axial element density to obtain proper power density resolution is 1.35 elements per inch or 27 evenly distributed axial elements in Region 4. Region 5 has a similar element density. In Region 5, the element density is rounded up to the nearest integer density value.

The element densities in Region 4 and 5 were iterated by integer multiples of this base density to achieve a grid independent solution. The details of this element density parametric sweep will be discussed at length later.

Region 6 again employs the highly structured mapped mesh. The element density at the trailing edge of the fuel plate is very high due to the need to resolve the strong vortex that resides there. This vortex contributes to the relatively high temperatures that are observed at the trailing edge of the fuel plate through the recirculation of the warm fluid.

The distribution in the x direction is dictated by the shared boundary between Region 5 and Region 6 and thus has the same distribution as Region 4 in that direction. The axial distribution is set to 270 elements with an element ratio of 2000. As the flow redistributes itself after expansion past the fuel plate, it settles and the effects of the plate on the momentum of the fluid are no longer observed. Thus the element density decreases downstream from the plate.

The same grid structure is used in all models (i.e., 563,730 elements). The iterative convergence is set to 1×10^{-6}.

2.1.2 Turbulent Conjugate Heat Transfer (TCHT) Analysis: Constant Heat Flux Case with Constant and Variable Fluid Properties

The discussion regarding the constant heat flux model will use the same model geometry shown in Fig. 2.1. The 2-D TCHT analysis uses the Low Reynold's number k-ε (LRN) turbulence model coupled with thermal diffusion in both the solid and fluid domain. As previously stated, the LRN model allows for the evaluation of thermo-fluid variables through the laminar sublayer of the turbulent boundary layer.

Both the constant fluid property (CFP) case and the NIST fluid property (NFP) case will be discussed. The CFP were evaluated at the average bulk fluid temperature, $\overline{T_b}$ = 347.58 K (i.e., the sum of the inlet and outlet bulk fluid temperature divided by 2) from the NIST Steam Tables[37] and are listed in Table 2.1. The thermal conductivity of the clad, k_{clad}, was set to a value of 167 W/m/K. The thermal conductivity of the fuel, k_{fuel}, was set to a value of 132.06 W/m/K.

Table 2.1: Constant fluid properties evaluated at the average bulk fluid temperature, $\overline{T_b}$ = 347.58 K

Property	Value
Thermal Conductivity, $k(\overline{T_b})$	0.6678 W/m/K
Isobaric Specific Heat, $C_p(\overline{T_b})$	4186.6 J/kg/K
Dynamic Viscosity, $\mu(\overline{T_b})$	3.8133×10^{-4} Pa-s
Mass Density, $\rho(\overline{T_b})$	976.54 kg/m^3

The NFP were determined from the NIST Steam Tables and established as look-up tables in the COMSOL environment over the temperature range 320.00 K < T < 394.26 K, and over the pressure range 2.5 MPa < P < 3.5 MPa. These ranges encompass the standard operational range of the HFIR. It is important to note that the fluid properties (i.e., mass density, isobaric specific heat capacity, viscosity, and thermal conductivity) are relatively insensitive to pressure variation over the aforementioned range. For completeness, the variation of the mass density, isobaric specific heat capacity, thermal conductivity, and molecular viscosity with respect to the pressure was found to be of order 10^{-7}, 10^{-6}, and 10^{-10}, respectively. The property variation with respect to temperature, however, is much more pronounced. The variation of the mass density and the isobaric specific heat capacity with respect to the temperature is of order 1. The variation in the thermal conductivity and the molecular viscosity with respect to temperature is of order 10^{-4} and 10^{-3}, respectively. Therefore, the fluid properties are assumed to be a function of the fluid temperature only since a negligible effect is expected from fluid pressure variance.

Theoretical developments show that as the flow becomes thermally fully developed[38]; i.e.,

$$\frac{d}{dz}\left[\frac{T_s(z)-T_f(x,z)}{T_s(z)-T_b(z)}\right] \rightarrow 0, \quad (2.1)$$

the convection coefficient becomes constant for the constant heat flux constant fluid property (CFP) case using the bulk fluid temperature as the reference temperature in Newton's law of cooling. Here $T_f(x,z)$ is the fluid temperature, $T_s(z)$ is the clad surface temperature, and $T_b(z)$ is the bulk fluid temperature. The flow direction variable, z, is defined as

$$z \equiv y_{EAR} - y \quad (2.2)$$

here y_{EAR} is the location of the entrance to the active region (i.e., $y_{EAR} = 0.8127m$) as shown in Fig. 2.1. The introduction of this flow direction variable makes it easier on the reader to understand the subsequent figures.

It is instructive to discuss the calculation of the bulk fluid temperature, T_b, at this point as it plays a fundamental role in what follows. The bulk fluid temperature is a marginal distribution in the mathematical sense (i.e.,,

$$T_b(z) \equiv \frac{1}{\dot{m}\overline{C_p}}\int_{x_s}^{x_{mp}} \rho\left(T_f(x,z)\right) C_p\left(T_f(x,z)\right) u(x,z) T_f(x,z) dx \quad (2.3)$$

Here the limits of the integration procedure are from the heated surface, x_s, to the flow channel midplane, x_{mp}. To use this definition of the bulk fluid temperature to determine its distribution in the flow direction requires one to perform the integration at different locations in the flow direction. In the COMSOL model, this integration was performed at 51 uniformly spaced locations along the flow direction (i.e.,

$$z_{n+1} = y_{ear} - \left(0.508/50\right)n; \quad n = 0 \cdots 50 \quad (2.4)$$

Another way to represent the bulk fluid temperature follows from the relationship for the total power supplied to the fluid up to position z.

$$\int_0^{A_{HT}} q''(x,z) dA_{HT} = \dot{m}\overline{C_p}\int_{T_b(0)}^{T_b(z)} dT_b \quad (2.5)$$

Here $A_{HT}$is the heat transfer area. Since only a single surface is heating the fluid in the model, the heat transfer area is L*z, however, the 2-D model assumes a lateral length of unity. Therefore, Equation 2.6 may be written as

$$\int_0^z q'' dz = \dot{m}\overline{C_p}\int_{T_b(0)}^{T_b(z)} dT_b. \quad (2.6)$$

Carrying out the integration in Equation 2.6 for the constant heat flux case and rearranging the symbols yields the following relationship for the bulk fluid temperature distribution in the flow direction

$$T_b(z) = \left(\frac{q''}{\dot{m}C_p}\right) z + T_b(0). \quad (2.7)$$

This relationship is significantly easier to evaluate than that shown in Equation 2.3. For instance, consider the constant heat flux with NIST fluid properties (NFP) case; all quantities in the integrand of

Equation 2.3 are variable and therefore must be evaluated at each location, however, in Equation 2.3, only the specific heat capacity of the fluid needs to be evaluated. It will be shown that the two forms of the bulk fluid temperature yield identical results as one would expect. It is important to note that if the heat flux is distributed along the flow direction then one must either be able to represent the heat flux distribution using common mathematical functions or employ a quadrature rule to evaluate the heat flux integral in Equation 2.6. This case of a distributed heat flux will be discussed in Section 2.1.3.

The constant convection coefficient is due to the parallel nature of the affine functions associated with the solid surface temperature and the bulk fluid temperature in the thermally fully developed region for the constant heat flux case (i.e. the temperature difference between the clad and the bulk fluid is constant). Using Newton's law of cooling, the definition of the convection coefficient is

$$\boldsymbol{h(z)} \coloneqq \frac{\boldsymbol{q_s''}}{\boldsymbol{T_s(z)-T_b(z)}}. \quad (2.8)$$

Here $\boldsymbol{q_s''}$ is the constant clad surface heat flux and $\boldsymbol{h(z)}$ is the convection coefficient as a function of the flow direction. The derivative of the convection coefficient in the flow direction is calculated to be

$$\frac{\boldsymbol{dh}}{\boldsymbol{dz}} = \frac{\boldsymbol{1}}{\boldsymbol{[T_s(z)-T_b(z)]}}\frac{\boldsymbol{dq_s''}}{\boldsymbol{dz}} - \frac{\boldsymbol{q_s''}}{\boldsymbol{[T_s(z)-T_b(z)]^2}}\frac{\boldsymbol{d}}{\boldsymbol{dz}}\boldsymbol{[T_s(z)-T_b(z)]}. \quad (2.9)$$

However, since a constant heat flux is being considered here, the first term evaluates to zero which leaves

$$\frac{\boldsymbol{dh}}{\boldsymbol{dz}} = -\frac{\boldsymbol{q_s''}}{\boldsymbol{[T_s(z)-T_b(z)]^2}}\frac{\boldsymbol{d}}{\boldsymbol{dz}}\boldsymbol{[T_s(z)-T_b(z)]}. \quad (2.10)$$

Therefore, it is determined that the change in the convection coefficient in the flow direction is inversely proportional to the square of the temperature difference between the clad surface and the bulk fluid, and directly proportional to the change of this temperature difference in the flow direction. Further, the relationship in Equation 2.10 indicates that the convection coefficient is a decreasing function of the flow direction, given that the surface temperature is larger than the bulk fluid temperature (i.e., the slope of the derivative of the convection coefficient is negative). Equation 2.10 further implies that if the temperature difference between the clad surface and bulk fluid is constant then the convection coefficient does not change in the flow direction and as a result remains constant. The temperature difference between the clad-surface and the bulk-fluid for both the CFP and NFP case is shown in Fig. 2.5 as a function of the hydraulic diameter normalized flow direction. From Fig. 2.4 one notices that the flow for the CFP case [i.e., (T_s-T_b)-CFP] becomes fully thermally developed at approximately 20 D_h. Also from Fig. 2.4, one notices that the temperature difference between the clad surface and the bulk fluid for the CFP case is indeed constant over most of the heated region with the exception of the entrance to the heated region where the flow is thermally developing. Therefore, one should expect the convection coefficient based on the bulk fluid temperature to be constant over most of the heated region with the exception of the thermal entry length where the convection coefficient should decrease to its constant value. These characteristics of the convection coefficient for the CFP case, h:(T_s-T_b)-CFP, are shown in Fig. 2.5. The increase in the convection coefficient for the CFP case that occurs at $\boldsymbol{z/D_h = 200}$ is due to the difference in temperature (i.e., $\boldsymbol{T_s - T_{bulk}}$, decreasing and the fact that the heat flux has not significantly decreased at this location).

For the NIST fluid property (NFP) constant clad surface heat flux case, Fig. 2.4 shows that the temperature difference between the clad surface and the bulk fluid is a decreasing function of the flow direction over most of the heated section. This is due to the increase in the thermal conductivity of the fluid with increasing temperature. As the thermal conductivity increases, more thermal energy is passed from the clad surface to the fluid. This has two effects: one, it increases the fluid temperature which further increases the fluid thermal conductivity, and two, the clad surface temperature increase is not as pronounced as it is in the CFP case. As a result, the clad surface temperature increases at a slower rate than the bulk fluid temperature and the representative affine functions are no longer parallel, thus resulting in a decreasing temperature difference between the clad surface and the bulk fluid, as observed in Fig. 2.5. Equation 2.10 demonstrates that the convection coefficient should increase due to its dependence on the inverse of the square of the temperature difference between the clad surface and the bulk fluid. This characteristic of the convection coefficient based on NFP is shown in Fig. 2.5 as the h:(T_s-T_b)-NFP data.

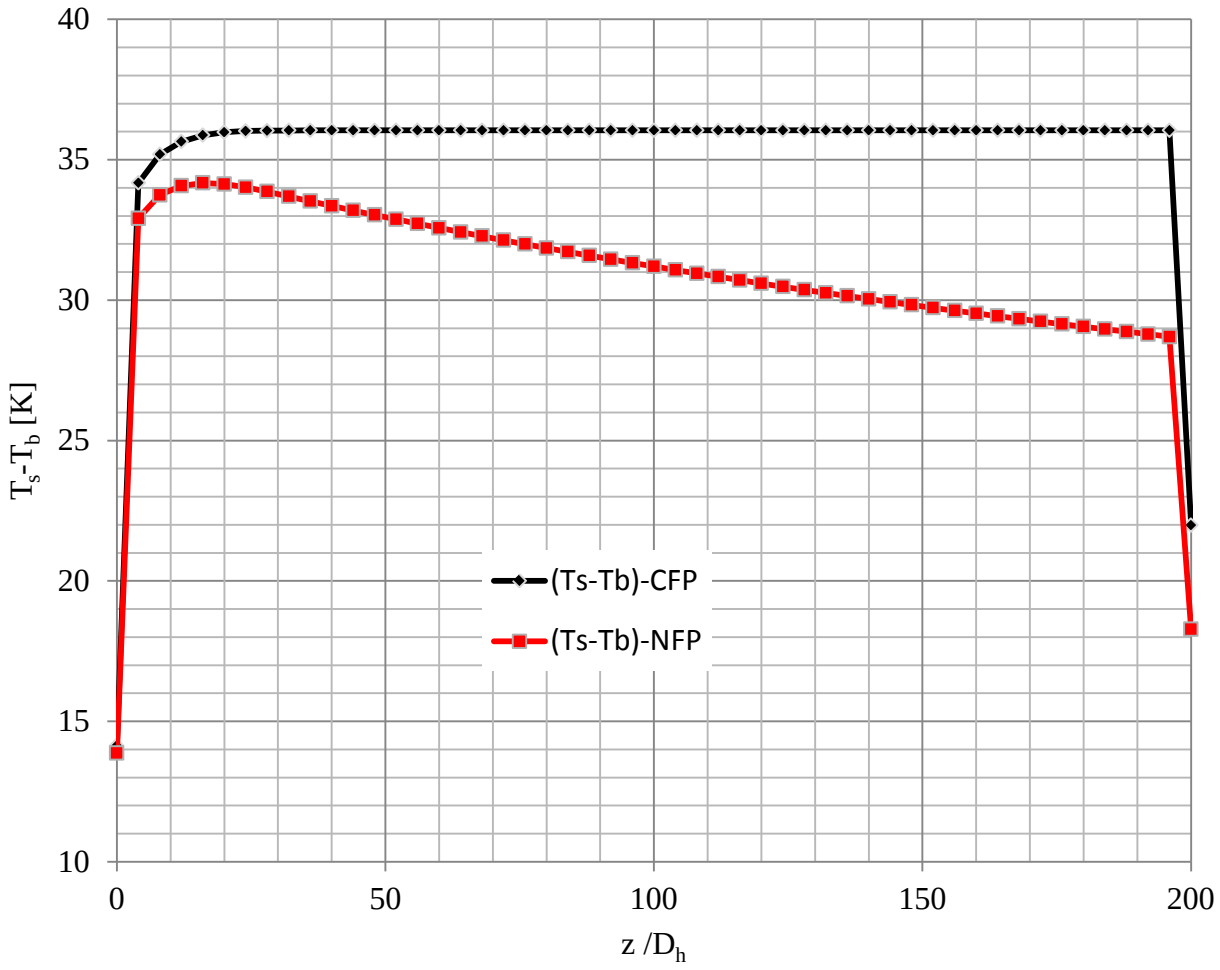

Fig.2.4. Temperature difference between the clad surface and the bulk fluid for constant fluid properties (CFP) and NIST fluid properties (NFP). One notices that the system becomes fully thermally developed at approximately 20 D_h for the CFP case.

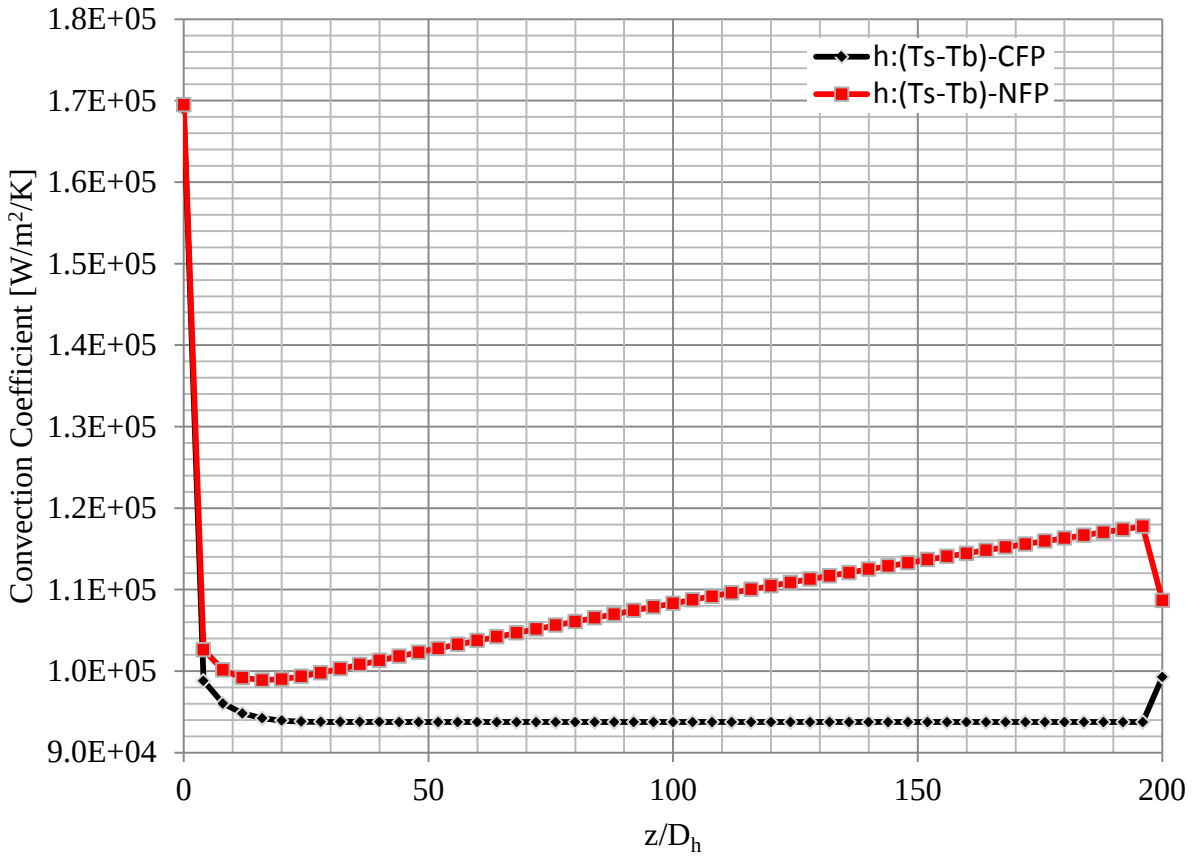

Fig. 2.5. Convection coefficient for constant fluid properties (CFP) and NIST fluid properties (NFP). The two outliers occurring at z = 200D_h is due to end effects where the end of the active region resides.

The distribution difference between the cross-sectional fluid temperature and the inlet bulk fluid temperature for the CFP case, $\boldsymbol{\Theta_{CFP}} = \boldsymbol{T_{f_{CFP}}}(\boldsymbol{x},\boldsymbol{z}) - \boldsymbol{T_{in}}$, is shown in Fig. 2.6 at several axial locations in the active section of the model. This plot shows the penetration of the thermal information from the heated surface into the flow field. From Fig.2.6, one notices that thermal information from the clad surface does not reach the channel mid-line before z = 5D_h. A similar plot is shown in Fig. 2.7 for the NFP case, $\boldsymbol{\Theta_{NFP}} = \boldsymbol{T_{f_{NFP}}}(\boldsymbol{x},\boldsymbol{z}) - \boldsymbol{T_{in}}$. Again, the thermal information from the clad surface reaches the channel mid-line at z = 5D_h.

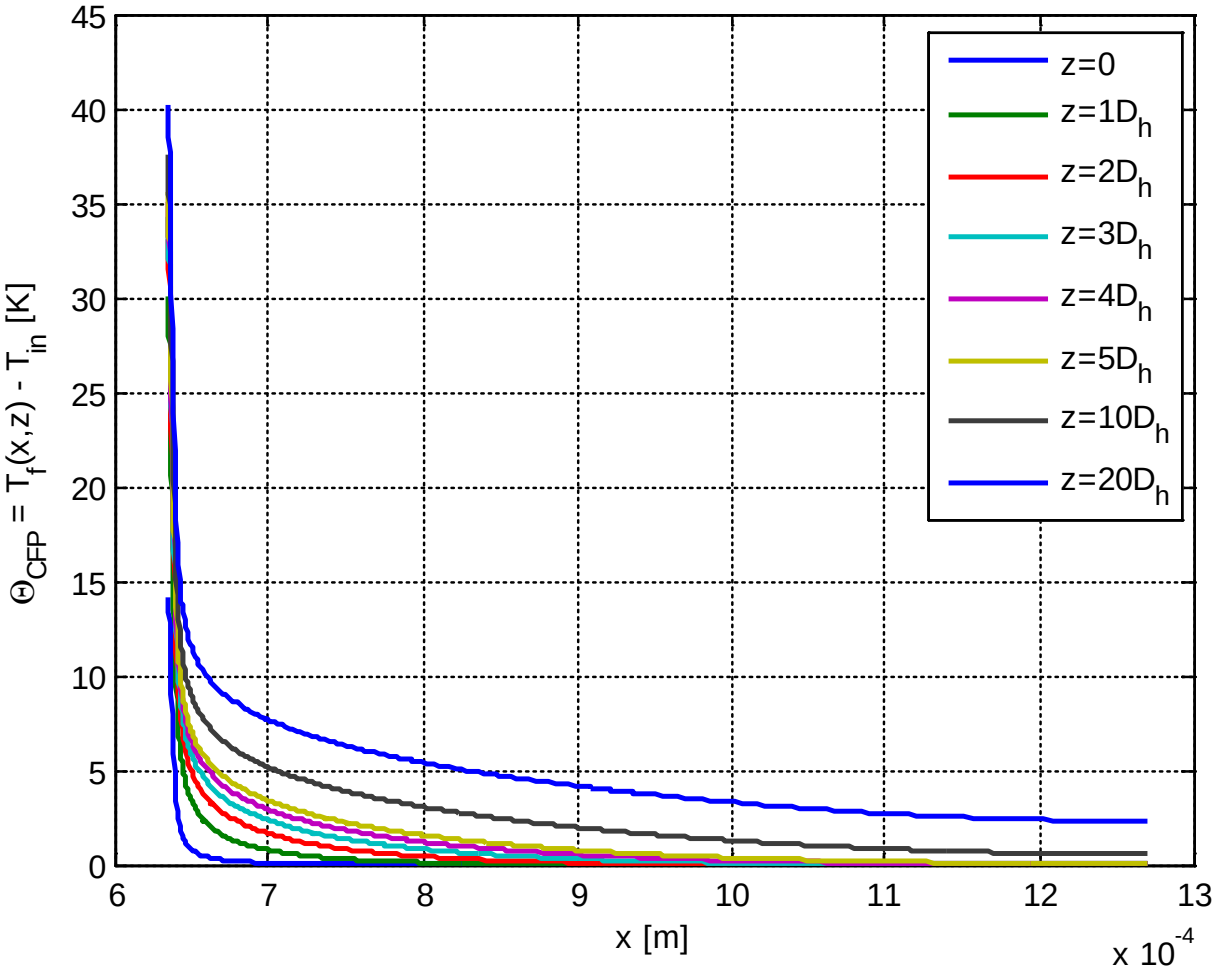

Fig. 2.6. Variation in the direction normal to flow direction (x) of the difference between the Local Fluid Temperature [Tf(x,z)] and the Inlet Bulk Fluid Temperature (Tin) for the Constant Fluid Property Case at Various Axial Locations Along the Heated Section of the Simulation Geometry. The x-coordinate begins on the clad surface (i.e.,. x = 6.35×10-4 m) and extends to the fluid mid-channel (i.e., x = 12.7×10-4 m). The heating effect of the clad surface reaches mid-channel for $z \geq 5Dh$.

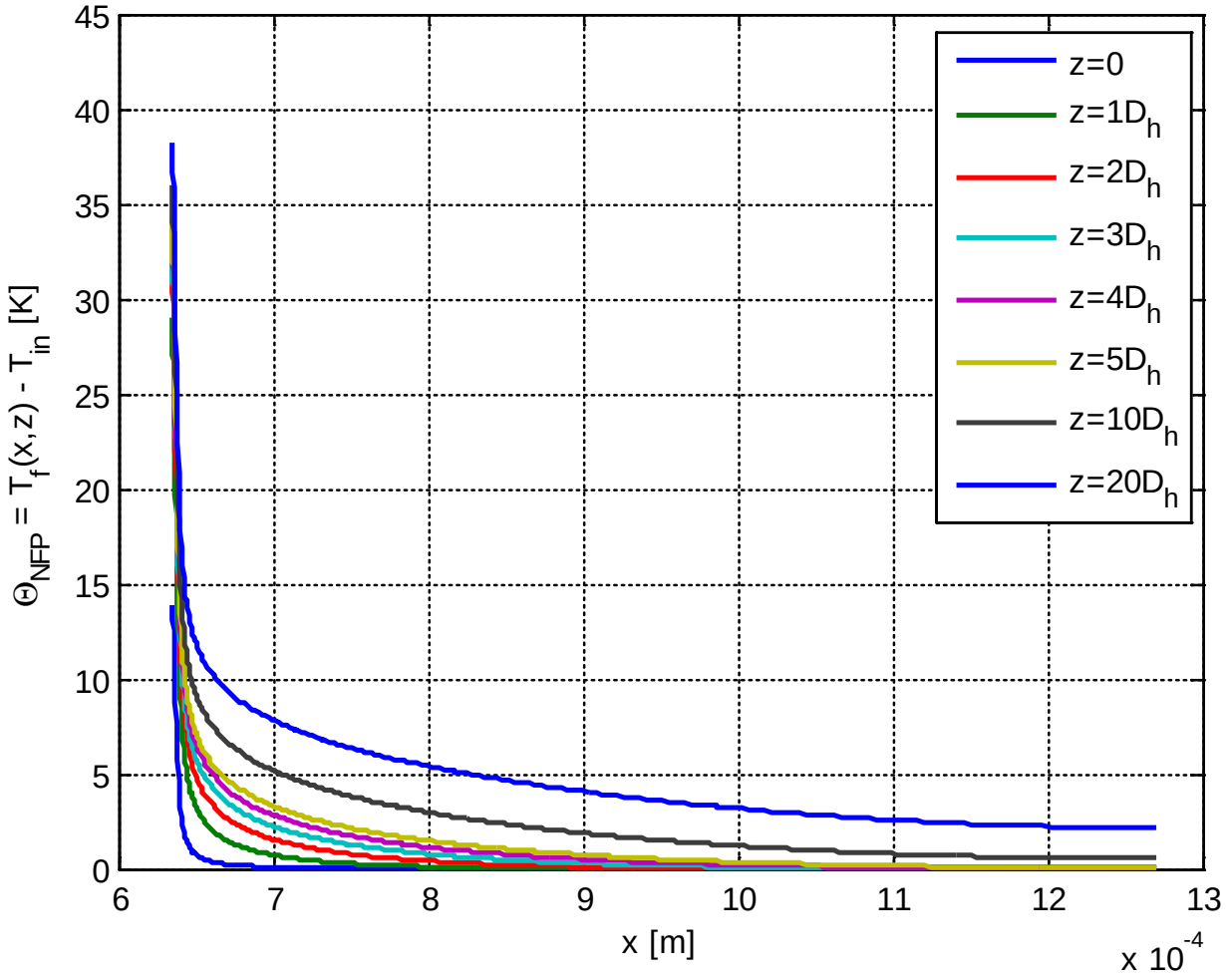

Fig. 2.7. Variation in the direction normal to flow direction (x) of the difference between the local fluid temperature and the inlet bulk fluid temperature for the variable fluid property case (NFP) at various locations along the heated section of the simulation geometry. The x-coordinate begins on the clad surface (i.e., x = 6.35×10^{-4}m) and extends to the fluid mid-channel (i.e., x = 12.7×10^{-4}m). The heating effect of the clad surface reaches mid-channel for $z \geq 5D_h$.

The difference between $\boldsymbol{\Theta_{CFP}}$ and $\boldsymbol{\Theta_{NFP}}$ is shown in Fig. 2.8. This plot translates into a difference between the fluid temperature for the CFP case and the fluid temperature for the NFP case [i.e., $\boldsymbol{\Theta_{CFP} - \Theta_{NFP} = T_{f_{CFP}}(x,z) - T_{f_{NFP}}(x,z)}$]. Figure 2.8 provides visual evidence of the differences between Figs. 2.6 and 2.7. It shows that at the wall (i.e., x = 6.35×10^{-4} m) the CFP fluid temperature is higher than the NFP fluid temperature for all values of z represented. One notices from Fig. 2.8 that as one proceeds in the axial direction, the value of $\boldsymbol{\Theta_{CFP} - \Theta_{NFP}}$ increases. This is due to the lower thermal conductivity of the fluid in the CFP case relative to the NFP case. Since the fluid thermal conductivity is lower in the CFP case the surface temperature is higher which implies that the fluid adjacent to the wall will also have a higher temperature than the NFP case. However, a short distance away from the wall in the normal direction, the NFP fluid temperature becomes higher and thermal energy penetrates further into the flow field as indicated by the negative values of $\boldsymbol{\Theta_{CFP} - \Theta_{NFP}}$ in conjunction with the extent of this negative region in the flow direction. This is a direct consequence of the increase in the fluid thermal conductivity with increasing temperature (i.e., more thermal energy is allowed to pass from the heated surface to the

fluid thus increasing the fluid temperature relative to the CFP case and as a result increase the thermal conductivity). The curves then again pass to positive values of $\boldsymbol{\Theta_{CFP} - \Theta_{NFP}}$which indicate that CFP fluid temperature is again higher in magnitude than the NFP fluid temperature.

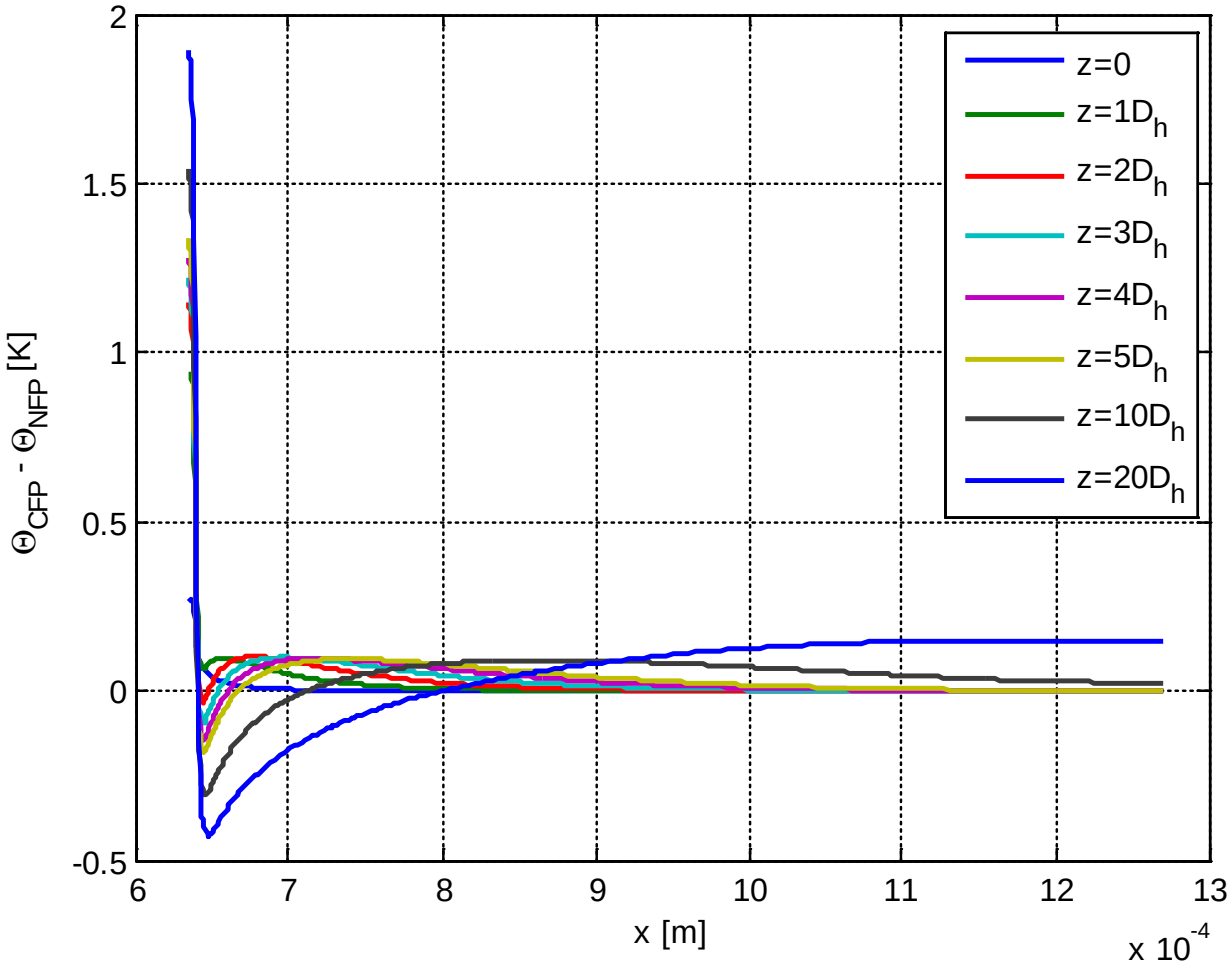

Fig. 2.8. The distribution of the Difference between the local fluid temperature for the constant fluid property case (CFP) and the variable NIST fluid property (NFP) case at different axial locations.

For completeness the flow direction variation of clad surface temperatures and the bulk fluid temperatures for both the CFP case and the NFP case are shown in Fig. 2.9. This figure shows that it is indeed the surface temperature that is most affected by the use of variable fluid properties (i.e., a clad surface temperature difference of 8K is observed at the exit of the active region between the two cases. Further, one observes that the rate of increase in the bulk fluid temperature for the NFP case is negligibly smaller than the CFP case. Therefore, the affine temperature functions (i.e., clad surface temperature and bulk fluid temperature) for the NFP case are indeed not parallel with the difference in the two temperatures decreasing in the flow direction. Further, the average bulk fluid temperature (i.e., $\overline{\boldsymbol{T}}_{\boldsymbol{b}} = \mathbf{347.58}\ \boldsymbol{K}$) is shown to be lower in magnitude than the surface temperature with the exception of the axial location z = 0 which was used in the explanation of Fig. 2.8. The temperature characteristics shown in Fig. 2.9 imply that the use of constant fluid properties for systems with constant heat flux and moderate bulk fluid temperature rises (i.e., $\boldsymbol{\Delta T_b \leq 40\ K}$) produce conservative (i.e., higher) estimates of the clad surface temperature. Another advantage of the use of constant properties relative to the use of variable properties is the reduction in computational expense. Variable properties are introduced into the computational environment either as look up tables or as analytical functions. During the computational process, the looks up tables are interpolated between thermodynamic states or the analytical functions are evaluated as needed for each computational node at each iteration of the computation. A typical grid structure is, at least, of the order of 10^5 nodes with iterations of the order 102 for convection problems, therefore, the evaluation of variable material properties is highly expensive in the computational sense. From the convection coefficient, one can form the Nusselt modulus by using its definition,

$$\boldsymbol{Nu_D \equiv \frac{hD_h}{k_f}} \quad \text{.....(2.11)}$$

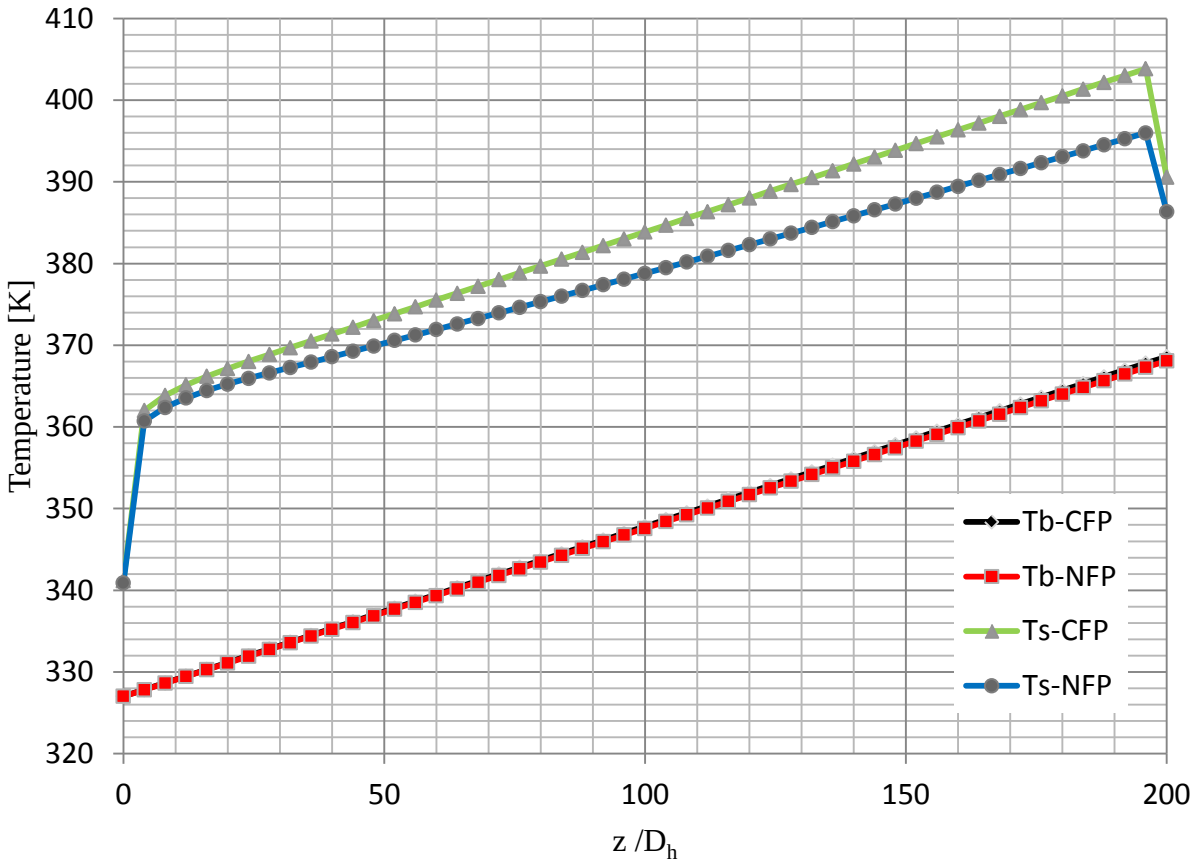

Fig. 2.9. Clad surface temperatures and bulk fluid temperatures for both for the constant fluid property (CFP) and the variable NIST fluid property (NFP) cases.

$$\boldsymbol{Nu_D \equiv \frac{hD_h}{k_f}}.$$

For the CFP case, as shown in Fig. 2.5, the convection coefficient is constant with a numerical value of 93,748.65 W/m^2/K. This value of the convection coefficient composed with the thermal conductivity evaluated at the average bulk fluid temperature (i.e., k = 0.6678 W/m/K) and the hydraulic diameter of the flow channel (i.e., 2.54×10^{-3}m) in a manner consistent with Equation 2.11) yields a value of 356.58 for the model Nusselt modulus. This value will now be compared with other well-known Nusselt correlations for which the system characteristics are consistent.

The Sieder-Tate correlation for the Nusselt modulus has the following form for use under the indicated conditions[38],

$$\boldsymbol{Nu_D = 0.027\, Re_D^{4/5}\, Pr^{1/3} \left(\frac{\mu}{\mu_w}\right)^{0.14}} \qquad \begin{cases} \boldsymbol{0.7 \le Pr \le 16,700} \\ \boldsymbol{Re_D \ge 10,000} \\ \boldsymbol{\frac{z}{D_h} \ge 10} \end{cases} \quad \text{.....(2.12)}$$

Here Re is the Reynolds number and Pr is the Prandtl number. The Prandtl number is calculated using the following relationship

$$\boldsymbol{Pr} = \frac{\boldsymbol{\mu C_p}}{\boldsymbol{k_f}} \quad (2.13)$$

This composite structure yields a value of 2.391 for the Prandtl number. The Reynolds number can be calculated using the mass flow rate.

$$\boldsymbol{Re} = \frac{\dot{\boldsymbol{m}} \boldsymbol{D_h}}{\boldsymbol{\mu A_c}} \quad (2.14)$$

Since the model in question uses CFP, the ratio of viscosities in Equation 3.56 is unity. Substituting relationships (2.13) and (2.14) into (2.15) , the Nusselt modulus has the value 369.95. The Sieder-Tate relationship, Equation 2.12), yields a relative difference of 3.75% with the Nusselt modulus calculated from the model results. This relative difference is calculated using the following structure

$$\boldsymbol{RD} = \left(\frac{\boldsymbol{Nu_{D_{COMSOL}} - Nu_{D_{ST}}}}{\boldsymbol{Nu_{D_{COMSOL}}}}\right) \times \boldsymbol{100} \quad (2.15)$$

Another Nusselt modulus correlation that is compatible with the given model was provided by Gnielinski[38]. This correlation has the following form

$$\boldsymbol{Nu_D} = \frac{(\boldsymbol{f/8})(\boldsymbol{Re_D - 1000})\boldsymbol{Pr}}{\boldsymbol{1 + 12.7(f/8)^{1/2}(Pr^{2/3} - 1)}} \quad \begin{cases} \boldsymbol{0.5 \leq Pr \leq 2000} \\ \boldsymbol{3000 \leq Re_D \leq 5 \times 10^6} \\ \boldsymbol{\frac{z}{D_h} \geq 10} \end{cases} \quad (2.16)$$

where $\boldsymbol{f}$ is the Darcy friction factor given by [**38**]

$$\boldsymbol{f = 0.184\, Re_D^{-1/5}} \quad \{\boldsymbol{Re_D \geq 2 \times 10^4} \quad (2.17)$$

The Gnielinski correlation for the Nusselt modulus yields a value of 377.62, which results in a relative difference of 5.90% with the model Nusselt modulus. The Hausen equation (i.e., Equation 2.3) yields a value of the Nusselt modulus of 372.62. This results in a relative difference of 4.50% with the model Nusselt modulus.

While the Seider-Tate, the Gnielinski, and the Hausen correlations agree well with the model Nusselt modulus, the information suggests that the Seider-Tate correlation is more representative of the HFIR system. This conclusion will also be drawn for the NFP case.

The NFP case is less straightforward than the CFP case. Given the variable nature of the fluid properties, the Reynold's number and the Prandtl number become distributed in the flow direction. Therefore, a local Nusselt modulus, in terms of the aforementioned correlations, will be distributed in terms of the previously mentioned dimensionless structures. The model Nusselt modulus will be distributed due to the distribution of the local convection coefficient and the thermal conductivity of the fluid.

A choice has to be made regarding how the fluid properties are to be evaluated for use in calculations (i.e., should the fluid property be evaluated at the local bulk fluid temperature or the local wall temperature). More specifically, what effect does this choice have on the local Nusselt modulus regarding the temperature dependent thermal conductivities? Using Equation 2.11, one can establish a ratio test to gain some qualitative idea of this effect on the local Nusselt modulus.

$$\frac{Nu_D(T_s)}{Nu_D(T_b)} = \frac{h_{Tb}D_h}{k_f(T_s)}\frac{k_f(T_b)}{h_{Ts}D_h} \quad (2.18)$$

Using Equation (2.8) (i.e., the definition of the convection coefficient) one finds, as expected, that $h_{Tb} = h_{Ts}$; therefore, Equation 2.18 results in

$$\frac{Nu_D(T_s)}{Nu_D(T_b)} = \frac{k_f(T_b)}{k_f(T_s)} \quad (2.19)$$

With the knowledge that $T_s > T_b$, one observes that the ratio of thermal conductivities is less than unity, for the heated wall case, and thus $Nu_D(T_s) < Nu_D(T_b)$. Physically, since the convection mechanism is driven by thermal phenomena at the heated surface, it stands to reason that the thermal conductivity of the fluid should be evaluated at the heated surface temperature [i.e., $k_f = k_f(T_s)$.].

The Nusselt modulus – Prandtl number (NP) ratio is plotted as a function of the Reynold's number in Fig. 2.10. The designation after the colon, in the legend of Fig. 2.10, represents the source of the Nusselt modulus (i.e., C ~ COMSOL, G ~ Gnielinski, ST ~ Sieder-Tate, H ~ Hausen). The model Nusselt modulus for the NFP case is larger in magnitude than the other correlations. This implies that the aforementioned Nusselt moduli provide larger surface temperatures, with the Gnielinski correlation providing the largest surface temperatures of the group. One notices, that again, the Sieder-Tate correlation provides the most similar results to the (COMSOL) model Nusselt number. Figure 2.11 shows the relative difference (i.e., Equation 2.15) between the aforementioned Nusselt correlations and the model Nusselt number.

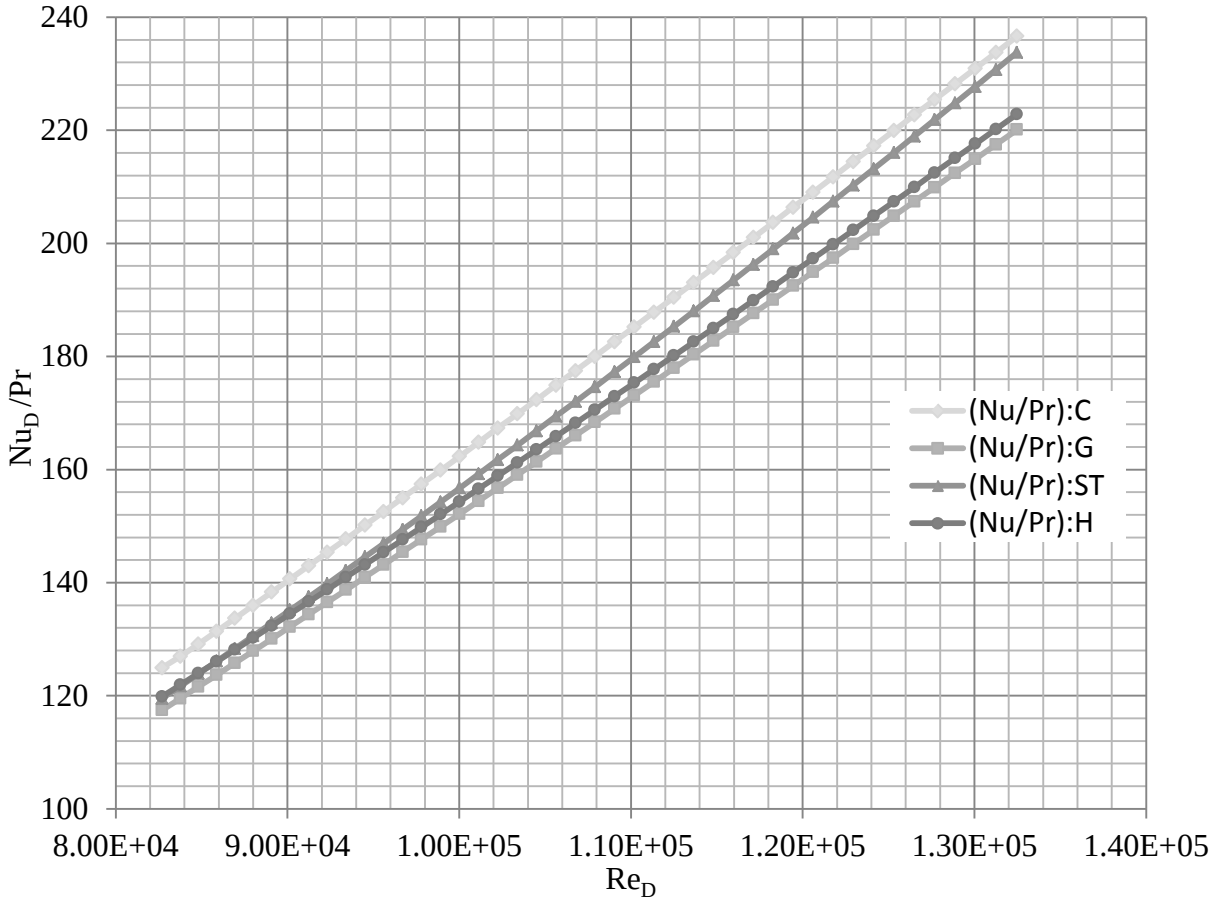

Fig. 2.10. Comparison of the Nusselt Modulus – Prandtl Number Ratio as a function of the Reynold's Number. To clarify the legend: C ~ COMSOL, G ~ Gnielinski, ST ~ Sieder-Tate, H ~ Hausen.

Figure 2.11 shows that for increasing Reynolds numbers the relative difference between the Sieder-Tate correlation and the model value decreases, again showing that the Sieder-Tate correlation is more representative of the model in question. The lower bound of the relative difference for the Sieder-Tate correlation is 1.2% for a Reynolds number of 1.32×10^5 and an upper bound of 4.3% for a Reynolds number of 8.27×10^4. The relative difference between the Hausen correlation and the model Nusselt modulus is shown to increase with increasing Reynolds number. The relative difference for the Hausen correlation has a lower bound of 3.8% for a Reynolds number of 8.27×10^4 and an upper bound of 5.9% for a Reynolds number of 1.32×10^5.

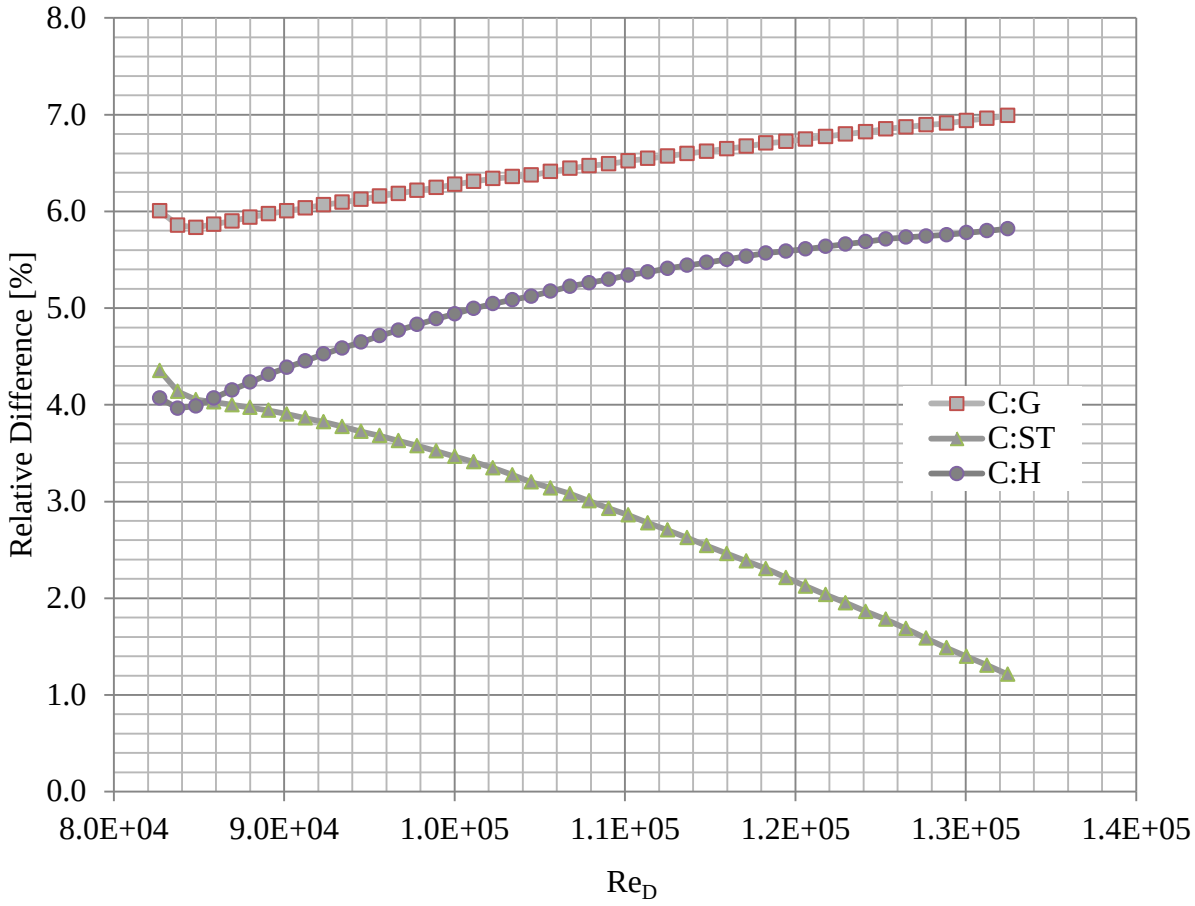

Fig. 2.11. Relative differences of the Gnielinski, Sieder-Tate, and Hausen correlations compared with the (COMSOL) model Nusselt modulus.

To complete the constant heat flux section, the surface temperature distributions derived from the Gnielinski, Sieder-Tate, and the Hausen correlations compared with the COMSOL determined surface temperature are shown in Figs. 2.12 and 2.13 for the CFP case and the NFP case, respectively. For the CFP case, it is observed that the COMSOL determined surface temperature is higher and thus more conservative than those surface temperatures derived from the correlations. This is to be expected since the model Nusselt modulus for the CFP case was lower in magnitude than the correlation values. On the other hand, for the NFP case, the COMSOL determined surface temperature distribution is lower in magnitude than the distributions derived from the correlations. This too was expected since it was shown that the correlations produce Nusselt moduli of lower magnitude than that derived from the model.

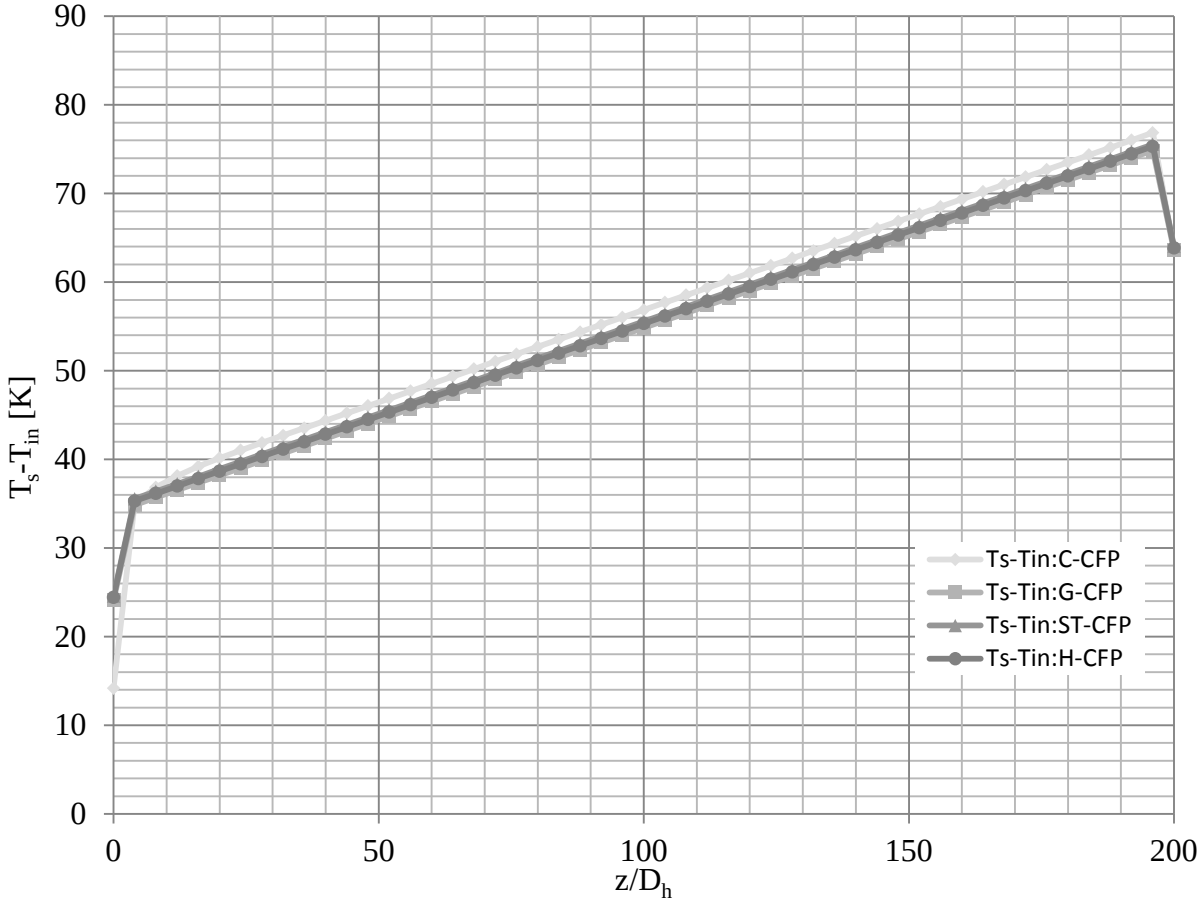

Fig. 2.12. Difference between the surface temperature and the inlet bulk fluid temperature as derived from the correlations used for the CFP case.

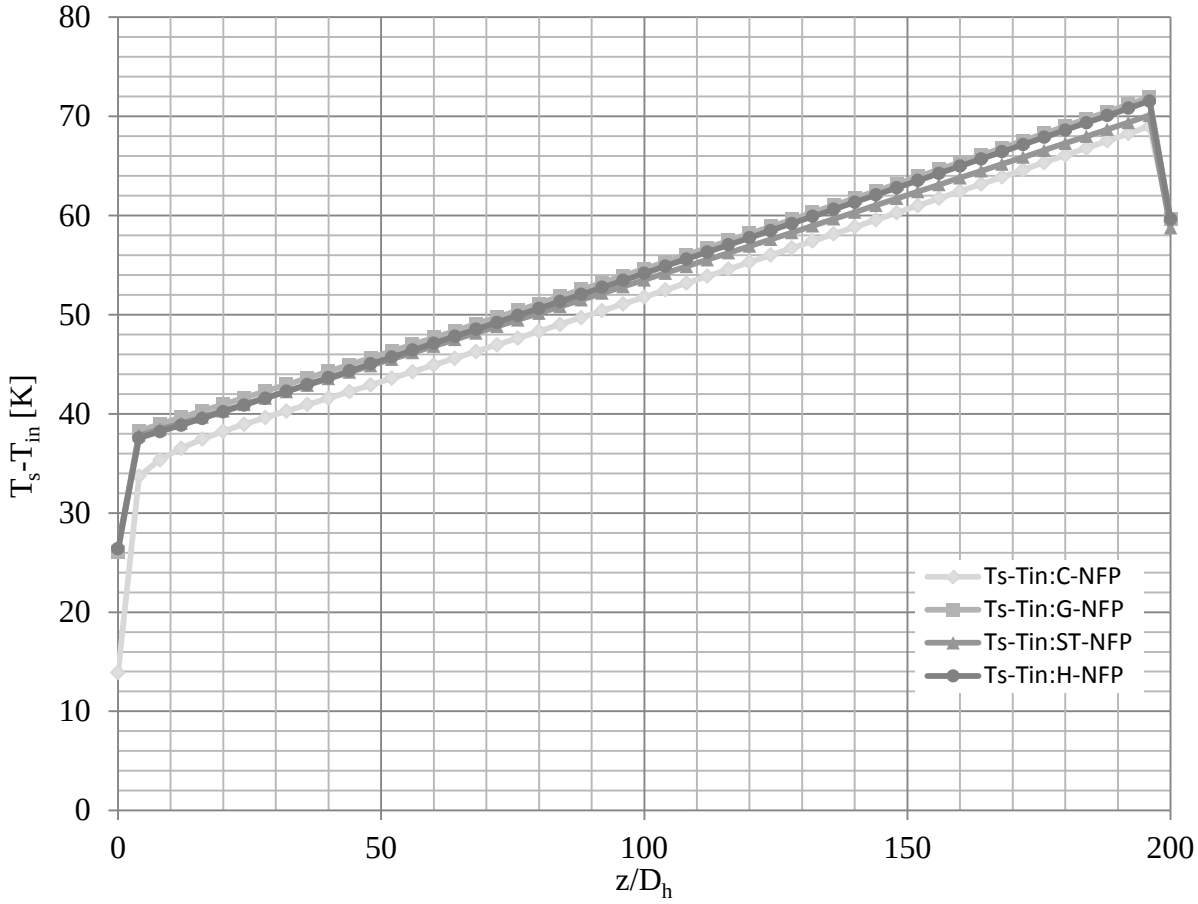

Fig. 2.13. Difference Between the surface temperature and the bulk fluid inlet temperature as derived from the Nusselt correlations used for the NFP case.

2.1.3 2D Turbulent Conjugate Heat Transfer: HFIR Distributed Power Density Case with Constant and Variable Fluid Properties

The model geometry and boundary conditions for the HFIR distributed power density (DPD) is the same as that used for the constant heat flux case discussed in the previous section, refer to Fig. 2.1. The grid structure is identical to that used in the previous section. The DPD imported into the model as an input parameter in the fuel domain is that shown in figure . It is important to mention here that the abrupt increase in the DPD shown in Fig. 2.14 at $\mathbf{z/D_h = 100}$ is not a physical phenomenon that occurs in the High Flux Isotope Reactor. Instead it is part of a strategy used by the developers of the Steady State Heat Transfer Code to model the thermal consequences of fuel defects, which is further discussed in Chapter 3.

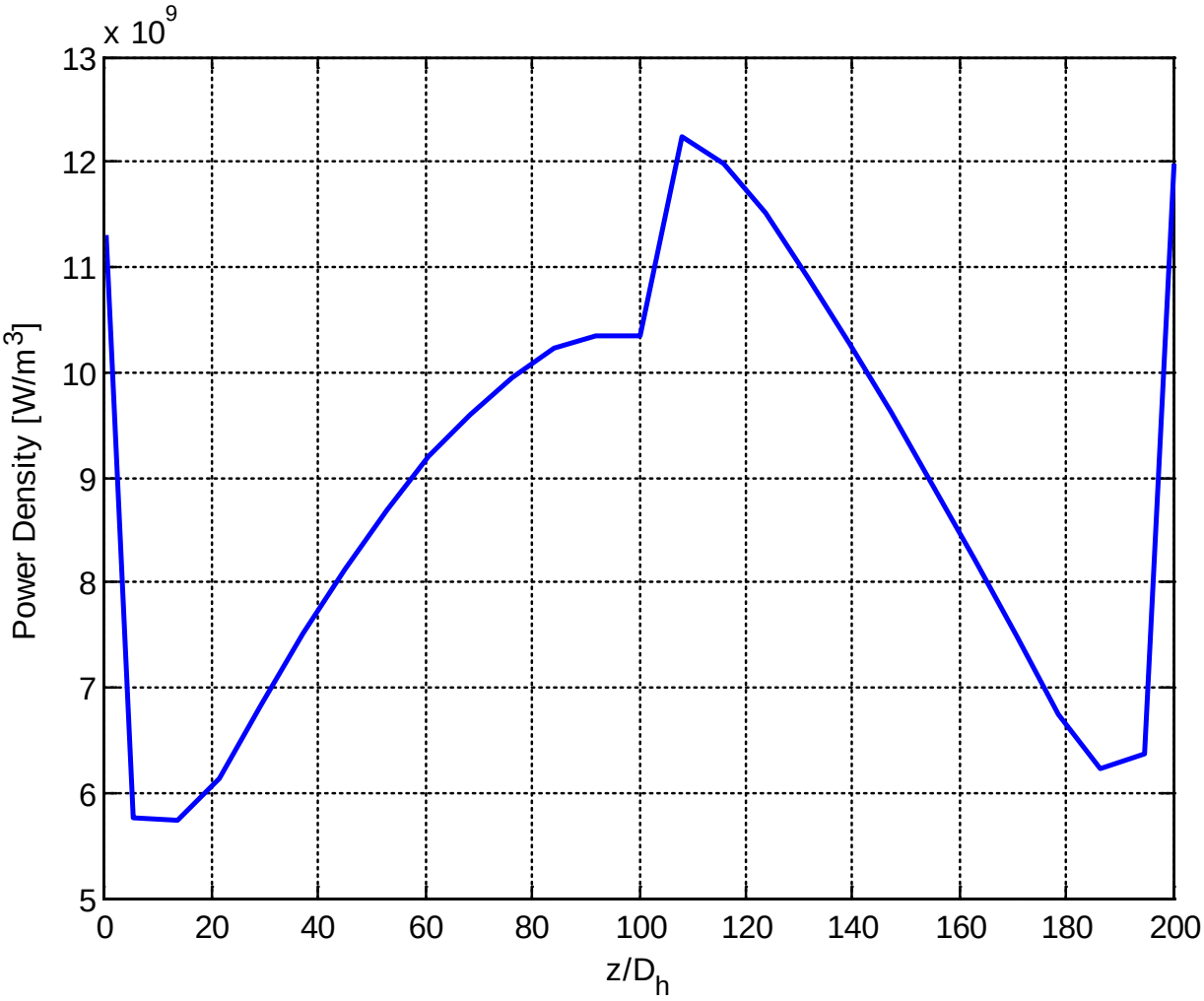

Fig. 2.14. Distributed power density (DPD) input for model.

The surface heat flux resulting from the use of the DPD is shown in Fig. 2.15. Again, the LRN turbulence model is employed due to its ability to resolve thermo-fluid variables within the laminar sublayer of the turbulent boundary layer. The constant fluid properties used for this model are the same as those used in the constant heat flux case (i.e., those shown in Table 2.1). However, the NIST fluid properties will not be the same as those in the constant heat flux case especially those evaluated at the temperature of the heated surface due to its non-linear distribution.

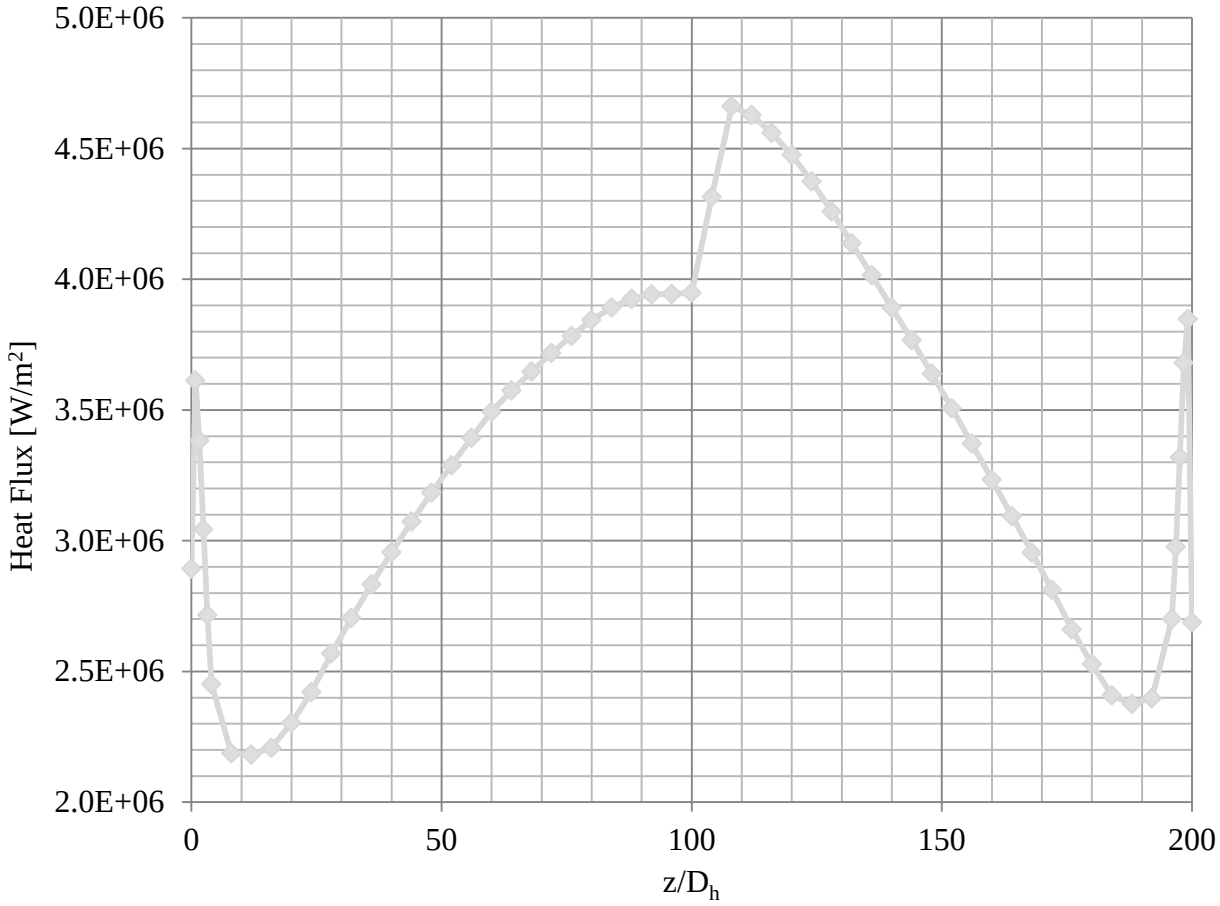

Fig. 2.15. HFIR DPD resultant surface heat flux distribution.

The difference between the clad surface temperatures and the bulk fluid temperatures, or for brevity, the temperature difference, for both the CFP case and the NFP case are shown in Fig. 2.16 as a function of the dimensionless flow direction. Again, the temperature difference of the constant fluid property (CFP) case produces a larger magnitude distribution than the temperature difference of the NIST fluid property (NFP) case. This was explained in the previous section, however, the discussion will be recapitulated here. The thermal conductivity of the fluid increases as the fluid temperature increases, refer to Appendix A, therefore, with a higher thermal conductivity more thermal energy is passed to the fluid thus decreasing the surface temperature.

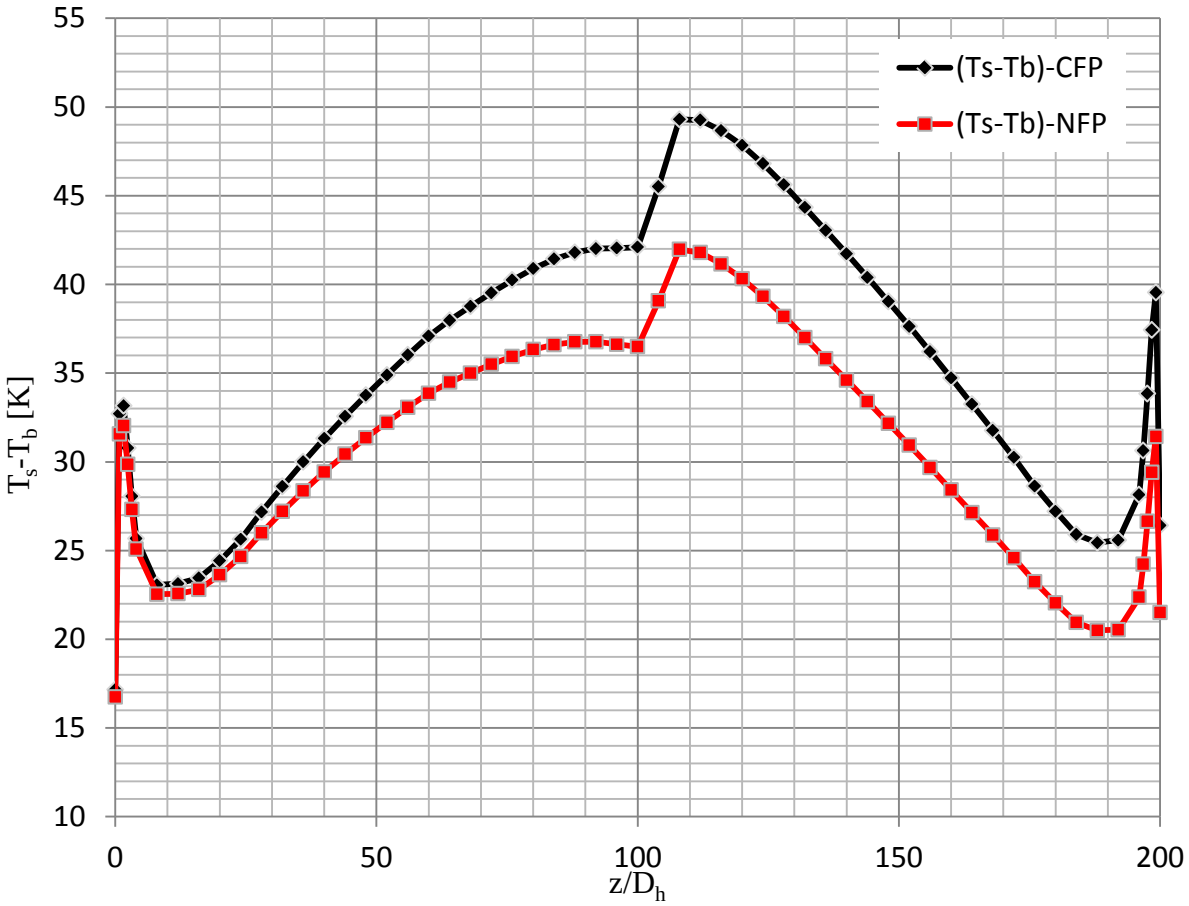

Fig. 2.16. Resultant profiles of the difference between the surface temperature and the bulk fluid temperature.

The convection coefficient for both the CFP and the NFP cases are shown in Fig. 2.17. Interestingly, the convection coefficient profiles are not too dissimilar from those convection coefficient distributions of the constant heat flux case comparing Fig. 2.17 with Fig. 2.5. To discuss the shape of the convection coefficient profiles, consider again Equation 2.19.

$$\frac{dh}{dz} = \frac{1}{[T_s(z)-T_b(z)]}\frac{dq_s''}{dz} - \frac{q_s''}{[T_s(z)-T_b(z)]^2}\frac{d}{dz}[T_s(z) - T_b(z)] \quad (2.19)$$

Since the heat flux is distributed in this model, the first term cannot be neglected. This expression can be written in a more concise manner

$$\frac{dh}{dz} = \frac{1}{(T_s-T_b)^2}\left[(T_s - T_b)\frac{dq''}{dz} - q''\frac{d}{dz}(T_s - T_b)\right]. \quad (2.20)$$

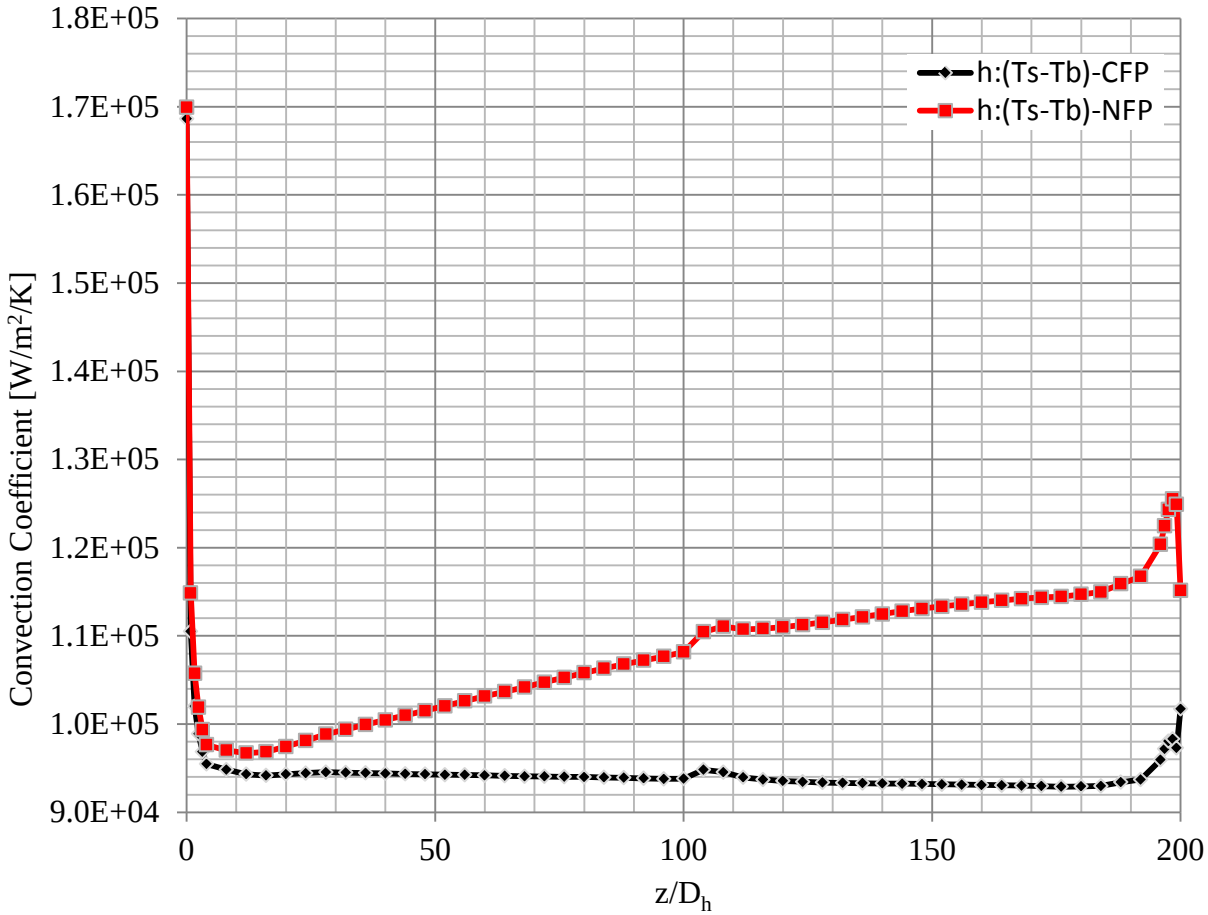

Fig. 2.17. Resultant convection coefficient for the CFP case and the NFP case.

Equation 2.20 is slightly easier to read than Equation 2.9. The evaluation of the spatial variation of the convection coefficient shows that deviations in the heat flux profile will have a direct effect on the results. There is a very subtle interplay between the heat flux and the temperature difference established in Equation 2.20. The heat flux has a very similar profile to the temperature difference (i.e., the profiles in question increase and decrease over the same intervals with the exception of the NFP case in the range $90 < z/D_h < 100$ where the temperature difference suffers a slight decrease in magnitude). The magnitudes of the changes, however, are significantly different. By inspection, the maximum changes occur in the entrance and exit regions. Calculation reveals that the maximum change occurs at the entrance

$$\frac{dq''}{dz} \sim \boldsymbol{O}(\mathbf{10^5})\left[\frac{d}{dz}(T_s - T_b)\right]; \quad \left\{\frac{z}{D_h}\middle|\mathbf{1.6} \le \frac{z}{D_h} \le \mathbf{3.2}\right\} \quad (2.21)$$

The dominant term in Equation 2.20 is not intuitively obvious, and in fact the dominance switches between terms. This oscillatory dominance will be explained qualitatively. The argument can be made that over the range $10 < z/D_h < 100$, the second term is dominant for the CFP case since all quantities in Equation 2.20 are positive and the convection coefficient decreases in the flow direction as shown in Fig. 2.17. For the range $108 < z/D_h < 190$, both derivatives are negative while all other quantities are positive, therefore, the first term is dominant since the convection coefficient continues to decrease over this range. The bump in the convection coefficient (i.e., $100 < z/D_h < 108$) is caused by the first term being dominant with the heat flux derivative being the major contributor. The relative magnitudes of the derivatives in this range are the same as those shown in Equation 2.21.

Figure 2.17 shows that the convection coefficient for the NFP case is an increasing function of the flow direction. In the range $10 < z/D_h < 90$, both derivatives are positive as well as all of the other quantities, therefore, the first term of Equation 2.20 is dominant over this range. For the range $90 < z/D_h < 100$, the heat flux derivative approaches zero while the derivative of the temperature difference decreases slightly which implies that the second term in Equation 2.20 is dominant over this range. The bump occurring in the range $100 < z/D_h < 108$ is indicative of a first term dominance due to the large acute increase in both derivatives. Finally, in the range $108 < z/D_h < 190$, both derivatives are negative which implies that the second term in Equation 2.20 dominates the derivative of the convection coefficient.

The value of the model average Nusselt number for the HFIR DPD CFP model is calculated to be 358.05 using Equation 2.11. The model Nusselt number is different than that recorded in the constant heat flux CFP case due to the decreasing nature of the convection coefficient shown in Fig. 2.17. Since the property values are identical to those used in the constant heat flux CFP case, the values of the different correlations (i.e., Seider-Tate, Gnielinski, and Hausen) are also identical to those calculated from those results. To refresh one's memory the values follow: $\boldsymbol{Nu_D = 369.95}$ (Sieder-Tate: Equation 2.12)), $\boldsymbol{Nu_D = 377.62}$ (Gnielinski: Equation 2.16, and $\boldsymbol{Nu_D = 372.62}$ (Hausen). Since the CFP case results in single value Nusselt numbers from the above mentioned correlations, the average Nusselt number for the model will be compared instead of the instantaneous value. The Seider-Tate correlation results in a difference of 3.32 % with the model value. This difference is calculated using Equation 2.15. The Gnielinski correlation results in a difference of 5.46 %, and the Hausen correlation results in a difference of 4.07 %.

The values of the Nusselt number found from the above correlations divided by the Prandtl number are compared with the model Nusselt number-Prandtl number ratio for the NFP case in Fig. 2.18. First, one notices the bump in the model curve [i.e., (Nu/Pr) that occurs over the range $\boldsymbol{1.02 \times 10^5 \leq z/D_h \leq 1.08 \times 10^5}$]. This is a relic of the way in which this information was constructed. It was explained earlier, with the aid of Equation 2.20, that the convection coefficient suffers an acute increase in magnitude, over this same range, due to the relative magnitudes of the derivatives in the flow direction of both the heat flux and the temperature difference. It was shown that the derivative of the heat flux over this range was five orders of magnitude larger than the derivative of the temperature difference. Therefore, one expects to see this effect reflected in the convection coefficient and, by extension, in the Nusselt number since neither the hydraulic diameter nor the thermal conductivity have the capacity to mitigate this effect. Further, one notices that the Hausen correlation is more representative of the model Nusselt number in the range $\boldsymbol{82,000 \leq Re \leq 113,000}$. It is interesting to note that of all the cases considered to this point the, Seider-Tate correlation was the better fit. However, the most physically representative model (i.e., the HFIR DPD NFP case) yields a conclusion similar to that of Gambil and Bundy [32], at least within the above mentioned range of Reynolds numbers, that the Hausen correlation provides the most accurate representation of the Nusselt number. Toward the upper end of the Reynolds number range (i.e., $\boldsymbol{113,000 \leq Re \leq 130,000}$) again, it is the Seider-Tate correlation that matches best.

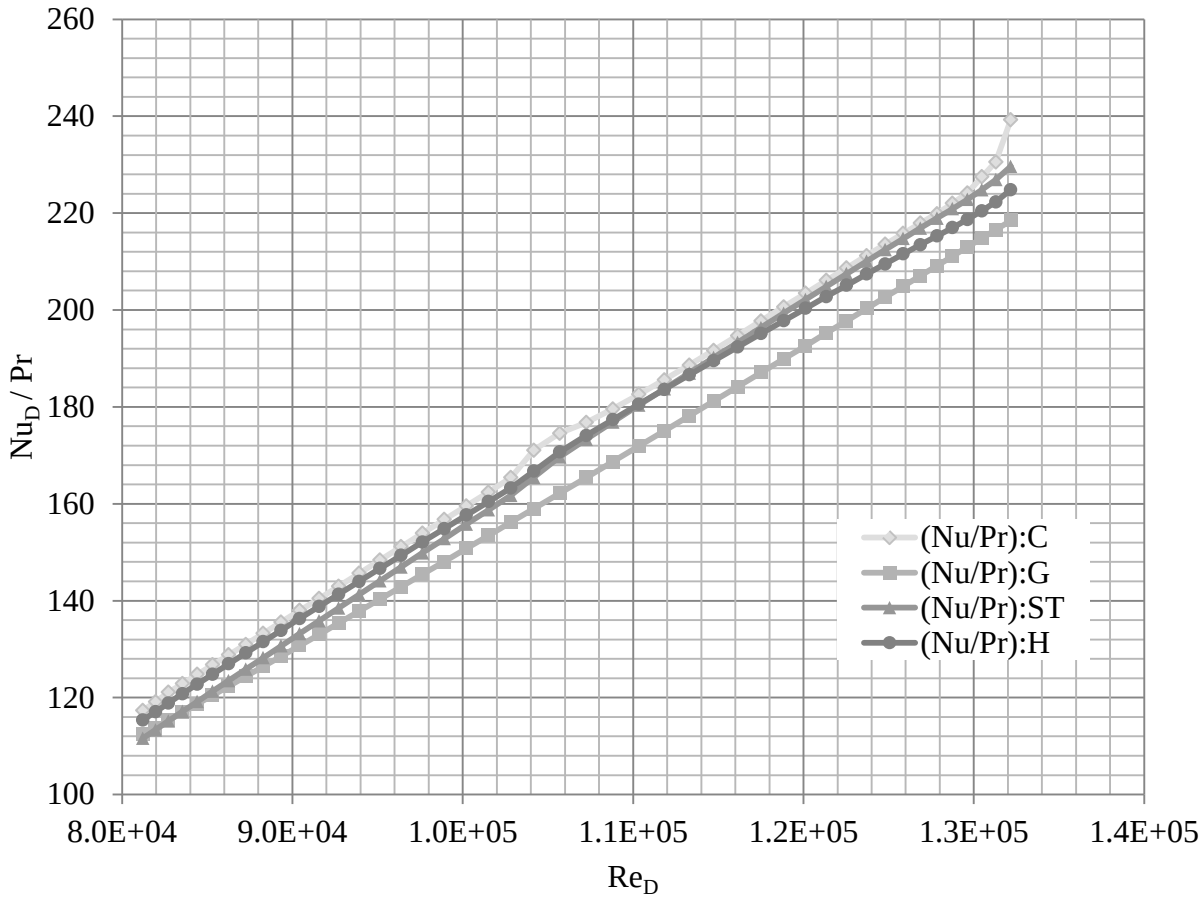

Fig. 2.18. Nusselt number correlation results compared with the model Nusselt number for the NFP.

The relative differences between the model Nusselt number distribution and the Nusselt number correlations are shown in Fig. 2.19. Again, the relative difference was constructed using Equation 2.15. The large upturns that occur in each curve (i.e., $\boldsymbol{Re \geq 130,000}$) are due to the increase of the Nusselt-Prandtl ratio found in Fig. 2.19. This effect is based on the same argument as that presented for the acute increase in the convection coefficient (i.e., the magnitude of the derivative in the heat flux is much larger than the magnitude of the derivative in the temperature difference). This effect permeates all subsequent calculations.

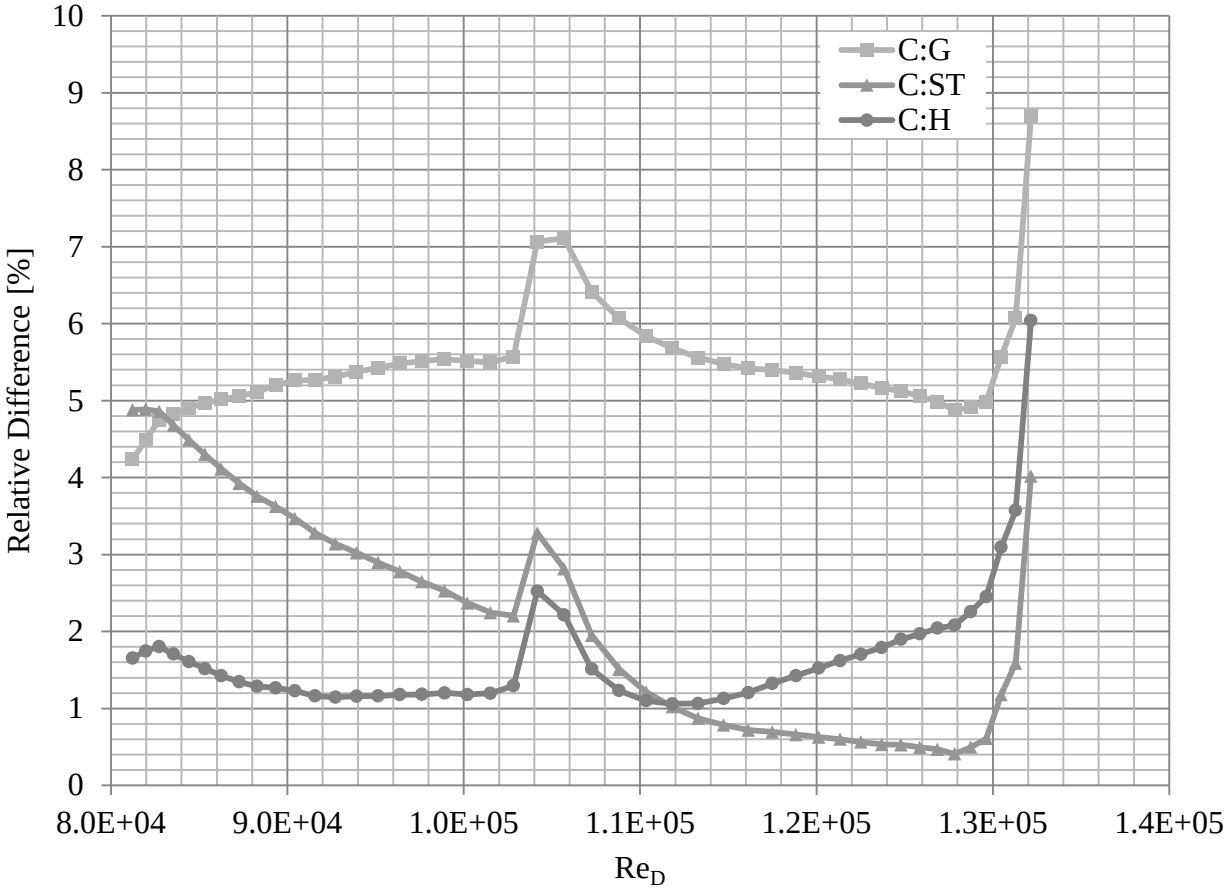

Fig. 2.19. Relative differences of the Gnielinski, Sieder-Tate, and Hausen correlations compared with the model Nusselt modulus.

From Fig. 2.19, the Gnielinski correlation produces the largest consistent difference over the range of Reynolds numbers presented. Therefore, the Gnielinski correlation will produce the larger surface temperatures than the other correlations. It is recommended here that, due to its production of higher surface temperatures in these model configurations, the Gnielinski correlation be used for less detailed models (i.e., models where the influence of the flow field is not directly modeled), which employ variable fluid properties with the LEU fuel as the thermal source. The Gnielinski correlation has been consistent in producing lower values of the Nusselt number for the NFP cases considered in this document.

Figure 2.19 shows that the Hausen correlation produces values within 2% of the model NFP case over most of the range of Reynolds number considered with the exception of the acute increase in the convection coefficient which, in Fig. 2.18, occurs in the range $\mathbf{103,000} \leq \boldsymbol{Re_D} \leq \mathbf{108,500}$. Further, the Hausen correlation is more consistent (i.e., maintaining its value) with the model Nusselt-Prandtl ratio than the Sieder-Tate correlation. The Seider-Tate correlation begins (i.e., on the low end of the Reynolds number scale) at approximately 4.8% compared with 2.6% for the Hausen correlation. The relative difference of the Sieder-Tate correlation with the model decreases with the Reynolds number overall. At a value of $\boldsymbol{Re} \cong \mathbf{112,000}$ the relative differences of the Sieder-Tate correlation and the Hausen correlation are equal, and subsequent values of the Seider-Tate correlation produce values more representative of the model.

The temperature profiles for the CFP case generated from the Seider-Tate, Gnielinski, and Hausen correlations are shown in Fig. 2.20 compared with the model CFP temperature distribution. As with the constant heat flux CFP case, the model temperature distribution is larger in magnitude than the distributions derived from the correlations. The Sieder-Tate and Hausen correlation generated temperature distributions are almost coincident and lie above the Gnielinski correlation generated distribution.

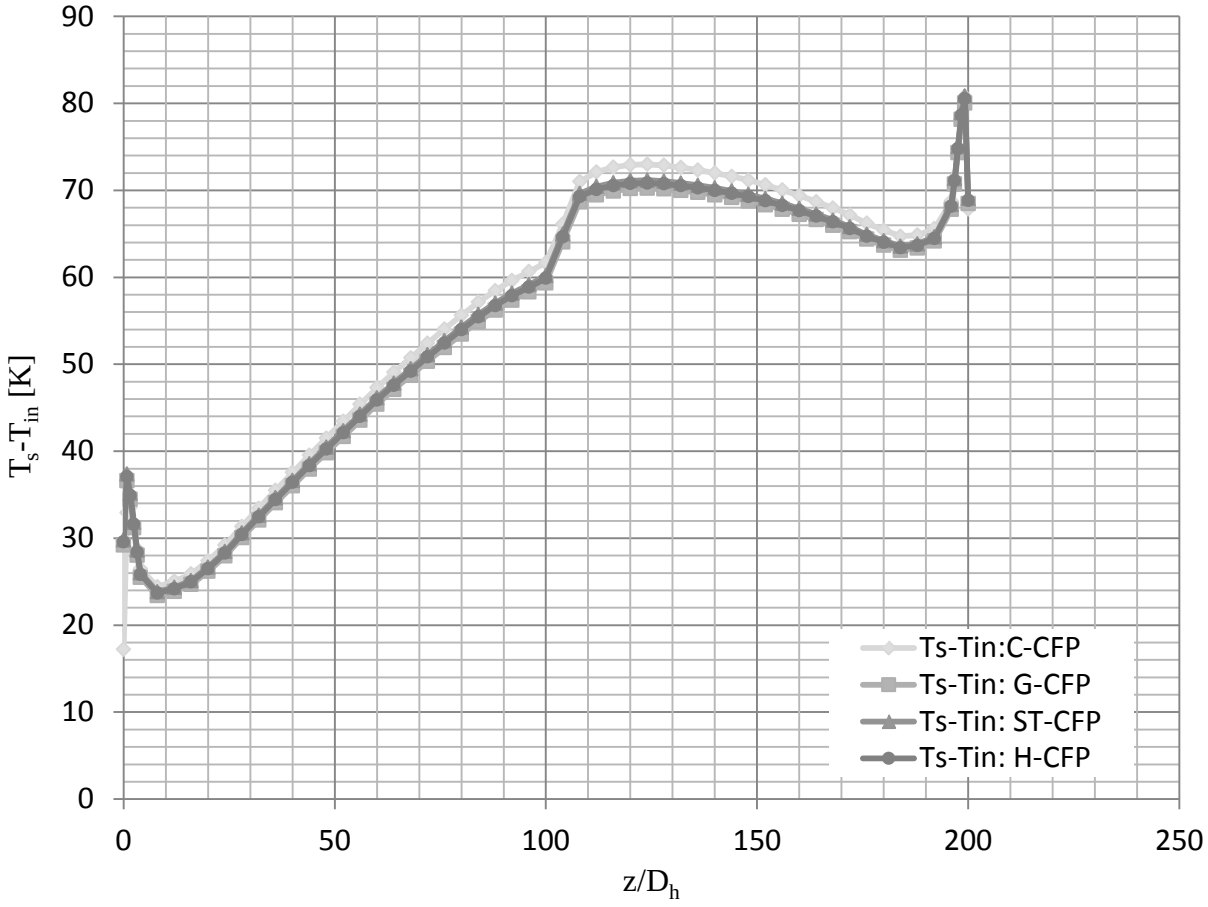

Fig. 2.20. Diff temperature distribution for the cfp case generated by the Gnielinski (G-CFP), Sieder-Tate (ST-CFP), and the Hausen (H-CFP) correlations compared with the model temperature distribution (C-CFP).

The temperature distributions for the NFP case generated from the same Nusselt number correlations are shown in Fig. 2.21 compared with the model NFP temperature distribution. As in the constant heat flux NFP case the model temperature distribution is lower in magnitude than the correlation generated temperature distributions. As stated earlier, the Gnielinski correlation generated temperature distribution is the most conservative of the correlations considered in this document. The Hausen correlation generated temperature distribution matches the model distribution very well over the entire range. It is observed that the Sieder-Tate correlation generated temperature distribution also matches the model distribution, however, there exists more of a deviation in the range $\mathbf{0 \leq z/D_h \leq 100}$ than that produced by the Hausen distribution.

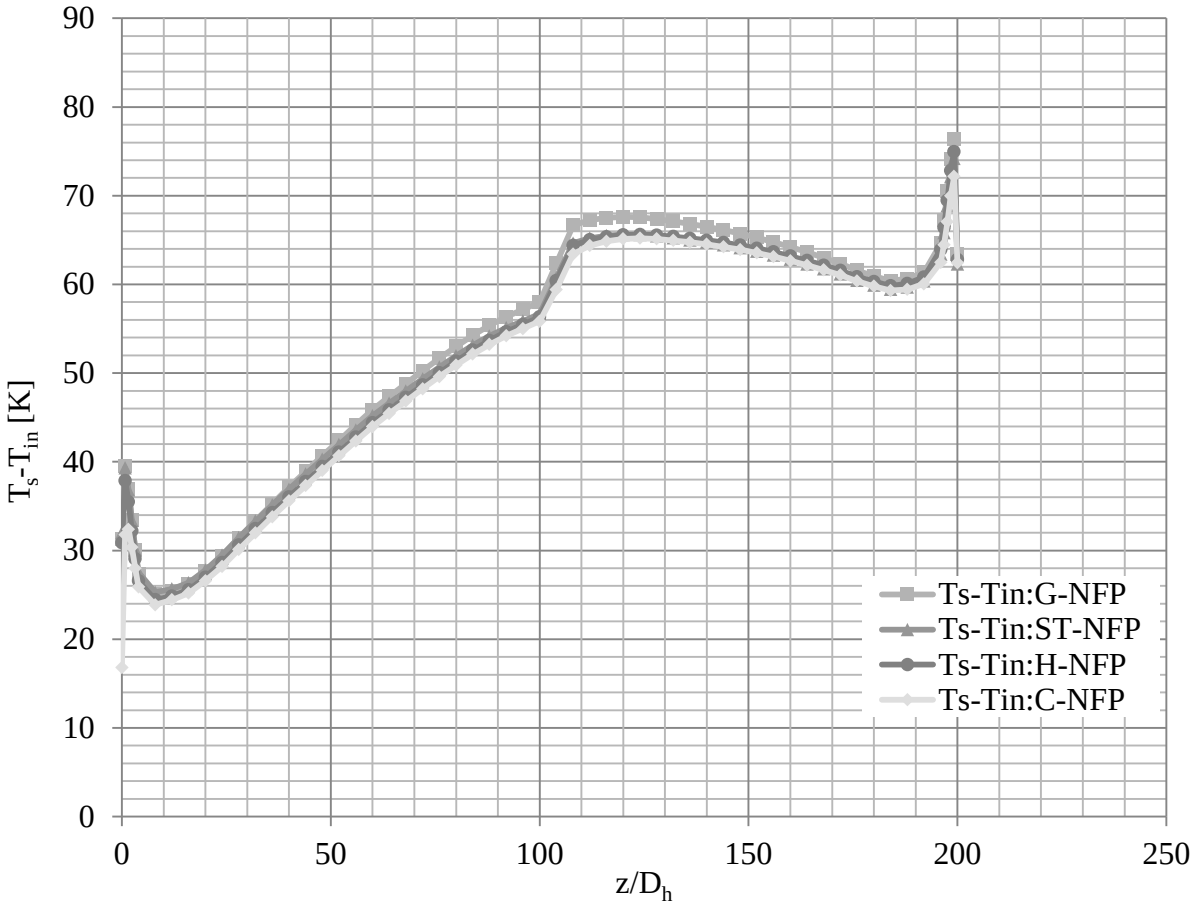

Fig. 2.21. Correlation generated temperature distributions compared with the model distribution for the NFP case.

It has been shown that the model temperature distribution for the HFIR distributed power density with NIST fluid properties is closely matched by the Hausen distribution (i.e., the Hausen generated temperature distribution). One should recall that the Hausen correlation was chosen based on experimental data regarding turbulent flow in thin channels performed by Gambil and Bundy[32]. Here it is shown that the Hausen correlation is very well matched with the computational model. Therefore, the model produces surface temperature distributions in accordance with the experimentally determined correlation.

2.1.4 Discussion of the 2D Conjugate Heat Transfer Results

The 2-D modeling case provides a useful test bed within which to investigate the heat transfer characteristics associated with different scenarios (e.g., distributed heat flux with constant fluid properties compared with variable fluid properties). This 2-D investigation suggests that the constant fluid property (CFP) case provides higher clad surface temperatures thus decreasing the thermal margin (i.e., $\boldsymbol{T_{sat} - T_s}$) defined here as the difference between the saturation temperature of the fluid and the surface temperature of the clad. It was shown that for the CFP case, for both constant and distributed heat flux profiles, the convection coefficient remained relatively constant. This information provides confidence in the results of a thermal diffusion code which employs constant convective boundary conditions provided that the appropriate magnitude of the convection coefficient is used. The convection coefficient can be

appropriately determined from the Sieder-Tate relationship shown in Equation 4.12 given that the thermal-fluid conditions are consistent with the use of this relationship.

2.2 3D MODELS AND COMPARISON

In this chapter we attempt to demonstrate and validate the 3-D model predictive capabilities of COMSOL by comparing the predictions with experimental data. For this purpose, the 3-D Advanced Neutron Source Reactor Thermal Hydraulic Test Loop (ANSR THTL) model was developed in COMSOL and used for validation with experimental data. The test conditions from the ANSR THTL have been used as inputs into the 3-D model. The results from the model, developed in COMSOL version 4.3a, were post processed and compared with the experimental results.

"The Thermal Hydraulic Test Loop (THTL) was a facility for experiments constructed to support the development of the Advanced Neutron Source Reactor (ANSR)"[39,40]. "The facility was built to simulate a full length coolant subchannel of the ANSR core, allowing experimental determination of thermal limits under expected ANSR thermal hydraulic conditions"[39,40].

Experimental data from the ANSR thermal-hydraulic test loop (THTL) will be used in the code validation effort. The ANSR THTL presents a unique experimental data set that has similar characteristics to that of the flow channels in the HFIR core (i.e., high surface heat flux and a long narrow coolant channel). The aspect ratio of the THTL coolant channel, length to thickness, is 399, which is only 16.9% less than that of the HFIR. Flow velocities through the THTL range from 62.34 fps (19.00 m/s) to 88.58 fps (27.00 m/s) which are also comparable to, albeit larger than, the flow velocity characteristic of the HFIR which, as previously stated, is approximately 52.00 fps (15.85 m/s) at steady state operation. The average and peak heat fluxes produced in the THTL are stated to be 6 MW/m^2 and 12 MW/m^2, respectively[39]. The average heat flux through the HFIR core is calculated to be 2.13 MW/m^2. Therefore, with higher flow velocities and higher average heat fluxes, the THTL provides extreme cases, relative to HFIR conditions, with which to validate the code.

2.2.1 ANSR THTL Model Geometry and Boundary Conditions

The cross section of the geometry of the THTL is shown in Fig. 2.22. The flow channel gap has the same thickness as the HFIR flow channel gap (i.e., 1.27 mm). Also, the solid material creating the heat transfer surface and thermal energy generating medium is made of the same material as the HFIR fuel plate cladding (i.e., Al 6061). The reduced wall thickness at the curved ends of the flow channel was designed to reduce heat flux peaking on the ends of the flow channel [39]. This cross section is extended through 507 mm in the flow direction. To expedite the computation, the model geometry was reduced to one-quarter of the entire geometry. The quarter section used is indicated by the red dashed line in Fig. 2.22. The red dashed lines represent heat transfer and flow symmetry planes. The boundary conditions established at these symmetry planes are thermal and flow symmetry conditions.

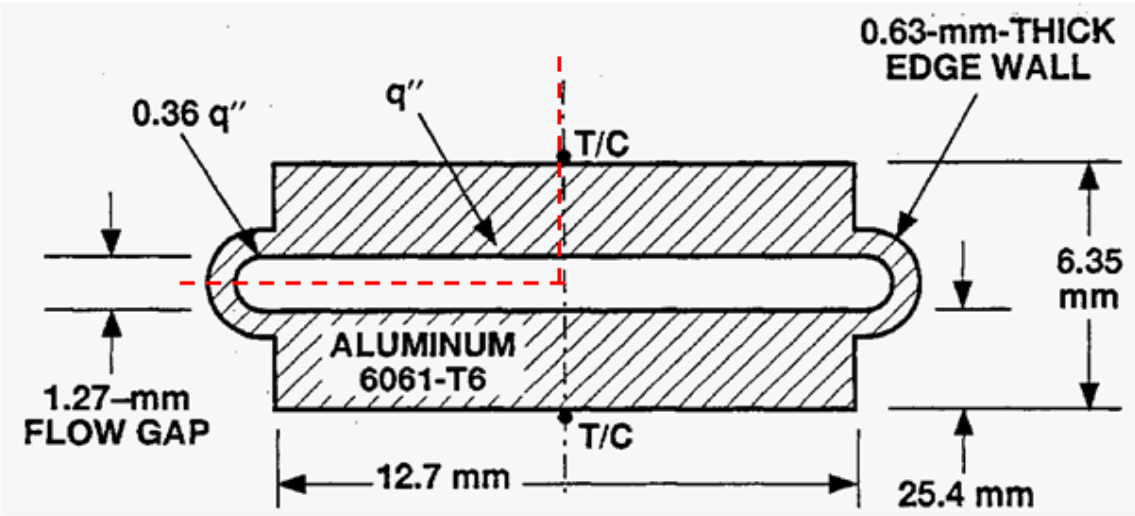

Fig. 2.22. ANSR THTL test loop cross section. The label T/C represents thermocouple locations along the test section. The red dashed lines represent the symmetry boundaries used in the creation of a quarter geometry to simplify the computational effort.

The full model of the ANSR THT is shown in Fig. 2.23 (i.e., the extruded cross section). It is important to bear in mind that only a quarter of this model was used in the COMSOL environment. The entrance extension is 30.7 mm long in the flow direction. The first 18.0 mm was not part of the THTL, but is an artificial extension constructed to ensure that the flow entering the active region of the model is hydro dynamically fully developed. The remaining 12.7 mm outside of the active region provides a location for upstream pressure measurement consistent with the experimental setup[39,40]. The exit extension is 12.7 mm long and was constructed to provide a location for downstream pressure measurement consistent with the experimental setup. Therefore, the global exit of the model represents the location of the downstream pressure tap in the experimental loop. The experimental data used for validation is labeled FE306B03 in the set supplied from ORNL.

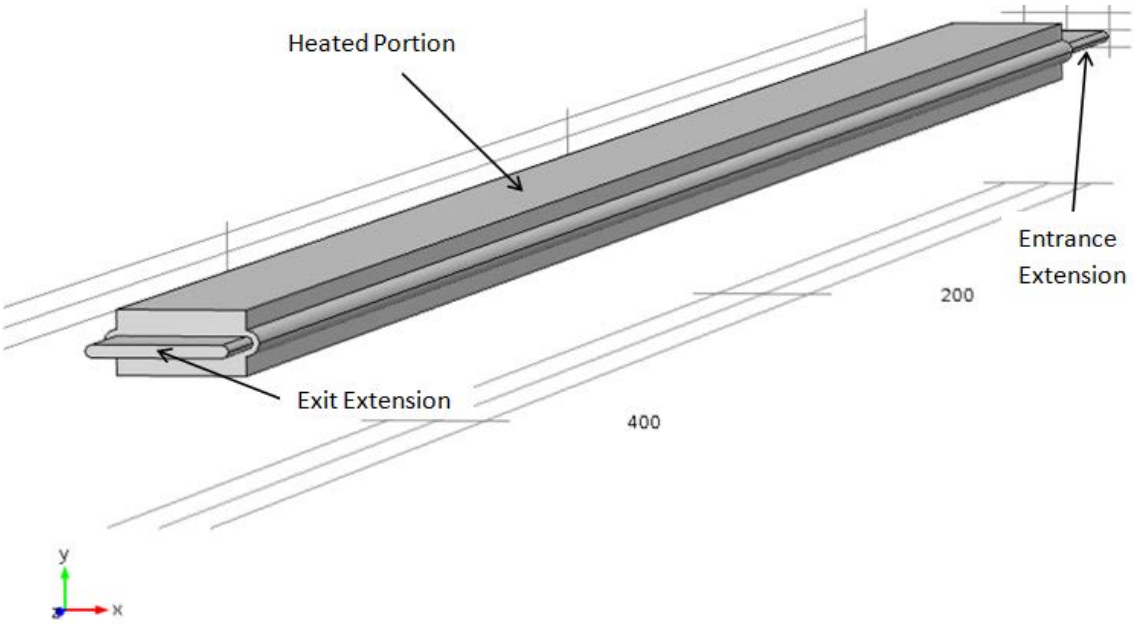

Fig. 2.23. Isometric view of the ANSR THTL model.

Joule heating was used in the experimental setup by supplying a potential difference across the test section in the axial direction. The power input was recorded and the amount of heat loss through the exterior lateral surfaces was measured. The difference between these quantities is the amount of heat passing into the test section and was given the label TS Power. The computational model uses the value of the TS Power as input for the volumetric heat generation rate within the Al 6061 domain. This power density is uniform throughout the solid domain. As a result, the heat flux too will be uniform in the computational domain. Therefore, one expects the results of the THTL model to be similar to the constant heat flux NFP case discussed in the last chapter.

The inlet to the computational domain is isothermal with a temperature of 45.45˚C which is consistent with the experimental setup. Since no thermal sources exist between the global entrance and the active section of the model, one expects that the flow will remain isothermal in this region of the model. The inlet velocity is set to a uniform profile with a magnitude of 21 m/s. The global outlet pressure was set with a uniform magnitude of 1.698 MPa which is consistent with the experimental data and a convective flow condition for thermal variables. The lateral boundaries of the model are adiabatic since the power supplied to the test section is already adjusted to account for lateral losses. The iterative convergence criterion was set to 1×10^{-6} and all grid structures to be discussed have converged with respect to this criterion.

2.2.2 Computational Grid Structure Development

Three different grid structures were created for the simulation. The coarsest grid structure has a total of 82,200 elements. The cross sectional grid structure (i.e., normal to the axial direction) for both the flow channel and solid domain, has an element density of

$$\boldsymbol{\rho_{ele}} = \frac{\mathbf{2}}{\mathbf{6.35\times10^{-4}}} \quad \text{.....(2.22)}$$

Each boundary which makes up the cross section in the model geometry has the number of elements prescribed by the following relationship

$$\boldsymbol{n_{cs} = s * \rho_{ele} * BL}. \quad (2.23)$$

Here $\boldsymbol{n_{cs}}$ is the number of elements in the cross section, $\boldsymbol{BL}$ is the individual cross sectional boundary length and $\boldsymbol{s}$ is a constant adjustment factor used to construct finer grid structures in as much a consistent way as possible. The axial grid structure is created by sweeping the cross sectional grid structure in the axial direction. This portion of the grid structure is constructed using the relationship

$$\boldsymbol{n_{axial} = s * 200} \quad (2.24)$$

The boundary layer grid structure is constructed by specifying the number of layers as

$$\boldsymbol{n_{Layer} = s * 25} \quad (2.25)$$

The total number of elements, $\boldsymbol{n}$, is given by

$$\boldsymbol{n = (n_{cs} + n_{Layer})n_{axial}} \quad (2.26)$$

The stretching factor used in the boundary layer grid construction was set to 1.25, which as stated in Chapter 3, increases the adjacent quadrilateral element size by 25% in the direction normal to the boundary. The thickness adjustment factor was different for the finest grid structure, being set to 2.5 instead of 0.05, due to errors occurring during grid generation.

The adjustment constant, $\boldsymbol{s}$, was given values of 0.75, 1.1, and 1.77 to produce a total number of elements, $\boldsymbol{n = 82,200}$; $\boldsymbol{n = 222,222}$; and $\boldsymbol{n = 496,154}$, respectively. These particular grid structures were chosen to comply with the Grid Convergence Index calculation to be performed on the model results. This will be discussed in detail shortly. It is important to mention that the grid structure described above is the result of many months of trial and error. Many different grid structures were conceived and analyzed, however, energy balance issues for the NFP cases prohibited their use (i.e., between 13% and 15% error). The structures described above represent an error in the balance of energy between 6.83% and 9.96%.

2.2.3 Comparison of Model Results with Experimental Data

The FE306B03 data and the model results are shown in Table 2.2. The results for each grid structure are given below its column heading and the relative error associated with these results is presented in the adjacent column. The relative error is defined as

$$\boldsymbol{Error}[\%] \equiv \left|\frac{\psi_{comp} - \psi_{exp}}{\psi_{exp}}\right| \cdot \boldsymbol{100} \quad (2.27)$$

Table 2.2: FE306B03 experimental data compared with the COMSOL model results

Quantity	Experiment	n = 82,200	Error [%]	n = 222,222	Error [%]	n = 496,154	Error [%]
Tout (˚C)	163.09	165.413	1.424	164.642	0.952	165.021	1.184
Pin (MPa)	2.693	2.508	6.870	2.492	7.464	2.701	0.297
TS Power (W)	173459	173835	0.217	173762	0.175	173717	0.149
Max q" (MW/m^2)	13.514	13.01	3.729	13.061	3.352	13.506	0.059
Ave q" (MW/m^2)	11.875	11.553	2.712	11.748	1.069	11.688	1.575
Ave v (m/s)	21.000	20.604	1.885	20.704	1.409	20.678	1.535
Δp (Mpa)	0.995	0.810	18.593	0.794	20.201	1.003	0.804

The outlet bulk temperature was higher than the experimentally measured value for all grid structures. The outlet bulk temperature for the 222,222 element grid produced the smallest error with a magnitude of 0.95% as shown in Table 2.2. It is assumed that the reason for the intermediate grid structure producing the most accurate result for the outlet bulk fluid temperature is due to the boundary layer grid spacing being further from the wall in the 496,154 element grid than in the 222,222 element grid. The literature associated with the THTL states that a single thermocouple in the flow field was used to measure this quantity. The uncertainty associated with thermocouple readings, in general, can be as high as $\pm \mathbf{3}$℃. The uncertainty in the measurement, however, was not recorded in the data set.

The accuracy of the inlet pressure improved as the grid structure became finer. The relative error associated with the 496,154 element structure was calculated to be 0.297%. This is a marked improvement over the coarser structures where the errors are 6.87% and 7.46% for the 82,200 element structure and the 222,222 element structure, respectively. It should also be pointed out that the finer structure produces an inlet pressure magnitude higher than the measured value whereas the coarser structures produce inlet pressure magnitudes less than the measured value.

The test section power (i.e., TS Power) exhibits a very low error for all three mesh cases, the error decreasing as the grid structure becomes finer. The final value of the relative error of the TS Power is calculated to be 0.149%. The magnitude of the test section power was evaluated by integrating the power density over four times the model volume (i.e., total geometric volume).

$$\boldsymbol{TS\ Power_{model} = 4 * \int q''' dv} \quad \text{.....(2.28)}$$

The volume is an extensive property. Therefore, to obtain a total value of the power generated in the system, one must integrate over the entire material volume.

The maximum heat flux magnitude, measured at the interface between the solid and the fluid, also approached the measured value as the grid structure was refined. The relative error associated with the finest grid structure was 0.059%. Interestingly, the relative error in the average heat flux magnitude at the interface between the fluid and the solid is minimized, with respect to the other grid structures, using the intermediate grid structure. The minimum error calculated is 1.069%. The relative error associated with the fine grid structure (i.e., 496,154 elements, is 1.575%).

The average velocity at a cross section was calculated by evaluating the mass flow rate through the system then dividing out the mass density and the cross sectional area; i.e.,

$$\overline{\boldsymbol{V}} = \frac{\dot{\boldsymbol{m}}}{\boldsymbol{\rho A_c}} \quad \text{(2.29)}$$

The average velocity at the entrance of the computational domain was calculated using Equation 2.29 with the mass density evaluated at the entrance temperature. The average velocity at the exit was calculated using Equation 2.29 with the mass density evaluated at the exit temperature. These values were added then divided by 2 to give the average velocity through the system. The average velocity through the system follows the same pattern where the intermediate grid structure provides the minimum relative error. The minimum relative error for the average velocity is 1.409%.

In light of the above mentioned uncertainties associated with the experimental values, although the errors shown in Table 2.2 seem small, they should be viewed with some caution. In general, the numerical results generally have much higher resolution than experimental measurements. For the experimentalist, accurate temperature measurement with thermocouples under joule heating conditions is very challenging.

To improve further upon the confidence of the numerical models, alternate approaches , that are independent of experimental results, should be considered. One such approach is the Grid Convergence Index as a method for estimating the uncertainties associated with discretization. This method is applied to the 3-D model and the uncertainties are determined.

2.2.4 Computational Grid Convergence Index

The Grid Convergence Method (GCM) is an acceptable and recommended method for the calculation of discretization error associated with numerical computations[41]. The representative grid size is calculated by

$$\boldsymbol{GS} = \left(\frac{\boldsymbol{V_{grid}}}{\boldsymbol{n}}\right)^{\mathbf{1/3}} \quad (2.30)$$

Here $\boldsymbol{GS}$ is the grid size, $\boldsymbol{V_{grid}}$ is the volume occupied by the grid structure, and $\boldsymbol{n}$ is the total number of elements within $\boldsymbol{V_{grid}}$. Using Equation 2.20, the representative grid sizes of the three grids under consideration for the THTL are 1.28×10^{-10}, 4.739×10^{-11}, 2.122×10^{-11} from coarsest to finest. The grid refinement factor is

$$\boldsymbol{r} = \frac{\boldsymbol{GS_{coarse}}}{\boldsymbol{GS_{fine}}} \quad (2.31)$$

It is recommended that $\boldsymbol{r > 1.3}$. The values of $\boldsymbol{r}$ for the grid structures considered here are 2.7009 and 2.2327 for the ratios of coarse grid to intermediate grid and intermediate grid to fine grid, respectively. In what follows, $\boldsymbol{\psi}$, will represent any one of the experimentally determined quantities shown in Table 2.2. The apparent order of the method, *M*, is evaluated using

$$\boldsymbol{M} = \frac{\mathbf{1}}{\boldsymbol{r_{if}}}\left|\boldsymbol{ln}\left|\frac{\boldsymbol{\psi_c - \psi_i}}{\boldsymbol{\psi_i - \psi_f}}\right| + \boldsymbol{ln}\left[\frac{\boldsymbol{r_{if}^M - 1 \cdot sgn}\left(\frac{\boldsymbol{\psi_c - \psi_i}}{\boldsymbol{\psi_i - \psi_f}}\right)}{\boldsymbol{r_{ci}^M - 1 \cdot sgn}\left(\frac{\boldsymbol{\psi_c - \psi_i}}{\boldsymbol{\psi_i - \psi_f}}\right)}\right]\right|; \quad \boldsymbol{sgn(x)} = \begin{cases} \boldsymbol{-1\ for\ x < 0} \\ \boldsymbol{0\ for\ x = 0} \\ \boldsymbol{1\ for\ x > 0} \end{cases} \quad (2.32)$$

Here the subscript $\boldsymbol{c}$ stands for coarse grid, the subscript $\boldsymbol{i}$ stands for intermediate grid, and $\boldsymbol{f}$ stands for fine grid, therefore, $\boldsymbol{r_{if}} = \frac{\boldsymbol{GS_{intermediate}}}{\boldsymbol{GS_{fine}}}$. One notices that Equation 2.30 is a transcendental equation for $\boldsymbol{M}$, this calculation is done in an iterative process. A good initial guess with which to begin the iteration process is

$$\boldsymbol{M_0} = \frac{\mathbf{1}}{\boldsymbol{r_{if}}}\left|\boldsymbol{ln}\left|\frac{\boldsymbol{\psi_c - \psi_i}}{\boldsymbol{\psi_i - \psi_f}}\right|\right| \quad (2.33)$$

The Grid Convergence Index, GCI, is then determined by

$$\boldsymbol{GCI} = \frac{\boldsymbol{1.25 e_{rel}}}{\boldsymbol{r_{if}^M - 1}} \quad (2.34)$$

Here $\boldsymbol{e_{rel}}$ is the relative error in quantity of interest; (i.e.,

$$\boldsymbol{e_{rel}} = \left|\frac{\boldsymbol{\psi_i - \psi_f}}{\boldsymbol{\psi_f}}\right| \quad (2.35)$$

The GCI provides a quantitative measure of the uncertainty associated with discretization error. The results of the fine grid values of the quantities presented in Table 2.2 with the discretization error are given in Table2.3.

Table 2.3. Fine grid structure with discretization error compared with experimental data

Quantity	Experiment	n = 496,154 Value ± Discretization Error
Tout (°C)	163.09	165.021 ± 0.34%
Pin (MPa)	2.693	2.701 ± 1.34%
TS Power (W)	173,459	173,717 ± 0.12%
Max q" (MW/m^2)	13.514	13.506 ± 0.93%
Ave q" (MW/m^2)	11.875	11.688 ± 0.37%
Ave v (m/s)	21	20.678 ± 0.08%

The data for the inlet pressure are within the uncertainty associated with the domain discretization. The remainder of the quantities lies outside the discretization error. It is unfortunate that the experimental error associated with the physical measurements were not reported to better determine the fit of the computational results. However, the relative errors for the fine grid structure reported in Table 2.2 indicate that the model reproduces the experimentally measured results fairly well.

2.2.5 Conclusions for the 3D Modeling Case

The model errors presented in Table 2.2 are based on the presumption that the experimental values as the true values, whose uncertainties are not known. The discretization errors shown Table 2.3, calculated with Grid Convergence Index method, are independent of experimental results. They are calculated utilizing a model with three levels of meshes, each finer that the one before. The solutions for the three meshes are used to determine the discretization errors (or uncertainties) of the results. Those uncertainties are associated with the results for the finest mesh model as shown in Table 2.3. So it can be concluded that modeling uncertainties from the Grid Convergence Index method added confidence to the validation of the 3-D COMSOL model.

2.3 TURBULENCE MODEL CLOSURE EFFECTS

The effects of using a wall-offset model incorrectly (i.e., not having the grid sufficiently far from the wall, are shown in Fig. 2.24). Figure 2.24 is based on a test case which imposes a turbulent flow field over a flat plate. This discussion is necessary due to the default value for y^+ within COMSOL being set to a minimum value of 11.06. The variable y^+ is a measure of the distance from the wall where the logarithmic layer of the turbulent boundary layer begins. Experimentally, the valid range is $30 < y^+ < 300$ [42,43]. Here the k-ε wall-offset model is compared with the low Reynolds number k ε-(LRN) model for different minimum values of y^+ set for the first element away from the wall. The first element is located a distance of 1.75×10^{-7}m from the wall for all models considered. It should be noted that the k-ω model produces the same results as the k-ε model. The LRN is used as the basis for this comparison due to the models ability to match the experimentally determined turbulent velocity boundary layer (i.e., to resolve thermal-fluid variable in the viscous sublayer of the turbulent boundary layer). Figure 2.24 shows that forcing a minimum value of $y^+ = 30$ at a distance of 1.75×10^{-7}m from the wall overestimates the fluid velocity by a factor of 52.8! Similarly, forcing a minimum value of $y^+ = 1$ at the same distance over estimates the fluid velocity by a factor of 24.4. An over estimate of the fluid velocity produces an over estimate of the shear stress in the fluid at the wall and, more importantly for this case, an over estimate of the convection coefficient. An over estimate of the convection coefficient leads to artificially low surface temperatures. Given the importance associated with the surface temperature distribution for the HFIR (i.e., potential for boiling, it is necessary to predict this distribution as accurately as possible). Therefore,

if one is to use the wall-offset models, it is imperative that the grid be appropriately spaced to avoid inaccurate results.

From these results, it can be concluded that the k-ε LRN model should be preferred over the k-ε wall-offset models, as it more accurately represents the velocity distribution within the viscous wall sublayer with negligible slip at the wall. Consequently, the temperature distribution in the fluid and the heat fluxes should be more accurate.

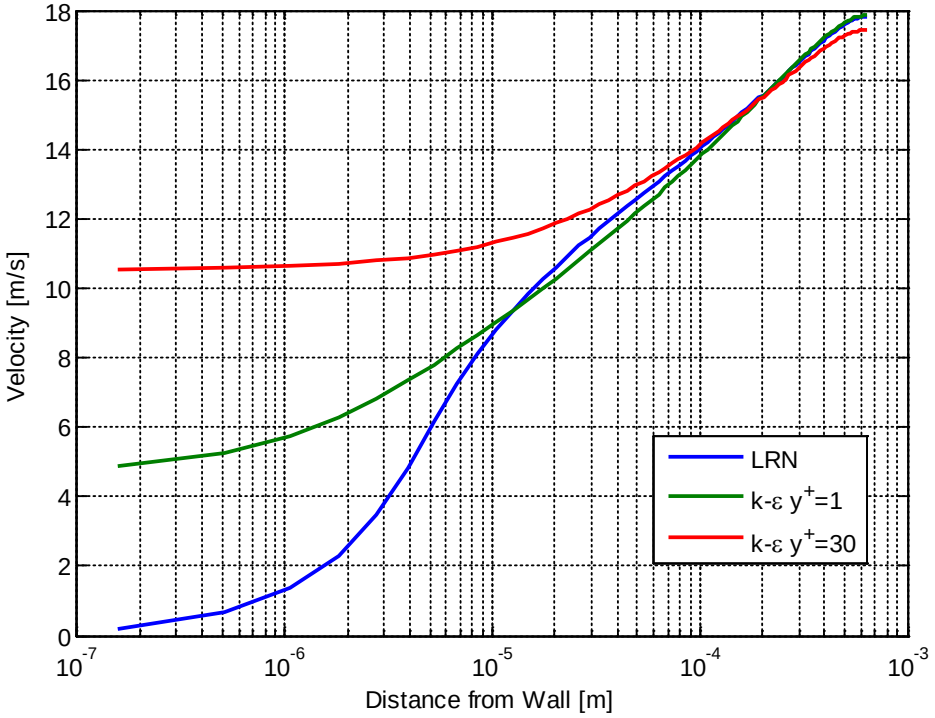

Fig. 2.24. The Effect of Wall-Offset Models with Grid Elements Too Close to the Wall. The cut-line used for this plot was created at $y = 0.3047$ m (i.e., at the exit of the heated section). The first element is located a distance of 1.75×10^{-7}m from the wall for all the three models.

This page intentionally blank.

3.0 FUEL DEFECTS

3.1 REVIEW OF FUEL DEFECT MODELING

Arguably, the most important aspect of the thermal hydraulic analysis has to do with the limited fuel defects that occur during the fuel plate manufacturing process that may not be detected by the resolution of the subsequent inspection process. The defects considered are those associated with the lack of metallurgical bond between different interfaces on the interior of the fuel plate and where the local quantity of ^{235}U is in excess of nominal values for the U_3O_8 - Al 1100 cermet but by no greater that 30% [10]. The lack of metallurgical bond is known as a blister or non-bond and the interesting locations within the fuel plate where this defect occurs are the fuel meat-clad interface, the filler-clad interface, and the fuel meat-filler interface. The local excessive quantity of ^{235}U is known as fuel segregation[44].

Hilvety & Chapman[35], Kirkpatrick[44], and Giles[45] have studied the thermal consequences of these defects on the fuel plate materials using axisymmetric simulation geometries. The simulation geometry used in[35] and[44] is shown in Fig. 3.1. Giles[45] uses a similar geometry, however the dimensions and the fuel meat components and locations are different as the analysis was based on the Advanced Neutron Source Reactor (ANSR) which was to use U_3Si_2 as the fuel instead of U_3O_8. It was determined by all investigators that the combination of the fuel defects in a single axial location at the interface of the fuel meat and filler (i.e., between the U3O8-Al 1100 and the B_4C-Al 1100 materials) respectively, was considered "the most unfavorable situation"[44,35,45] due to the relatively high heat flux peaking factors calculated at this interfacial location as opposed to those calculated at the other interfacial locations within the fuel plate. For clarity, the heat flux peaking factor ($\boldsymbol{\alpha}$) is defined by Hilvety & Chapman[35] as the quantity by which the local heat flux produced by a fuel defect would need to be multiplied to achieve the incipient boiling heat flux for a specified power level. In mathematical terms, the heat flux peaking factor is written as

$$\boldsymbol{\alpha} \equiv \frac{|q''_{ib}|}{|q''_{defect}|}. \quad (3.1)$$

Here $|\boldsymbol{q''_{ib}}|$ is the magnitude of the incipient boiling heat flux and $|\boldsymbol{q''_{defect}}|$ is the magnitude of the local heat flux associated with the defect being considered.

The heat flux peaking factor is used in the SSHTC in the calculation of the "hotspot uncertainty factor", shown in Equation 3.2.

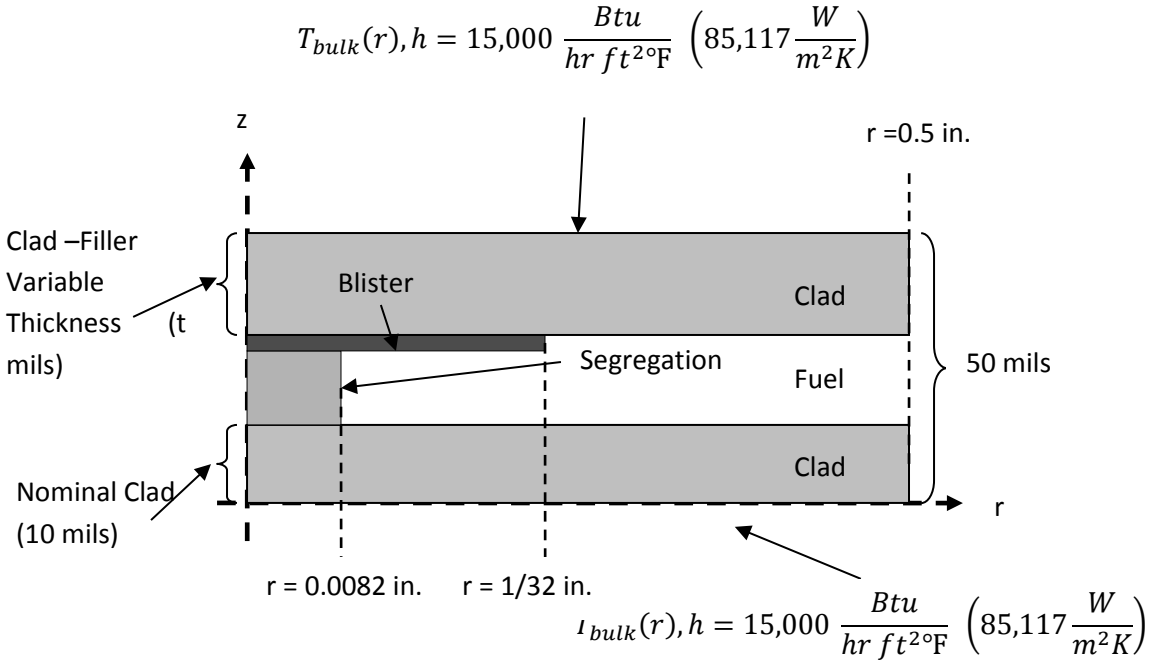

Region	Thermal Conductivity $\left[\frac{\boldsymbol{BTU}}{\boldsymbol{hr\ ft}\text{°F}}\right], \left(\frac{\boldsymbol{W}}{\boldsymbol{mK}}\right)$	Heat Generation Rate: 100MW $\left[\frac{\boldsymbol{BTU}}{\boldsymbol{hr\ in^3}}\right], \left(\frac{\boldsymbol{W}}{\boldsymbol{m^3}}\right)$
Fuel	[97.0], (168)	[1.82×10^{7}/t], (3.26×10^{11}/t)
Segregation	[27.1], (46.9)	[1.87×10^{8}/t], (3.34×10^{12}/t)
Blister	[97.0], (168)	[1.51×10^{4}/t], (2.70×10^{8}/t)

Fig. 3.1. Axisymmetric Geometry used for fuel defect simulations[35,44]. The *t* mils measurement indicated for the thickness of the clad plus filler domain is used as an adjustment factor to vary the thickness of this region (i.e., $\boldsymbol{10mils \le t \le 50mils}$). This thickness adjustment factor is also used to adjust the heat generation rate for the fuel and segregation domains as indicated in the table.

$$\overline{\boldsymbol{u}} = \boldsymbol{1.0} + (\boldsymbol{\alpha_{seg}\ \alpha_{blister}} - \boldsymbol{1.0})\frac{\boldsymbol{h_{hs}}}{\boldsymbol{15{,}000}\left[\frac{\boldsymbol{Btu}}{\boldsymbol{hr\ ft^{2}}\text{°F}}\right]} \quad \text{.....(3.2)}$$

Here $\boldsymbol{\alpha_{seg}}$ is the heat flux peaking factor associated with the fuel segregation defect, $\boldsymbol{\alpha_{blister}}$ is the heat flux peaking factor associated with the blister defect, $\boldsymbol{h_{hs}}$ is the film coefficient at the location of the defect, and the numerical value of $\boldsymbol{15{,}000}\left[\frac{\boldsymbol{Btu}}{\boldsymbol{hr\ ft^{2}}\text{°F}}\right]$ is the average value of the film coefficient used in the defect simulations of Hilvety & Chapman[35] and Kirkpatrick[44]. The hotspot uncertainty factor is used as a factor of safety in the thermal-hydraulic safety analysis of the HFIR system. It is important to determine a conservative value for this quantity regarding LEU fuel. It will be discussed later how this is to be done.

These defects have the potential to raise the local clad surface temperature in excess of the saturation temperature of the fluid thus resulting in a potential boiling event. The formation of vapor bubbles in the coolant flow channels could result in coolant flow starvation (i.e., lack of sufficient flow to cool the fuel

plates). This in turn would result in further increased clad surface temperatures which would eventually lead to a burnout event and failure of the fuel plate.

The author was unable to find material in the literature regarding thermal hydraulic studies of fuel defects caused by the fuel manufacturing process. Several articles exist regarding the formation of defects during irradiation. Pastore, et al.[46] ,discuss physics based modeling of fission gas (i.e., Xenon and Krypton) swelling and release in UO_2 fuel during irradiation using the TRANSURANUS fuel rod analysis code. This work is focused on the material grain-face bubble formation and the subsequent swelling and release on the local hydrostatic stress. Boulore, Struzik, and Gaudier[47] discuss the uncertainty and sensitivity analysis of thermal behavior of nuclear fuel during irradiation. This analysis is carried out using the fuel rod simulation code METEOR V2. Boulore, et al.[47], identify the thermal conductivity of the UO_2 fuel, the radial distribution of power in the fuel pellet, local linear heat rate in the fuel rod, and geometry of the pellet as the most sensitive sources of uncertainty. The uncertainty in these parameters is modeled using inverse methods. Boulore, et al., state that measurements on irradiated fuel samples show that "the irradiation temperature has an effect on the accumulation of irradiation defects thus impacting the thermal conductivity of the fuel material." Khvostov, Mikityuk, and Zimmermann[48] develop the model GRSW-A to analyze gaseous swelling and fission gas release in UO_2 during irradiation. The model that Khvostov, et al. developed is comprehensive and incorporates other models published in the open literature. Locke[49] discusses the behavior of defective fuel, however, the defects that are discussed are mechanical breaks in the cladding material which release fission gas.

Defects in nuclear fuel occur both during device operation as a result of irradiation damage and during the manufacturing process. This work does not consider the transient development of the defects due to irradiation during device operation, but instead considers the global steady state response of the system to the existence of defects, which occurred during fuel manufacturing.

As discussed in Chapter 2, previous investigations were based on 2D analysis and numerical simulations. This previous work only concentrated on the local response of the system to a local defect[35,44]. A constant convection coefficient boundary condition in conjunction with a variable bulk fluid temperature was used in lieu of the turbulent flow field. This limits the system response in that the ratio of surface heat flux in a neighborhood of the defect location to the temperature difference in the same neighborhood is always constant.

The defects to be analyzed are a lack of metallurgical bond between the fuel and the clad (i.e., a blister defect — regions in the fuel where the local loading of ^{235}U is large relative to nominal values). The upper limit of the fuel segregation for pre-irradiated fuel is 30% in an area of diameter 5/64 inch[10] , anything larger will be identified by the inspection process which will result in the rejection of the plate. The upper limit for the blister defect is a diameter of 1/16 inch in the pre-irradiated fuel, any larger blister defects result in the rejection of the plate[10].

3.2 3D MODEL FOR COMPARISON

3.2.1 Plate Geometry and Grid Structure

The HEU model geometry is that of a flat plate with an internal structure composed of the contoured fuel meat (i.e., U_3O_8-Al 1100 cermet). The flat fuel plate resides between two one-half flow channels (i.e., the fluid domain completely surrounds the fuel plate). Figure 3.2 shows a cross-sectional view of the model geometry looking in the flow direction. The fuel plate is 24 inches (0.6096 m) long. The fluid domain extends 39.37 inches (1m) in the axial direction. The fluid domain extends 3.58 inches (0.091m) upstream of the fuel plate and 11.81 inches (0.3m) downstream of the fuel plate. Again, these extended regions upstream and downstream of the fuel plate are to allow the simulated flow to adjust to the fuel

plate obstruction. The contour of the fuel meat was constructed from the detailed drawing of the HEU inner fuel plate[50].

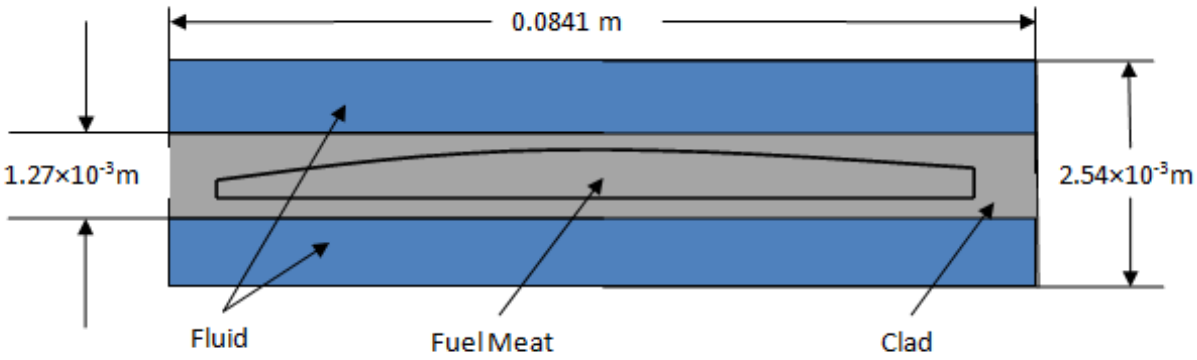

Fig. 3.2. Cross-sectional view of the fuel defect model geometry. The vantage is in the flow direction. The dimensions are given for reference. The model geometry is 1 m long in the flow direction. The contoured side of the fuel meat domain is obvious and will be referenced throughout the chapter.

The global boundary condition of the upstream fluid domain is set with a uniform inlet velocity of 7.925 m/s and an isothermal value of 327K. The global boundary condition on the downstream fluid domain is set to a uniform pressure of 2.606 MPa. The fluid boundaries on the lateral measure (i.e., 0.0841m length in Fig. 3.2) are set to thermal and fluid dynamic symmetry conditions. The boundaries on the thickness measure (i.e., 2.54×10^{-3}m length in Fig. 3.2) are adiabatic walls.

The power density used in fuel meat domain is shown in Fig. 3.3, which is a graphical representation of the power density distribution array.

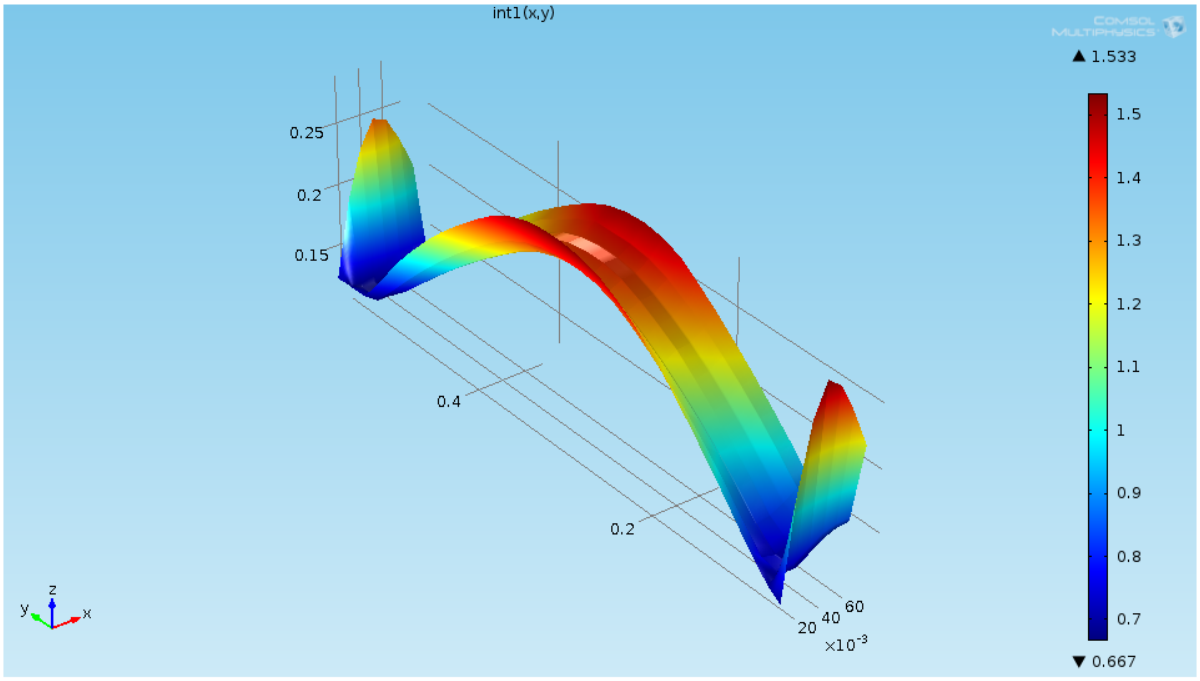

Fig. 3.3. The 3-D Power Density Profile used in the Fuel Meat Domain of the Simulation Geometry.

The magnitude of this power density distribution array was adjusted to be consistent with the HFIR power density. The adjustment calculation is based on the total power generated in the HFIR divided by the total volume of fuel meat in the core; i.e.,

$$q''' = \frac{Q}{V_{total}} = \frac{Q}{V_{inner}+V_{outer}} \quad (3.3)$$

Here, as before, Q is the total core power (i.e., 85 MW). The total volume of the fuel meat in the core, V_{total}, is the sum of the inner core fuel loading and the outer core fuel loading. These values are $V_{inner} = 3.64 \times 10^{-3}\ m^3$ for the inner core and $V_{outer} = 6.39 \times 10^{-3}\ m^3$ for the outer core. These fuel volumes were obtained using cubic spline interpolation of the HFIR plate fuel meat contour points[50] in conjunction with Simpson's quadrature rule. Equation 3.3 may now be evaluated and it is found that the total power density of the HFIR core is 8.47×10^9 W/m^3. This value is multiplied by the power density distribution function which then adjusts the magnitude of the array. However, the resultant power generated by the plate is inconsistent with the amount of energy generated by a single inner fuel plate and in fact is 15.3% too large. The power generated by a single inner fuel plate is

$$q_{inner} = \frac{q'''V_{inner}}{171} \quad (3.4)$$

Equation 6.2 yields a value of $q_{inner} = 1.80 \times 10^5 W$. This 15.3% discrepancy is due to the power density distribution array. The power density distribution array is not a unit normal distribution. Therefore, the sum of all the values in the array does not equal unity, but instead results in a value larger than unity. As a result, only 84.6% of the power density magnitude (i.e., 7.17×10^9 W/m^3) is distributed by the array and produces energy consistent with the 1.80×10^5W generated per inner fuel plate. This value was calculated by executing the simulation with the generation rate 8.47×10^9 W/m^3, then evaluating the volume integral of the generation rate in the fuel meat from the results.

The turbulence equation set used for the fuel defect analysis was Wilcox's k-ω closure model as described in Section 3.2.1. The complexity of the geometry made a grid structure suitable for the Low Reynolds Number k-ε model prohibitively large regarding memory requirements.

The grid structure is established using a mixture of tetrahedral elements and boundary layer elements (i.e., rectangular prisms). The tetrahedral grid structure in the fluid domain has a maximum element size of 4.13×10^{-3}m, a minimum element size of 2.51×10^{-4}m, and a maximum growth rate of 1.25. The tetrahedral grid structure in the clad and fuel domains have a maximum element size of 0.19 m, a minimum element size of 2.51×10^{-4}m, and a maximum growth rate of 1.7. The boundary layer grid structure (i.e., those elements closest to the solid domain extending into the fluid) has a maximum element size of 2.13×10^{-3}m, a minimum element size of 6.35×10^{-4}m, and a maximum element growth rate of 1.05. The boundary layer grid structure has 10 elements with a boundary layer stretching factor of 1.1. The above described details are adequate for recreation of the grid structure within the COMSOL environment.

The solution method uses a segregated solver with a maximum iteration number of 400. The tolerance factor was set to unity with a relative tolerance of 1×10^{-6}.

The first segregation encompasses the velocity, the pressure, and the temperature. The Newton iterations use a constant damping factor of 0.5 and the Jacobian is updated on every iteration. The Generalized Minimum RESidual (GMRES) method is used to solve the system of equations. Preconditioning of the system matrix is carried out using the Successive Over Relaxation (SOR) iterative method with the velocity as the line variable. The maximum line length is set to 5 with a relaxation factor of 0.5.

The second segregation encompasses the turbulence variables (i.e., the specific turbulent kinetic energy and the dissipation rate of the turbulent kinetic energy). The Newton iterations, for the second segregation, use a constant damping factor of 0.3 and the Jacobian is updated on every iteration. Again the GMRES algorithm is used to solve the system of equations with the SOR algorithm preconditioning the system matrix. The turbulent kinetic energy is used as the line variable for this segregation with a maximum line length set to 5 with a relaxation factor of 0.5.

Three different models will be discussed in this section. The three models are the nominal fuel plate model, the blister defect model and the fuel segregation model. The nominal fuel plate case will be used to establish a base line with which to compare the blister defect model and the fuel segregation model.

3.2.2 Nominal Plate Case

The nominal plate case is an idealization where the fuel is free of any defects. To expand on this definition of idealism, the fuel, the clad, and the fluid are considered to be in perfect thermal contact and the fuel meat is homogenous throughout the fuel meat domain.

The temperature distribution on the surface of the clad material for the nominal plate case is shown in Fig. 3.4 with the maximum and minimum surface temperature locations superposed on the figure. The maximum temperature is found to be 211.72˚F (372.99 K), which occurs on the uncontoured (i.e., side of the fuel plate where the fuel meat is not contoured) side of the fuel plate at a location just slightly upstream of the fuel meat-clad interface (i.e., z = 0.0508 m) on the lower end of the fuel plate [i.e., 0.1004 in (2.55×10^{3}m) in the positive z-direction above the interface]. The spatial location of the maximum surface is at x = 0.04593 m, y = 0 m, and z = 0.05335 m. The saturation temperature range is from 463.33˚F to 438.88˚F (i.e., from the leading edge of the fuel plate to the trailing edge), respectively. The saturation temperature and pressure at the location of the maximum temperature on the uncontoured side of the fuel plate is calculated to be 439.29˚F (499.42 K) and 379.3 psig (2.615×10^{6} Pa), respectively.

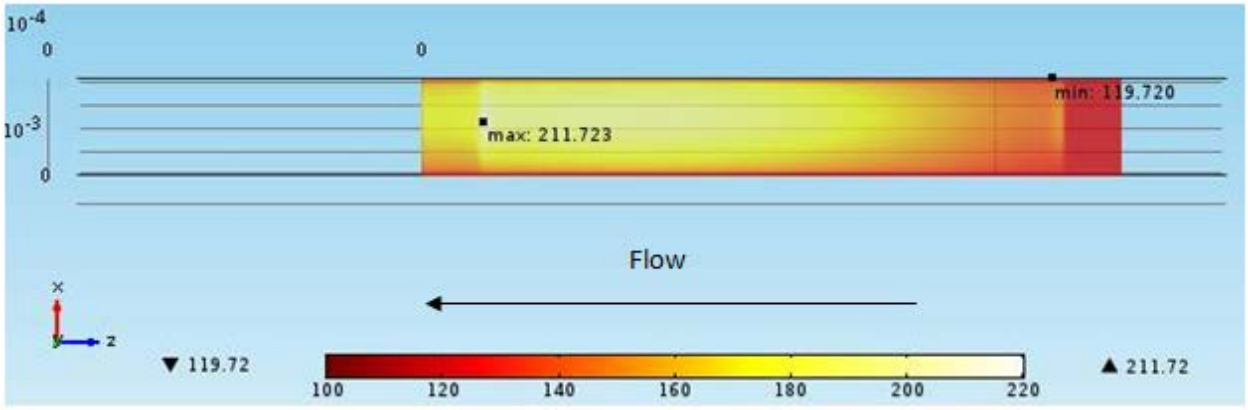

Fig. 3.4. Nominal case clad surface temperature along the uncontoured side of the fuel plate. The maximum (211.72˚F) and minimum (119.721˚F) surface temperatures are superposed on the image at the location of their occurrence.

Therefore, induced two-phase flow is not a concern for the nominal plate case on the uncontoured side. Since the maximum temperature for the nominal case occurred on the uncontoured side, it stands to reason that the contoured side of the fuel plate does not pose a potential two-phase flow threat. Indeed, the maximum temperature occurring on the contoured side of the nominal fuel plate was calculated to be 209.89˚F (371.98 K) at an equivalent location for x and z, but at y = 0.00127 m.

The absolute maximum heat flux from the plate to the fluid occurs on the uncontoured side of the fuel plate with a magnitude of 3.331×10^{6} W/m^2 at the lateral and axial center (i.e., x = 0.04483m, y = 0m, and z = 0.31057m). The surface heat flux is shown in Fig. 3.5. The heat flux occurring at the maximum temperature location was calculated to be 9.586×10^{5} BTU/hr/ft^2 (3.024×10^{6} W/m^2), which represents a 9.3% decrease in heat flux from the maximum. It will be shown that the blister defect has a similar characteristic (i.e., that the maximum heat flux does not occur at the defect); however, the segregation defect does indeed shift the location of the maximum heat flux to the defect location.

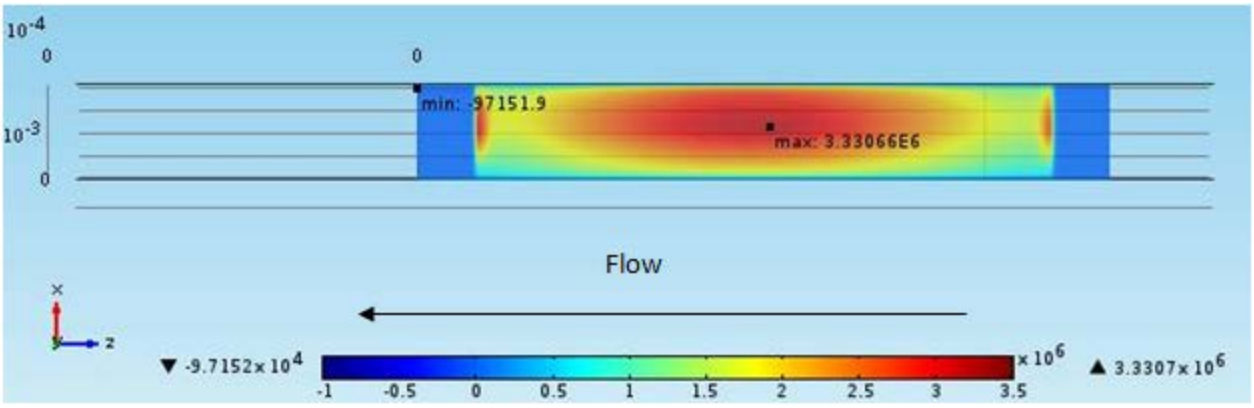

Fig. 3.5. Nominal case clad surface heat flux along the uncontoured side of the fuel plate. The maximum (3.331×10^{6} W/m^2) and minimum (-9.7152×10^{4} W/m^2) heat flux values are superposed on the image at the location of their occurrence.

The minimum heat flux shown in Fig. 3.5 has a negative magnitude, due to the reversal of the heat flux in the unfueled portion of the fuel plate. This reversal of heat flux is due to the bulk fluid temperature being higher than the clad surface temperature in the unfueled region of the fuel plate (i.e., heat is passed from the fluid back into the fuel plate in this region).

The convection coefficient will be defined using the inlet bulk fluid temperature, $\boldsymbol{T_{b_{in}}}$, as the reference temperature, which is established as a global boundary condition for the model and has a magnitude of 120.00˚F (322.04 K); i.e.,

$$\boldsymbol{h} \equiv \frac{q''}{\left(T_s - T_{b_{in}}\right)} \quad \text{.....(3.5)}$$

The choice to use the inlet bulk fluid temperature as the reference temperature is one of convenience. This choice removes the cumbersome evaluation of the bulk fluid temperature at various locations along the fuel plate. In many ways, this is a more practical measure of the convection coefficient as the inlet bulk temperature is easier to determine experimentally than the downstream bulk fluid temperature at various locations where thermal energy is being exchanged. Using Equation 3.5, the magnitude of the convection coefficient at the location of the maximum clad surface temperature is found to be 1.044×10^{4} BTU/hr/ft^2/˚F (5.927×10^{4} W/m^2/K). This result provides a more conservative estimate of the convection

coefficient than that used in previous analyses [i.e., 1.5×10^4 BTU/hr/ft^2/°F (8.5×10^4 W/m^2/K)]. The convection coefficient evaluated using Equation 3.5 produces a value lower in magnitude than the value used in previous analyses, therefore, allowing less thermal energy to pass from the plate to the fluid thus resulting in higher plate surface temperatures.

The pressure drop through the nominal case system is calculated to be 86.7 psig (5.98×10^5 Pa). This deficiency in pressure drop (i.e., from the measured 103 psi drop through the core) can be partially attributed to the idealized surface condition associated with the computational model (i.e., the clad surface is mathematically smooth). Another cause of the pressure drop deficiency could be due to grid resolution. The error in the conservation of energy for the computational model of the nominal plate is calculated to be only 3.83% (i.e., the net efflux of thermal energy minus the thermal energy passed from the fuel plate to the fluid normalized by the integrated plate-to-fluid heat flux).

$$\boldsymbol{E_{energy}} \equiv \left\{\frac{[(\int \boldsymbol{\rho C_p UT dA_{outlet}})-(\int \boldsymbol{\rho C_p UT dA_{inlet}})]-\oint \boldsymbol{q'' dA_{clad}}}{\oint \boldsymbol{q'' dA_{clad}}}\right\}\mathbf{100} \quad (3.6)$$

The error in the conservation of mass was calculated to be 4.77×10^{-3}%. This quantity was calculated by the ratio of the net areal integrated mass flux into the system normalized by the inlet areal integrated mass flux.

Knowledge of the position at which the maximum clad surface temperature occurs allows one to determine the most unfavorable location for a defect (i.e., unfavorable in the sense of increasing surface temperatures further). Since the defect acts either as a region of lack of thermal contact (i.e., blister defect) or as a region of excessive local thermal energy generation (i.e., segregation defect) one can summarize the effect as a region which causes a local increase in the clad surface temperature. With this in mind, it stands to reason that the placement of a fuel defect at the location where the clad surface temperature has its maximum value in the nominal case will have the effect of further increasing the clad surface temperature at that location. As a result, the defects to be investigated further in this work will be created at the axial location of the maximum clad surface temperature found for the nominal case.

3.2.3 Blister Defect Case

As previously stated, a blister is a region where the metallurgical bond between the clad material and the fuel meat has deteriorated (i.e., no thermal contact between the clad and fuel exists at the location of the defect). The geometry of the blister defect and its relative location to the fuel and clad material is shown in Fig. 3.6 for visualization purposes only. The blister defect exists at the interface between the contoured side of the fuel and the clad. The blister defect case is similar to this. The blister defect was introduced into the nominal case model by the creation of an adiabatic disc 1/16 inch in diameter which follows the contour of the fuel meat and lies at the interface between the fuel meat and the clad at the location of the maximum temperature occurring in the nominal case. The 1/16 inch diameter disk is consistent with the rejection criteria used in the inspection of the fuel plate after fabrication. A significant effort was required to create the blister defect region within the computational environment. The adiabatic nature of the interfacial disk sufficiently represents the lack of thermal contact between the fuel meat and the clad that occurs in the physical set-up. It is important to note that with the exception of the blister defect all domains of the model are in perfect thermal contact.

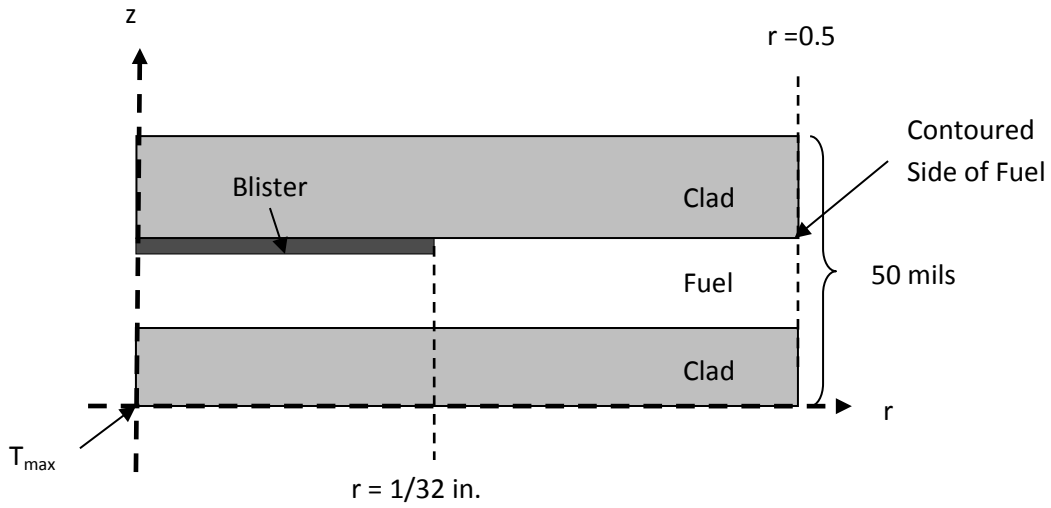

Fig. 3.6. Blister Defect Geometry Relative to the Surrounding Fuel and Clad. This model does not consider segregation defects. The location of the maximum clad surface temperature, Tmax, from the nominal case is indicated.

The maximum temperature associated with the blister defect case again occurs on the uncontoured side of the fuel plate and has a magnitude of 212.92˚F (373.66 K), which is located at x = 0.0478m, y = 0m, z = 0.05398m, as shown in Fig. 3.7. The slight shift in the location of the maximum temperature relative to the nominal case is likely due to the slight adjustment in the grid structure necessary to incorporate the blister defect. The pressure of the fluid at the defect location is 379.56 psig (2.617×10^6 Pa), which yields a saturation temperature of 439.34˚F (499.45 K). Again, the blister defect does not produce sufficient surface temperatures to transition to two-phase flow.

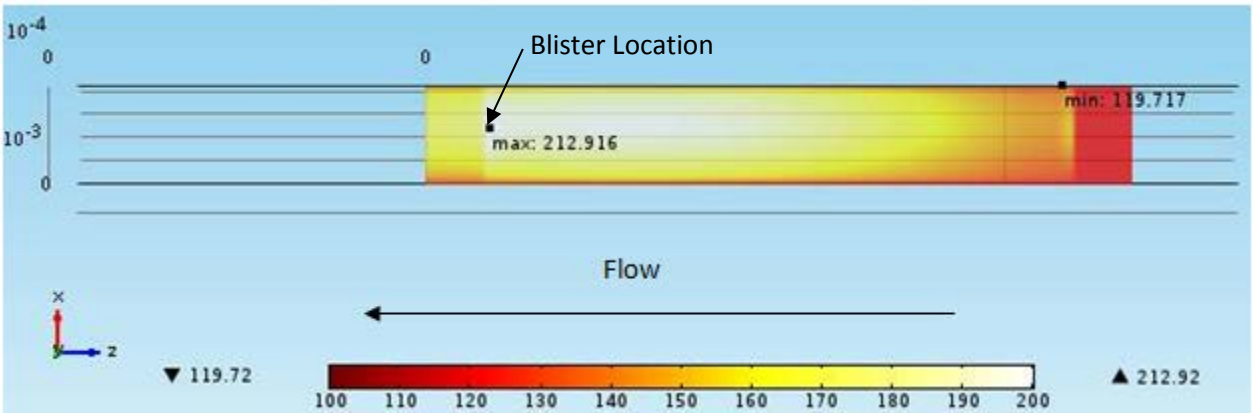

Fig. 3.7. Blister Case Clad Surface Temperature Along the Uncontoured Side of the Fuel Plate. Maximum (212.92˚F) and minimum (119.72˚F) temperatures and their locations are shown on the image.

The absolute maximum heat flux for the blister defect case, shown in Fig. 3.8, occurs on the uncontoured side of the fuel plate as well and has a magnitude of 1.057×10^6 BTU/hr/ft^2 (3.335×10^6 W/m^2), which represents a 0.12% increase from the nominal case. As previously stated, the maximum heat flux occurs near the center of the clad surface and not at the defect location. The absolute maximum heat flux is located at x = 0.0456m, y = 0m, z = 0.3093m. The heat flux at the defect location was found to be 9.824×10^5 BTU/hr/ft^2 (3.099×10^6 W/m^2). The heat flux at the defect location has increased by 2.48% over the nominal case at essentially the same location. Again, the minimum heat flux is represented by a

negative quantity over the downstream, unfueled, region of the clad, which implies a reversal of heat flux. The defect acts to decrease the available heat transfer area of the plate. Decreasing the available heat transfer area while maintaining the thermal generation rate increases the overall heat flux from the plate. The largest increase occurring at the location of the defect with a diminishing influence through the rest of the plate. This is observed in comparing the nominal and blister cases. As stated, the absolute maximum surface heat flux, which occurs 0.26 m upstream of the blister defect, increased slightly by 0.12%. However, the surface heat flux at the blister defect location increased by 2.48%. The convection coefficient at the defect location, defined in Equation 3.6, yields a value of 1.06×10^{4} BTU/hr/ft^{2}/°F (6.00×10^{4} W/m^{2}/K), which is only a 1.18% increase over the nominal case at the same location.

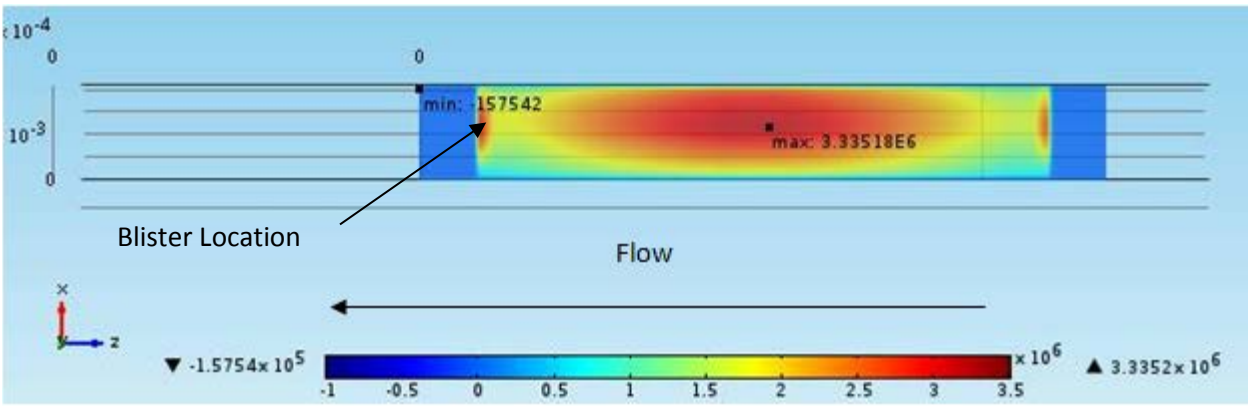

Fig. 3.8. Blister case clad surface heat flux along the uncontoured side of the fuel plate. The maximum (3.33518×10^{6} W/m^{2}) and minimum (-1.5754×10^{5} W/m^{2}) values of the heat flux are superposed on the image at the location of their occurrence.

The pressure drop through the blister defect model was calculated to be 86.9 psig (5.99×10^{5} Pa). The error in the global energy balance was calculated using Equation 3.6 and was found to have a magnitude of 4.03%. The error in the global balance of mass was calculated to be 8.34×10^{-3} %.

It was shown that the blister defect caused an overall increase in the surface heat flux of the fuel plate. This overall increase is maximized at the defect location and dissipates as one moves away from the defect location. The absolute maximum surface heat flux remained at the center of the uncontoured side of the fuel plate surface. The increase in surface heat flux caused an increase in surface temperature with the maximum temperature occurring in approximately the same spot as in the nominal case. However, the maximum was only 0.18% higher in the blister case. The convection coefficient increased slightly from 5.927×10^{4} W/m^{2}/K in the nominal case to 6.00×10^{4} W/m^{2}/K in the blister case.

3.2.4 Segregation Defect Case

The segregation defect was introduced into the nominal case geometry as a cylinder with a diameter of 5/64 inch (i.e., consistent with the rejection criteria) and extending through the fuel meat domain [i.e., approximately 0.030 inch (7.6×10^{-4}m)]. The geometry of the segregation defect and its relative location to the fuel and clad material is shown in Fig. 3.9 for visualization purposes only. The segregation cylinder was made to conform to the contour of the fuel meat. The segregation defect was positioned at the location of the maximum temperature encountered in the nominal case. As previously stated, the segregation defect is physically characterized by excess loading of ^{235}U. To model this defect the thermal energy generation rate per unit volume within the defect cylinder was increased by an order of magnitude (i.e., 7.17×10^{10} W/m^{3}). This order of magnitude increase was taken from previous studies of segregation defects[10,44,35].

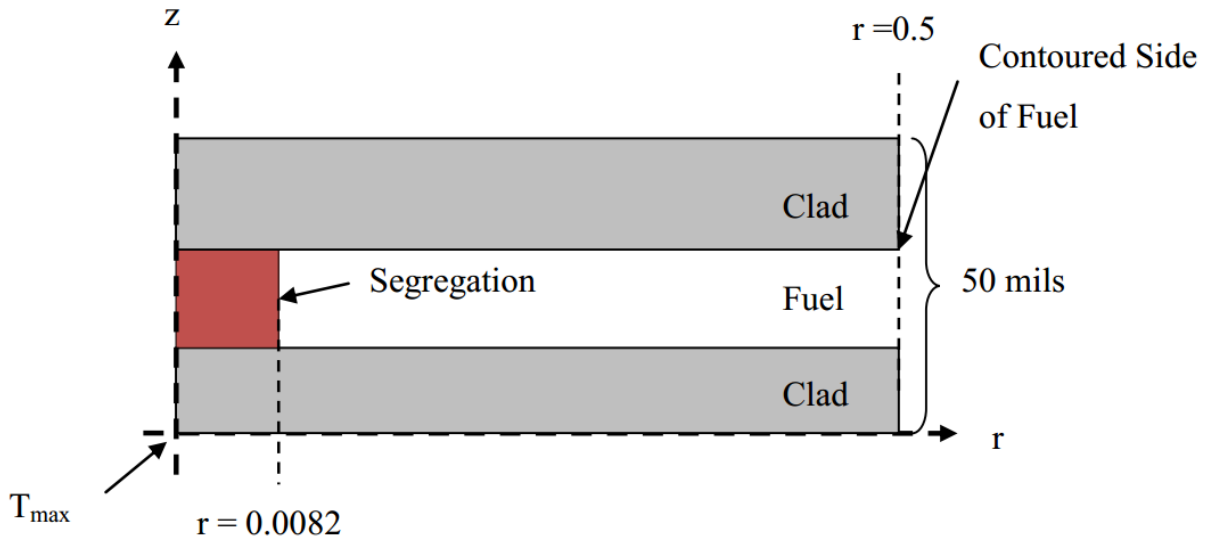

Fig. 3.9. Segregation defect geometry relative to the surrounding fuel and clad. This model does not consider blister defects. The location of the maximum clad surface temperature, T_{max}, from the nominal case is indicated.

The grid structure used to discretize the segregation defect domain is identical to the grid structure for the fuel meat domain described earlier. Here the defect and all other domains within the model are assumed to be in perfect thermal contact.

The maximum temperature associated with the segregation defect was found to be located on the fuel contour side of the fuel plate with position coordinates x = 0.04756m, y = 0.00127m, and z = 0.05376m. The magnitude of the maximum temperature was found to be 219.24˚F (377.17 K) as shown in Fig. 3.10. The pressure of the fluid at the defect location was calculated to be 380.6 psig (2.624×10^6 Pa) that yields a saturation temperature of 439.61˚F (499.60 K). The segregation defect does not produce clad surface temperatures consistent with the saturated state of the fluid therefore the probability of two-phase flow is very low.

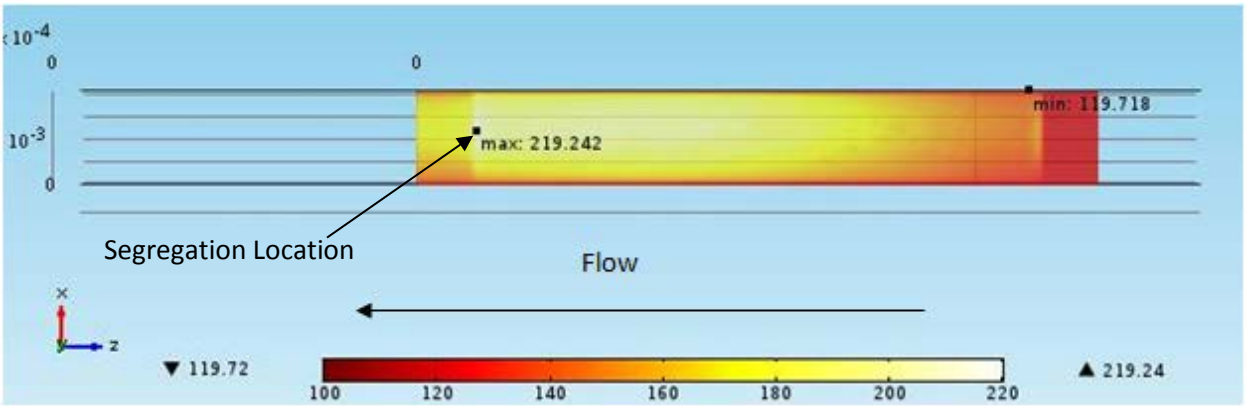

Fig. 3.10. Clad surface temperature on the fuel contour side of the fuel plate. The maximum and minimum temperatures are superposed on the image at the location of their occurrence.

The location of the absolute maximum heat flux for the segregation case shifted to the segregation defect location. This is an intuitive result since the thermal energy generation rate per unit volume was

increased by an order of magnitude at this location. This is indeed a most unfavorable condition since the bulk fluid temperature is a maximum in the region where the absolute maximum heat flux occurs (i.e., lower fueled region of the fuel plate). However, it has been shown that the probability of two-phase flow is very low. The absolute maximum heat flux magnitude was found to be 1.10×10^{6} BTU/hr/ft^2 (3.48×10^{6} W/m^2). This represents an increase of 4.19% over the absolute maximum heat flux found in the blister defect case, and a 4.50% increase over the absolute maximum heat flux found in the nominal case. Since the location of the absolute maximum heat flux has shifted downstream relative to the location found in the other cases (i.e., nominal and blister defect cases) the heat flux at the segregation defect location should be compared with the heat fluxes for the other cases at this location. The segregation defect heat flux is12.3% higher than the heat flux at the blister defect location, and it is 15.1% higher than the heat flux in the nominal case at the same location. The surface heat flux on the fuel contour side of the fuel plate is shown in Fig. 3.11. Again, the minimum heat flux occurs at the downstream unfueled region of the fuel plate that, as previously stated, represents a reversal of heat flux (i.e., from the fluid to the fuel plate).

The convection coefficient at the defect location was calculated to be 1.111×10^{4} BTU/hr/ft^2/°F (6.307×10^{4} W/m^2/K). This value represents a 5.17% increase over the convection coefficient at the blister defect location and a 6.46% increase over the nominal case at the same location.

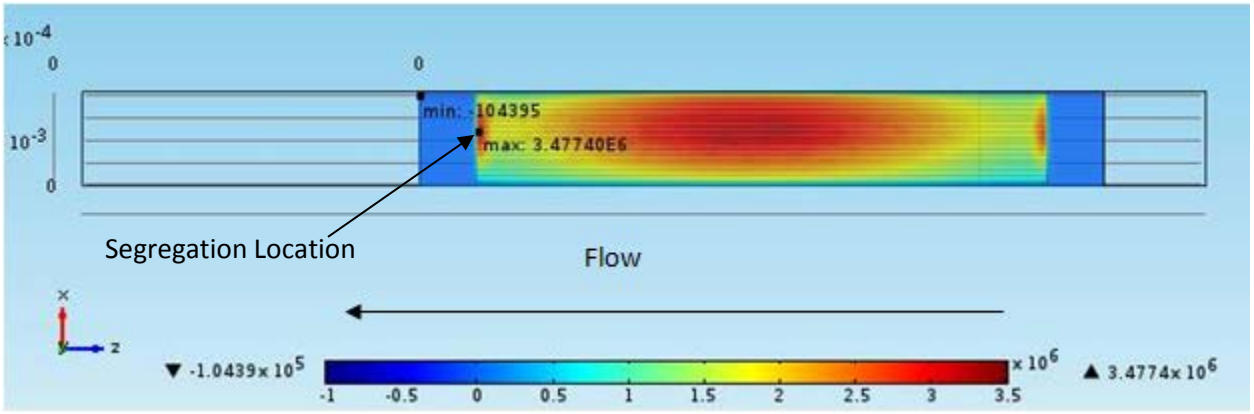

Fig. 3.11. Clad surface heat flux on the fuel contour side of the fuel plate. The maximum and minimum surface heat flux values have been superposed on the image at the location of their occurrence.

The pressure drop through the segregation defect system was calculated to be 81.3 psig (5.60×10^{5} Pa). The error in energy conservation was calculated to be 3.83%. The error in mass conservation was calculated to be 5.96×10^{-3}%.

It has been shown that of the two defects analyzed (i.e., blister defect and segregation defect), the segregation defect caused the largest changes in the system. This was expected since the thermal generation rate per unit volume was increased in the segregation defect thus increasing thermal output from the plate. The absolute maximum heat flux for the segregation case was found to have shifted position to the defect location instead of the center of the plate as was found in both the blister defect case and the nominal case.

A summary of the results of the fuel defect analysis is presented below in Table 3.1 .

Table 3.1. Summary of results for the fuel defect analysis

Quantity	Nominal case	Blister case	Segregation case
T_{max} [K]	372.99	373.66	377.17
q" [W/m^2] at T_{max} location	3.024×10^{6}	3.099×10^{6}	3.48×10^{6}
T_{sat} [K] at T_{max} location	499.42	499.45	499.6
P [Pa] at T_{max} location	2.615×10^{6}	2.617×10^{6}	2.624×10^{6}
$q"_{max}$ [W/m^2]	3.331×10^{6}	3.335×10^{6}	3.480×10^{6}
h [$W/m^2/K$] at T_{max} location	5.927×10^{4}	6.00×10^{4}	6.307×10^{4}
ΔP [Pa] Through system	5.98×10^{5}	5.99×10^{5}	5.60×10^{5}
Energy Conservation Error [%]	3.83	4.03	3.83
Mass Conservation Error [%]	4.77×10^{-3}	8.34×10^{-3}	5.96×10^{-3}

This page intentionally blank.

4.0 FLUID-STRUCTURE INTERACTIONS

4.1 OVERVIEW OF PAST FUEL PLATE FSI ANALYSIS

The conversion of the HFIR from HEU fuel to LEU fuel presents an opportunity to improve the predictive capability of the tools used to verify the performance of the reactor. The HFIR SAR is largely based on empirical data on the dynamic and static interaction that occurs between the fuel plates and cooling fluid. Empirical data is not yet available for the proposed LEU fuel.

Research reactors, by nature, are designed with specific scientific goals, which oftentimes require novel design elements. The HFIR, with its emphasis on a high neutron flux, utilizes involute fuel plates in two concentric circles to create its "flux trap." The Advanced Test Reactor at INL is designed to facilitate many different experiments as well as changes to the experiment during the fuel cycle[51] and a "clover-leaf" fuel design has been implemented as seen in Fig. 4.1. The reactor at the Massachusetts Institute of Technology (MIT) utilizes a grid pattern for experiment and fuel placement Fig. 4.1.

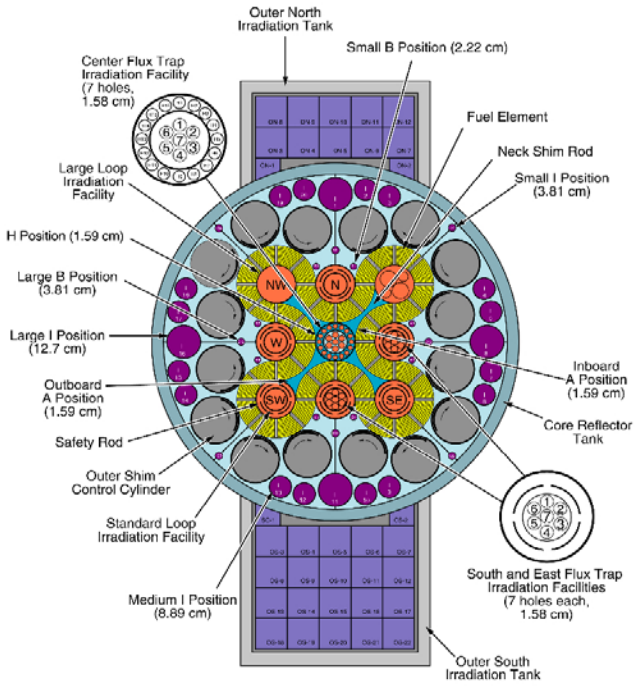

Fig.4.1. The ATR core with its clover-leaf fuel design[52].

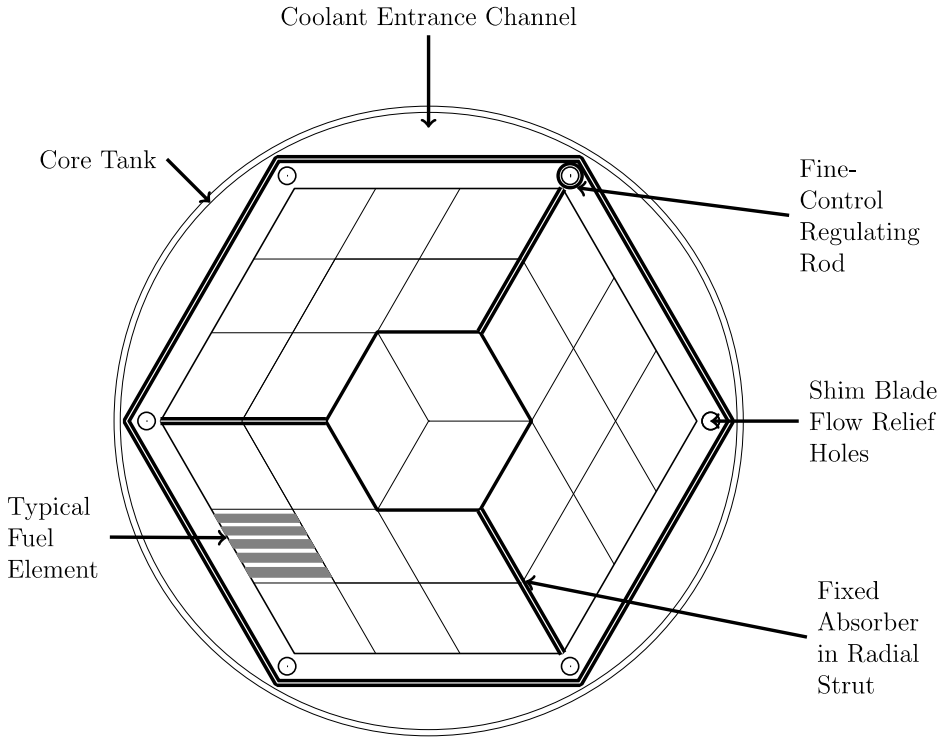

Fig. 4.2. Top-down view of the MIT core[53]. The coolant flows into the page.

All of the five remaining HPRRs that have yet to convert to LEU utilize an array of fuel plates. This use of flat fuel plates is in contrast to power reactors, which typically utilize fuel rods and a significantly larger mass of uranium. Because the HPRRs use high aspect ratio flat plates, a significant effort has been performed to quantify the deflections caused by the coolant flow. One of the first experiments exploring the effects of the fluid-structure interaction of an array of fuel plates was performed at ORNL for preliminary research for the HFIR in 1948[54]. Stromquist and Sisman were able to observe plate vibration with plates similar in thickness to the current HFIR design. Their experiments found that extreme spacing between plates (one channel was 15.9mm while the adjacent was 3mm) could produce buckling at the plate leading edges. Under nominal plate spacing, the maximum deflection of the plates was found to be approximately 2 mils (0.05mm).

Later, Miller developed a theoretical approach to determine the maximum velocity that a series of plates with fixed sides can sustain before collapse[55]. Miller's Critical Velocity, $\boldsymbol{M_c}$, was based upon the assumption of incompressible, potential flow and it utilized an elastic wide-beam theory; Miller also assumed that the mass flow between all of the channels remained the same. Miller's approach determined the velocity in which the pressure difference between two plates is sufficient to maintain a deflection. The Miller Critical Velocity soon became the safety basis used in analyzing the critical flow velocity of parallel reactor fuel plates. For a flat plate with fixed edges, the Miller Critical Velocity is defined as

$$\boldsymbol{M_c} = \left[\frac{\mathbf{15}\boldsymbol{gEa^3h}}{\boldsymbol{\rho b^4(1-\nu^2)}}\right]^{\mathbf{1/2}} \quad (4.1)$$

where $\boldsymbol{g}$ is the gravitational constant, $\boldsymbol{E}$ is the Young's Modulus of the plate, $\boldsymbol{a}$ is the plate thickness, $\boldsymbol{h}$ is the flow channel thickness, $\boldsymbol{\rho}$ is the density of the coolant, $\boldsymbol{b}$ is the width or span of the plate, and $\boldsymbol{\nu}$ is the Poisson's ratio of the plate.

Experimental testing of the Miller Critical Velocity has been performed by many researchers[56-59]. These experimenters found that the Miller Critical Velocity was conservative, with flows tested to $\boldsymbol{2M_c}$ with no total plate collapse. In fact, Groninger and Smissaert found that vibration occurs at approximately twice the Miller Critical Velocity. The only experiment in which total plate collapse occurred was performed by Ho et al.[60]. The collapse occurred at a velocity lower than $\boldsymbol{M_c}$ suggesting that this experiment may be an outlier.

In support of the conversion to LEU fuel, two facilities have been constructed to produce plate deflection data. A generic test plate experiment is being designed, constructed, and tested at the Oregon State University (OSU) that uses a flat plate, multi-channel design to measure both static and dynamic fuel plate deflections[61]. The OSU experiments will utilize strain gages to determine the deflections along the plate. Single plate experiments are being designed and tested at the University of Missouri that incorporate a Perspex flow channel allowing the use of a laser to measure the plate deflections[58].

Most of the experimental research has been focused on static deflection of perfectly flat fuel plates. A few experiments have been performed to investigate the deflections for curved fuel plates. Ha and Garland[62] conducted an experiment for a curved plate following a circular arc. Researchers at ORNL, in the design of the proposed Advanced Neutron Source Reactor (ANSR), conducted experiments using a series of involute shaped fuel plate[63]. A range of inlet velocities was conducted and revealed a much smaller deflection for the curved plates than an equivalent flat plate.

The shortcomings and inherent conservative approach of the Miller Critical Velocity led many researchers to focus efforts on improving the theory. Johansson[64], a colleague of Miller's, first expanded on the Miller Critical Velocity by including friction terms and the flow redistribution caused by the movement of plates. Kane[65] explored how deviations from the design thickness can affect the deflections. He found that large deviations, as expected, could lead to larger deflections. Further, Scavuzzo[66] included the entrance and exit effects at the leading and trailing edge of the plate. Wamsganss[67] argued that the derivation first proposed by Miller could be improved upon by including second-order effects in the calculation of the critical velocity.

Researchers began to reevaluate the assumptions Miller made in his derivation of the critical flow velocity. Other analysis techniques were developed including a wave propagation/water-hammer approach[68], solving the series of plates as a system[69], and using Schlichting boundary layer theory[70]. Cekirge and Ural[71] used small deflection plate theory to derive the critical flow velocity gaining only a four percent margin over the Miller Critical Velocity. In order to better capture the plate deflections, Pavone and Scarton[72] employed a fourth order structural model with laminar flow. Kebuoa et al.[73] used a potential flow analysis of one plate to analyze a multi-plate channel and found that their method matched Miller's Critical Velocity.

All the researchers up to this point had assumed one dimensional, steady state flow. A Galerkin method was employed by Guo and Paidoussis[74] to analyze a two-dimensional plate with a three-dimensional flow field. By combining turbulent effects with a frequency analysis of thin rectangular plates, Kim and Davis[75] were able to obtain natural frequencies of a series of plates. They found that the natural frequency of the plates in a fluid was lower than the plates in vacuum; they also found that by decreasing the channel gap, the natural frequency of the plate would decrease. On the other hand, Cui et al.[76], used a wetting method to determine the natural frequency of the plates and found that the added fluid did not greatly affect the natural frequency of the plate. Using a stability criterion, Michelin and Llewellyn Smith[77] analyzed an n-series of plates to determine the stability of the system as it relates to flutter.

Until recently, the use of computer codes to simulate fluid-structure interactions between the fuel plates and the coolant flow has been too computationally expensive. Roth[78] simulated the fluid flow between

the fuel plates but was not able to model plate deflections. Kennedy and Solbrekken[79] have used two separate codes, one for solving the fluid domain and the other one for solving the structural domain. Their approach utilizes a time-dependent solver for each code to complete the runs. The decoupling of the physics resulted in an unstable solution process. A fully coupled approach has been performed that eliminates the stability issues found with the decoupled approach[27] and this technique will be used for the analysis of the HFIR core.

4.2 CYLINDER IN CROSS-FLOW

The cylinder in cross-flow is a fundamental fluids problem in which the physics allows for a stringent testing of the different aspects of a code. The cylinder will naturally begin to shed vortices for $\boldsymbol{Re}$ greater than approximately 35 and will continue to shed into the turbulent regime. These shedding vortices are known as Kármán vortex streets and are related to the Strouhal number defined as

$$\boldsymbol{St = fD/U} \quad (4.2)$$

For flows with $\boldsymbol{Re}$ between 100 and $\mathbf{10^5}$, the Strouhal number is approximately $\mathbf{0.2}$, which means that the vortex shedding cycle is approximately the length of time it takes the free stream, flow to move 5 cylinder diameters[43].

This phenomenon will occur for almost any bluff body for which $\boldsymbol{Re \geq 35}$. The shedding vortices can cause significant vibrations in the structure. This vibration, if not carefully accounted for, can cause large oscillations and eventual failure of the structure. Such an example is the flutter that caused the Tacoma Narrows Bridge[80] to fail in 1940. The shedding and subsequent oscillations have been studied at length experimentally[81,82] and numerically[83-90]. The progression for the modeling of the cylinder in cross-flow for this section will follow the following outline:

1. Stationary Cylinder
2. Oscillating Cylinder: Prescribed Displacement
3. Oscillating Cylinder: Free Displacement
4. Stationary Cylinder with Moving Tail

This progression was chosen as a way to test the code capabilities incrementally. The complexity of both the flow solver and the structural solver was increased with each section. First, we employ only the flow solver while holding the cylinder stationary and computing only the vortex shedding of the fluid. Later, we incorporate different moving cylinders: one type that follows a prescribed displacement and one that allows the cylinder to move freely in the transverse direction based upon the lift created by the shedding vortices, respectively. Finally, we model a stationary cylinder with a long tail attached to the end. This simulation tests the ability of the mesh generator to handle large displacements of the tail caused by the shedding vortices.

4.2.1 Stationary Cylinder

The stationary cylinder in cross-flow is used to test and verify the capabilities of the flow solver. The solver should be able to capture the shedding of the vortices without any external manipulation from the user. The development of the Kármán vortex streets should occur naturally and progressively using a transient solver. Here, we consider a range of Reynolds numbers that result in laminar flow about a stationary cylinder.

(1) Domain and Boundary Conditions

The 2-D domain for the stationary cylinder was chosen to be a large rectangular domain. The cylinder diameter is 1mm. The domain is 40 times the cylinder diameter in height and 40 times the cylinder diameter in length. In order to ensure enough resolution of the trailing vortices, the cylinder was offset in the flow direction with a larger section placed on the trailing edge of the domain. The top and bottom boundaries are taken to be periodic boundaries. The periodic boundary conditions are described by the following equations

$$\boldsymbol{u_{source} = u_{destination}} \quad \text{.....(4.3)}$$

$$\boldsymbol{p_{source} = p_{destination}} \quad \text{.....(4.4)}$$

where the source is the top boundary and the destination is the bottom boundary. The left boundary is an inlet with specified velocity based upon the $\boldsymbol{Re}$ number. The right boundary is a pressure boundary set to 0. The boundary around the cylinder is a no slip condition. Fig. 4.3 provides the domain dimensions and boundary conditions used for the simulations.

The working fluid for the simulation was taken to be incompressible water with the following properties at 293K:

- Density: 1000 kg/m $^{\mathbf{3}}$
- Viscosity: 0.01 Pa·s

Water was chosen because the working fluid for the majority of the simulations performed for analysis of the HFIR would be water.

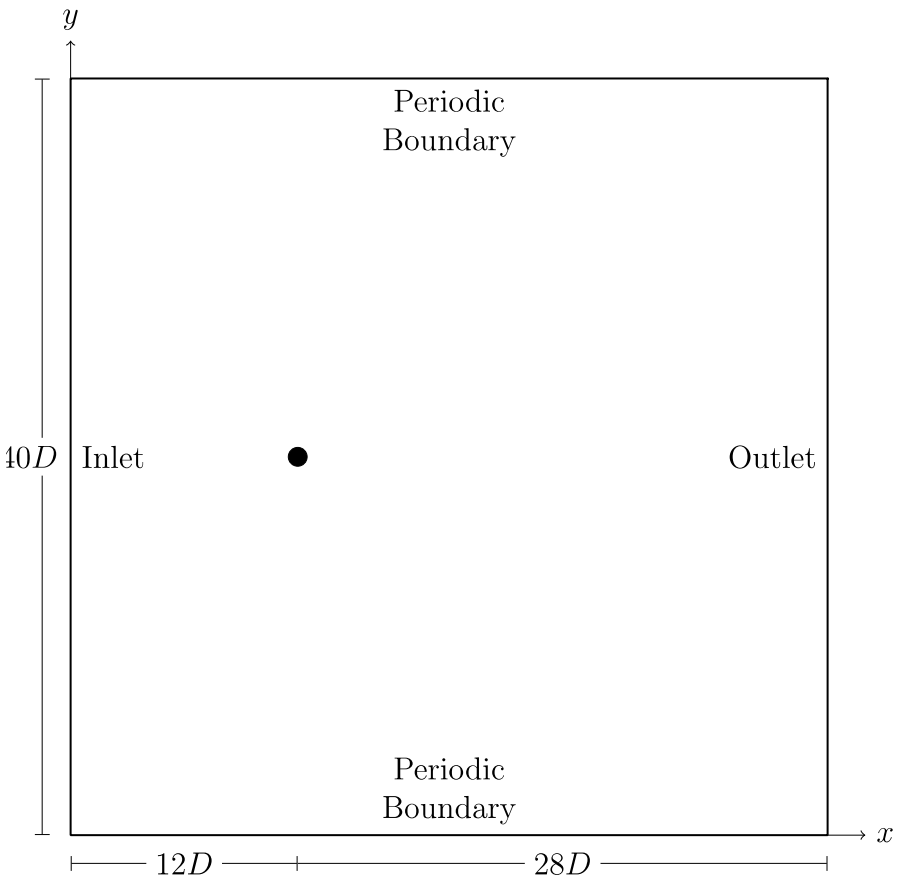

Fig. 4.3. Domain for the 2-D stationary cylinder.

A free triangular mesh was created for the simulation in order to handle the more complex geometry created by using a circular cylinder and a rectangular domain. This free triangular mesh posed a problem, which is made evident in Section 4.3, in which a non-uniform mesh is created at the trailing edge of the cylinder; this non-uniform mesh caused a spurious shift in the lift[26]. This non-uniformity was corrected by placing a horizontal line that divides the domain in half; this line is not used in any calculations but simply allows the creation of a symmetric mesh. The free mesh is created by first meshing the top half of the domain and then mirroring the mesh along the horizontal line giving a perfectly symmetric mesh and avoiding any discrepancies in results due to the grid asymmetry. Figure 4.4 provides the progression from the non-uniform mesh to the perfectly symmetric mesh. In order to capture the physics involved accurately, a boundary layer mesh was inserted with 8 layers in the boundary. The final mesh consists of 29,558 mesh elements.

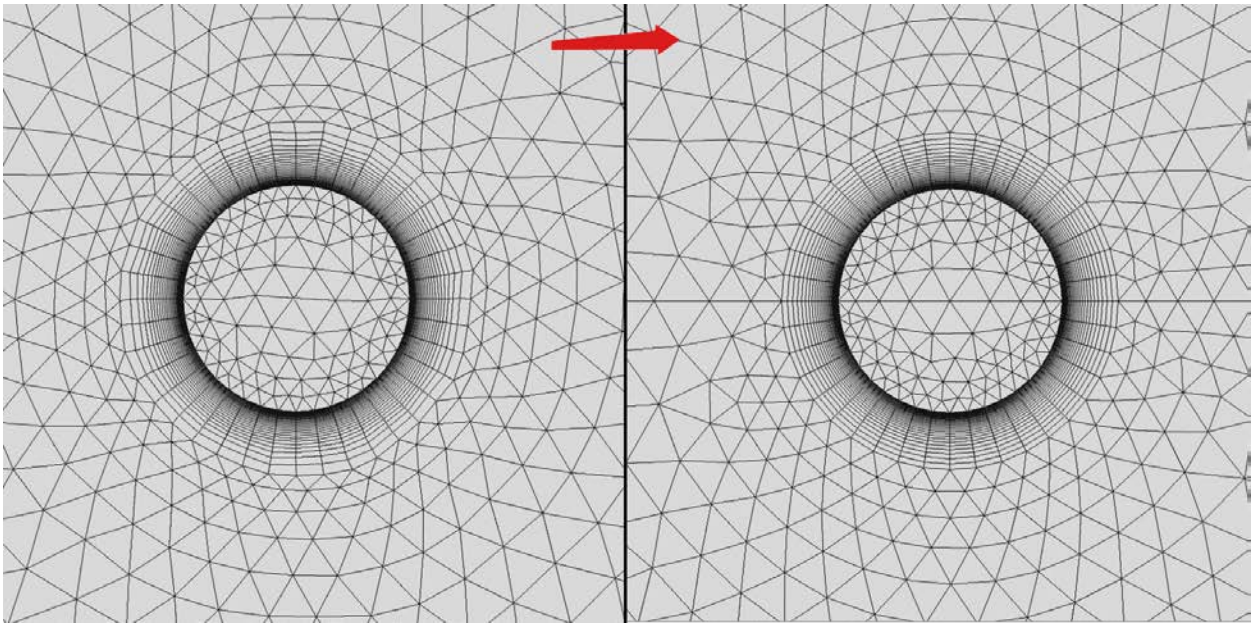

Fig. 4.4. Mesh comparison for the 2-D Cylinder.

Simulation and Results

The simulation for the stationary cylinder in cross-flow was run using a fully implicit time domain solver. A steady-state solution was used to obtain an initial condition in order to reduce the computational costs needed to solve the start-up of the flow solver. The initial condition for the $\boldsymbol{Re = 100}$ case is provided in Fig. 4.5.

The fully implicit solver is stable and lends itself to large time-step iterations[91]. When a steady-state solution with no periodic tendencies is desired, this greatly reduces the computational costs needed to obtain a steady-state solution. The cylinder in cross-flow, as stated earlier, should result in a time-accurate solution that converges into a periodic state in which a limit cycle is observed. If a solver is implemented for the determination of the time-step used in the time-stepping scheme, certain physical phenomena may be missed. For the cylinder in cross-flow case with a steady-state initial condition, the time-step may be too large to allow the solver to capture the instability that induces the vortex shedding. This phenomenon was seen with the present study in which the cylinder failed to produce the predicted vortex shedding.

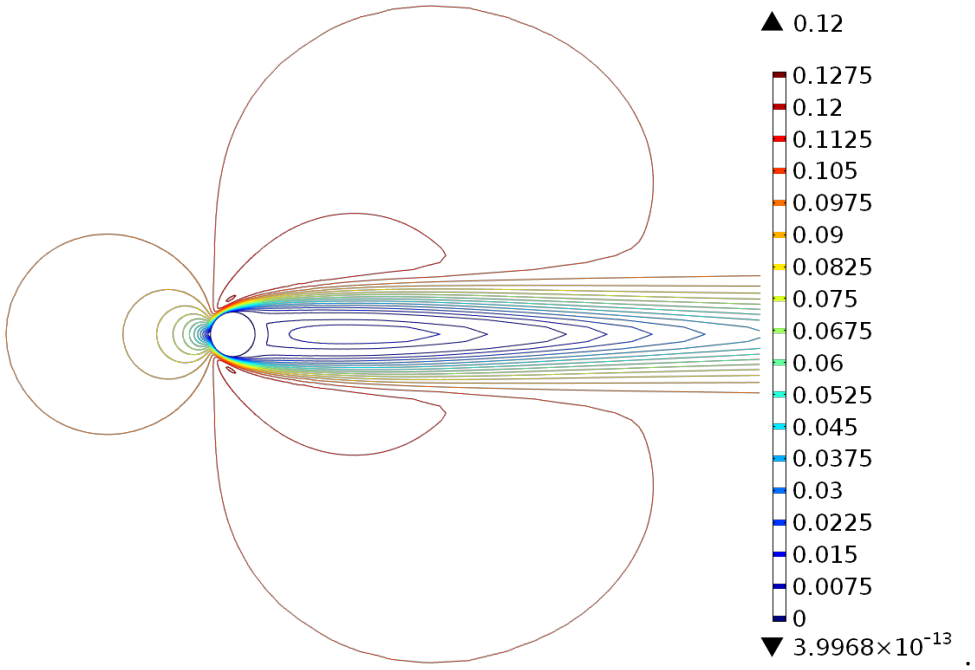

Fig. 4.5. Initial condition using the steady-state solver for $\boldsymbol{Re = 100}$. The velocity contours are represented in m/s.

For example, with $\boldsymbol{Re = 100}$, the cylinder should shed within 10 physical seconds from the initial condition (here, physical seconds represents the time in the time domain as opposed to the computational time which is the interval it takes to run the code on a given machine and is dependent upon the number of cores and solving method used (i.e., direct or iterative method and is typically referred to as the 'wall-clock time'). When the time-step was calculated for any interval, the code would compute time-steps much too large to capture the vortex shedding. The solution would remain in steady state and no shedding would be observed; the solution would be indistinguishable from the initial condition seen in Fig. 4.5.

To correct this problem, a limit on the maximum time-step was imposed. This limit was taken to be 1/20 of the approximate period of shedding for a particular Reynolds number. Again using $\boldsymbol{Re = 100}$ as an example and the other physical properties described above, the shedding frequency can be estimated from Equation 1 with $\boldsymbol{St \approx 0.165}$ to be approximately 16.5 $\boldsymbol{Hz}$. Using the estimated frequency, a maximum time-step of approximately 0.00151s produces the desired vortex shedding. This method was employed for all of the simulations, allowing the code to properly capture the flow physics.

In order to verify the vortex shedding capabilities of the flow solver, a variety of Reynolds numbers were computed. Because the phenomena are not observed for all Reynolds numbers, a simulation with $\boldsymbol{Re = 20}$ was performed to ensure that the code could capture shedding as well as non-shedding cases. To establish a good basis, the following Reynolds numbers were considered: 50, 75, 100, 150 and 200. This range ensures laminar flow while allowing the analysis to remain two-dimensional. A sample of the solution obtained once the cylinder begins to shed vortices is provided in Fig. 4.6 for $\boldsymbol{Re = 100}$.

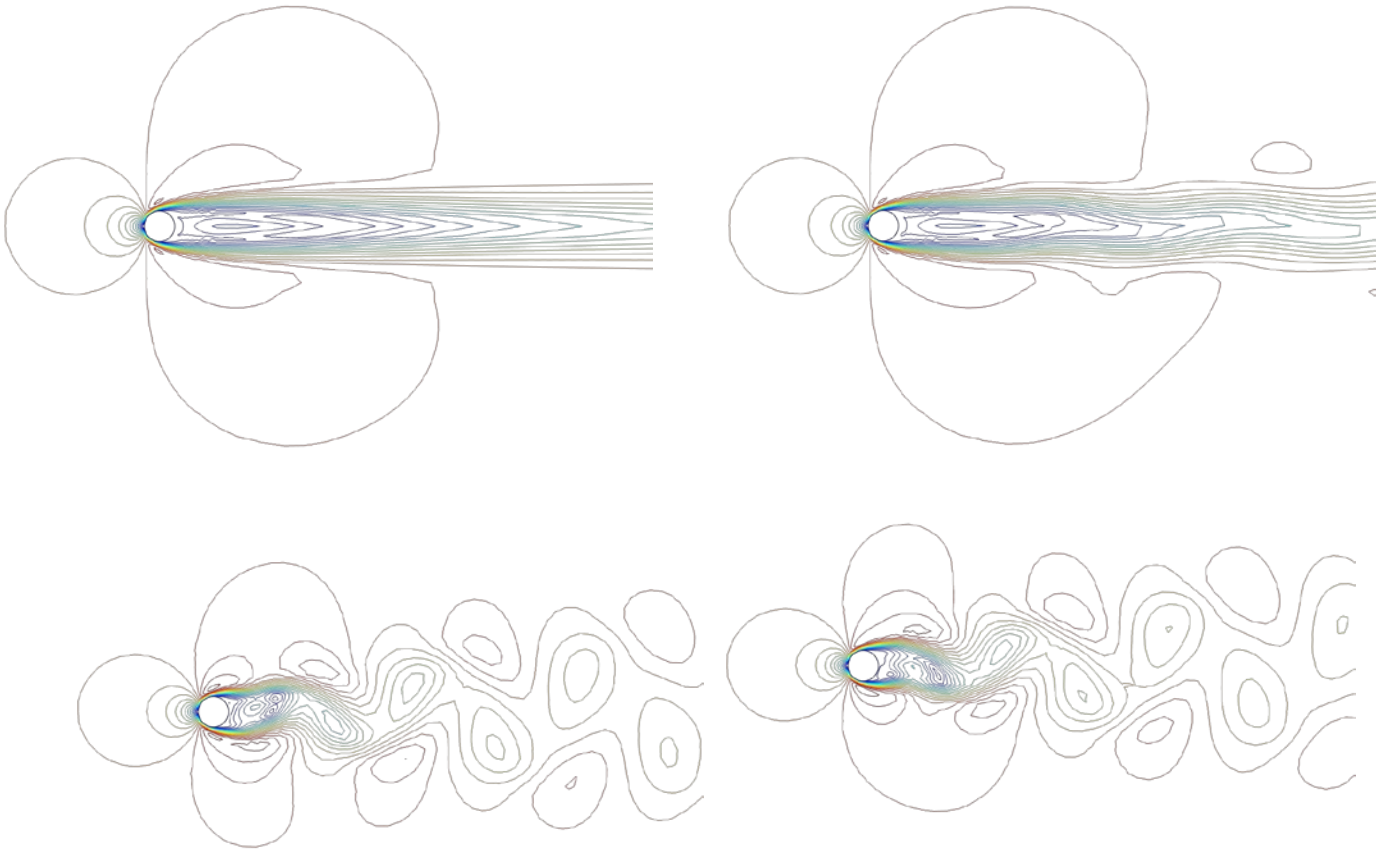

Fig. 4.6. Set of time-domain solutions for $Re = 100$. Shown are velocity magnitudes.

The fundamental way to measure the shedding frequency is to observe the coefficient of lift, C_l, defined by:

$$C_l = \frac{l}{1/2\rho_f U_\infty^2 d} \quad (4.5)$$

where l represents the lift on the cylinder per unit length, ρ_f represents the free-stream fluid density, U_∞ represents the free-stream fluid velocity and d is the cylinder diameter. Observation of the lift in the time domain shows that the vortex shedding has gone into a limit cycle but it is difficult to determine the exact frequency of the shedding (Fig. 4.7). A Fast-Fourier Transform (FFT)[92] is employed to determine the dominant frequencies of the solution Fig. 4.8.

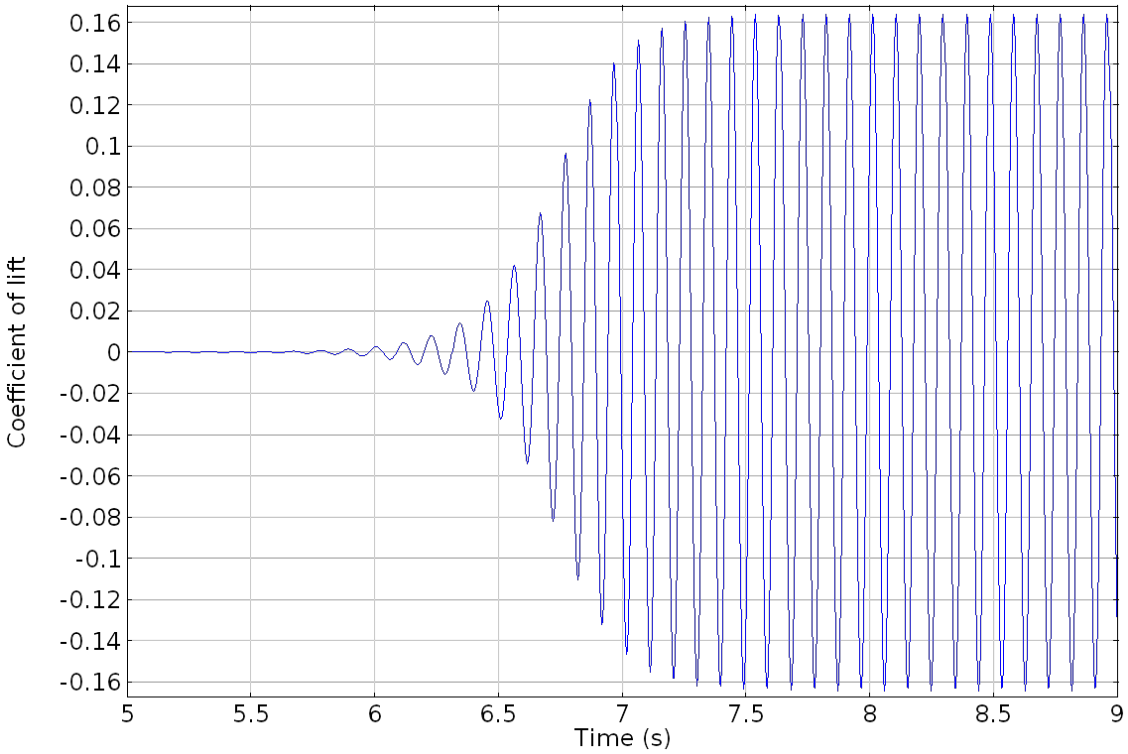

$\boldsymbol{Re = 75}$

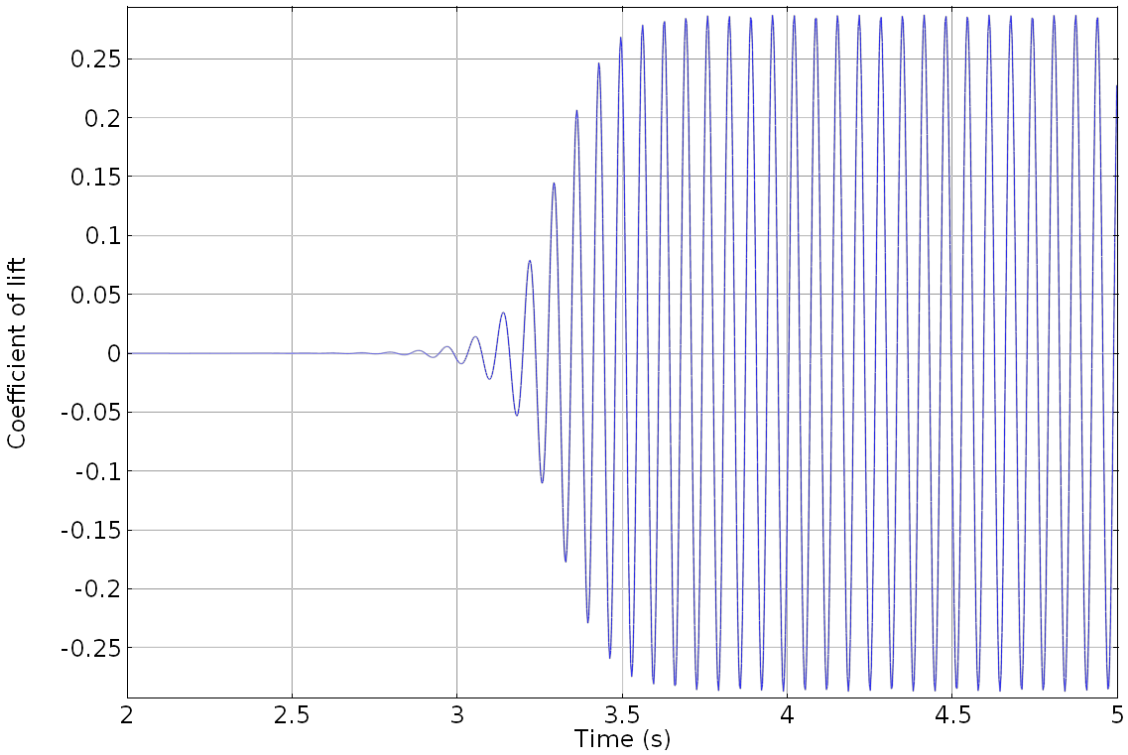

$\boldsymbol{Re = 100}$

Fig. 4.7. Time accurate C_l for the stationary cylinder (part 1 of 2).

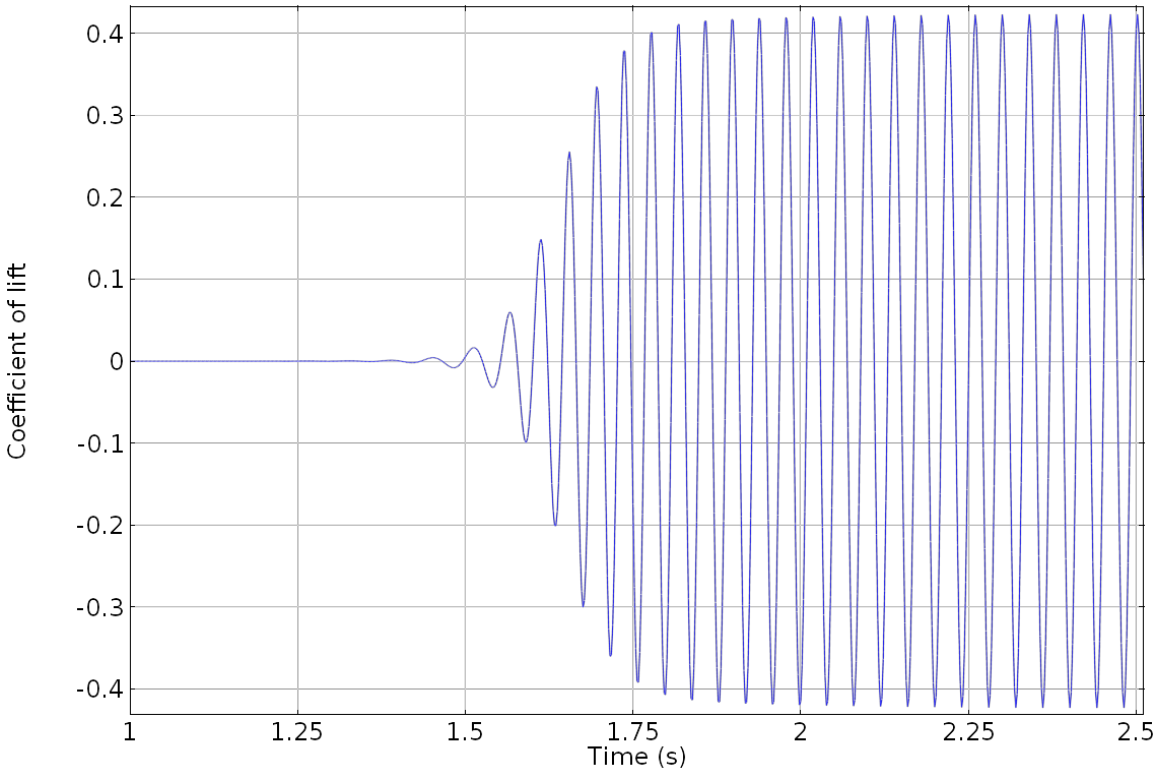

$\boldsymbol{Re = 150}$

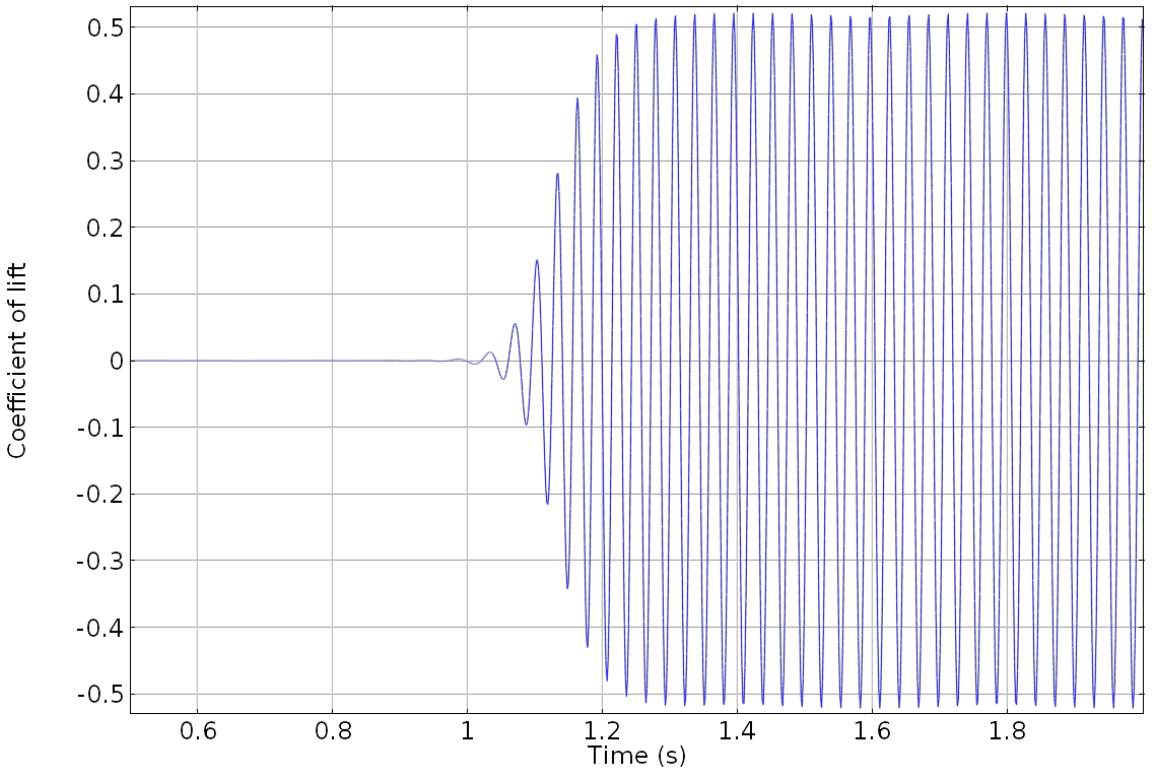

$\boldsymbol{Re = 200}$

Fig. 4.7. Time accurate C_l for the stationary cylinder (part 2 of 2).

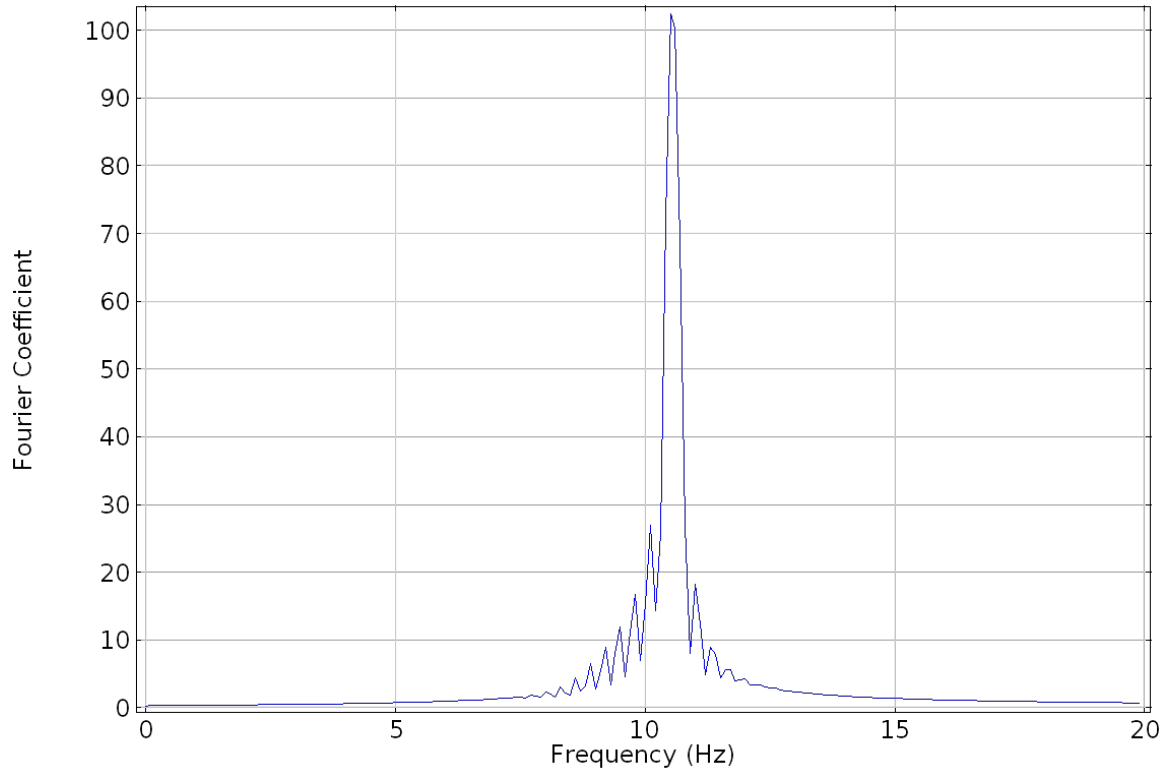

$\boldsymbol{Re = 75}$

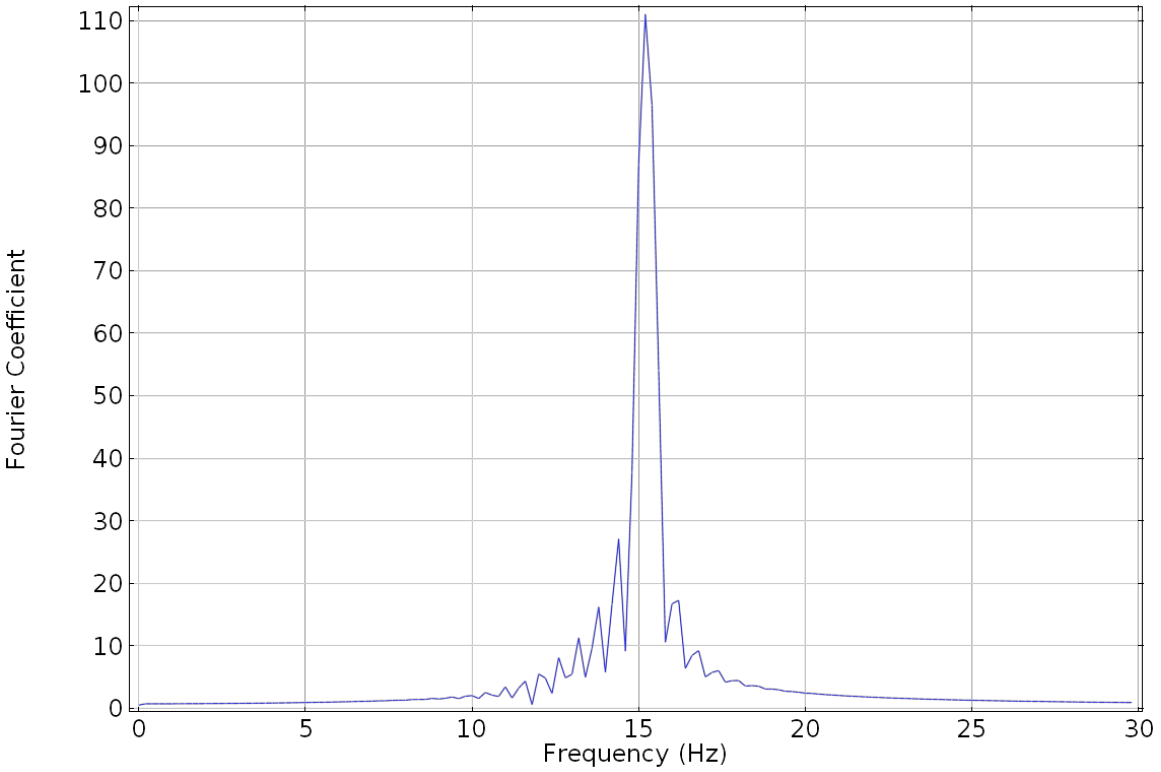

$\boldsymbol{Re = 100}$

Fig. 4.8. FFT of the C_l for the stationary cylinder (part 1 of 2).

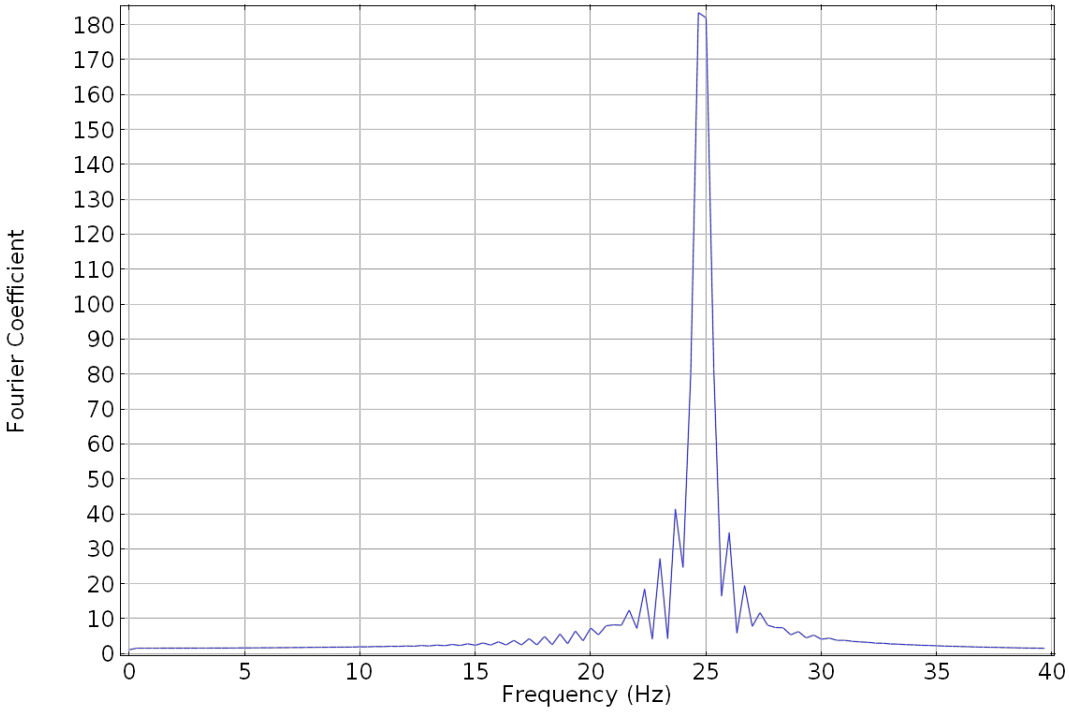

$\boldsymbol{Re = 150}$

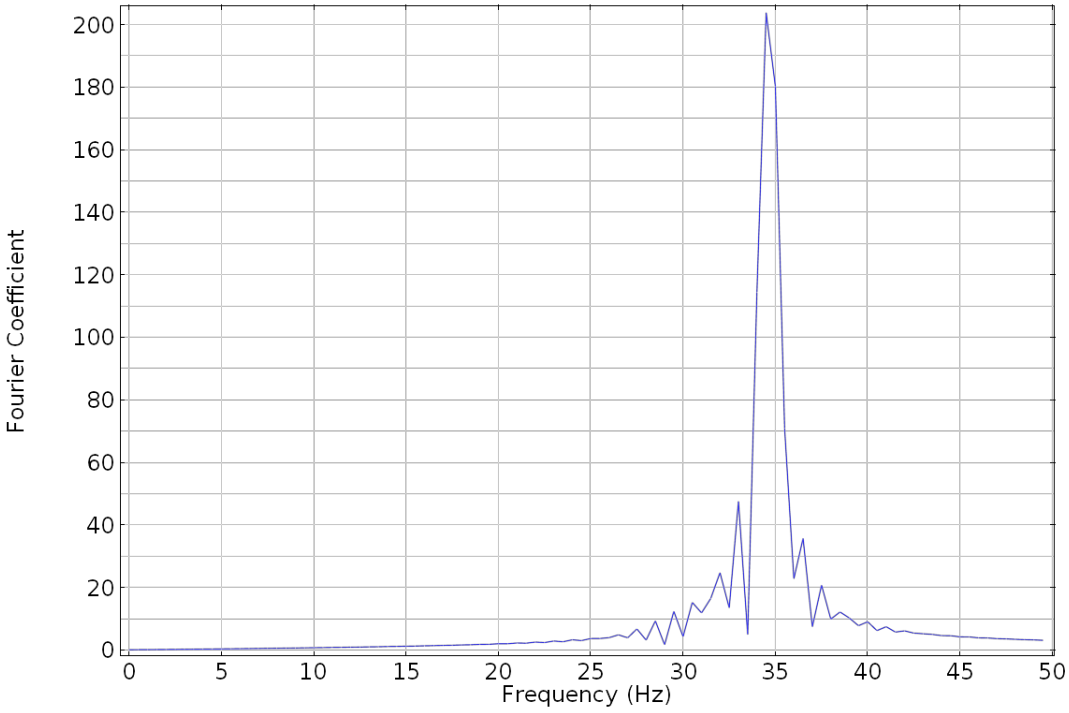

$\boldsymbol{Re = 200}$

Fig. 4.8. FFT of the C_l for the stationary cylinder (part 2 of 2).

The subfigures of Fig. 4.8 are used to obtain the shedding frequency for each case. Williamson[93] performed experiments for the cylinder in cross-flow and presented his results in graphical form. For a direct comparison of our solution with the experimental data, the open source program called Engauge Digitizer was used to extract the data from the published paper. The extracted experimental data is compared to the simulations in Table 4.1.

Table 4.1. Shedding frequencies of the stationary cylinder in cross-flow compared to experimental results of Williamson [Williamson(1988)].

	Experimental		Numerical	
Re	St	Freq, Hz	St	Freq, Hz
20	0.0000	0.00	0.0000	0.00
75	0.1424	10.70	0.1398	10.50
100	0.1600	16.03	0.1517	15.20
150	0.1800	27.05	0.1642	24.68
200	0.1825	36.57	0.1723	34.52

Discussion

The stationary cylinder in cross-flow provides a context to test real-world instabilities with a numerical code. The simulations show that the code is capable of reproducing these naturally occurring phenomena when careful consideration of the numerical tools is employed. By limiting the transient solver time-step to 1/20 the time it takes to shed one vortex, the code is able to capture the expected Kármán vortex streets close to the experimentally obtained Strouhal number.

Because the small time-step could result in large data files, it was originally proposed to record the data at intervals larger than the 1/20 time-step but smaller than the shedding interval. This resulted in very manageable file sizes but it was quickly discovered that the interval, as with all digital recording, could induce unwanted aliasing[94]. This aliasing is evident as a smaller frequency on top of the main frequency as seen in Fig. 4.9. In order to alleviate the aliasing, the sampling rate was configured to be the same as the maximum time step allowed for each simulation. This change eliminated the aliasing problem from the solution and aliasing effects were considered for any other time-dependent solutions.

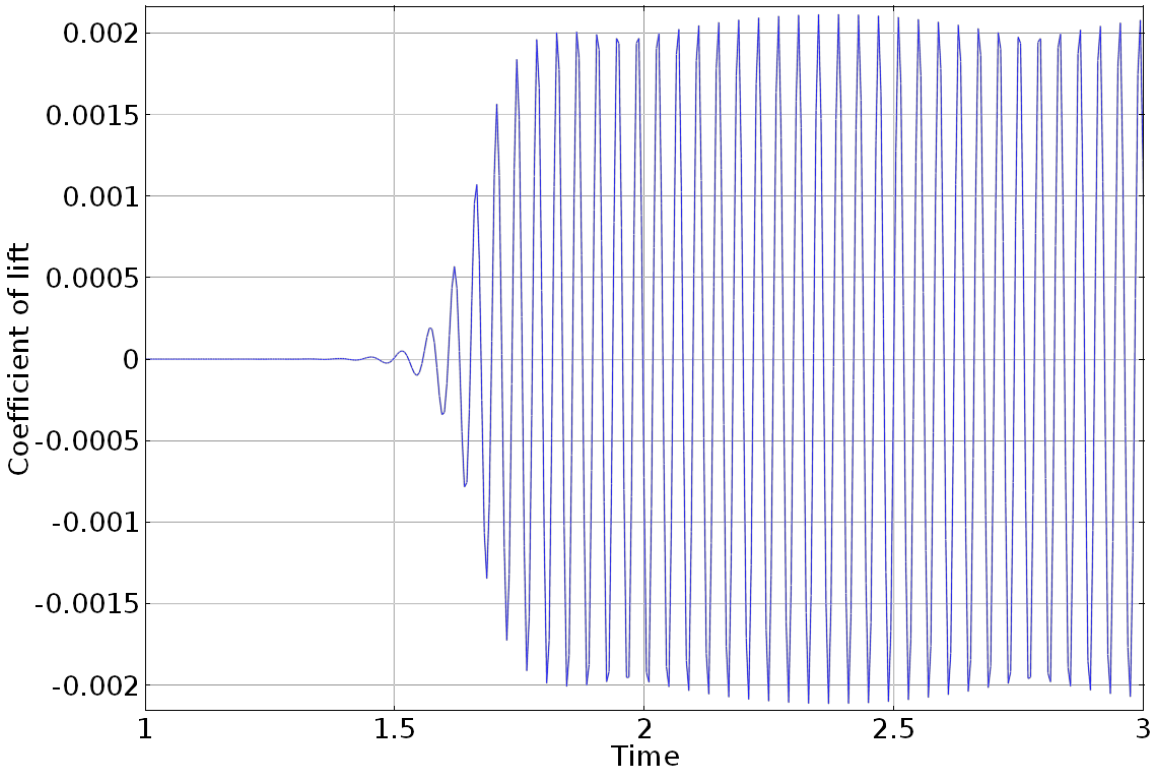

Fig. 4.9. C_l for the $Re = 150$ case with aliasing present due to large recording intervals.

The code has proven to effectively capture the shedding vortices for a 2-D cylinder in cross-flow. Table 4.1 shows that the numerical simulation provides reasonable results compared to the experiment. Using the stationary cylinder as proving grounds and stepping stone for analysis, it is now appropriate to move on to more complicated cases.

4.2.2 Oscillating Cylinder: Prescribed Displacement

The next logical step in testing the FSI capabilities of the code is to allow the cylinder to move. In this section, the cylinder movement will follow a prescribed periodic displacement that is not affected by the flow of the fluid and its subsequent shedding vortices. This will allow the testing of both the mesh deformation capability and the fluid solver for a moving cylinder. The cylinder will be allowed to oscillate in the transverse direction of the free-stream flow velocity. This case was also considered experimentally by Koopman[82]for Reynolds numbers of 100 and 200.

The vortex streets that are shed from the oscillating cylinder can fall into two categories: lock-on and non lock-on. In the lock-on region, the vortices are shed at the same frequency of the oscillating cylinder. When one investigates the coefficient of lift, there is only one principle frequency present. For the non lock-on case, the cylinder sheds vortices at its ‘natural’ frequency based upon the Strouhal number for the flow conditions. This will result in two principal frequencies being present in the coefficient of lift calculations (the cylinder oscillation and the ‘natural’ vortex shedding). A representation of the cylinder lock-on and non lock-on regions is presented in Fig. 4.10.

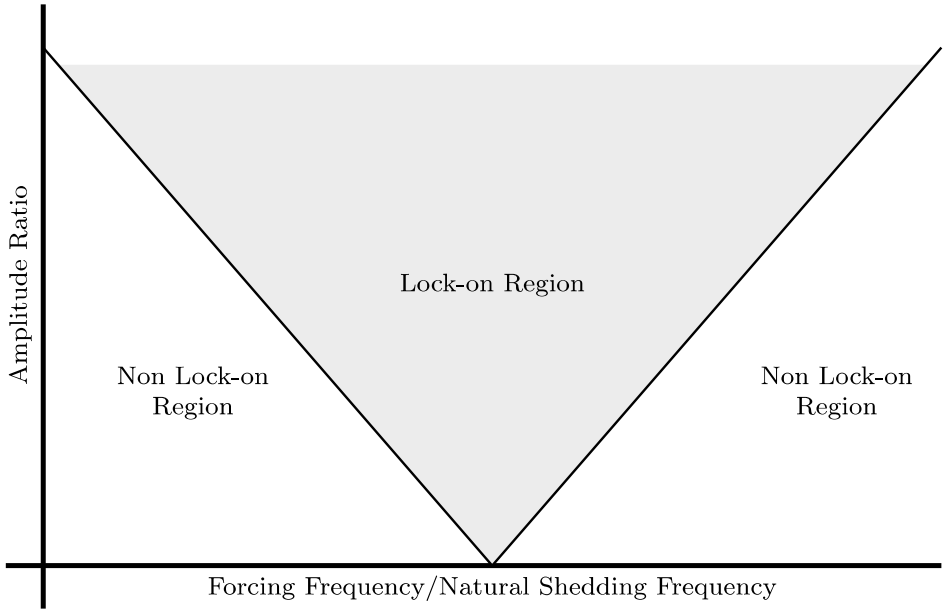

Fig. 4.10. Graphical Representation of the lock-on region.

Domain and Boundary Conditions

The domain for the oscillating cylinder with prescribed displacement is the same as that used for the stationary cylinder. The only boundary condition that is different from the one used for the stationary cylinder is the solid moving boundary around the cylinder. The boundary will now follow the general wall boundary condition such that the fluid velocity is equal to the velocity of the wall such that $\boldsymbol{u_{fluid} = u_{solid}}$.

The cylinder will follow a periodic sinusoidal motion normal to the free-stream velocity. The maximum amplitude and frequency will vary depending on the particular case being examined during the simulation. The equation of motion for the cylinder is given by:

$$\hat{\boldsymbol{j}} \cdot \boldsymbol{u_{solid}} = \boldsymbol{h}\sin(\boldsymbol{\omega t}) \quad (4.6)$$

where $\hat{\boldsymbol{j}}$ is the unit vector in the direction transverse to the inlet flow, $\boldsymbol{h}$ is the cylinder amplitude and $\boldsymbol{\omega}$ is the oscillation frequency. The baseline mesh for this case is the same as that used for the stationary cylinder.

Now that movement is to take place during the simulation of the flow around the cylinder, it is necessary to allow the mesh to deform and move with the cylinder. In COMSOL, there are 3 different types of mesh smoothing techniques:

- Laplace
- Winslow
- Hyperelastic

The Laplace technique, first described by Buel and Bush[95] for a structured mesh and refined by Field[96] for a free triangular mesh, applies the Laplace operator on the computational coordinates $(\boldsymbol{\xi}, \boldsymbol{\eta})$

in the physical space $(\boldsymbol{X}, \boldsymbol{Y})$. When the Laplace Equation 4.7 is satisfied, a smooth distribution of the computational coordinates is present.

$$\begin{aligned} \boldsymbol{\nabla^2 \xi} &= \frac{\partial^2 \xi}{\partial x^2} + \frac{\partial^2 \xi}{\partial y^2} = \mathbf{0} \\ \boldsymbol{\nabla^2 \eta} &= \frac{\partial^2 \eta}{\partial x^2} + \frac{\partial^2 \eta}{\partial y^2} = \mathbf{0} \end{aligned} \quad \text{.....(4.7)}$$

The Laplace equations should satisfy the max-min conditions such that parameters inside the domain will not exceed the boundary of the domain which ensures that the grid lines will not cross resulting in inverted meshes. In Equation 4.7, the known variables are $(\boldsymbol{\xi}, \boldsymbol{\eta})$ and the unknown variables are $(\boldsymbol{x}, \boldsymbol{y})$. Applying the Laplacian of Equation 4.7 to the computational space results in the Laplace smoothing equation:

$$\begin{aligned} \boldsymbol{\nabla^2 x} &= \frac{\partial^2 x}{\partial \xi^2} + \frac{\partial^2 x}{\partial \eta^2} = \mathbf{0} \\ \boldsymbol{\nabla^2 y} &= \frac{\partial^2 y}{\partial \xi^2} + \frac{\partial^2 y}{\partial \eta^2} = \mathbf{0} \end{aligned} \quad \text{.....(4.8)}$$

Although Equation 4.8 satisfies the max-min condition for a structured mesh, this is not always the case for an unstructured mesh where some of the elements may be inverted, resulting in negative cell volumes.

To overcome the limitations of the Laplace smoothing technique, Winslow[97] proposed a transformation resulting in the following set of equations:

$$\begin{aligned} &\boldsymbol{\alpha \frac{\partial^2 x}{\partial \xi^2} - 2\beta \frac{\partial^2 x}{\partial \xi \partial \eta} + \gamma \frac{\partial^2 x}{\partial \eta^2} = 0} \\ &\boldsymbol{\alpha \frac{\partial^2 y}{\partial \xi^2} - 2\beta \frac{\partial^2 y}{\partial \xi \partial \eta} + \gamma \frac{\partial^2 y}{\partial \eta^2} = 0} \\ &\boldsymbol{\alpha = \left(\frac{\partial x}{\partial \eta}\right)^2 + \left(\frac{\partial y}{\partial \eta}\right)^2} \\ &\boldsymbol{\beta = \frac{\partial x}{\partial \xi}\frac{\partial x}{\partial \eta} + \frac{\partial y}{\partial \xi}\frac{\partial y}{\partial \eta}} \\ &\boldsymbol{\gamma = \left(\frac{\partial x}{\partial \xi}\right)^2 + \left(\frac{\partial y}{\partial \xi}\right)^2} \end{aligned} \quad \text{.....(4.9)}$$

This set of equations can greatly improve the accuracy and may alleviate the problems of inverted meshes found using the Laplace smoothing equations[98].

The last mesh smoothing technique available in the code is a hyperelastic technique inspired by neo-Hookean materials[99]. The technique searches for the minimum of the mesh deformation energy in which the energy is given by:

$$\boldsymbol{W = \int_{\Omega} \frac{\mu}{2}(I_1 - 3) + \frac{\kappa}{2}(J-1)^2 dV} \quad \text{.....(4.10)}$$

where $\boldsymbol{\mu}$ is the artificial shear modulus and $\boldsymbol{\kappa}$ is the artificial bulk modulus. The invariants $\boldsymbol{J}$ and $\boldsymbol{I_1}$ are given by:

$$\begin{aligned} \boldsymbol{J} &= \boldsymbol{\det(\nabla x^x)} \\ \boldsymbol{I_1} &= \boldsymbol{J^{-2/3} \mathrm{tr}\left((\nabla x^x)^T \nabla x^x\right)} \end{aligned}$$

Each of the three mesh smoothing techniques has their benefits and trade-offs. The fastest and least computationally expensive technique would be the Laplace smoothing. The most robust of the three techniques is the hyperelastic smoothing technique. Because of the large mesh displacements possible in the upcoming simulations, the Laplace smoothing technique will not be used. In order to retain some accuracy, to prevent inverted meshes, and to obtain solutions in a reasonable amount of time, the Winslow smoothing technique will be used for all of the moving mesh simulations of this report.

Simulation and Results

The issues seen with the stationary solver and the use of the implicit solvers are not observed with the moving cylinder because the simulation does not have to rely on a natural instability to begin to shed. Although any time-stepping scheme may be used, the issue of aliasing could still be present such that the restriction on the time-step of 1/20 of the predicted frequency will still be used. There will be 35 cases run for the prescribed cylinder motion with a Reynolds number of 100. The cases were chosen in order to span across the lock-on and non lock-on regions. The frequency ratio, $\boldsymbol{f/f_n}$, spans from 0.8 to 1.2 and the amplitude ratio, $\boldsymbol{h/D}$, spans from 0.05 to 0.35. The results are presented in Fig. 4.11 where the plus (+) symbols represent the case in which lock-on occurs and the cross (×) symbols represent the case in which no lock-on occurs.

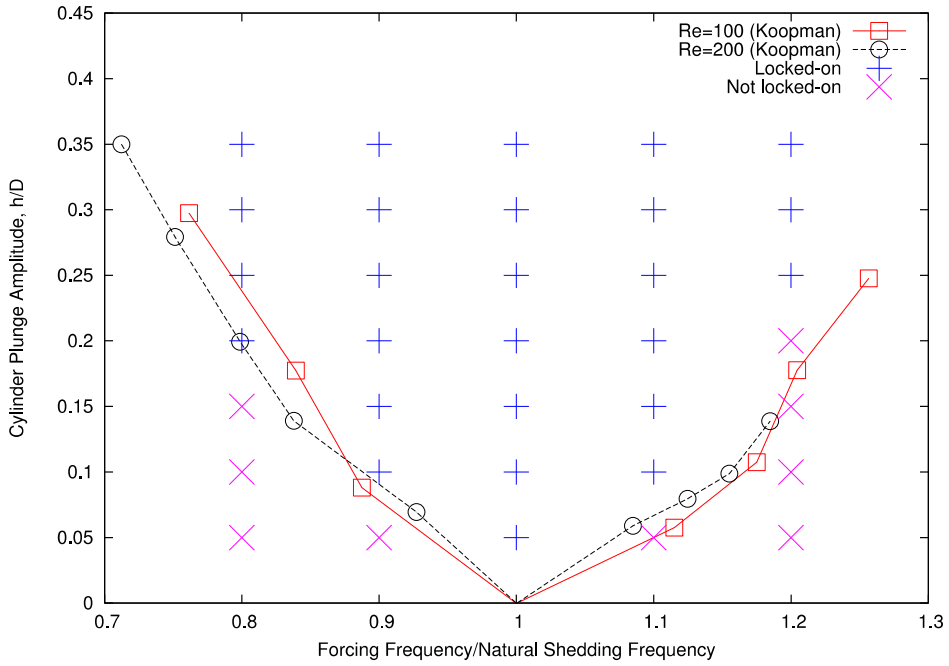

Fig. 4.11. The cylinder lock-on simulations compared to the experiment by Koopman. The plus symbols (+) represent cases in which lock-on was achieved and the cross symbols (×) represent the cases in which no lock-on were present.

Discussion

The oscillating cylinder with prescribed displacement follows the experimental setup quite well. There is one simulation that does not follow the experimental results presented by Koopman at a plunge amplitude of 0.2 and a frequency ratio of 1.2. This ‘extreme’ case is an outlier in all of the other lock-on cases, and based upon the success of the other simulations does not negate the solver. For instance, the simulations around the ‘fork’ of the experimental results follow the lock-on/non lock-on progression as expected. The

most reasonable explanation for this outlier is the fact that experiments, by their nature, have error involved and thus the 'fork' may be in a different place. The next step in establishing the validity of the FSI code is to allow the cylinder to move freely based upon the lift created by the shedding vortices.

4.2.3 Hydroelastic Analysis: Free Displacement

Following the progression described previously, the cylinder will now be allowed to move freely based upon the lift created by the shedding vortices. This oscillation will be restricted to movement only in the transverse direction to the free-stream inlet velocity. The movement for the 2-D cylinder will be described as a spring-mass-damper system. The cylinder with free displacement lends itself to a full FSI study in 3-D utilizing the coupling of the Navier-Stokes equations with the structural dynamic equations. This progression was previously followed in other simulations[85].

Domain and Boundary Conditions

As with the previous two sections, the domain for the free oscillating cylinder is a rectangle with the same dimensions as presented earlier. The inlet, outlet and periodic boundary conditions remain unchanged from the previous two sections. In this section however, the cylinder is displaced not based upon a prescribed motion known *a priori*, but based upon the periodic lift created by the oscillating vortices. For the 2-D simulation, the cylinder displacement is determined from the equation of motion for a spring-mass-damper system:

$$\boldsymbol{m\ddot{x} + c\dot{x} + kx = f(t)} \quad \text{.....(4.11)}$$

where the forcing function, $\boldsymbol{f(t)}$, is determined by the lift on the cylinder. Figure 4.12 provides a visual representation of the mass-spring-damper assumption used for the 2-D simulation.

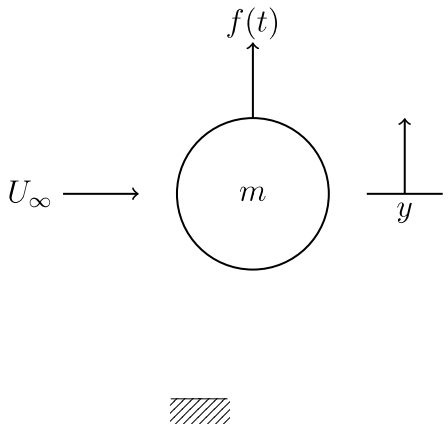

Fig. 4.12. Spring-mass-damper model used for the hydroelastic simulations.

The spring constant, $\boldsymbol{k}$, is determined using beam theory for a cantilevered beam:

$$\boldsymbol{\delta_l = \frac{FL^3}{3EI}} \quad \text{.....(4.12)}$$

where $\boldsymbol{\delta_l}$ is the deflection at the end of the beam, $\boldsymbol{F}$ is the force at the end of the beam, $\boldsymbol{L}$ is the length of the beam, $\boldsymbol{E}$ is the Modulus of Elasticity of the beam and $\boldsymbol{I}$ is the area moment of inertia of the beam[100]. Rearranging Equation 4.12 such that $\boldsymbol{F/\delta_l = k}$ yields the effective stiffness of the beam:

$$\boldsymbol{k_{effective} = F/\delta_l = \frac{3EI}{L^3}} \quad (4.13)$$

Assuming that there is no internal damping yields $\boldsymbol{c = 0}$ and the mass is assumed to be the total mass of the cylinder such that $\boldsymbol{m = \rho_{cyl} \cdot V_{cyl}}$. Equation 4.11 is a single degree of freedom (SOF) ordinary differential equation (ODE), which will be solved using an ODE solver.

The 3-D case is the first test of the coupling of the structural mechanics and fluid mechanics to form a Fluid-Structure Interaction problem. The 3-D domain has an identical setup to the 2-D domain except that the domain is 'swept' so that a cylinder is created. The boundary conditions are the same for the fluid domain except that the new walls created by the 'sweeping' of the domain are held as slip boundaries such that

$$\boldsymbol{u_f \cdot n = 0} \quad (4.14)$$

$$\boldsymbol{K - (K \cdot n)n = 0} \quad (4.15)$$

where $\boldsymbol{K = \left[\mu\left(\nabla u_f + \left(\nabla u_f\right)^T\right)\right] n}$. During the sweep, 4 cuts are made to create a 3-D simulation. This limited number of cuts is utilized in an effort to speed up computational times; this is also made possible because of the low Reynolds number of the flow and the slip boundary conditions along the two specified walls of the domain. This results in a mesh consisting of 118,232 points.

Simulation and Results

The displacement of the cylinder should match the frequency of the shedding vortices. For completeness, two simulations will be performed to ensure that both are excited at the natural shedding frequency. The simulations will use inlet conditions such that the Reynolds number is 100 and 200. The working fluid is again chosen to be water with the properties previously described in Section 1. The cylinder properties are as follows: $\boldsymbol{\rho = 7800 kg/m^3}$, $\boldsymbol{E = 70 GPa}$, $\boldsymbol{\nu = 0.35}$, and $\boldsymbol{L = 0.01}$m. These parameters result in a cylinder with an area moment of inertia of $\boldsymbol{I = 4.909E-14 m^4}$ and an effective spring stiffness of $\boldsymbol{k_{effective} = 10,308}$N/m. As with the previous two sections, a steady-state solution is used as the initial condition for the transient simulation.

The FSI problem (in both 2D and 3D) can be solved numerically in three different ways: fully coupled, segregated, and one-way coupled. The fully coupled method, as the name implies, solves for all of the physics (fluid and structure) in the same matrix. This method is the most expensive yet most robust solution technique. The solver iterates on the fully coupled matrix until the convergence criteria is met. Figure 4.13 provides a flow chart for the visualization of the fully coupled solver.

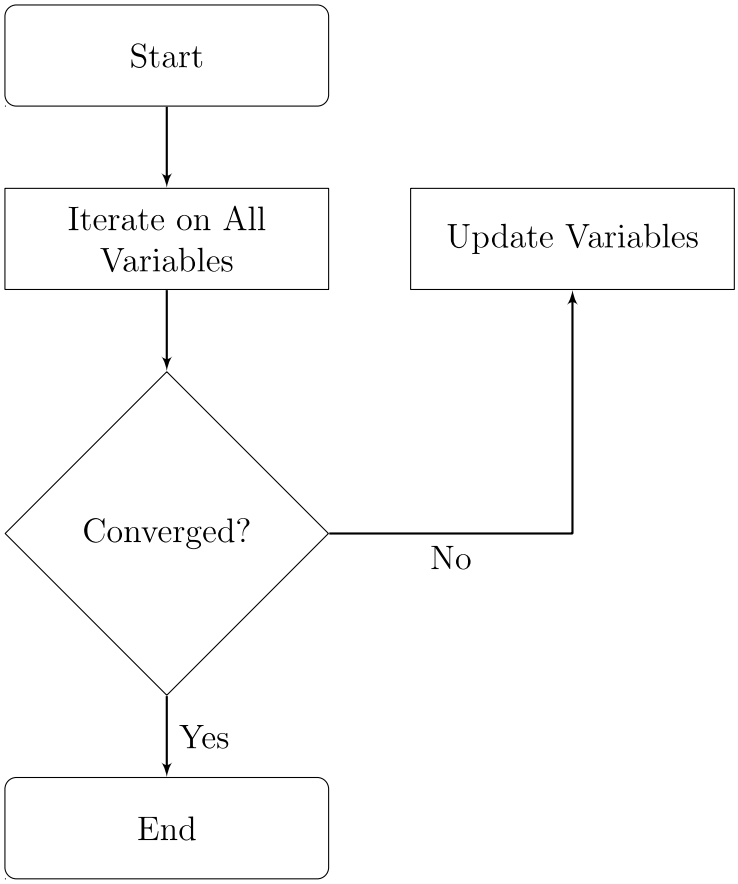

Fig. 4.13. Flow chart for the fully coupled solver.

The segregated solver allows the dependent variables to be solved independently of each other. For the FSI problem, the most logical segregation is the separation of the fluid mechanics and the solid mechanics. First, the fluid variables are iterated upon until a stopping criterion is met (typically a set number of iterations), and then the fluid solution is used to establish the boundary conditions for the structural model. The solver then computes the structural variables. The overall convergence is checked; if the convergence criterion is not met, the boundaries for the fluid domain are updated and the process continues. Figure 4.14 shows the progression of the segregated solver. One of the strongest benefits of the segregated solver is the smaller memory requirement needed. Because the structural mechanics is solved second, the structure lags by one outer iteration, and depending on the coupling approach this could cause stability issues.

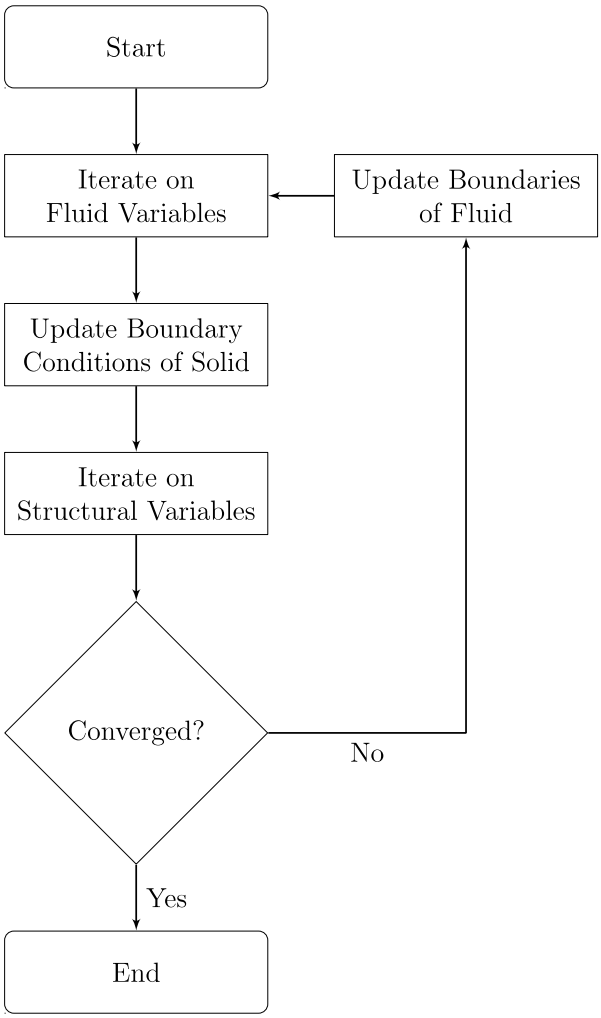

Fig. 4.14. Flow chart for the segregated solver.

The one-way coupled solution technique fully decouples the fluid and structural variables. First, the fluid domain is fully solved for using the initial conditions of the structural domain for its boundary conditions. Once the fluid variables are fully converged, they are used to establish the boundary conditions for the structural mechanics solver. The structural variables are computed without updating the fluid solution and the process is completed. The flow chart for the one-way coupled solver is provided in Fig. 4.15. This solution technique is the fastest of the three solvers discussed. If the fluid and structure are not strongly coupled, then this technique works very well. For example, a very stiff structure in which the flow-induced displacement is very small and does not greatly affect the characteristics of the flow is a very good candidate for the one-way coupled solver.

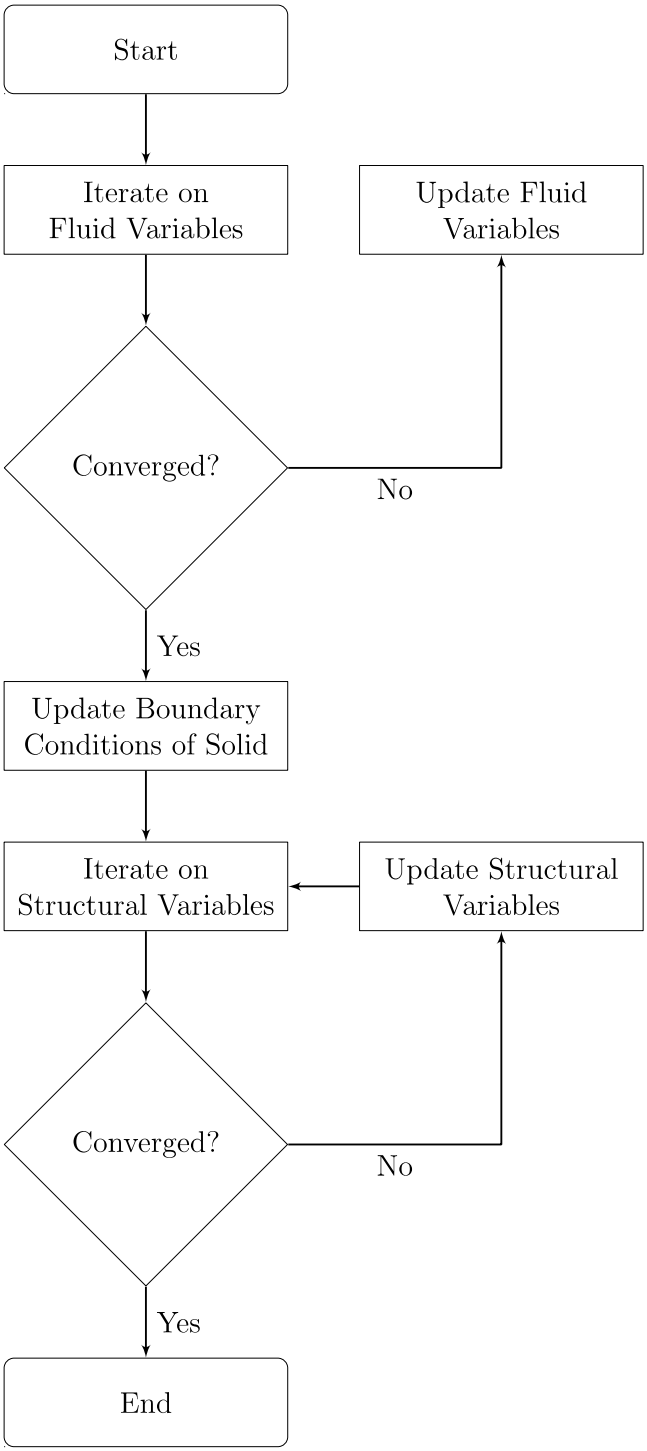

Fig. 4.15. Flow chart for the one-way coupled solver.

2D CASE

For the 2-D case, all three solvers will be explored. For the transient cases, the fully coupled and segregated solvers work similarly in that for each time-step, the solver is run until convergence before the next time-step is computed. For the one-way coupled solver, the transient fluid solution is computed and then the transient structural solution is computed using the previously computed fluid solution as the boundary condition at each time step. The one-way coupled solver solves the fluid solution to completion and then uses the fluid solution to obtain the transient structural solution. The results for the first case, the fully coupled solver, are provided in Fig. 4.16.

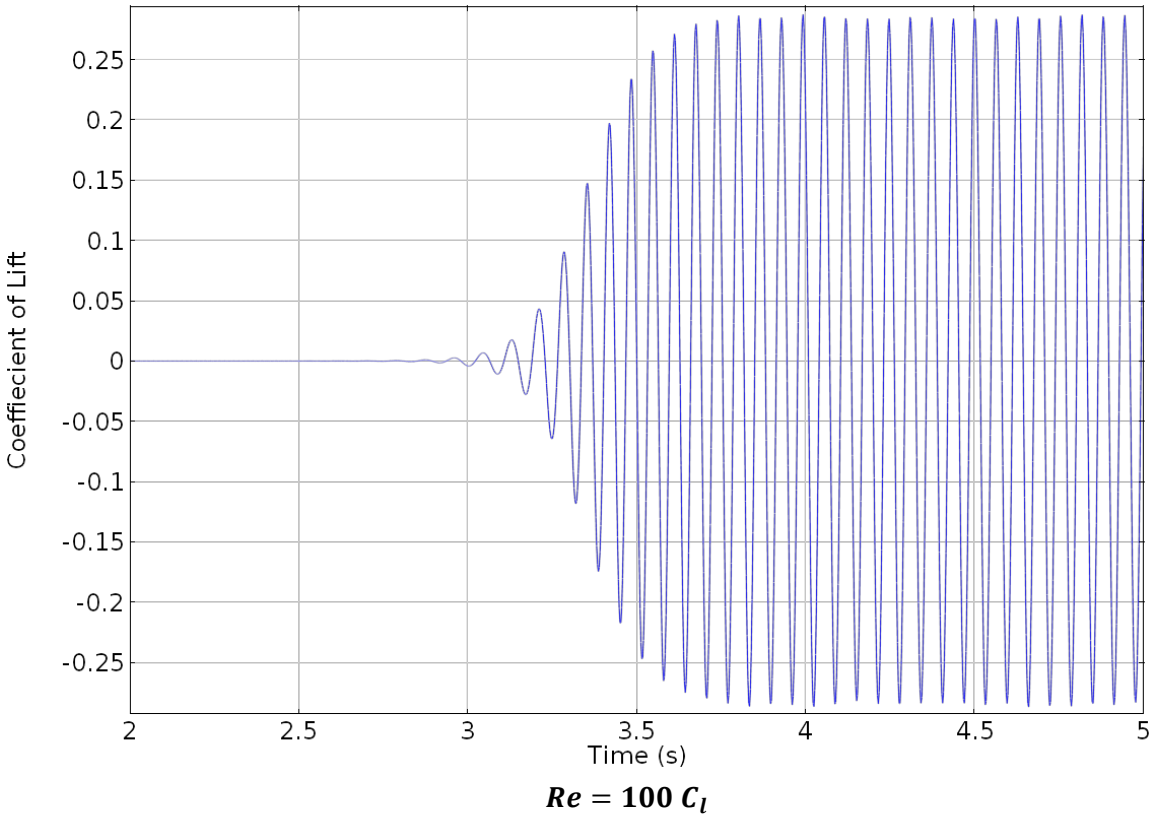

Fig. 4.16. Solution of the fully coupled 2-D free displacement cylinder (part 1 of 3).

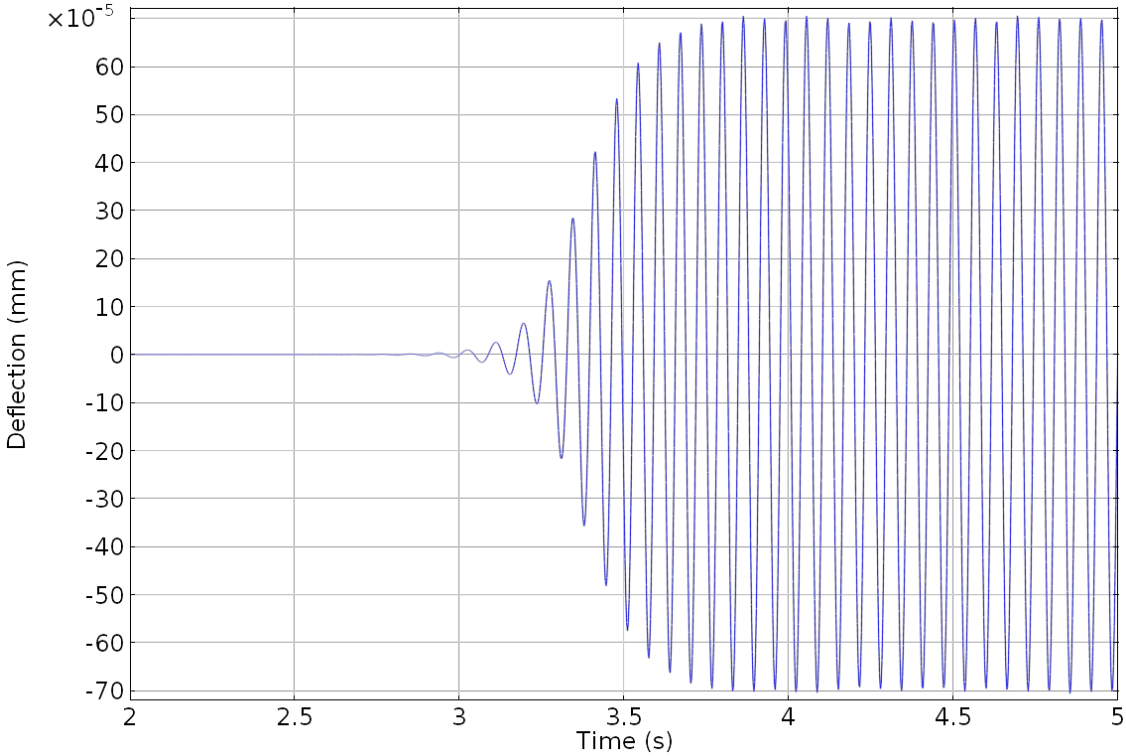

$\boldsymbol{Re = 100}$ Displacement

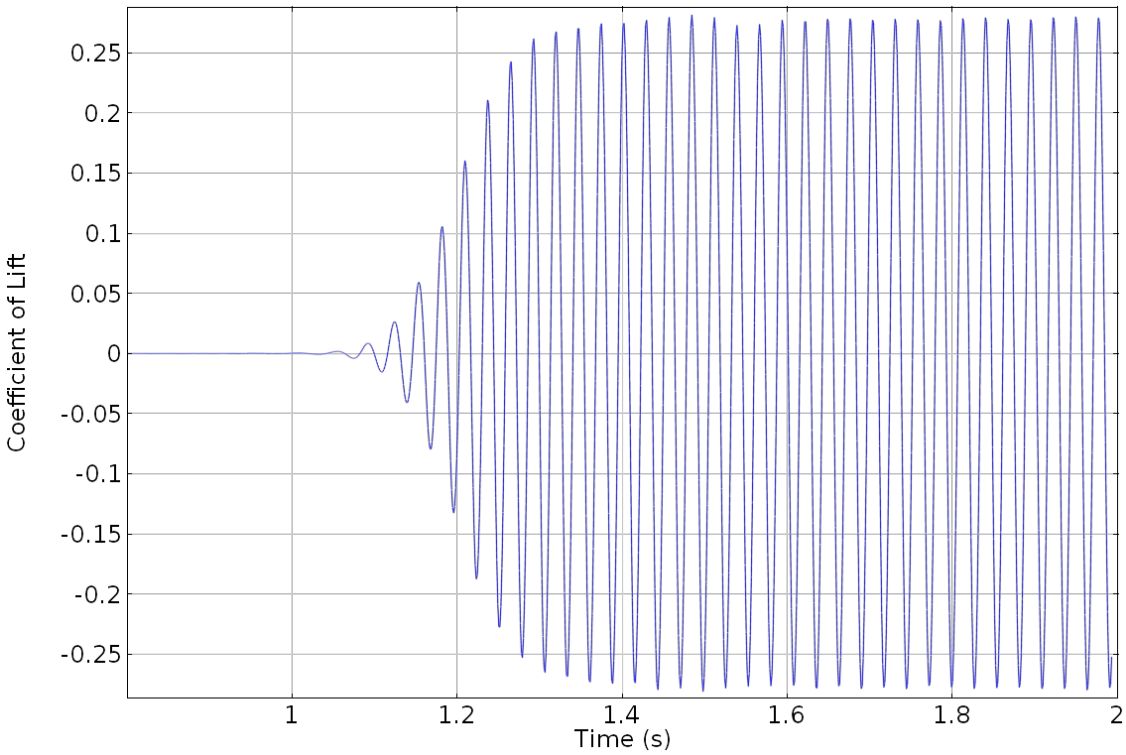

$\boldsymbol{Re = 200\ C_l}$

Fig. 4.16. Solution of the fully coupled 2-D free displacement cylinder (part 2 of 3).

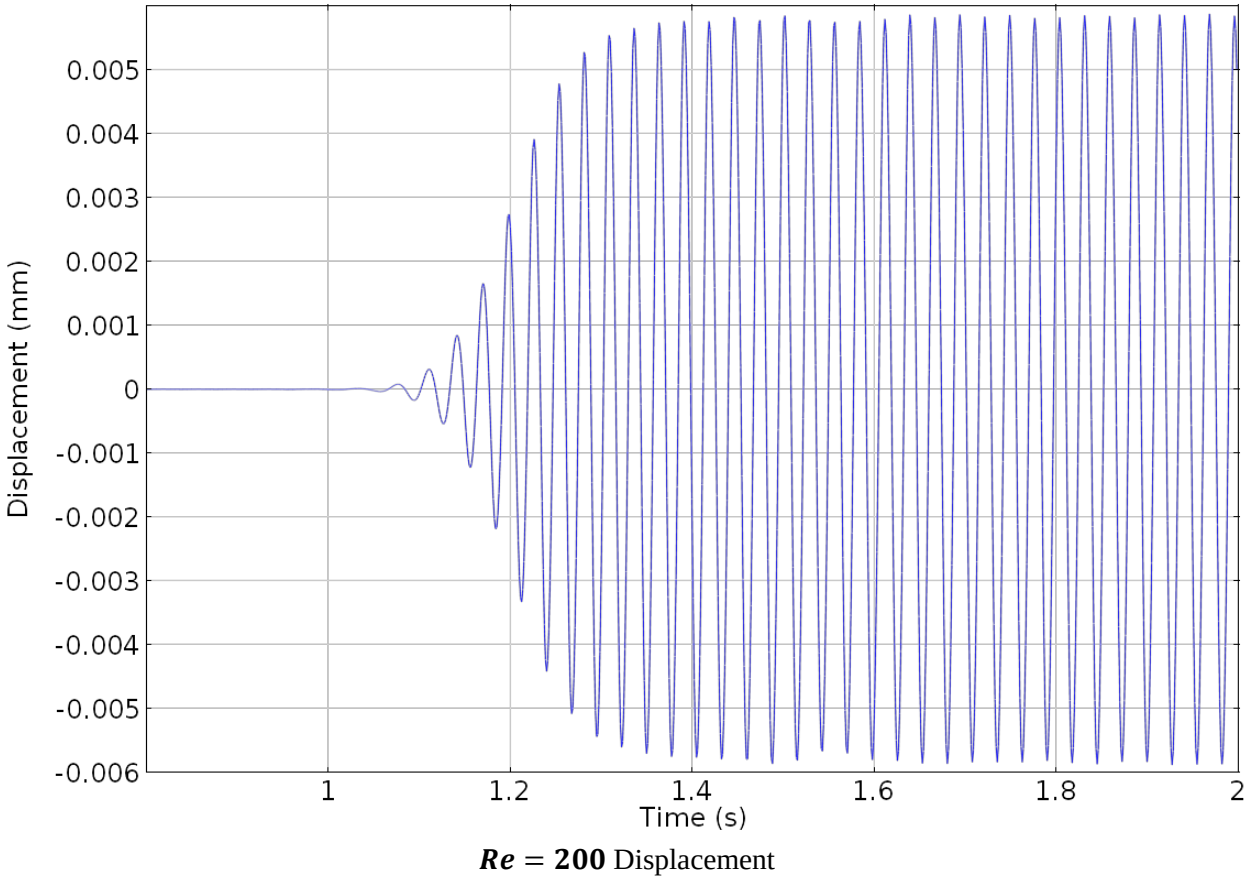

Fig. 4.16. Solution of the fully coupled 2-D free displacement cylinder (part 3 of 3).

The frequencies of the coefficient of lift and displacement as well as the solution time are provided in Table 4.2. A solution was not obtained for the segregated solver because of instabilities created with the segregation process.

Table 4.2. Results for the 2-D simulation for the free displacement cylinder. The frequencies were obtained using the FFT. The simulations were performed on a 12 core machine with 192GB RAM

Re		C_l, Hz	Displacement, Hz	Max. Disp., mm	Time, s
100	Fully-Coupled	15.67	15.67	$\mathbf{69.5 \times 10^{-5}}$	10107
	Segregated	——	——	——	——
	One-Way	15.2	15.2	**0.0058**	890
200	Fully-Coupled	37.5	37.5	$\mathbf{13.9 \times 10^{-5}}$	6888
	Segregated	——	——	——	——
	One-Way	34.2	34.5	**0.001**	746

3D CASE

The 3-D simulation, as previously described, is a simple extrusion of the 2-D setup. The extrusion, along with the mesh cuts, is provided in Fig. 4.17. This simulation is run using the fully coupled solver in order to retain the interaction between both the cylinder and the fluid. The cylinder is modeled as a cantilevered beam with a fixed boundary on one side and a free boundary on the other. The results for the coefficient of lift and cylinder displacement are provided in Fig. 4.18.

The fully coupled, 3-D simulation, as expected, took a much longer time to complete than the 2-D cases. The cases took 68,743 and 46,303 seconds for the $\boldsymbol{Re}$ 100 and 200 cases, respectively. The oscillating frequency and displacement frequency matched for both cases at 15 Hz for $\boldsymbol{Re = 100}$ and 34 Hz for $\boldsymbol{Re = 200}$.

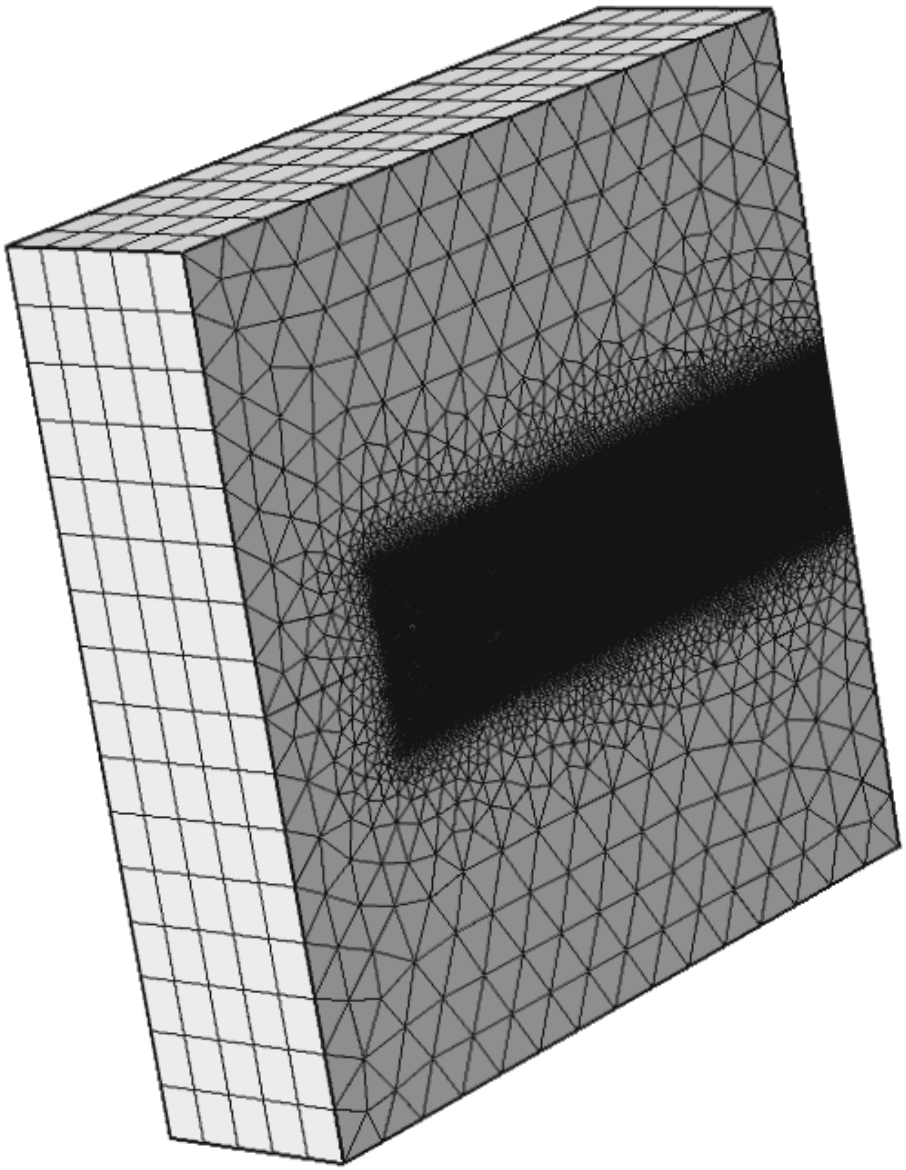

Fig. 4.17. Mesh for the 3-D cylinder in cross-flow simulation.

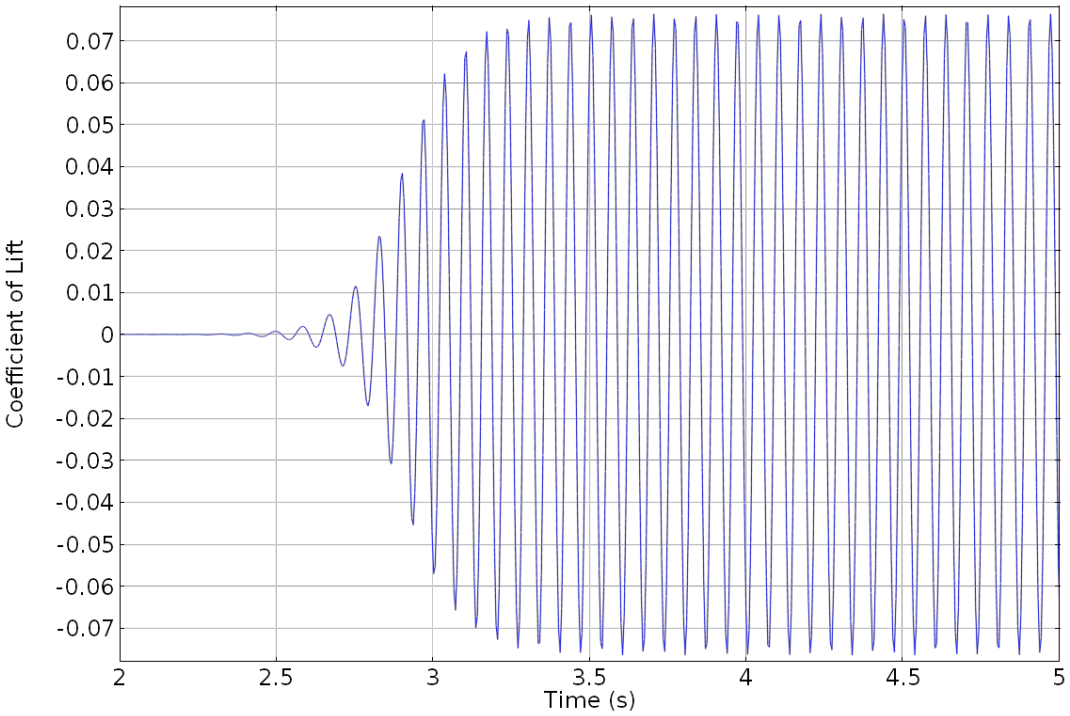

$\boldsymbol{Re = 100\ C_l}$

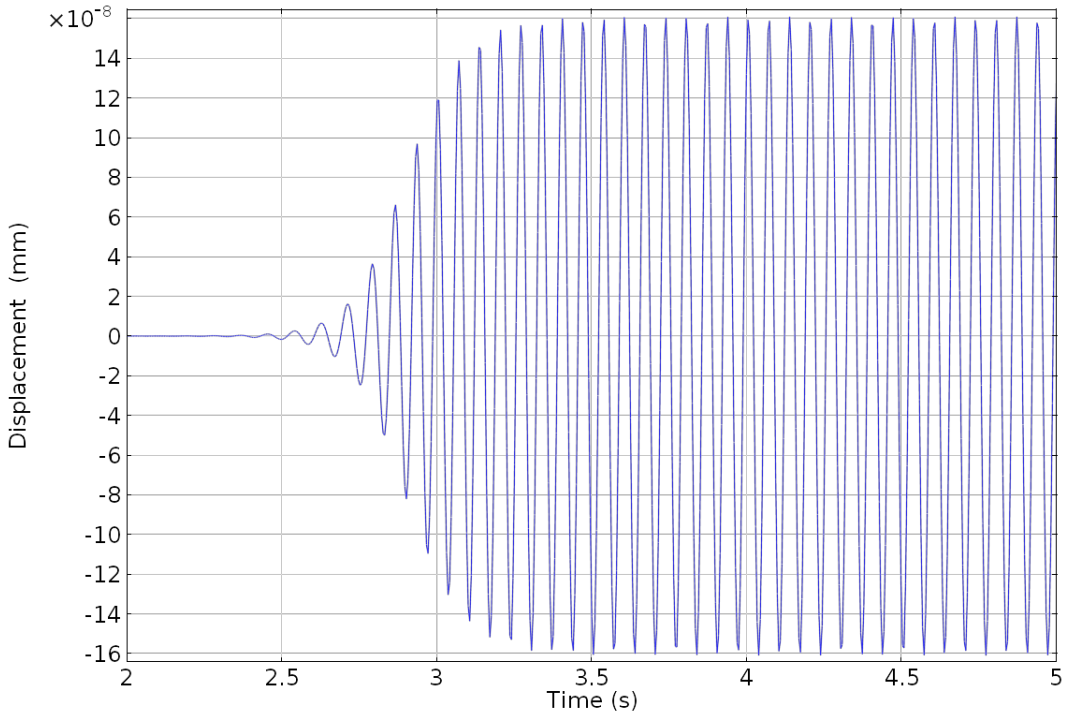

$\boldsymbol{Re = 100}$ Displacement

Fig.4.18. Solution of the fully coupled 3-D free displacement cylinder. The results are taken at the free end of the cylinder (part 1 of 2).

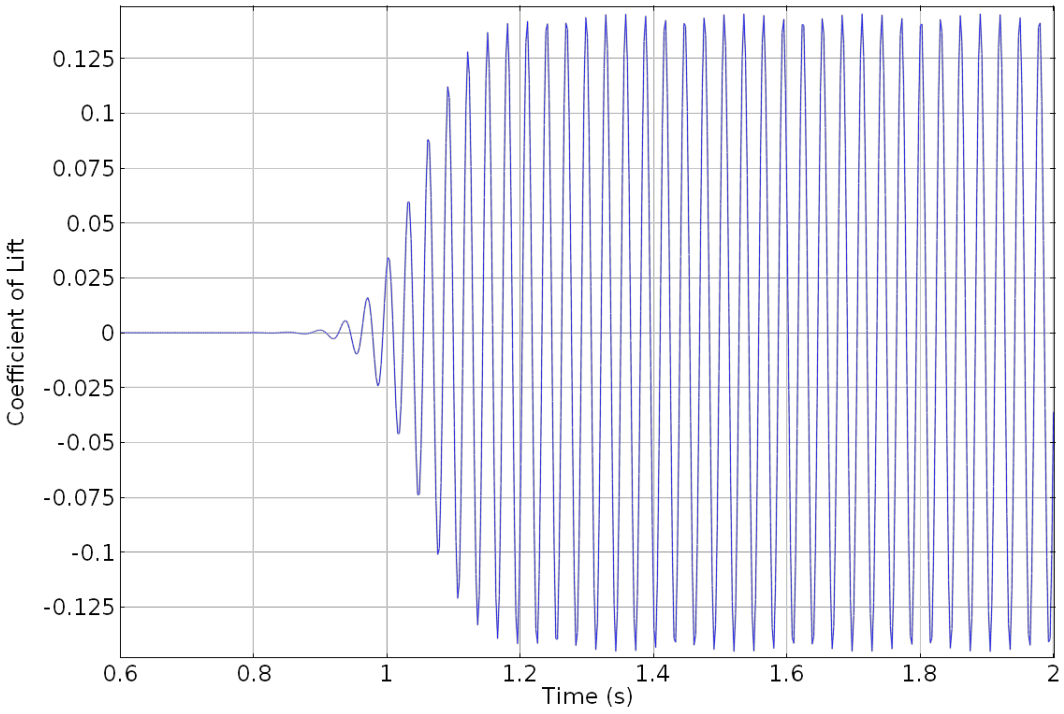

$\boldsymbol{Re = 200\ C_l}$

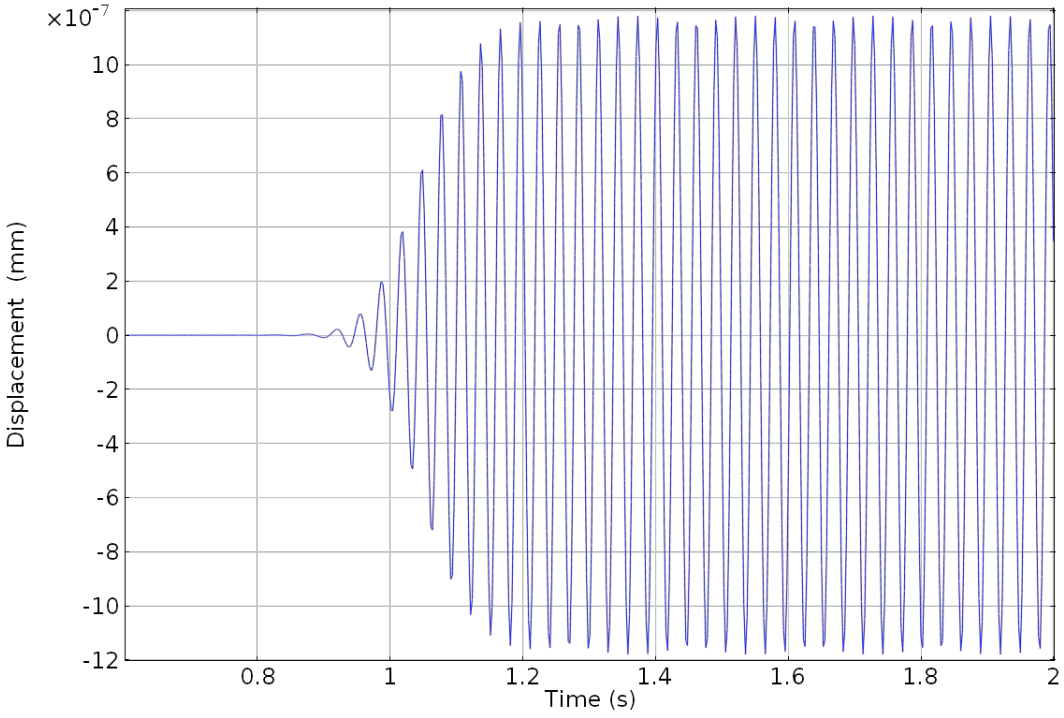

$\boldsymbol{Re = 200}$ Displacement

Fig.4.18. Solution of the fully coupled 3-D free displacement cylinder. The results are taken at the free end of the cylinder (part 2 of 2).

Discussion

The oscillating cylinder with free displacement provides insight into the capabilities of the FSI solver to capture the physics of the phenomena. The exploration of the 3 solving techniques available in the code for the 2-D case allows for an assessment of the applicability of the methods for the FSI cases. Looking at the results in the previous table, it can be seen that the fastest solution can be obtained using the one-way coupling. While the one-way coupled solver produced oscillating frequencies similar to the fully coupled solver, the maximum deflections were smaller than the fully coupled case. The segregated solver was not able to capture the physics correctly resulting in an unstable solution in which the residual would diverge. The 2-D, free displacement case revealed the need for the perfectly symmetric mesh described in section 1. Observing the displacement of the cylinder once it reached its limit cycle revealed the need for this new meshing technique. Assuming a perfectly round cylinder, the displacement should oscillate around the original position of the cylinder but when the mesh was not symmetric, the cylinder would initially drift up and begin to oscillate about another position, which can be seen in Fig. 4.19.

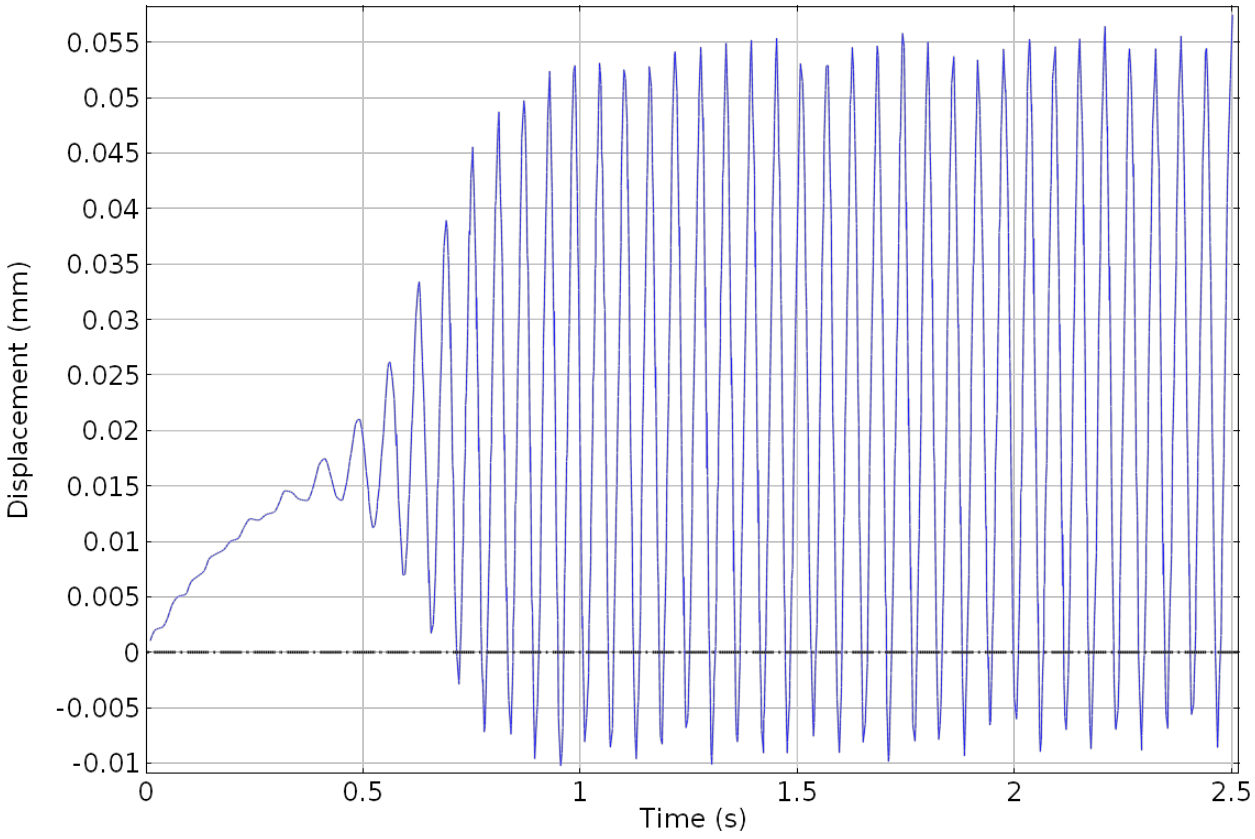

Fig. 4.19. Incorrect displacement of the 2-D cylinder for the condition of $Re = 100$. The dashed line represents the initial position and the displacement should oscillate about it.

The 3-D case, which included the linear-elastic structural model, was able to capture the physics as well. For each case, the maximum displacement was smaller than the 2-D cases. This can be attributed to the assumptions made for the spring-mass-damper system: all of the mass of the cylinder is at the end, increasing its momentum and there is no internal damping to decrease the displacement for a given input force. Taking these assumptions into account, the displacements obtained from the simulations are within reason.

4.2.4 Stationary Cylinder with Moving Tail

The last section for the cylinder in cross-flow will incorporate a stationary cylinder with a moving tail. This numerical test, proposed by [88], allows the testing of large displacement FSI models using a 2-D setup. The published paper for the numerical test case includes a multitude of results for three different laminar cases that demonstrate the effectiveness of both the fluid and structural solver. The cylinder, as seen in the previous sections, will begin to shed vortices under the ideal conditions; these vortices will then create changes in pressure that will cause the cylinder tail to deform. This deformation, in conjunction with the vortex shedding, is the main focus of this section.

Domain and Boundary Conditions

The stationary cylinder with moving tail is placed in a rectangular domain as proposed by Turek and the domain is presented in Fig. 4.20.

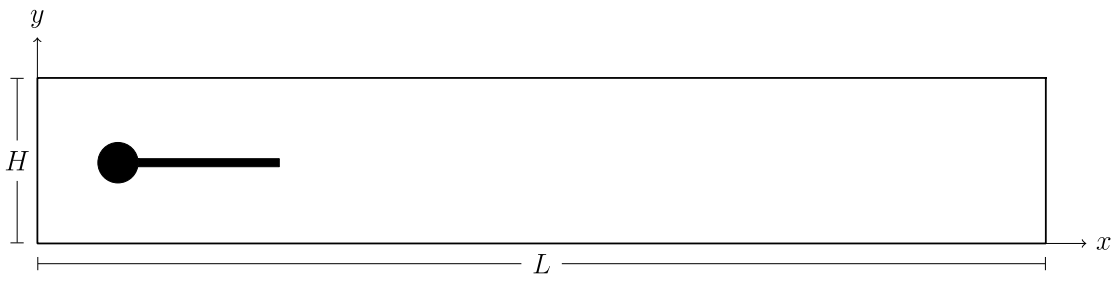

Fig. 4.20. Domain for the 2-D stationary cylinder with moving tail.

The domain has the following dimensions: The length of the channel, $\boldsymbol{L}$, is 2.5m and the height, $\boldsymbol{H}$, is 0.41m. The cylinder has a radius, $\boldsymbol{r}$, of 0.05m and its center is positioned at (0.2, 0.2)m measured from the bottom left corner of the domain. The bar has a length, $\boldsymbol{l}$, of 0.35m and height, $\boldsymbol{h}$, of 0.02m with the bottom right corner placed at (0.6, 0.19) m and it is rigidly attached to the cylinder. The boundary conditions are as follows:

- Inlet: $\boldsymbol{u(0,y) = 1.5\bar{U}\frac{y(H-y)}{\left(\frac{H}{2}\right)^2}}$
- Outlet: Pressure, $\boldsymbol{P = 0}$
- Wall: No-slip, including the fluid-structure interfaces between the fluid and the stationary cylinder and tail

where $\boldsymbol{\bar{U}}$ is the average velocity across the inlet.

The cylinder is held fixed and no structural computations are performed for the cylinder. As the cylinder begins to shed vortices, the tail will begin to experience a pressure differential that will result in deformation of the tail. This deformation is calculated using the structural mechanics equations in a similar manner to the 3-D cylinder in cross-flow.

Simulation and Results

The simulation of the cylinder with moving tail includes four cases, three of which were performed and presented by Turek and Hron (FSI1, FSI2, and FSI3). The first three simulations have the following fluid and structural properties based upon the cases presented in Turek and Hron's paper and repeated in Table 4.3 below.

Table 4.3. Properties of the fluid and structure used for the FSI test cases

Parameter	FSI1	FSI2	FSI3	Steel
$\boldsymbol{\rho^s}$, density of solid [10^3 kg/m^3]	1.00	10.00	1.00	7.80
$\boldsymbol{\nu^s}$, Poisson's Ratio of solid	0.40	0.40	0.40	0.29
$\boldsymbol{\mu^s}$, shear modulus of solid [10^6 kg/(ms^2)]	0.50	0.50	2.00	81400.00
$\boldsymbol{\rho^f}$, density of fluid [10^3 kg/m^3]	1.00	1.00	1.00	1.00
$\boldsymbol{\nu^f}$, dynamic viscosity of fluid [10^{-3} m^2/s]	1.00	1.00	1.00	1.00
$\bar{\boldsymbol{U}}$, average inlet velocity [m/s]	0.20	1.00	2.00	2.00
$\boldsymbol{Re}$, Reynolds number	20.00	100.00	200.00	200.00

The Reynolds number of 20 is run to ensure that the code will not begin to artificially shed vortices for conditions below $\boldsymbol{Re \approx 35}$[43]. The final simulation, labeled 'Steel,' was performed to observe the characteristics of a material similar to that in the HIFR; this material was not used in the simulations of the paper.

Each run was performed using the implicit transient solver with a maximum time step of 5e^{-3}s for a total of 10s. The physics were modeled as fully coupled. Unlike all previous cylinder simulations in cross-flow, the initial condition for the transient solver was not the steady-state solution for the corresponding Reynolds number; instead the initial conditions were all set to zero. In order to overcome any instability, the inlet velocity was increased from zero using a smoothing function with the following parameters:

$$\boldsymbol{u}(t,0,y) = \begin{cases} \boldsymbol{u}(0,y)\frac{1-cos(\frac{\pi}{2}t)}{2} & \boldsymbol{if\ \ t < 2.0} \\ \boldsymbol{u}(0,y) & \boldsymbol{otherwise} \end{cases} \quad (4.16)$$

The use of the smoothing function also demonstrates the ability of the code to capture the transients that can happen during start-up of the HFIR.

Turek and Hron present four parameters for comparison of their data: x and y displacement at the end of the tail and the lift and drag around the entire cylinder and tail. As expected, FSI1 did not create any vortex shedding or subsequent tail oscillations. FSI2 and FSI3 produced very comparable results to Turek and Hron and the results for FSI2 are presented in Fig. 4.21. The data is presented well after the cylinder has gone into a limit cycle. The results for FSI3 and the Steel case show similar trends.

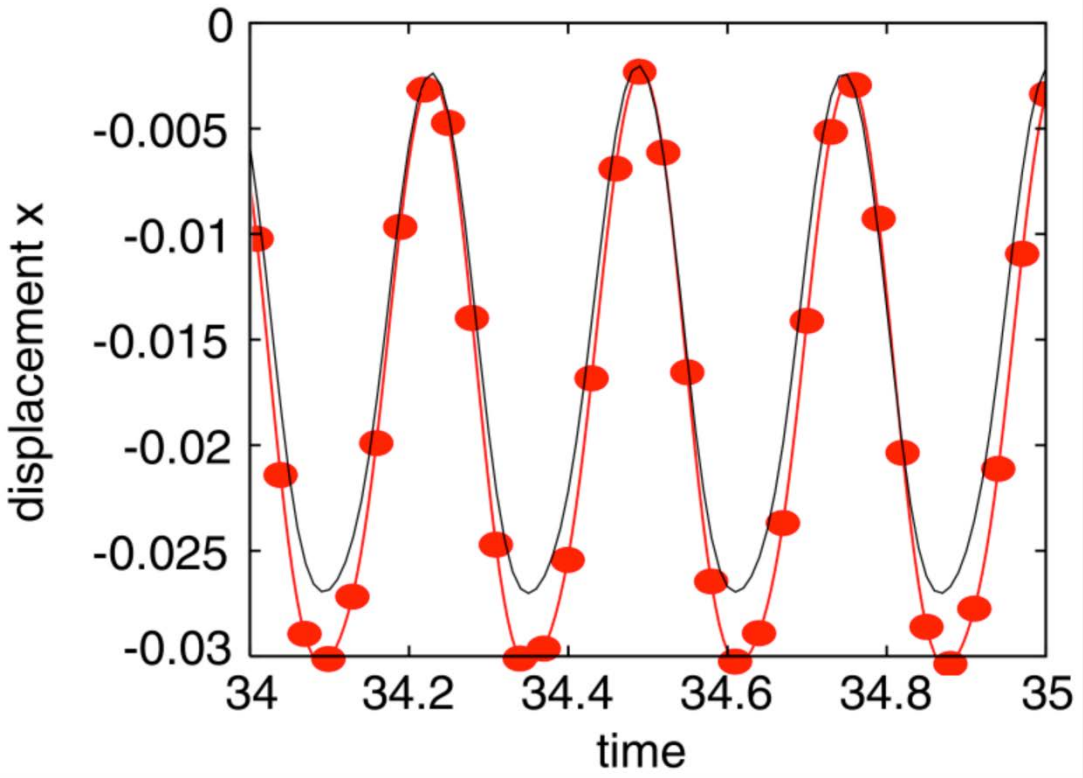

(a) X displacement (m)

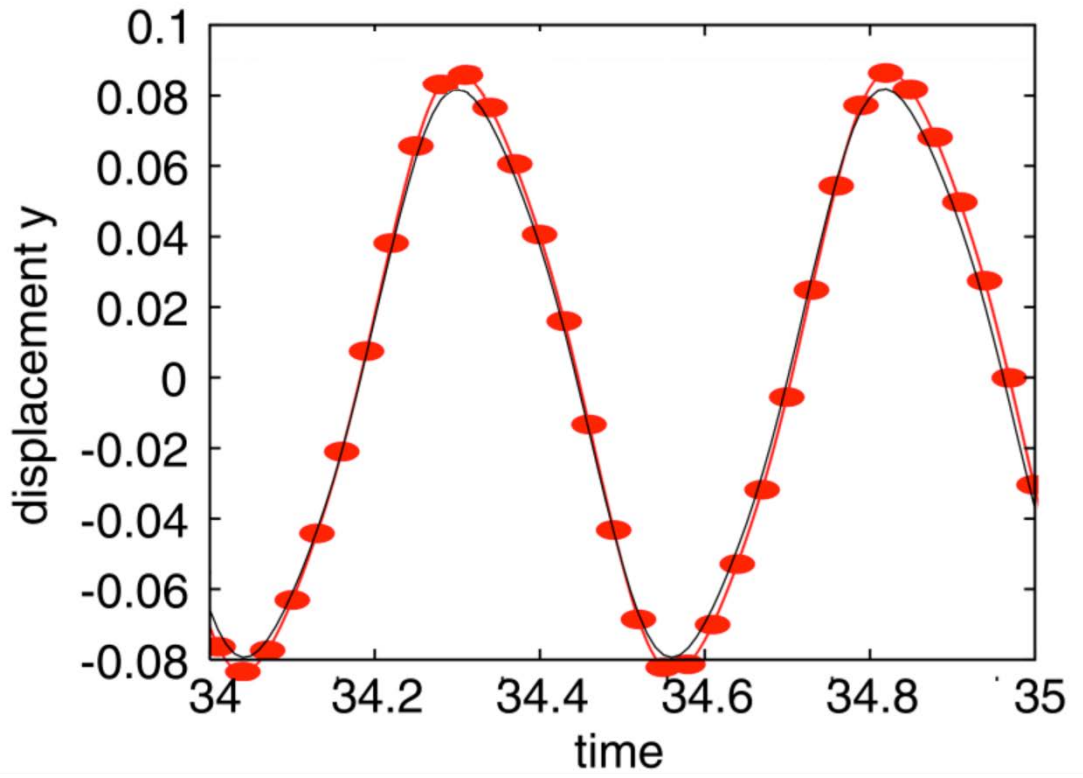

(b)Y displacement (m)

Fig.4.21. Results for the FSI2 test case. The results (red line with circles) are compared to the data provided by Turek and Hron (black line) [part 1 of 2].

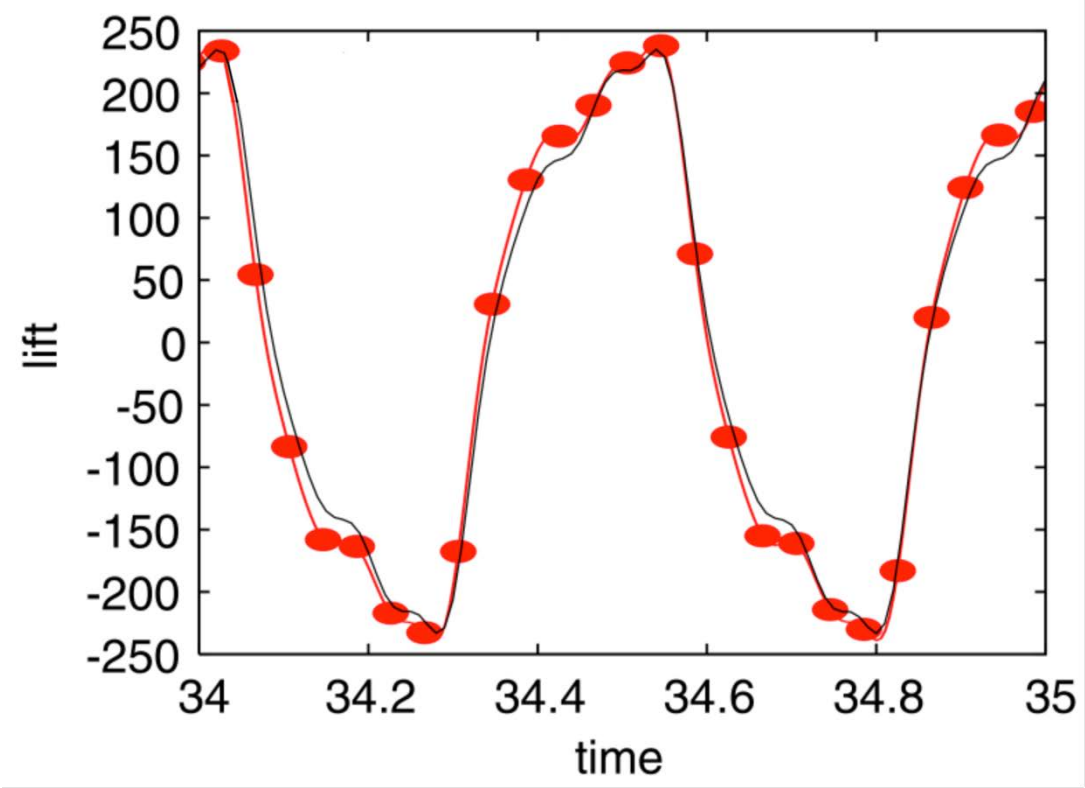

(c) Lift around cylinder and tail (N/m)

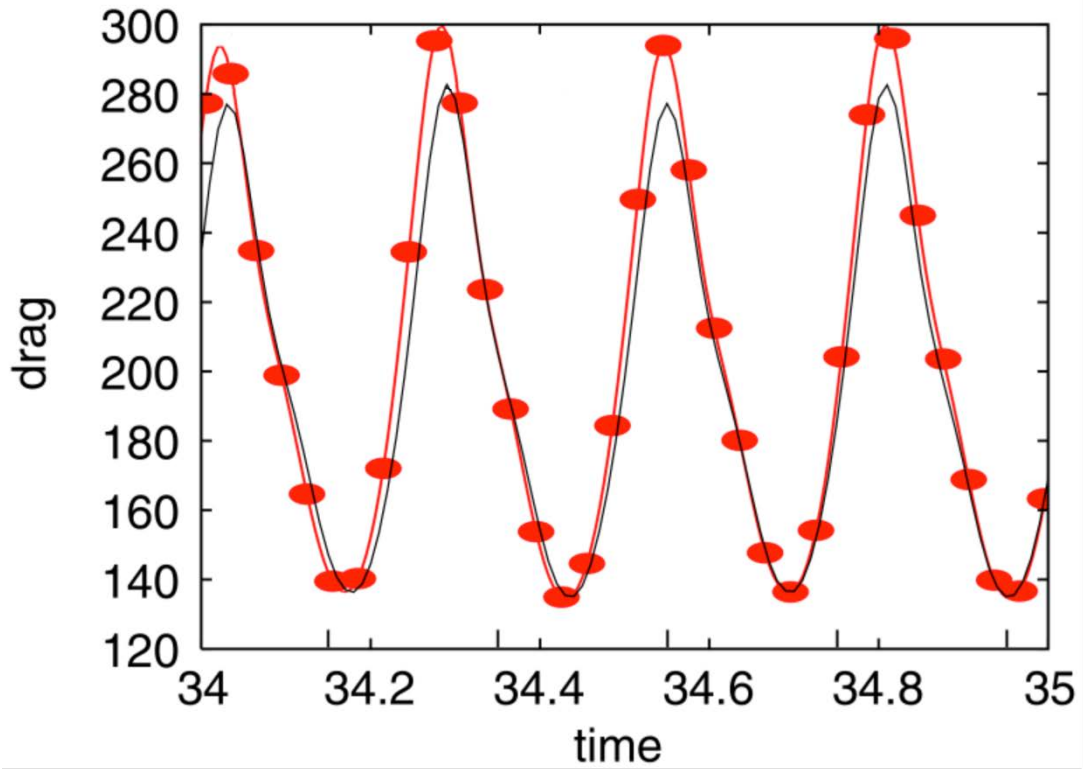

(d) Drag around cylinder and tail (N/m)

Fig.4.21. Results for the FSI2 test case. The results (red line with circles) are compared to the data provided by Turek and Hron (black line) [part 2 of 2].

Observation of Fig. 4.21 will reveal that the results presented exceed the computational time domain performed for the simulation. This discrepancy results from the fact that Turek and Hron presented their results for this time. Because the current simulation had reached a limit cycle, it was not necessary to run the simulation for the extended period.

Discussion

The cylinder with tail provides a context to explore large deflections produced by the fluid. In particular, the FSI2 case produces results in which the deflection at the tail is approximately 8 times larger than the thickness of the plate. This large deflection tests the code's ability to resolve the large stresses in the linear-structural model, to adapt the mesh as the structure deforms, and to capture the change in fluid characteristics, especially around the end of the tail. The final solution of FSI2 demonstrating these attributes is provided in Fig. 4.22. The simulation matched the test cases provided by Turek and Hron very well and also produces deflections for a much stiffer plate as seen in the Steel case. Using unsteady cylinder cases as benchmark simulations for the FSI capabilities of the code, it is now appropriate to explore experiments and cases related to the stacked plate configuration of the HFIR.

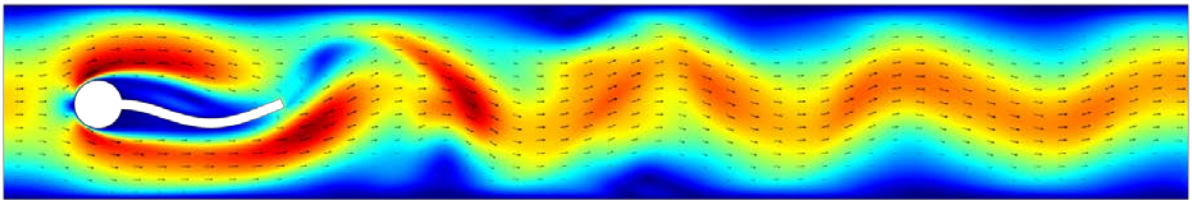

Fig. 4.22. 2-D solution for the FSI2 case at 10s.

4.3 FLOW OVER FLAT PLATE FUELS

Smissaert performed a series of flat plate experiments at the Pennsylvania State University in 1968 in order to better quantify the Miller Critical Velocity[57]. Smissaert constructed a hydraulic loop with a test section consisting of a series of parallel flat plates made out of PVC plastic; his experiment utilized pressure taps and strain gauges to measure the pressure drop and plate deflections, respectively. All of the plates were 0.0625 inches thick, 4.5 inches wide, and 45.0 inches long. The test section was designed to allow multiple plate configurations of 5, 9, and 15 plates. The 5 plate/6 channel case with a channel thickness of 0.250 inches was chosen for the validation case for the FSI code. The physical properties of the PVC plate are provided in Table 4.4. Smissaert chose to use plastic plates in order to observe larger deflections and to induce vibrations at a lower mass flow rate. There are discrepancies between the stated plate thickness in Smissaert's written description and what is provided in a table in the paper. The plate thickness in the table shows a value of 0.058 ± 0.002 in suggesting that this is the as built thickness of the plates. A thickness of 0.058 in will be used in the simulations.

Table 4.4. Properties of the PVC plate used by Smissaert in his experiment

Property	English values	Metric Values
Width	4.500 in	0.1143 m
Thickness	0.058 ± 0.002 in	1.473 ± 0.0513 mm
Length	45.000 in	1.143 m
Modulus of Elasticity	4.8×10^5 lb_f/in^2	3.310×10^9 Pa
Poisson's Ratio	0.25	0.25
Density	90.4 lb_m/ft^3	1448.1 kg/m^3

4.3.1 Single Plate Smissaert Simulations

Domain and Boundary Conditions

There are several configurations to consider for simulation for a series of parallel flat plates. The most simplified simulation, while maintaining a 3-dimensional setup, would be a single plate. As with all numerical simulations, the boundary conditions play a vital role in the convergence and accuracy of a solution. Because the plates are parallel and in series, a logical one-plate simulation would utilize periodic boundary conditions incorporating flow channels half the size of the full channel on both sides of the plate.

The half-channel with periodic boundary conditions makes the assumption that all of the plates deflect in the same direction seen in Fig. 4.23 for an infinite number of plates. This assumption is not physical because experiments have shown that the parallel plates deflect in opposite directions[56,57] as seen in Fig. 4.24. Due to this configuration being nonphysical, the simulations will not converge and the convergence rate stagnates. Two other boundary conditions have proven to work much better in reproducing accurate deflections for a single plate case: symmetry and wall.

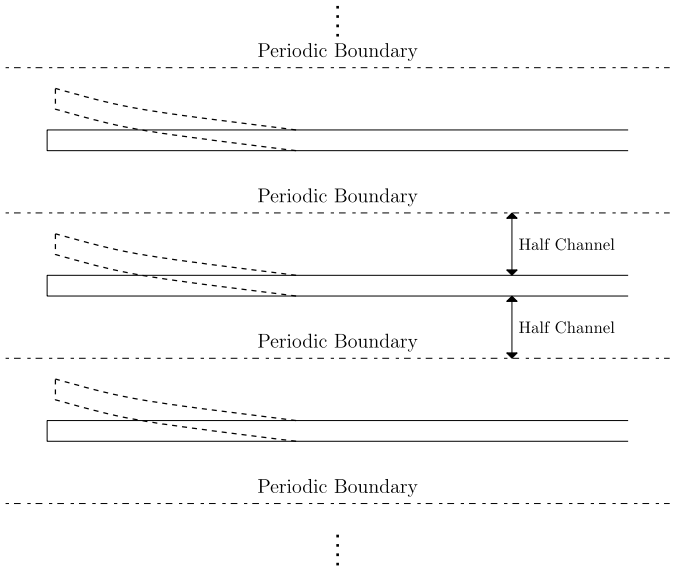

Fig. 4.23. Deflection of a series of plates using periodic boundary conditions. The periodic boundary condition, applied to a single plate, assumes that all of the fuel plates deflect in the same direction.

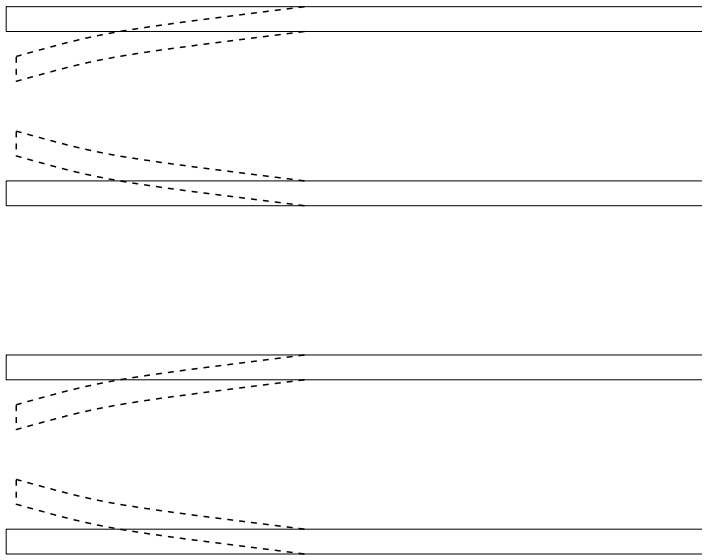

Fig. 4.24. Bending of a series of plates with deflections of adjacent plates going in the opposite direction, which is a more physical assumption.

The alternating small and large channels predicted by experiments due to the deflections can be replicated by utilizing a half channel setup similar to Fig. 4.23 except the boundaries are now symmetric. The symmetric boundary imposes no velocity penetration and vanishing shear stress and is described by the following equations:

$$\boldsymbol{u_f} \cdot \boldsymbol{n} = \boldsymbol{0} \quad (4.17)$$

$$\left(-\boldsymbol{p} + \boldsymbol{\mu}\left(\boldsymbol{\nabla u_f} + \left(\boldsymbol{\nabla u_f}\right)^{\boldsymbol{T}}\right)\right)\boldsymbol{n} = \boldsymbol{0} \quad (4.18)$$

where $\boldsymbol{n}$ is the normal vector to the boundary. Where the periodic boundary condition assumes the plates all deflect in the same direction, the symmetry boundary condition assumes that each plate deflects in the opposite direct of the adjacent plate in a similar fashion to Fig. 4.24.

The wall boundary conditions take a different approach to solving the series of parallel plates. For this configuration, a full channel is simulated on each side of the plate with wall boundary conditions at the outside of the channels demonstrated in Fig. 4.25. This simulation makes the assumption that the adjacent plates do not move and instead imposes a wall boundary condition along the entire length of the channel. This configuration has proven to be the most stable for the one-plate models because of the wall function (no-slip) boundary conditions.

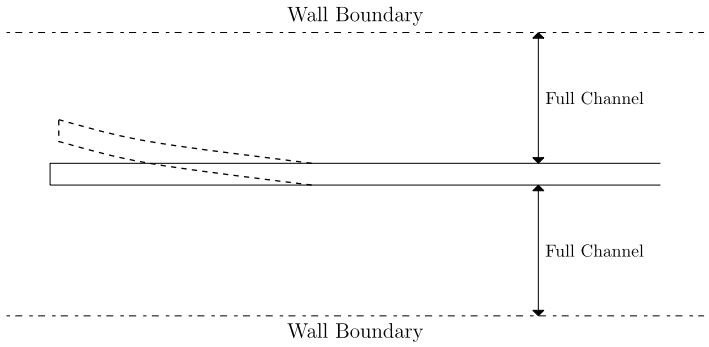

Fig. 4.25. Single plate setup with full channels and wall boundary conditions.

The special deviation from ideal geometries of the channels of parallel flat plates plays a major role in the amount of deflection observed for the plates. As Kane[65] showed in his theoretical work, the larger the deviations, the larger the leading edge deflections. The experiments performed by Stromquist and Sisman [54] showed that large deviations produced instabilities in the plates and the extreme cases resulted in plate buckling. The experiment by Kennedy, et al.[58], was designed with a single plate and two different sized flow channels 80 and 100 mils to ensure a predictable deflection utilizing the knowledge that the deviations create a pressure differential that produces a deflection. The most stringent manufacturing techniques can never guarantee a perfect geometry thus providing a context to include some deviations when simulating flat plates.

Numerical simulations, particularly ones with uniform meshes on each side of a plate, will fail to produce deflections if the channel sizes are the same. In fact, a fully coupled solution begins to show instabilities and issues with convergence if the channels are the same size. In order to circumvent this problem, a small deviation from the ideal geometry is introduced which provides an initial pressure difference between the plates to induce the deflection. These deviations do not have to be large in order to produce deflections. For the Smissaert case, full channels with no slip boundary conditions were used for the simulations presented in the following section.

Simulation and Results

The large aspect ratio of the Smissaert experimental setup (180 length to channel thickness ratio) presents a difficult computational problem when it comes to balancing computational time, size and stability. The long, thin flow channel requires a large number of elements in order to properly capture the flow field. For the flow field, a free tetrahedral mesh is utilized with a mapped quadrilateral mesh along the no-slip boundaries of the side wall and plate. The final mesh consists of approximately 750,000 elements.

As seen in Section 4.2.3, FSI simulations with strong fluid and structure coupling must be run using a fully coupled solver. In order to obtain a reasonable initial condition, one-way coupling is used to establish the initial condition for the fully coupled solver. Without this step, the solution process is not stable and no solution can be obtained. A segregated approach has been tried using COMSOL as well as with other codes to very poor success[79]. In order to obtain an FSI solution for high-aspect ratio fuel plates, the following solution process should be followed:

Use the one-way coupled FSI solver to obtain a fluid solution and solid mechanics solution with a coarse mesh.

Use the one-way coupled solution as an initial condition for the fully coupled solver using the same mesh that was used for the one-way coupling.

Refine the mesh using the previous solution as an initial condition for the fully coupled solver until the solution is mesh converged.

The above description was followed to obtain a solution for the Smissaert case of 1.23 M_c which corresponds to an inlet velocity of 3.087 m/s. The deflection obtained from COMSOL is compared to the Smissaert case in Fig. 4.26.

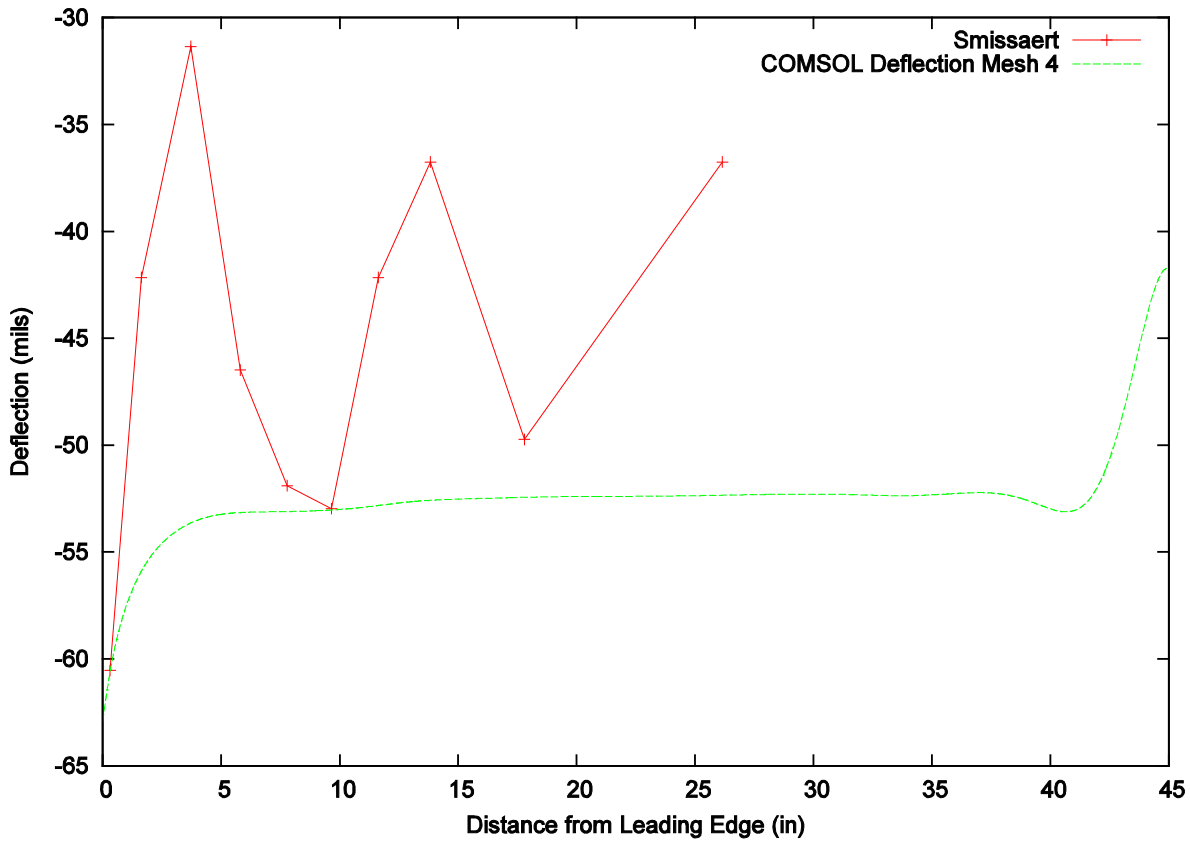

Fig. 4.26. Single plate deflection of the Smissaert case for an inlet velocity of 3.087 m/s (1.23 M_c).

The leading edge deflection of the COMSOL simulation somewhat matches the experimental data. Although the steady-state solution is unable to capture the deflection, the unsteady code is able to capture such a large leading edge deflection. However, additional runs using finer mesh resolutions are needed to ensure the validity of these predictions. In any case, further investigation of this rest case can shed light into future flow reduction and blockage calculations.

4.4 FLOW OVER CURVED PLATE FUELS

The Advanced Neutron Source Reactor (ANSR) was a proposed high-performance, heavy-water research reactor at ORNL. The reactor was to consist of involute fuel plates in a similar shape to the HFIR with cooling flow rates at approximately 25 m/s. The reactor design was to meet or exceed the neutron flux characteristics of the HFIR making it the highest neutron flux reactor in the world. Due to the extremely

high flow rates, extensive analysis was done to ensure the stability and integrity of the fuel plate structure in the reactor[101,63,102,103,59].

The ANSR was designed to have two fuel cores similar to the HFIR except the cores in the ANSR were to be stacked one after the other instead of the concentric configuration of the HFIR. The conceptual core design is provided in 4.27.

The flow through the core is from the bottom to top of Fig. 4.27 and the nomenclature of upper element and lower element will be used to describe the larger and smaller cores, respectively. The upper element consists of 432 plates with an inner diameter of 175 mm and an outer diameter of 235 mm; the lower element consists of 252 plates with an inner diameter of 102 mm and an outer diameter of 168 mm. Each fuel element is 527 mm long with 507 mm being fueled.

During the design process for the ANSR, many experiments were performed in order to establish a safety basis for the reactor operations and to better quantify the design requirements. Flow tests measuring thermal characteristics of the fuel plates were performed that were designed to measure the heat transfer capabilities of the design[104-107]. Another set of experiments were performed to test the deflection caused by the pressure differentials from the coolant flow[101,63,102,59,103, 108,109,110].

The emphasis of this chapter will be on the experiments performed to establish the deflection characteristics of the plates. The experimental setup consisted of five “fuel” plates made out of PVC plastic. The experiment was run on plates with the involute shape of the upper element with six full flow channels around the plates. A dimensional analysis was performed in order to predict the leading edge deflection for a series of aluminum plates. The analysis, which is described by Swinson, et al.[63], assumes that the Poisson's ratio of each material is approximately the same and thus the measured deflection of the PVC plate (referred to as the model) equals the deflection of the aluminum plate (referred to as the prototype), leading to the following equations:

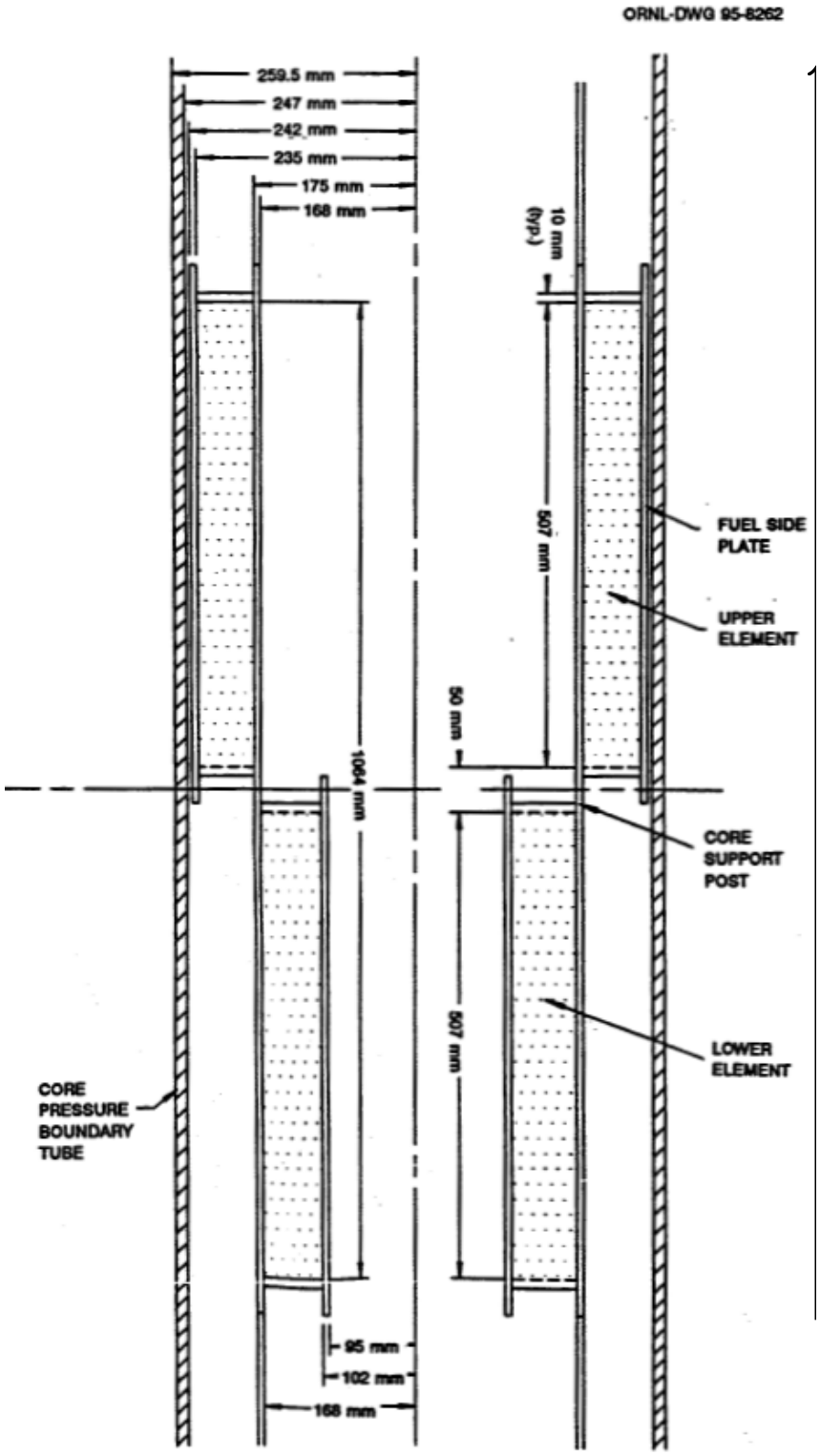

Fig. 4.27. Proposed configuration of the ANSR core[109].

$$\boldsymbol{\delta_p(\text{prototype deflection}) = \delta_m(\text{model deflection})} \quad (4.19)$$

$$\boldsymbol{V_p = V_m\sqrt{E_p/E_m}} \quad (4.20)$$

Using Equation 4.20, Table 4.5 presents the inlet velocities for both the prototype and models along with the $\boldsymbol{Re}$ of each inlet velocity. The Reynolds number in Table 4.5 is calculated using the assumption that the hydraulic diameter, $\boldsymbol{d_h}$, can be set to the channel thickness for a channel whose width is much greater than its thickness. For the upper element, the channel width, also the arclength of the involute curve, is approximately 71.2 mm long while the channel thickness is 1.27 mm; thus, $\boldsymbol{Re}$ is determined from the channel thickness of 1.27 mm.

Table 4.5. Inlet velocities for the ANS prototype and model simulations and experiments.

$\boldsymbol{V_m}$, m/s	$\boldsymbol{Re_m}$	$\boldsymbol{V_p}$, m/s	$\boldsymbol{Re_p}$
3.58	4537	17.35	21991
5.18	6561	25.09	31801
6.65	8431	32.34	40863
8.32	10543	40.32	51104
10.03	12717	48.63	61637

The deflection of the plates was measured using strain gauges located at 5 evenly spaced locations along the length of the plates. The deflection was measured at the leading and trailing edges and also at the 1/4, 1/2, and 3/4 locations along the plate. An inlet section of 527 mm was used. The outlet section length was not specified. Table 4.6 provides the physical properties for both the PVC and aluminum plates used for the analysis. The density of the PVC plate was not specified such that an average of the density range found in Titow[111] was used for the simulations.

In order to model the plates as closely to the specified design criteria, SolidWorks, a CAD software, was used to create the involute geometry used for the ANSR plates. The equations and background of the involute shape are discussed in Section 6.3. The geometry was then imported into COMSOL to begin the analysis.

Table 4.6. Properties used for the ANSR experiments.

Material	$\boldsymbol{E}$, GPa	$\boldsymbol{\rho}$, kg/m^3	$\boldsymbol{\nu}$
PVC	2.937	1350	0.35
6061 Aluminum	69	2700	0.33

4.4.1 Single Plate ANSR Analysis

As was done in the previous section for the flat plate analysis, a single plate with multiple channels was simulated using COMSOL. The simulation included analysis of both the plastic plate used in the experiment and the aluminum plate used in the dimensional analysis. The steady-state solutions were obtained by using the one-way coupled solver to get an initial condition and then using the fully coupled solver to obtain a final solution.

Domain and Boundary Conditions

The computational domain consisted of the involute shaped plate, the inlet and outlet plenums and full flow channels (50 mils) on each side of the plate. The inlet section was specified as 527 mm while the outlet was not specified. The outlet plenum was chosen to be 100mm long. As seen with the flat plate case, perfectly symmetrical flow channels do not produce stable deflections such that the plate was offset

for its entire length by 5 mils. The offset of 5 mils was chosen as that is the largest deviation allowed in the HFIR SAR[7]. The flow domain is provided in Fig. 4.28.

The top and bottom of the flow domain are held as wall boundary conditions following the solution strategy for the flat plates. The inlet is specified as one of the velocities in Table 4.5 and the outlet is set to 0 pressure. The plates, depending on the inlet velocity, are either specified as aluminum or PVC and have the properties described in Table 4.6. The final mesh for this case consists of a combination of free mesh and boundary layer meshing. The mesh consists of 4 boundary layer elements and 24 cuts in the span-wise direction for a total of 270,264 mesh elements. The mesh at the leading edge of the plate is provided in Fig. 4.29.

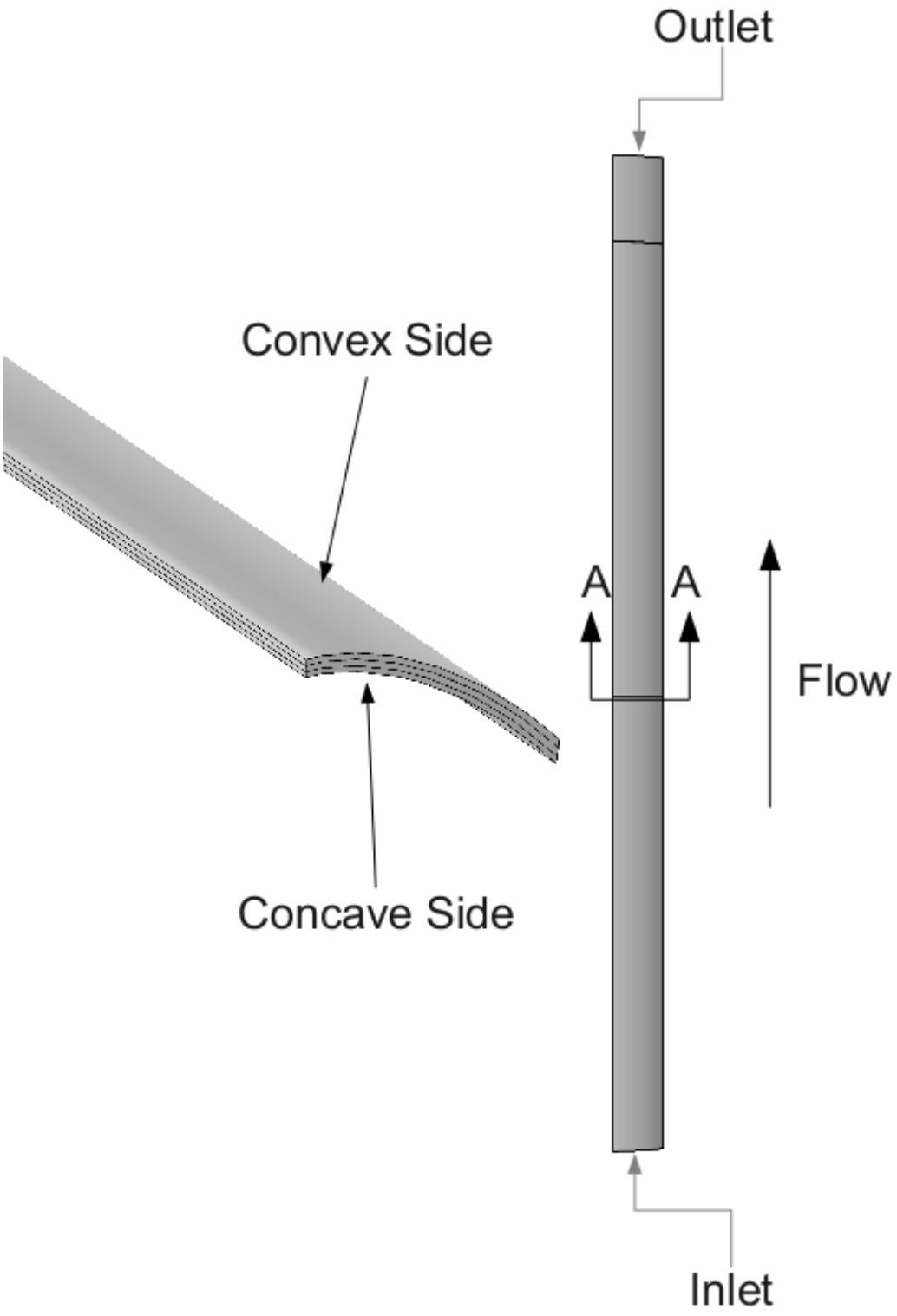

Fig. 4.28. One plate ANSR simulation geometry.

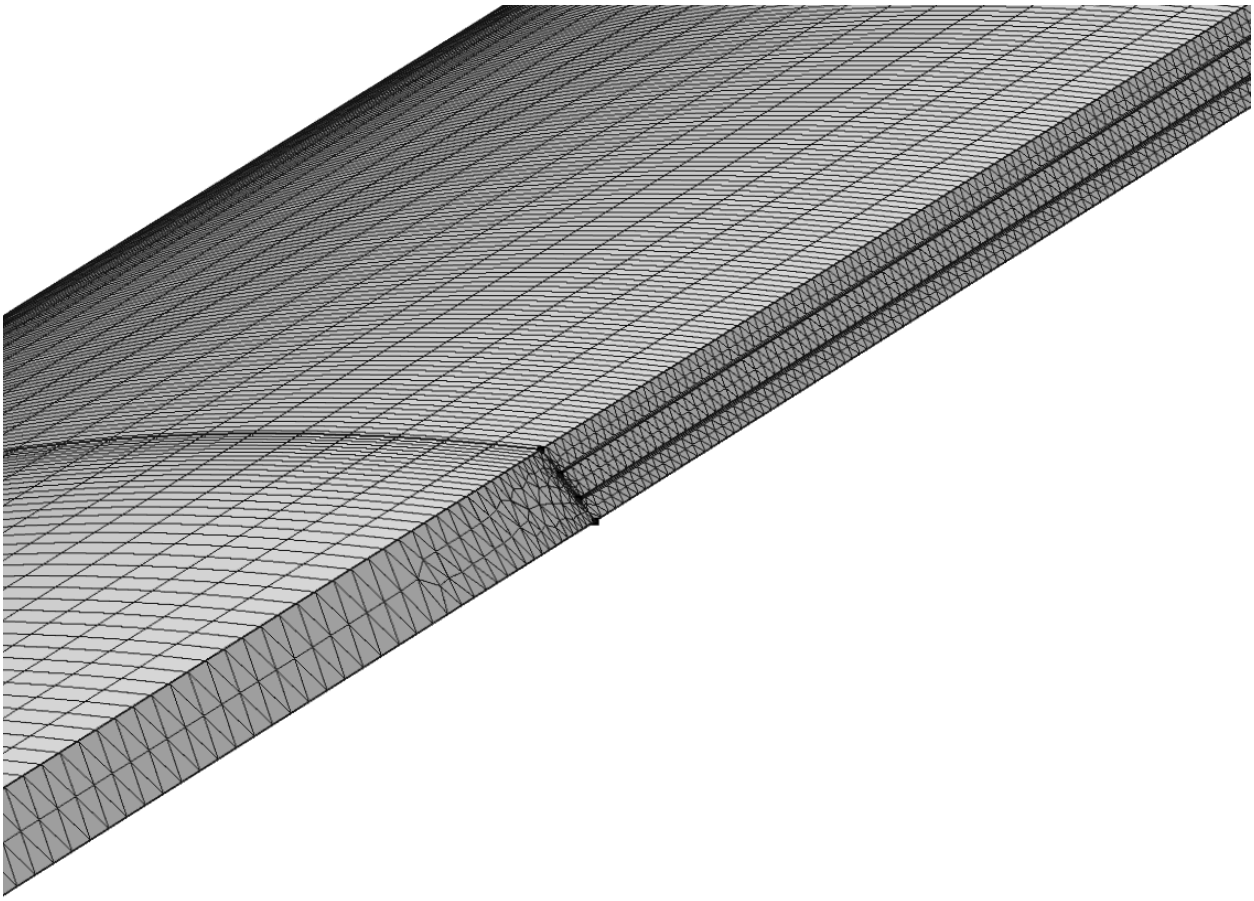

Fig.4.29. Mesh at the leading edge of the one-plate ANSR case.

Simulation and Results

Again, starting with the one-way coupled solver to obtain an initial flow and deflection solution and feeding that into the fully coupled solver, has proven to be the most stable for these strongly coupled FSI simulations. For this simulation, a coarse mesh solution was obtained and then fed into finer mesh solutions in order to maintain stability and convergence.

The HFIR SAR predicts, using an Eigen frequency analysis, that the first mode of the involute plates will have an 'S' shape at the leading edge[7]. This has also been confirming using the Eigen Frequency analysis techniques in COMSOL. The fully coupled FSI solution also exhibits this 'S' shaped leading edge deflection and the deflection of the plate is provided in Fig. 4.30.

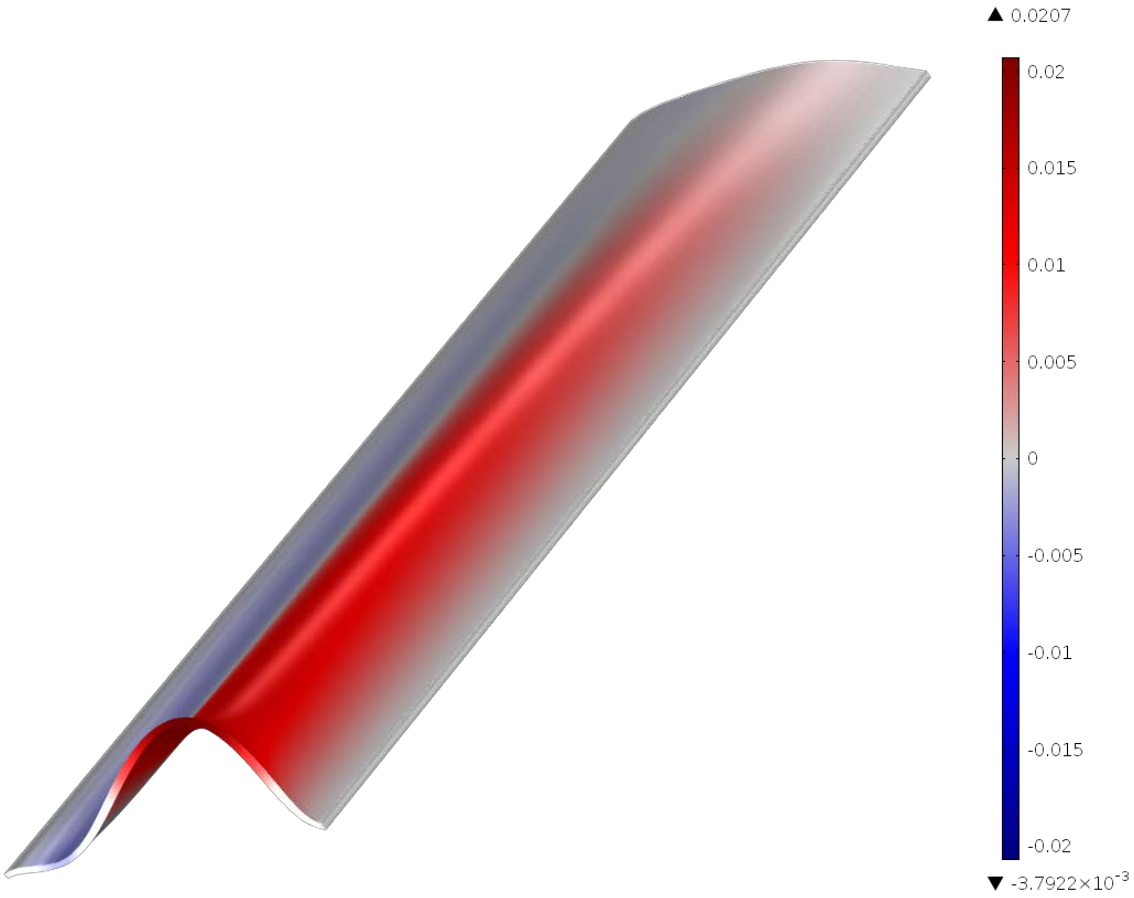

Fig. 4.30. Exaggerated deflection for the ANSR single aluminum plate at an inlet speed of 17.35 m/s. The deflection is measured in mm and the deformation is scaled to accurately show the mode shape of the deflection. The red depicts a positive deflection and the blue depicts a negative deflection while the grey is zero deflection.

Simulations were successfully completed for both the PVC and aluminum plate. The simulation was unable to be completed for an inlet velocity of 48.63 m/s due to stability issues. The COMSOL solutions are compared to the aluminum ANSR experimental deflections in Fig 4.31. The COMSOL simulation matches the experimental deflections quite well except for the inlet velocity of 40.32 m/s where the deflection at 400mm is quite smaller than the experiment.

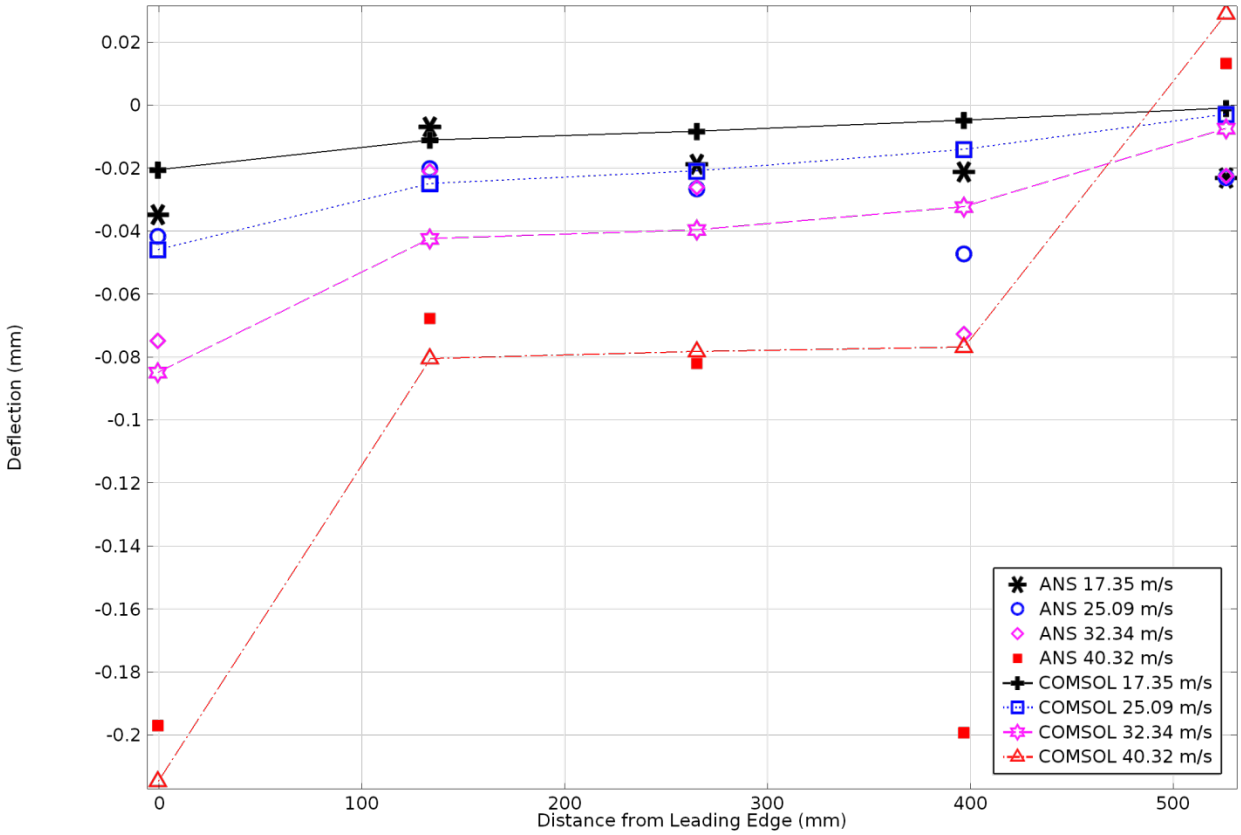

Fig. 4.31. ANSR experimental deflections compared to the COMSOL results for the aluminum plate.

This page intentionally blank.

5.0 3D MODEL SIMPLIFICATIONS AND COMPARISONS

5.1 OVERVIEW

This chapter presents three models. The first of these is a fully explicit, fully three-dimensional one-plate one-channel LEU IFE model, referred to herein as the 3D model. The intent of the 3D model is to model the thermal-hydraulic characteristics of the HFIR core with as much detail and accuracy as is reasonably possible given available computational resources. The 3D model will then be used as a basis for comparison for two simplified models, providing a metric for the degree of inaccuracy and loss of fidelity associated with the respective simplifications in each.

The first of the simplified models is the *t*-*z*[1] plane coolant simplification known as the coupled model. The coupled model seeks to simplify the 3D model by reducing the coolant channel to a 2D slice oriented every perpendicular to the fuel plate surface. The fuel plate and fuel meat are unaltered from the 3D model. Pairing of the two dimensionally inconsistent domains, solid and coolant, is achieved through interdimensional model coupling—a three step process in which solution variables are collected, formatted, and applied across dimensionally inconsistent boundaries.

The second of the simplified models is the *s*-*z* plane coolant simplification known as the bulk model. Where the coupled model simplifies the coolant domain by homogenizing the *s*-direction, the bulk model seeks to achieve additional computational savings by reducing the widthwise fidelity of a fully explicit coolant channel to a single cell width. Bulk coolant properties are then calculated as a straight average of bounding wall values. In order to do this the bulk model neglects no-slip wall effects, boundary layer formation, and turbulent flow. This has the effect of greatly reducing the degrees of freedom associated with the coolant domain by minimizing both the number of mesh points as well as the number of solution variables associated with each one.

Lastly, results will be presented only for the coupled model with comparable outputs for the 3D model serving as comparison. The bulk model is not yet matured enough to have produced results of sufficient quality for analysis. Results will also be used to provide justification for simplifications in the coupled model. The sum of the coupled model's results will be used to weigh, empirically, the model's benefits versus any potential detractions resultant of its simplifications.

5.2 3D MODEL FOR COMPARISON

5.2.1 Construction

All geometry pieces were created in SolidWorks and imported into COMSOL for assembly. The assembly process begins with the coolant geometries which are imported first. For ease of meshing the coolant domain is split into six axial components. The coolant channel geometries extend in the *t*-direction to midstream lines of periodicity between adjacent fuel plates. The six coolant components and their axial lengths are listed in Table 5.1.

---

[1] This chapter utilizes an involute coordinate system (*s*, *t*, *z*) for its primary frame of reference. The coordinate *s* denotes arc-length along an involute curve with its datum (*s* = 0) on the surface of the base circle (inner side plate). It is everywhere-parallel to the involute curve. The coordinate *t* is everywhere perpendicular to the involute curve in a horizontal (non-axial) plane. The coordinate *z* is unaltered from the traditional Cartesian coordinate system (*x*, *y*, *z*). It denotes axial position with its datum (*z* = 0) located at the leading edge of the fuel meat (not the fuel plate which is located at *z* = -5.08 cm). The direction of coolant flow is assumed positive with *z* increasing down the length of the channel. For additional information on the involute coordinate system, see Section 6.3.

Table 5.1. Coolant components

Component	Axial Region	Length (cm)
1	Entrance	2.032
2	Leading Edge Cap	0.178
3	Fuel Plate	60.782
4	Trailing Edge Cap	0.178
5	Exit 1	1.194
6	Exit 2	2.311

The exit region is divided into components due to a difference in lengths of the inner and outer side plates which will be added to the model assemblage last. The assembled coolant components are shown in Fig. 5.1.

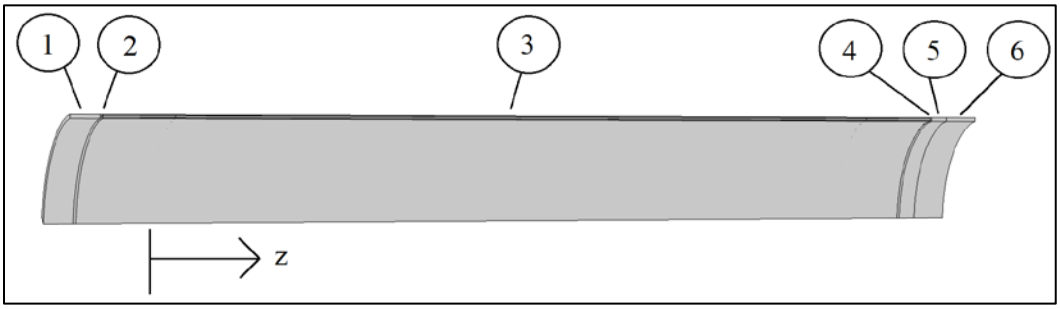

Fig. 5.1. Assembled coolant components. Flow direction is in the +*z*-direction.

Next, the fuel plate components are added to the assemblage. Again, for ease of meshing the fuel plate domain is subdivided into four components which are listed in Table 5.2.

Table 5.2. Fuel plate components

Component	Axial Region	Length (cm)
1	Leading Edge	0.089
2	Unfueled Top	4.991
3	Fueled Section	50.800
4	Unfueled Bottom	5.080

The leading edge is separated from the unfueled top region because it is rounded and is easier to mesh separately. The fuel plate components are imported into the COMSOL assemblage and a Boolean subtraction performed in order to remove the overlapping coolant domain. The fuel meat is then imported and subtracted from the fuel plate using the same process. A generalization of the side profile that this produces is shown in Fig. 5.2.

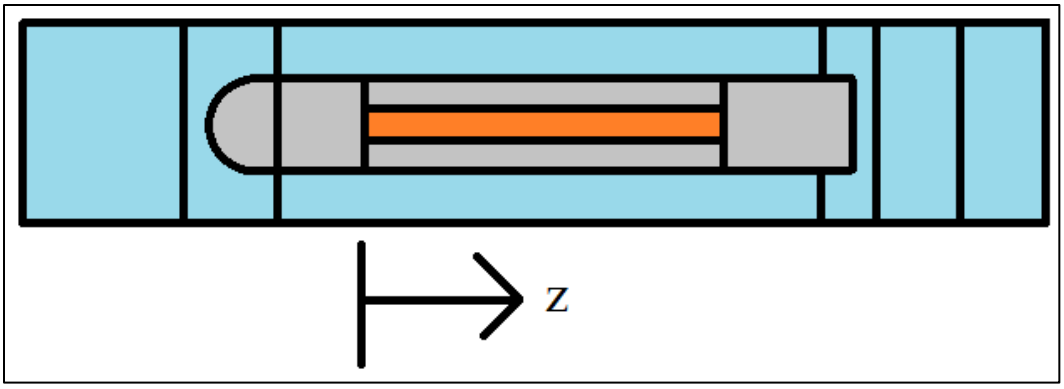

Fig. 5.2. COMSOL assemblage side profile diagram. Note that the diagram is not to scale. The coolant channel is shown in blue, the fuel plate in grey, and the fuel meat in orange. While the coolant and fuel plate extend to both side plates, the fuel meat does not.

The side plates are imported last. The inner side plate has an axial length of 64.364 cm and the outer side plate a length of 66.675 cm. They are aligned equally with their leading edges 2.121 cm upstream of the fuel plate's leading edge. This is even with the entrance boundary on the top of the leading coolant component. This placement leads both side plates to extend downstream of the fuel plate's trailing edge. Their disparity in length dictates that the outer side plate extends 2.311 cm farther downstream than the inner side plate. The orientation is shown in Fig. 5.3.

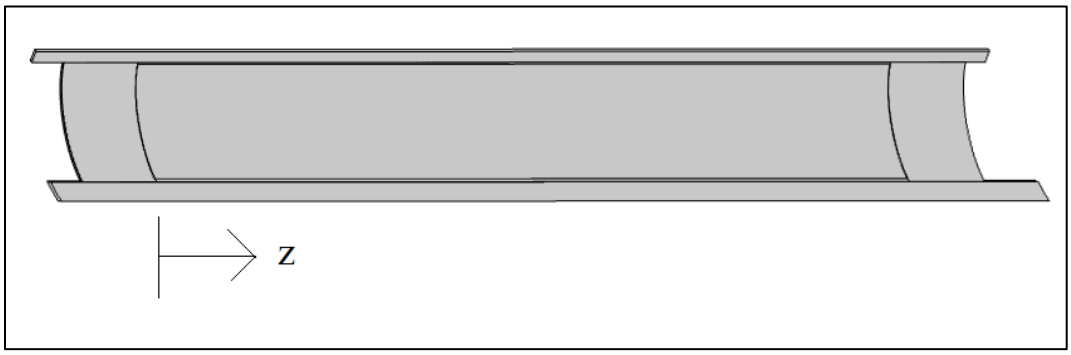

Fig. 5.3. Solid geometry assemblage. Flow direction is in the +*z*-direction. The inner side plate is shown on top in this figure. The geometry in between is the fuel plate. Coolant geometry components are not pictured.

This length disparity is an intentional design feature. After a core's operation cycle has ended it is removed from the reactor and placed in the spent fuel pool. Ideally, it is placed on top of a rack allowing ample water to enter into the core from below where natural convection due to heat generated by the leftover fuel expels the water upwards. The side plates are designed such that if a spent core should somehow fall off of its rack and come to rest upright on the floor of the pool, water is able to access the bottom of the core via the vacant flux trap in the center and then be driven upward through the fuel elements via convection. This opening must also be taken into account in the COMSOL model, thus the necessity for coolant components 5 and 6 to exist separately.

With the inclusion of the side plates, the model geometry is completely assembled in COMSOL. The last step is in stitching the geometry components together. COMSOL is capable of doing this in two ways via connections that are known as unions and assemblies. A union is the ideal inter-component connection as it directly links adjacent elements to one another. In a union, any shared face between connected components is considered a single entity. The mesh in one component must match the mesh in the other

component at the interface between the two. In an assembly, a shared face between components is considered as two elements, one for each component. For instance, two blocks stacked on top of one another would share a single surface—the bottom of the upper block and the top of the lower block. In an assembly, the top of the lower block and the bottom of the upper block are considered independent of one another. Meshes do not have to match across this interface and physics, such as heat flow, do not inherently maintain continuity across it. This can be remedied, however, by placing a boundary pairing on both sides of a shared surface so that continuity is enforced between them.

The assembly interface, while not ideal, can be necessary for complex geometries in which meshing is difficult. Such is the case with some of the components in the fully three-dimensional model with its extremely high-aspect ratio and narrow channels. The effect on results is miniscule. The requirement that the model analyze each assembly interface every iterate, interpolating values and fluxes across its surface from one side to the other and back again, does, however, slightly increase the time per iterate.

Components which can be connected via union are done so. All of the coolant components, for example, can be connected to one another via union as can the fuel meat to the fueled section of the plate. The fueled section, however, must be connected to the unfueled top and bottom of the plate via assembly. This is due to a disparity in meshes on their shared faces.

Given the need for this assembly, the fuel plate cannot be unionized with the coolant channel as one entity. The simplest way to divide them is to create an assembly between the external surface of the fuel plate and the adjacent wall surfaces of the coolant channel. The last required assemblies exist between the side plates and the adjacent coolant channel/fuel plate surfaces.

5.2.2 Inputs

The primary model inputs are composed largely of reactor design criteria. Initial conditions are specified for pressure, temperature, and velocity according to the inlet and outlet conditions in Table 5[14].

Table. 5.3. Initial Inlet and outlet conditions

Variable	Inlet	Outlet
p (MPa)	3.33	2.59
T (K)	322	342
u (m/s)	7.77	7.77

The initial conditions for pressure and temperature are specified as the linear interpolation between their respective inlet and outlet values. The initial condition for velocity was specified using the constant flow rate relation which states that flow through an area of A/2 will have a velocity twice that of the same flow through an area of A. Given the uniformity in thickness between the fuel plates and coolant channels, the flow area through the fuel section of the reactor core is half the area of the unimpeded section immediately upstream. Initial conditions for pressure, temperature, and coolant velocity as functions of axial position are given in Figs. 5.4, 5.5, and 5.6, respectively. In all three figures dotted red lines indicate extrapolated values. The initial temperature condition was applied to all domains, both solid and liquid. The initial pressure and velocity conditions were applied only to the coolant domain.

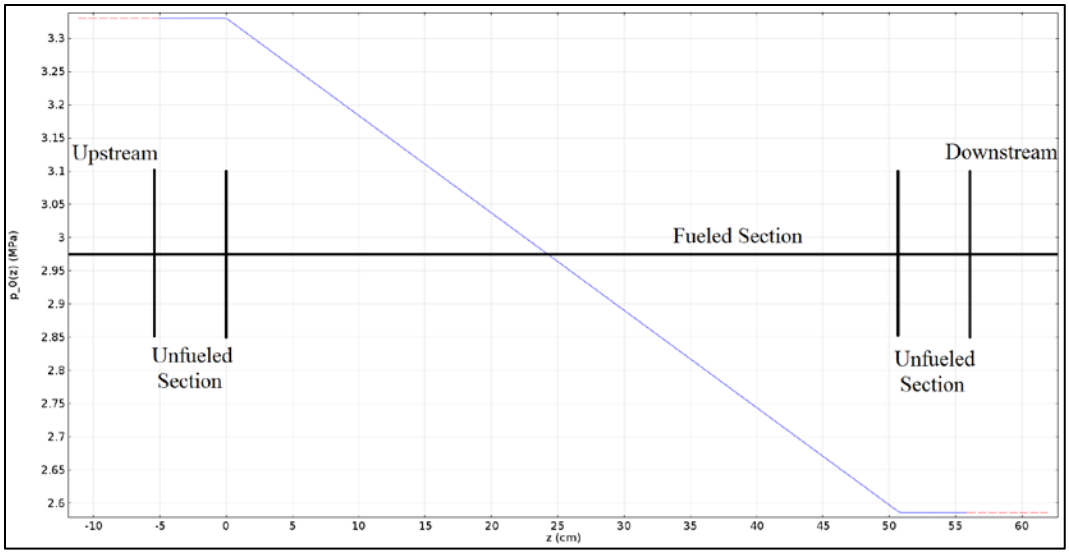

Fig.5.4. Initial pressure profile.

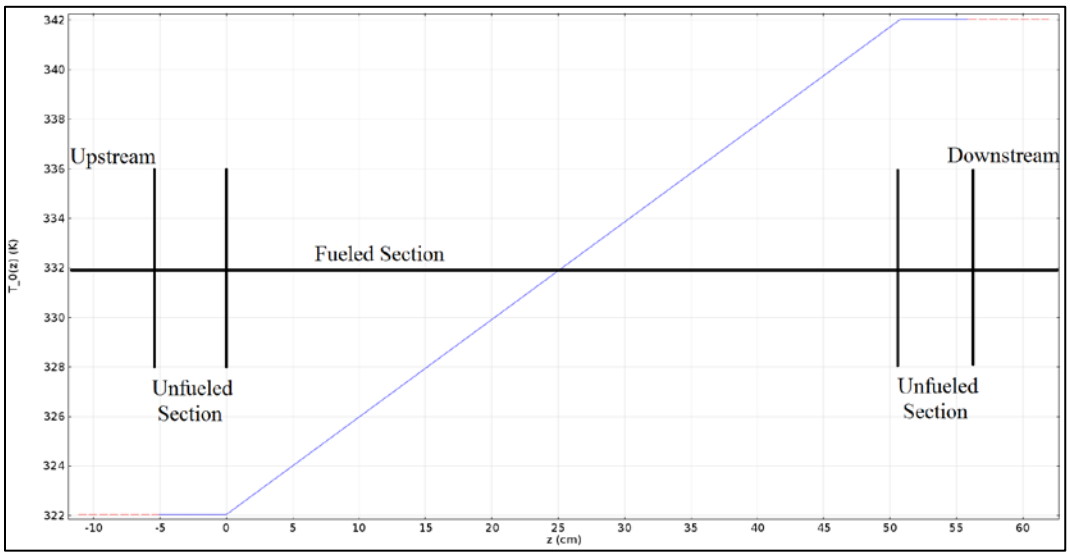

Fig. 5.5. Initial temperature profile.

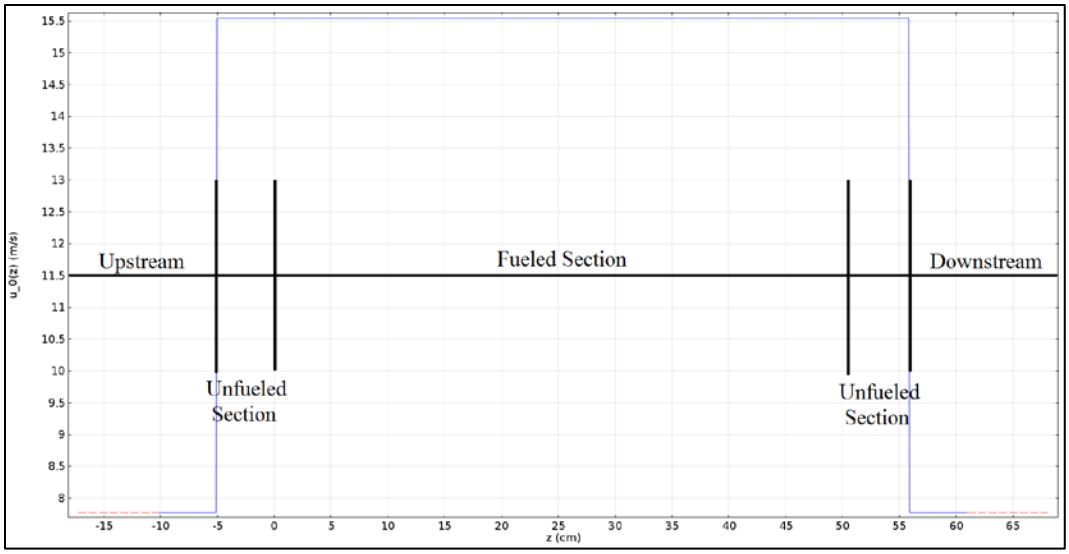

Fig. 5.6. Initial velocity profile.

The second model input is the nuclear power generation profile which is divided into two components: a power distribution and fuel thickness factor. The power distribution is a two-dimensional map of LEU beginning-of-cycle (BOC) power density (W/m^3) as a function of radial and axial position, (r,z). The power distribution is generated by the Monte Carlo N-Particle (MCNP) transport code[112]. MCNP is a neutronics code which models the release of nuclear energy throughout the core. It outputs neutron fluxes (neutrons/cm^2-s) as a function of (r,z). These can then be converted into fission rate densities (fissions/cm^3-s) by multiplying by the macroscopic fission cross-section (atoms/cm). Finally, these can be converted into power densities (W/cm^3) by multiplying by the amount of energy released per fission reaction (J/fission), which is a constant.

MCNP performs this simulation by homogenizing the reactor core internals (fuel meat, aluminum clad, coolant water, etc.) into a single entity and then dividing the core into axisymmetric cells along an r-z grid as shown in Fig. 5.7. As a result of this homogenized grid structure, power density profiles are output in the form of power-per-cell-volume, P'''_{cell}. The profile is shown in Fig. 5.8.

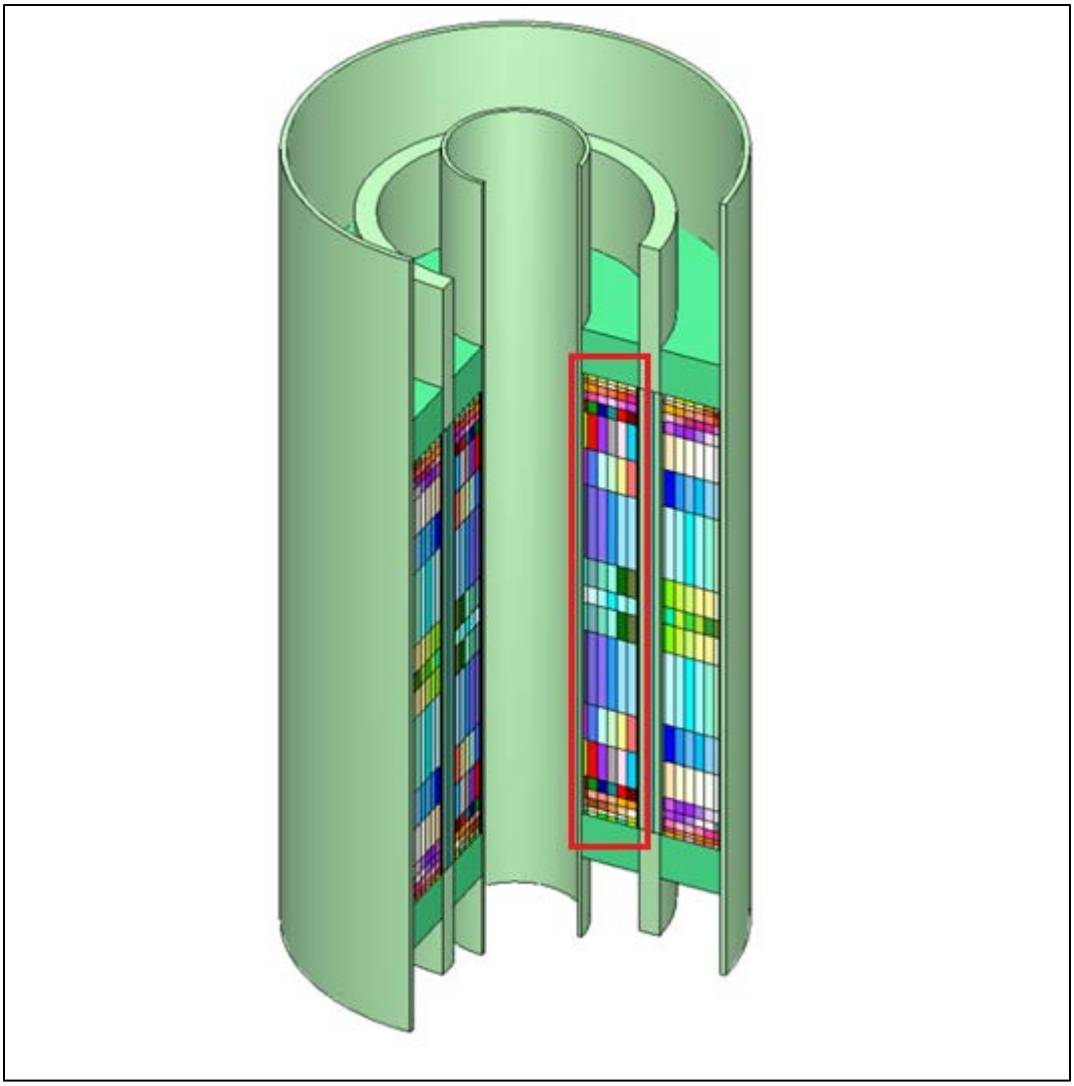

Fig.5.7. MCNP Cells. The inner fuel element cells are boxed in red.

For this thermal-hydraulic study, however, it is more convenient to restrict the nuclear power generation to the fuel meat alone. While not strictly physical it does produce a conservative temperature estimate as an equal power output is being produced in a smaller volume, thus raising the local power densities in the fuel. To make the conversion from power-per-cell-volume to power-per-fuel meat-volume, P'''_{fuel}, the MCNP power density output can be divided by the ratio of a cell's fuel meat volume-to-total volume, V_{ratio}. Given that width and height are equal for both fuel meat and total cell volume, it is essentially a ratio of the average fuel meat thickness in each cell normalized against the cell's thickness. The result is thus the fuel meat's thickness profile as a function of radius.

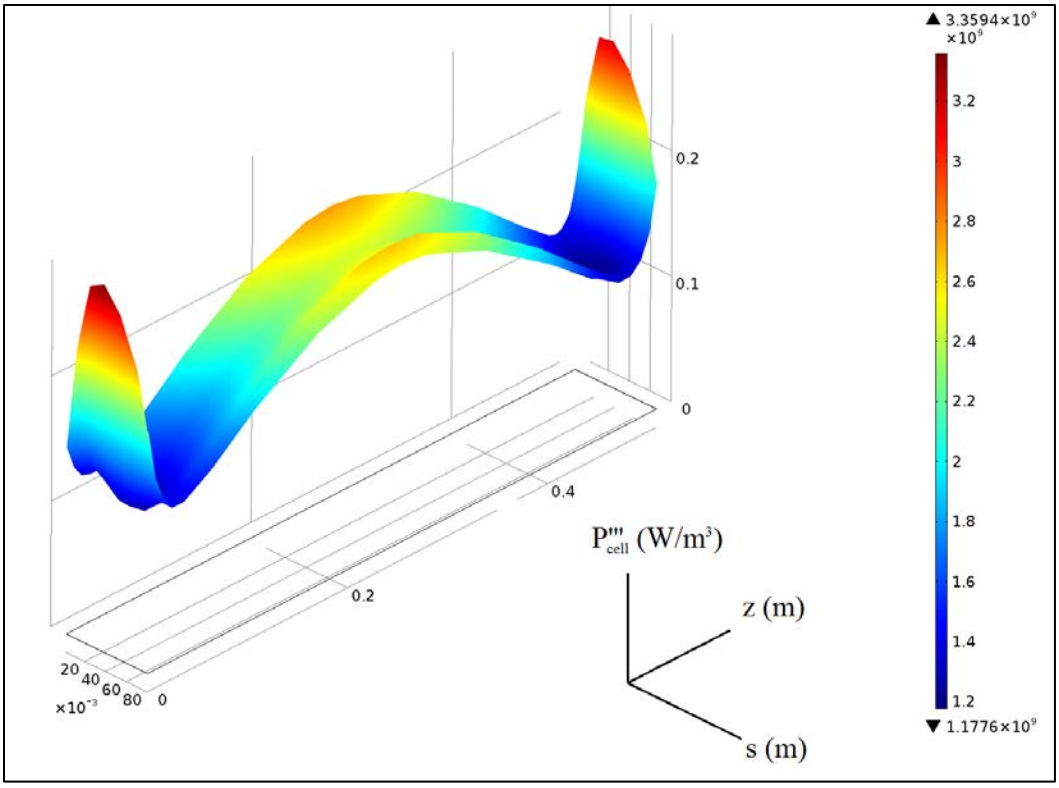

Fig. 5.8. MCNP power density profile. The direction of flow is in the +z-direction.

The thickness data is imported directly into COMSOL alongside the power-per-cell-volume nuclear power generation density. The final power-per-fuel meat-volume is calculated by dividing the MCNP power density output by the volume ratio of each cell as given in Equation 5.1.

$$P'''_{fuel}{}^{i} = c_1^i \times \frac{P'''_{cell}{}^{i}}{V^i_{ratio}} \quad \text{.....(5.1)}$$

where i is an index denoting cell-specific values and the coefficient c_1 is a correction factor that can be used to manually set the magnitude of the distribution in order to maintain the relation

$$P_{plate} = \sum_{i=1}^{I} P'''_{fuel}{}^{i} \times V^i_{fuel} \quad \text{.....(5.2)}$$

where I is the total number of MCNP cells in a single plate and the total power output, P_{plate}, is known to be 217.72 kW. The total power output can be determined independently according to

$$P_{plate} = P_{core} \times f_{IFE} / n_{IFE} \quad \text{.....(5.3)}$$

where P_{core} is the total power output of the core, 100 MW, f_{IFE} is the fraction of the total power output produced in the inner fuel element, 37.23%, and n_{IFE} is the total number of inner fuel element plates, 171. The final power density profile that is input into COMSOL is shown in Fig. 5.9.

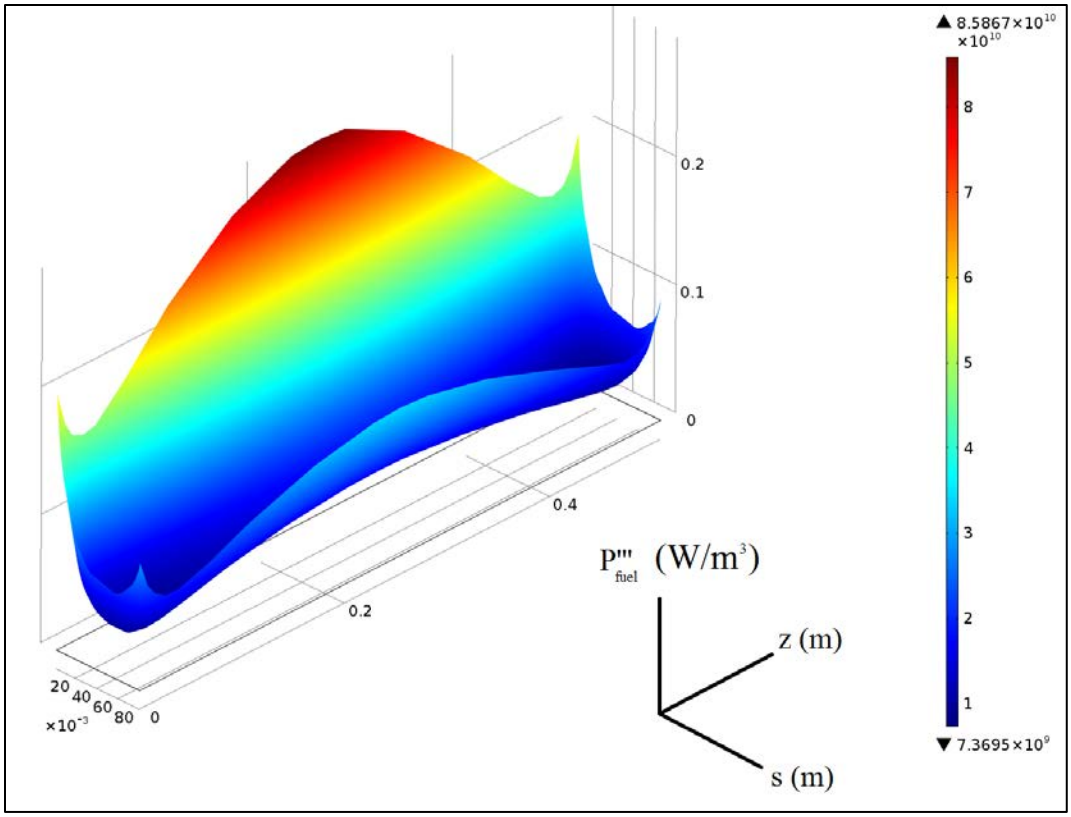

Fig. 5.9. COMSOL Power Density Profile. The direction of flow is in the +*z*-direction.

5.2.3 Physics

Energy transport occurs through three methods in the 3D model: heat transfer in the solid domains, heat transfer in the coolant domain, and turbulent mass transport in the coolant domain. Heat transfer in the solid domains is governed by the steady-state heat equation[38].

$$\nabla \cdot (\lambda \nabla T) + Q = 0 \quad \text{.....(5.4)}$$

where thermal conductivity, λ, is a function of T and thus dependent on position and Q is volumetric heat generation. The total volumetric heat generation, Q_{tot}, is defined such that all of the power generated in the fuel plate is assumed to be in form of heat energy

$$Q_{tot} = P'''_{plate} \quad \text{.....(5.5)}$$

It is important to note that the involute coordinate system (s, t, z) was developed only to aid with the specification of model inputs and the analysis of results. The computational scheme still operates in a Cartesian coordinate system (x, y, z). The gradient thus has the familiar form

$$\nabla = \frac{\partial}{\partial x}\hat{i} + \frac{\partial}{\partial y}\hat{j} + \frac{\partial}{\partial z}\hat{k} \quad \text{.....(5.6)}$$

The volumetric heat generation term *Q* in Equation 5.4 is present only in the fuel meat. In the surrounding aluminum fuel plate and side plates *Q* equals zero causing Equation 5.4) to reduce to Fourier's law, giving rise to linear heat flow according to

$$-\lambda \nabla T = \boldsymbol{q}'' \quad (5.7)$$

where $\boldsymbol{q}''$ represents the heat flux vector with components q_x'', q_y'', and q_z''. The solid domains experience three types of boundaries: thermally insulated, convective, and periodic. Thermally insulated boundaries are applied to the inner surface of the inner side plate and the outer surface of the outer side plate—the inner and outer circumferences of the model, respectively. The thermally insulated boundaries satisfy the Neumann-type constraint that the temperature gradient be zero. The convective boundaries ensure continuity of temperature and heat flux across the solid-liquid interface. The periodic boundaries, applied to the concave and convex faces of the side plates, enforce the same conditions.

Mass transport in the coolant domain is governed by the Reynolds-Averaged Navier-Stokes (RANS) equations with the *k*-*ε* turbulence model chosen to provide closure. In the most recent COMSOL release as of the onset of this project, version 4.3.A, the only available turbulence models were *k*-*ε*, *k*-*ω*, and Low-Reynolds Number (LRN) *k*-*ε*. The *k*-*ε* model was selected through the process of reduction. The models were considered on a two-tiered scheme with the two-equation *k*-*ε* and *k*-*ω* models being on a similar level of complexity and the LRN *k*-*ε* model adding an additional level.

The LRN *k*-*ε* model's added complexity comes from the fact that it explicitly models the fluid domain in its entirety, including all the way up to wall boundaries. The two other models, by contrast, utilize wall functions to simplify the already complex boundary layer region. Use of the LRN *k*-*ε* model requires considerably more boundary-layer mesh elements which in turn gives rise to added computational cost, stability issues, and meshing difficulties. Given the desire to produce as efficient a model as possible with the coupled model, the LRN *k*-*ε* turbulence model was considered too expensive for use.

The two remaining turbulence models were both tested on simplified proof-of-concept models and the completed 3D model. In the simplified models the *k*-*ω* model displayed a marginally faster convergence rate than the *k*-*ε* model. In the 3D model, however, the *k*-*ω* suffered from stability issues resultant of the high-aspect ratio mesh elements in the narrow coolant channel. These effects were especially pronounced in corners between the fuel plate and side plates where inter-element mesh structures often became mangled. While this problem can be overcome through the use of more advanced meshing techniques not incorporated in either model, the *k*-*ε* model proved the most stable and robust of the available turbulence models.

Both models consider variable-property flow in which coolant properties are given as functions of temperature. In order to model such a flow, the use of the semi-compressible N-S equations is required. Favre mass-averaging is used to decompose flow variables in lieu of the traditional Reynolds time-averaging which is insufficient for compressible flow. The final set of equations, therefore, will still be referred to as the RANS equations. They are

$$\nabla \cdot \left(\bar{\rho}\tilde{\boldsymbol{u}}\right) = 0, \quad (5.8a)$$

$$\bar{\rho}\tilde{\boldsymbol{u}} \cdot \nabla \tilde{\boldsymbol{u}} = -\nabla \tilde{p} + \nabla \cdot \left(\bar{\tau}_S + \bar{\rho}\tau_R\right) \quad (5.8b)$$

where a '–' overbar denotes a Reynolds time-averaged quantity and a '~' overbar denotes a Favre mass-averaged quantity and the viscous stress tensor and the specific Favre-averaged Reynolds stress tensor can be written, respectively, as

$$\bar{\tau}_S = \bar{\mu}\left[\nabla\tilde{\mathrm{u}} + (\nabla\tilde{\mathrm{u}})^T - \frac{2}{3}\nabla\cdot\tilde{\mathrm{u}}\right] \quad \text{.....(5.9)}$$

and

$$\bar{\rho}\tau_R = -\overline{\rho \boldsymbol{u}'' \boldsymbol{u}^{T''}} \quad \text{. .....(5.10)}$$

where a double quotation mark denotes the fluctuating component of a flow variable decomposed via Favre mass-averaging.

From here the two-equation *k*-*ε* model is chosen to provide closure for the RANS equations. This introduces two more transport equations for specific turbulent kinetic energy, *k*, and the dissipation rate of turbulent energy, *ε*. They are

$$\bar{\rho}\tilde{\boldsymbol{u}}\cdot\nabla k = \nabla\cdot\left[\left(\bar{\mu} + \frac{\mu_T}{\sigma_k}\right)\nabla k\right] + \mathrm{P}_k - \bar{\rho}\varepsilon \quad \text{,.....(5.11)}$$

$$\bar{\rho}\tilde{\boldsymbol{u}}\cdot\nabla\varepsilon = \nabla\cdot\left[\left(\bar{\mu} + \frac{\mu_T}{\sigma_\varepsilon}\right)\nabla\varepsilon\right] + C_{\varepsilon 1}\frac{\varepsilon}{k}\mathrm{P}_k - C_{\varepsilon 2}\bar{\rho}\frac{\varepsilon^2}{k} \quad \text{.....(5.12)}$$

where the turbulence production term, $\mathrm{P_k}$, is given by

$$\mathrm{P}_k = \bar{\rho}\tau_R\nabla\tilde{\boldsymbol{u}} \quad \text{.....(5.13)}$$

and the Favre-averaged Reynolds stress tensor by

$$\bar{\rho}\tau_R = \mu_T\left(\nabla\tilde{\boldsymbol{u}} + (\nabla\tilde{\boldsymbol{u}})^T - \frac{2}{3}\nabla\cdot\tilde{\boldsymbol{u}}\right) - \frac{2}{3}\bar{\rho}k = \frac{\mu_T}{\bar{\mu}}\bar{\tau}_S - \frac{2}{3}\bar{\rho}k \quad \text{. .....(5.14)}$$

The dynamic eddy viscosity, μ_T, is given by

$$\mu_T = \bar{\rho}C_\mu\frac{k^2}{\varepsilon} \quad \text{. .....(5.15)}$$

Dimensionless constants for both turbulent transport equations are given in Table 5.4[113].

Table 5.4. *k*-*ε* Transport constants

Constant	Value
C_μ	0.09
$C_{\varepsilon 1}$	1.44
$C_{\varepsilon 2}$	1.92
σ_k	1.00
σ_ε	1.30

Heat transfer in the coolant is governed by the heat equation for translating media

$$\bar{\rho} c_p \tilde{\boldsymbol{u}} \cdot \nabla T = \nabla \cdot \left(\lambda \nabla T \right) \quad \text{.....(5.16)}$$

At the inlet, Dirichlet boundary conditions are imposed for temperature and velocity based on the model inputs in Table 5.3. Dirichlet conditions are also imposed for specific turbulent kinetic energy and dissipation rate. They are

$$k_{in} = \frac{3}{2} \left(\left\| \boldsymbol{u}_{in} \right\| I_T \right)^2 \quad \text{.....(5.17)}$$

and

$$\varepsilon_{in} = C_\mu^{3/4} \frac{k_{in}^{3/2}}{L_T} \quad \text{.....(5.18)}$$

where I_T is the turbulence intensity and L_T is the turbulent length scale. Typical values for I_T in fully turbulent flows typically vary between 5% and 10%. Five percent was chosen for the 3D model. L_T was set to 7% of the hydraulic diameter, D_H, which is a standard value for fully developed pipe flow.

A Dirichlet condition was specified for pressure at the outlet boundary. Homogeneous Neumann conditions were imposed for specific turbulent kinetic energy, dissipation rate, and viscous stress.

The inward facing coolant boundary that is the result of the difference in lengths between the inner and outer side plates is constrained using an open condition. The open boundary condition can function as either a pseudo-inlet or pseudo-outlet boundary condition depending on the sign of $u \cdot \hat{\mathbf{n}}$. Given the open boundary's location adjacent to the coolant outlet at the bottom of the model, in this instance it functions purely under outlet condition restraints. The open boundary condition imposes outlet boundary conditions along with a homogeneous Neumann condition for temperature

Both the coolant outlet and the bottom faces of the side plates serve as heat outflows in which a homogeneous Neumann condition for temperature is imposed to ensure that the normal temperature gradient is zero. The open coolant boundary also serves as a heat outflow, with the condition of zero heat flux already specified.

The periodic coolant boundaries impose the same continuity conditions on temperature and its gradient as the periodic boundaries in the side plates. Additional continuity conditions are specified for coolant velocity, pressure, specific turbulent kinetic energy, and dissipation rate.

The final boundary type in the coolant domain is the solid, no-slip, impermeable wall. The *k*-ε turbulence model utilizes wall functions to model near-wall boundary layer flow. This creates a gap of thickness δ_w between the physical wall and the edge of the computational fluid domain across which the fluid flow is not explicitly modeled. This wall-offset distance is calculated according to

$$\delta_w^+ = \frac{\bar{\rho} u_\tau \delta_w}{\bar{\mu}} \quad \text{.....(5.19)}$$

where δ_w^+ is the dimensionless wall-offset distance and the shear velocity, u_τ, is provided by

$$u_\tau = C_\mu^{1/4} k^{1/2} \quad \text{.....(5.20)}$$

The wall-offset distance is calculated as half the height of the local wall-adjacent boundary mesh element or that value which produces a δ_w^+ of 11.06, whichever is greater. A δ_w^+ of 11.06 corresponds to the dimensionless distance from the wall, y_c^+, where the linear velocity profile relationship of the near-wall viscous sub-layer intersects the logarithmic relationship of the inner log-law layer. This intersection is shown in Fig. 5.10.

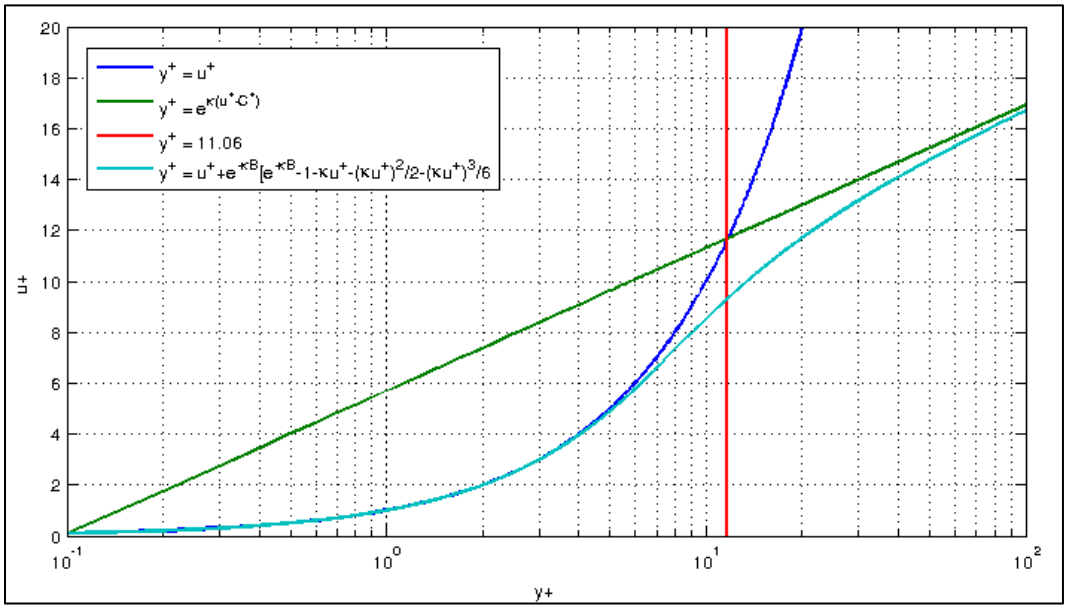

Fig. 5.10. Law of the wall. The linear relation for u^+, in blue, is valid to the left of the intersection point in the viscous sublayer. The logarithmic relation, in green, is valid to the right in the inner log-law layer. The smooth Spalding approximation, in teal, is valid throughout[43]. The von Kármán constant, κ, equals 0.41. B equals ~5.5.

5.2.4 Meshing

The axial consistency of the 3D model makes meshing a relatively straightforward affair. Many geometry components can be meshed by mapping a 2D surface in the *s-t* plane and extruding down their axial lengths. This extrusion process was modeled after the MCNP cell distribution. Tests showed that, as a minimum, the fuel meat, fuel plate, and adjacent coolant should be mapped with an axial mesh distribution at least equal to the MCNP cell distribution. The MCNP axial cell distribution is shown in Table 5.5. The MCNP distribution is only defined for the length of the fuel meat. It is symmetric about the axial midplane of the fuel meat with tighter cell spacing in the center and at the ends corresponding to areas with the greatest heat generation.

The MCNP distribution was continued into the adjacent coolant and side plates. For geometries up- and downstream of the fueled region, axial distributions were devised that were comparable to the MCNP distribution. In order to increase the smoothness of solutions, the MCNP mesh distribution was doubled in the final 3D model. Both axial distributions are shown in Fig. 5.11.

All of the distinct mesh domains are shown via diagram in Fig. 5.12. Mesh domains are color-coded according to the mesh type associated with them. The most predominant, and the most ideal, mesh type is the structured mesh which is applicable to every axially-consistent geometry component free of internal vacancies. The clad surrounding the fuel meat is the only axially-consistent geometry incompatible with the structured mesh type. Due to the hole in the geometry's center where the fuel meat sits, its *s*-*t* cross-section had to be mapped using a free-triangular mesh which was then extruded the same as the structured meshes. A cross-sectional cut-out showing the *s*-*t* plane through the fuel meat, surrounding clad, inner side plate, and coolant is shown in Fig. 5.13.

Table 5.5. MCNP axial cell distribution

Cell wall axial position (cm)	Cell height (cm)
50.8	0.5
50.3	0.5
49.8	1
48.8	1
47.8	1.4
46.4	4.2
42.2	4.2
38	8.4
29.6	3.2
26.4	2
24.4	3.2
21.2	8.4
12.8	4.2
8.6	4.2
4.4	1.4
3	1
2	1
1	0.5
0.5	0.5
0	

The remaining geometries—the rounded leading edge of the fuel plate and the leading and trailing edge coolant caps—were meshed using free-tetrahedral meshes unstructured in all three dimensions. They are shown in Fig. 5.14. Lastly, a boundary-layer mesh was added to every wall boundary in the coolant domain as demonstrated in Fig. 5.15.

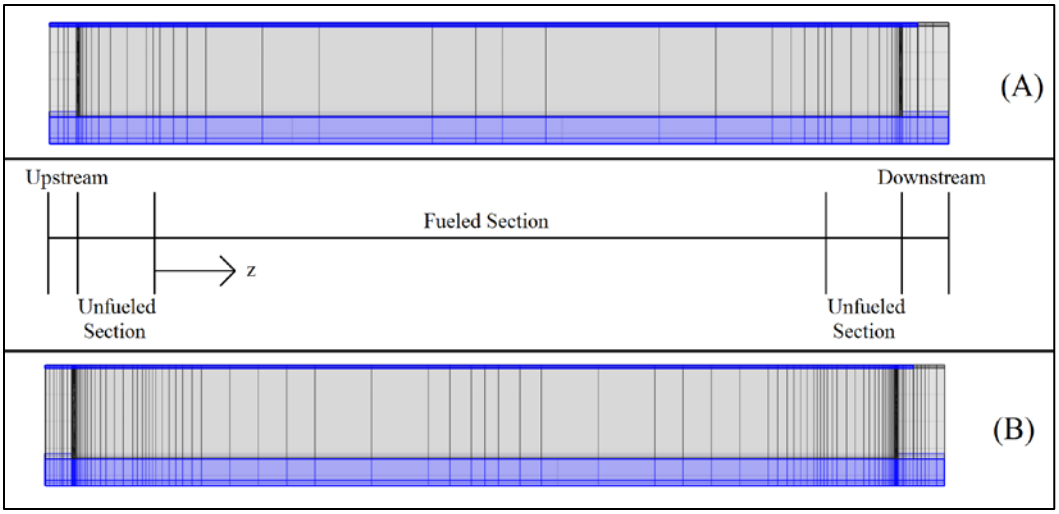

Fig. 5.11. 3D Axial Mesh Distributions. The MCNP axial mesh distribution is shown in (A) and the 2X MCNP distribution in (B). The side plates are highlighted in blue. The coolant channel is shown in grey. The fuel plate and fuel meat are obscured behind the coolant channel. Figure is not representative of final mesh as all spanwise (along the length of the involute curve) mesh distributions have been set to 1 for ease of viewing. The final mesh structure would not be discernible at this scale.

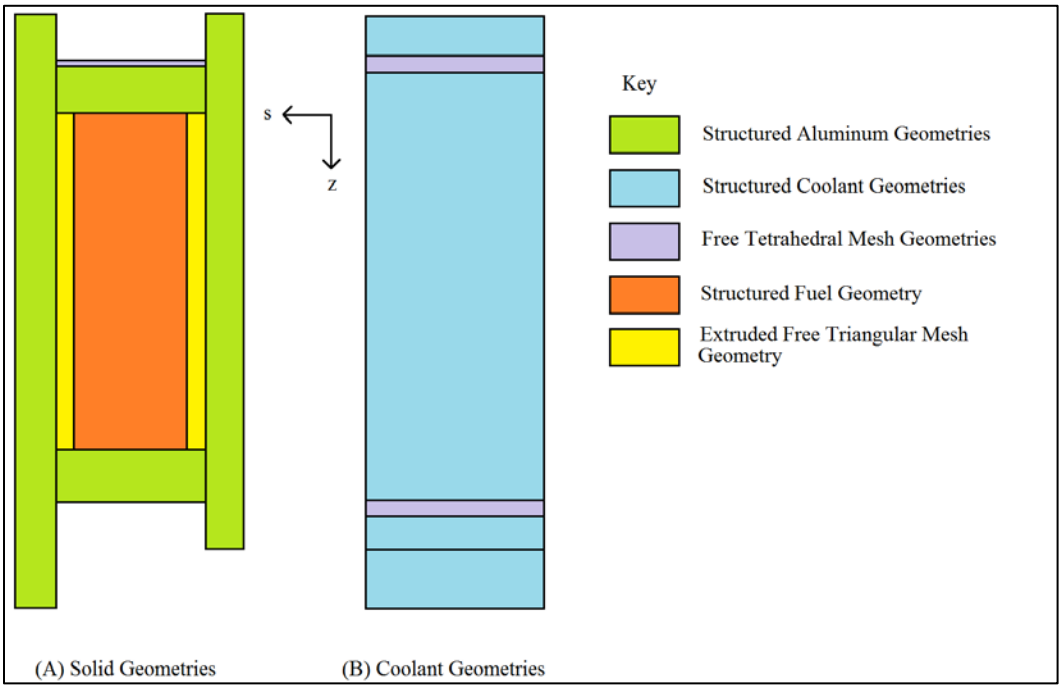

Fig. 5.12. Mesh Domains. Figure is not to scale.

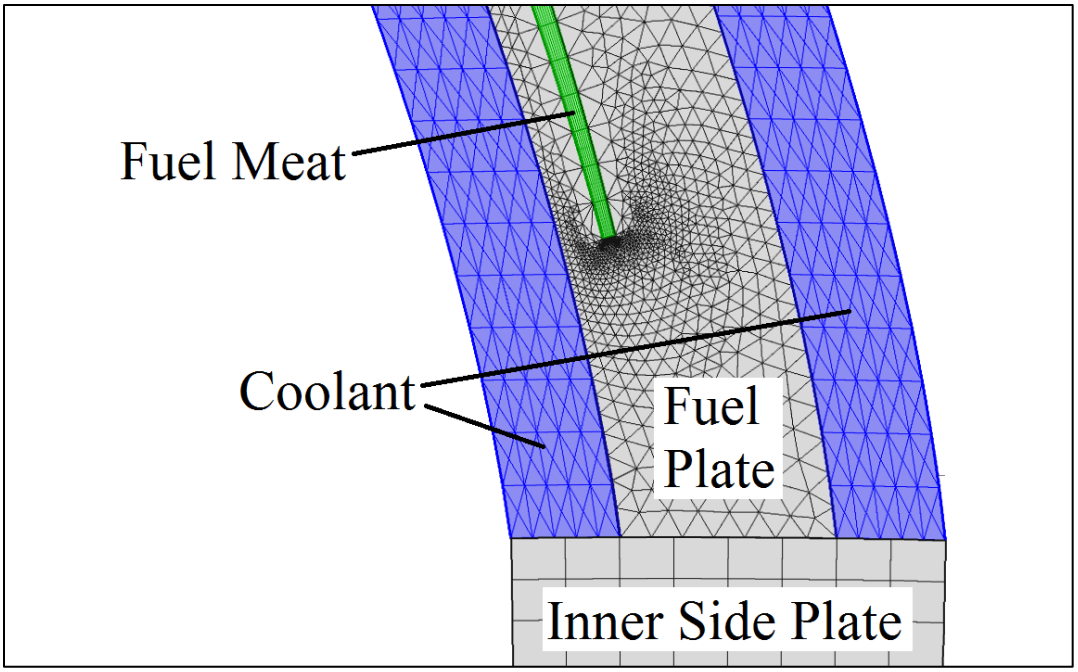

Fig.5.13. Fueled section cross-sectional mesh. Structured quadrilateral mesh elements in the coolant region have been converted to triangular elements in order to facilitate meshing between axial coolant components.

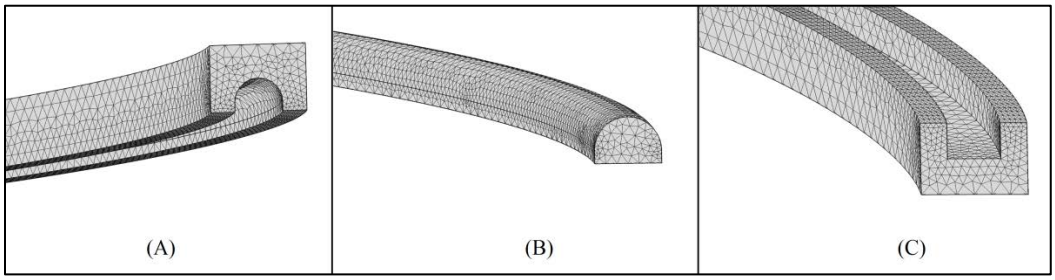

Fig. 5.14. Free-tetrahedral mesh domains. The leading edge coolant cap geometry is shown in (A), the rounded leading edge clad in (B), and the trailing edge coolant cap in (C).

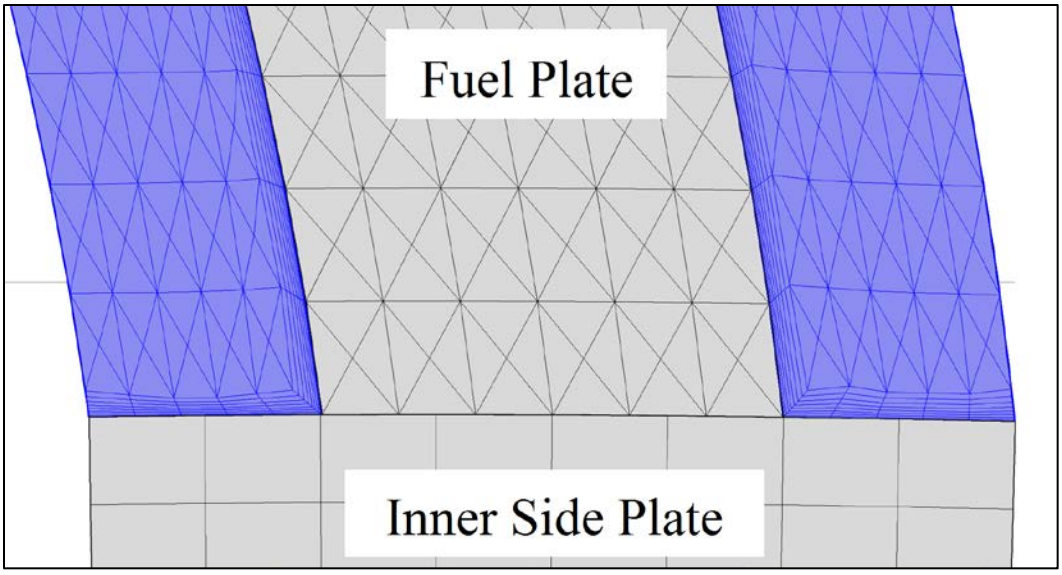

Fig. 5.15. Boundary-layer mesh detail.

Given the use of the MCNP axial cell distribution, mesh convergence studies were performed by varying the resolution of the *s-t* plain face meshes only. Mesh densities were driven by the competing needs to produce a scale that was sufficiently small so as to capture all, or enough of, the underlying physics in a domain without adding undue complexity to the model. In the coolant domain this is most evident in the creation of the boundary layer and its effect on perceived near-wall viscous shear stresses. In the fuel meat, the problem arises in capturing the quadratic nature of the temperature profile resultant of internal heat generation. This quadratic nature can easily be demonstrated via solution of the 1D heat equation with heat generation.

$$-\lambda \frac{d^2T}{dx^2} = Q \quad \text{.....(5.21)}$$

Integrating yields

$$-\lambda \frac{dT}{dx} = Qx + D_1 \quad \text{.....(5.22)}$$

Integrating again and dividing by λ produces a temperature profile with quadratic elements

$$T(x) = -\frac{1}{\lambda}\left[\frac{Qx^2}{2} + D_1 x + D_2\right] \quad \text{.....(5.23)}$$

The quadratic temperature profile is, obviously, most easily captured using quadratic basis functions. The continuity between the coolant and the solid domains in the 3D model, however, prevents multiple basis functions from being used, even in separate domains. In the COMSOL distribution utilized for this work, using quadratic basis functions to solve for temperature in the fuel meat means that they must also be used in the coolant. Such an approach proves computationally unfeasible as the model's degrees of freedom increases drastically due to the required resolution of the boundary-layer mesh. It is thus simpler and

more expedient to increase the mesh resolution in the fuel meat and use linear elements throughout the model.

5.3 SIMPLIFIED *T-Z* PLANE MODEL (COUPLED MODEL)

5.3.1 Construction

The three-dimensional fuel meat and fuel plate geometries used in the 3D model are also used in the coupled model. The coolant, however, is represented using a two-dimensional slice in the *t*-*z* plane as shown in Fig. 5.16. The axial heights of the entrance and exit coolant regions above and below the fuel plate, respectively, are the same as in the 3D model. The coolant domain is broken into three components for ease of meshing. The coolant domain's axial boundaries upstream and downstream of the fuel plate in the *t*-direction correspond to the midplane of the adjacent fuel plates.

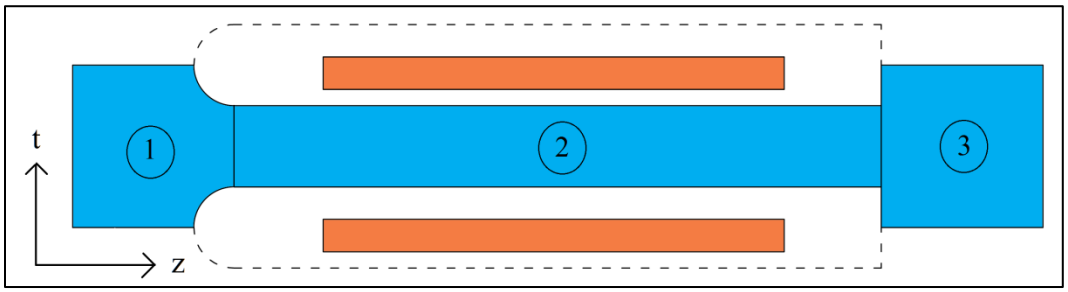

Fig. 5.16. Coupled model coolant domain. The coolant slice is shown in blue. The obstructions created by the adjacent fuel plates in the coolant channel are marked with dotted lines. Note, however, that the fuel plates are not included in the 2D geometry. The approximate position of the fuel meat within each fuel plate is shown in orange. Flow direction is in the +*z*-direction. Diagram is not to scale.

The side plates are not included in the coupled model. This is due, in part, to the issue of how to include them in the model. The contact interface with the fuel plate could easily be appended to the three-dimensional fuel plate domain. The coolant domain, however, homogenizes the *s*-direction. There would be no physically meaningful way to attach them to the coolant domain. This simplifying decision is validated by the 3D model. Energy balances performed on the coolant-facing surfaces of the side plates show that the heat transfer into both to be minimal compared to both the overall entropy change in the coolant channel and the heat generation in the fuel meat.

The use of unions and assemblies—continuous and discontinuous inter-component mesh boundaries—is the same in the fuel plate as in the 3D model. The coolant domain's three components are joined via union resulting in a single continuous mesh throughout.

5.3.2 Inputs

The coupled model had the same inputs as the 3D model for initial conditions as well as inlet and outlet conditions and nuclear heat generation. The only major difference is the addition of an involute coordinate system which was imported into the model for use in implementing the interdimensional coupling mechanism. Since there is no direct way to translate from an *x*-*y* Cartesian coordinate system to an *s*-*t* involute coordinate system, the impromptu coordinate had to be generated via a contour plot. A table of points with structured θ and *t* values was created in Matlab. The *x*- and *y*-coordinates were then calculated for each point and stored in a matrix. The grid that this produces is shown in Fig. 5.17.

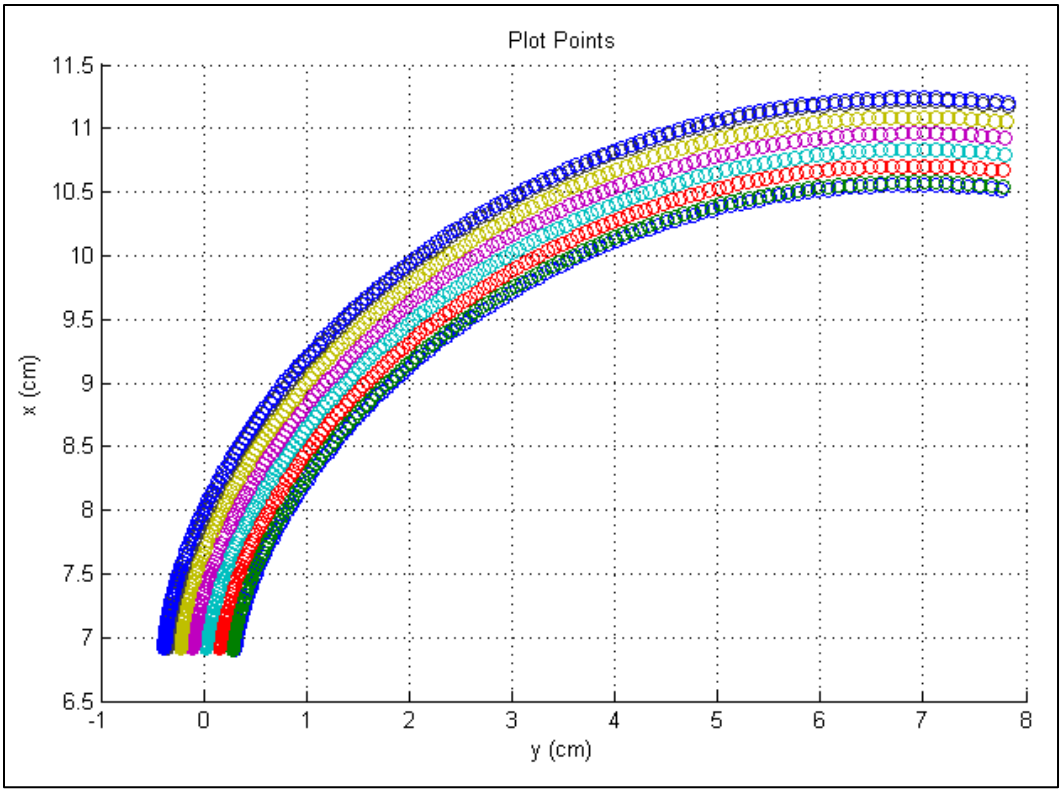

Fig. 5.17. Involute coordinate contour grid points. Each group of colored markers is associated with a constant *t* value in which *t* (in) = -0.12, -0.11, -0.06, -0.01, 0.04, 0.09, 0.14, 0.15. θ = 0.00 to 1.65 by 0.01 radian increments for each group.

All four coordinate values (x, y, θ, and t) were then imported into COMSOL. The x- and y-coordinates were treated as independent variables while θ and t were treated as dependent functions. This allowed for a contour map of each involute coordinate to be created. These are shown in Figs. 5.18 and 5.19.

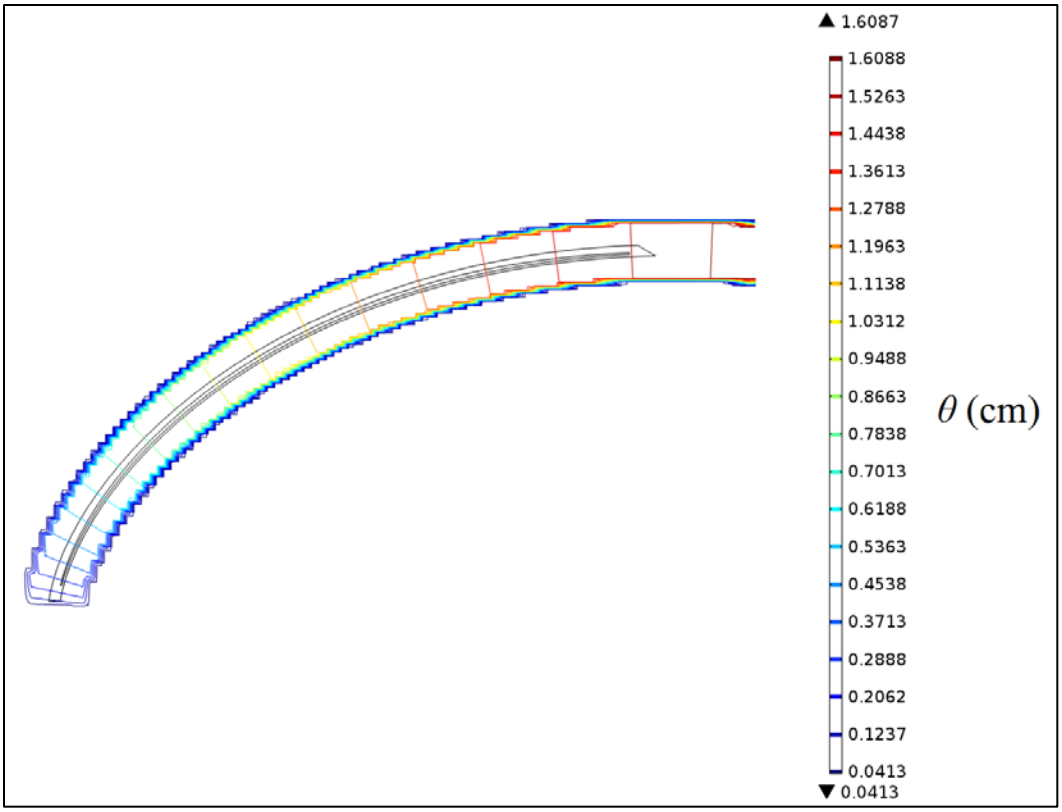

Fig. 5.18. θ-Coordinate contour map. The involute geometry is shown for reference.

Each coordinate map was made much larger than the involute geometry, which is shown underlain for reference. This was due primarily to the jaggedness of the contours on the edges of the maps where the coordinate grid ends. In order to prevent these discrepancies from infiltrating into the solution domain the boundaries were expanded to ensure smooth contours throughout. Once the functions $\theta(x,y)$ and $t(x,y)$ exist they can be referenced in COMSOL the same as a coordinate. The involute coordinate s was created as a function of the two dependent variable, $s(\theta,t)$.

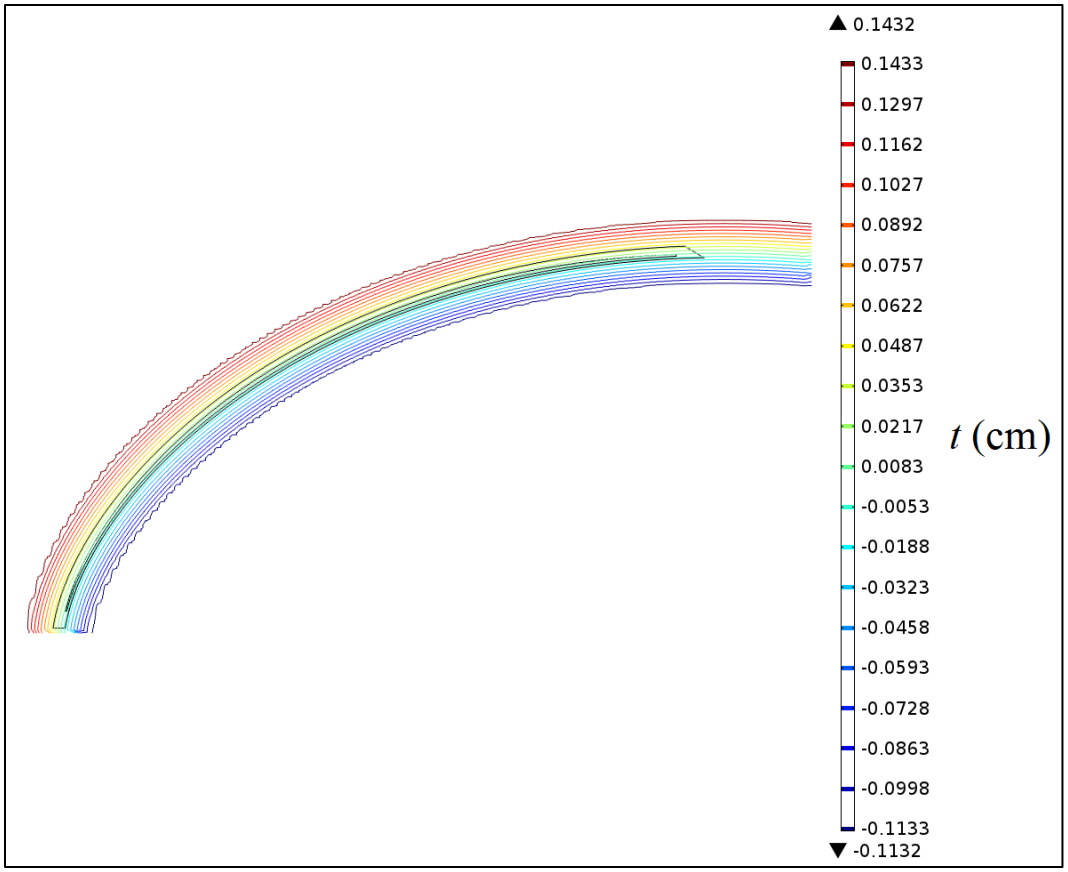

Fig. 5.19. *t*-Coordinate contour map. The involute geometry is shown for reference.

The other additional model input is the channel width as a function of axial position, $w_c(z)$. It is used in averaging flow properties across the width of the 2D channel slice. The channel width is constant for the length of the entire fuel plate except at the rounded leading edge (the right-hand side of coolant Region 1 in Fig.5.16. Therefore, the channel width function defines the axially-varying width along the length of the rounded leading edge. Constant-value extrapolations are used from the boundary values of the function to define the constant width along the rest of the length of the fuel plate.

The width of one-half of the rounded leading edge, w_r, is given as a function of its axial position

$$w_r(z) = \sqrt{r_c^2 - (z - z_o)^2} \quad \text{.....(5.24)}$$

where r_c is the radius of the rounded leading edge and z_o is the leading edge segment's axial center of rotation. The inverse of this width, the void width, w_v, is calculated by

$$w_v(z) = r_c - w_r(z) \quad \text{.....(5.25)}$$

Both functions are shown in Fig. 5.20.

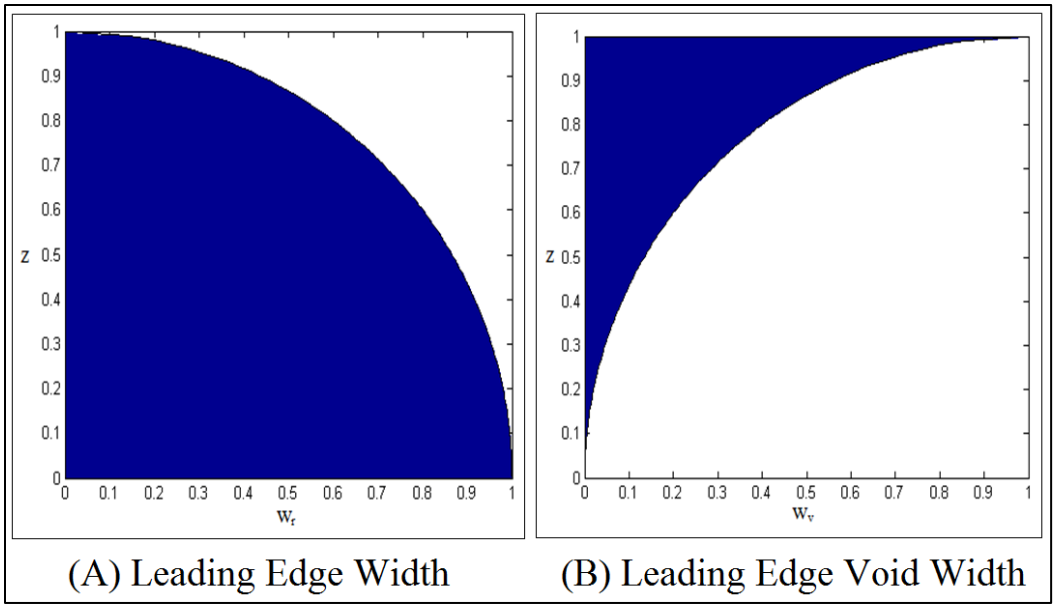

Fig. 5.20. Axially-dependent leading edge widths. r_c is set to 1 and z_o to 0. Flow direction is in the –z-direction.

At its widest (at the stagnation point at the tip of the rounded leading edge) the void width is $4r_c$. At its narrowest (once the rounded leading edge has reached the axially-constant width that it will maintain for the length of the fuel plate) this width is $2r_c$. The channel width in cm is thus provided by

$$w_c(z) = 4r_c - 2\sqrt{r_c^2 - (z - z_o)^2}, \quad -5.08 \le z \le -5.0165 \qquad (5.26)$$

where z_o equals -5.0165 cm. The channel width is only applicable for axial positions bounded by the fuel plate. Even though the function returns values in the entrance and exit coolant regions, they are irrelevant. The final function is shown in Fig. 5.21.

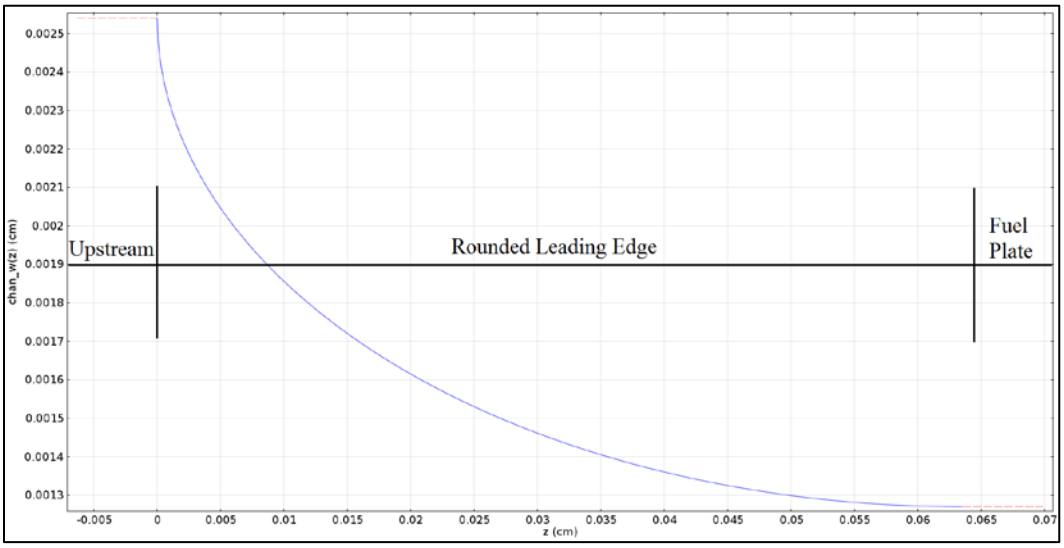

Fig. 5.21. Channel width input function. Flow direction is in the +*z*-direction. The *z*-coordinate in the figure is a localized coordinate system, not the global *s*-*t*-*z* system.

5.3.3 Interdimensional Model Coupling

The interdimensional model coupling mechanism functions in two directions: from the surface of the fuel plate to the surface of the coolant channel (3D-to-2D) and from bulk values in the coolant channel back to the surface of the fuel plate (2D-to-3D). In this way it produces a looped dependency between the two models in which their respective outputs and inputs are iteratively solved along with the domains to which they belong until the coupled system reaches a satisfactory equilibrium state.

Labeling the respective coupling mechanisms as such (3D-to-2D and 2D-to-3D) can be slightly misleading. The fuel plate-to-coolant channel coupling, for instance, involves the collection of variables on a 2D surface boundary (*s*-*z* plane) that are then reformatted and applied to a 1D edge boundary (*t*-*z* plane). It would not be incorrect to think of this as a 2D-to-1D coupling based on the dimensions of the collected and applied coupling variables.

The reverse coupling mechanism, however, involves the collection of fluid properties that are inherently 2D that are then reformatted and applied to a 2D surface. The destination surface exists in the *s*-*z* plane and the coolant channel in the *t*-*z* plane, however. Coupling variables can only be passed in a dimension that is shared between the two domains. In this case the axial dimension *z* is the only common dimension shared between the two. As with the first coupling mechanism, the result is a 2D-to-1D coupling. The respective coupling mechanisms are, therefore, most easily identified based on the dimensionality of the two respective domains, fuel plate (3D) and coolant channel (2D).

The 3D-to-2D coupling will be considered first. In many ways it is the simpler of the two couplings. Primarily, only a single variable, versus four in the reverse direction, is being coupled. Additionally, the manner in which the reformatted variable is applied to its destination domain is the simpler of the two. The only communication from the fuel plate to the coolant channel is in the passing of surface temperature values, T_{surf}. Inherently, surface temperature is a function of s and z_p, where a subscript p denotes a coordinate in the fuel plate domain. The original surface temperature variable is given by

$$T_{surf} = T(s, z_p) \quad (5.27)$$

The two-dimensional axial surfaces in the fuel plate domain become one-dimensional axial edges in the coolant domain. The T_{surf} variable must have its dependency in the *s*-direction removed in order to be applied to these edge boundaries. This can be achieved by integrating in the *s*-direction to produce a new variable, η_T, given by

$$\eta_T(z_p) = \int_{s_1}^{s_2} T_{surf}(s, z_p) ds \quad (5.28)$$

where s_1 is the *s*-coordinate at the fuel plate-inner side plate boundary and s_2 is the *s*-coordinate at the fuel plate-outer side plate boundary. This new variable has the correct spatial dependency but not the correct units—K-m versus the desired K. To rectify this, it is divided by the length it was integrated over. This produces a variable of spanwise-averaged surface temperature values as a function of axial position

$$\overline{T}_{surf}(z_p) = \frac{\eta_T(z_p)}{\Delta s} \quad (5.29)$$

where Δs is the span of the fuel plate. This spanwise-averaged temperature variable is then applied directly to the coolant domain boundaries such that

$$T_{surf}(z_c) = \overline{T}_{surf}(z_p) \quad (5.30)$$

where a subscript *c* denotes a coordinate in the coolant channel domain. The entire process is shown in the flow chart in Fig. 5.22.

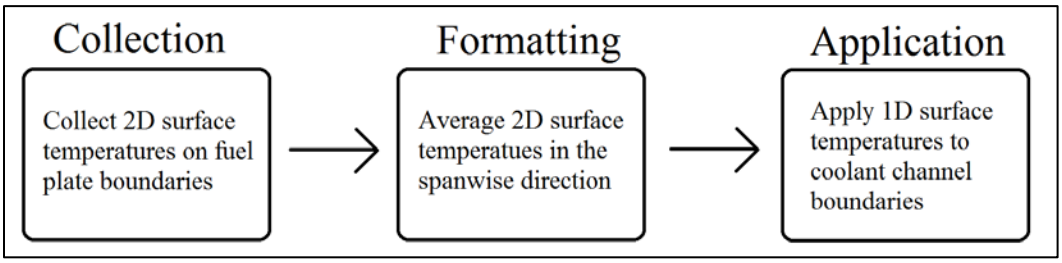

Fig. 5.22. 3D-to-2D Coupling mechanism flow chart.

This procedure is applicable for every axial surface on the fuel plate, including the rounded leading edge. Returning to Fig. 5.22 shows, however, that the trailing edge of the fuel plate (in the fuel plate domain) is confined to the *s*-*t* plane. Surface temperatures are thus given as a function of *s* and *t* instead of *s* and *z*

$$T_{surf} = T(s, t_p) \quad (5.31)$$

The *t*-coordinate is now the common coordinate shared between the two domains. The Surface temperature values are once again averaged along the span of the plate and stored as a function of *t*. The final application then takes on the form

$$T_{surf}(t_c) = \overline{T}_{surf}(t_p) \quad (5.32)$$

Additionally, the coupling of the convex and the concave sides must be kept separate so that they are allowed to vary independently of one another. Therefore there are technically two 3D-to-2D coupling variables, one for each side of the fuel plate. Surface temperature values are applied to the coolant channel edge boundaries via Dirichlet constraints. The coupling process, however, also inherently conserves the heat flux.

The reverse coupling mechanism is the 2D-to-3D coupling in which coupling variables are passed from the coolant to the fuel plate in order to complete the feedback loop. By the merit of its construction as a two-dimensional *t*-*z* slice, the coolant channel is, in essence, already representative of bulk flow properties in the *s*-direction. Given the coolant channel domain (*t*-*z*) and the fuel plate surfaces (*s*-*z*), the only common variable is again the axial coordinate *z*. In order to remove the *t*-coordinate dependency from the coolant channel flow variables, bulk values are taken in the *t*-direction as a function of *z*. The four coupling variables are T, ρ, μ, and Pr.

The definition for bulk temperature in a flow is

$$T_b = \frac{\dot{I}}{\dot{C}} = \frac{\text{total enthalpy flow rate}}{\text{heat capacity flow rate}} \quad \text{.....(5.33)}$$

In the *t*-*z* coolant channel, for variable-property flow, this takes on the form.

$$T_b(z_c) = \frac{\int_{-w_c(z_c)/2}^{+w_c(z_c)/2} \rho u C_p T \, dt}{\int_{-w_c(z_c)/2}^{+w_c(z_c)/2} \rho u C_p \, dt} \quad \text{.....(5.34)}$$

This operation, however, is extremely expensive in that each integral requires its own coupling mechanism. Every additional coupling mechanism in the model increases the solution time by a nontrivial fraction. This is especially true of the two mechanisms contained in this formulation given the relatively large number of operations contained within (compared to the coupling mechanism in Equation 5.28 in which only a single variable is collected). It is more computationally efficient to calculate bulk temperature in the same manner as surface temperature. While less accurate, the difference in passed bulk temperature values is small enough that the use of the more rigorously physical formulation is not warranted.

In this simplified formulation, bulk temperature, or any coupling flow variable, ϕ, represented by

$$\phi = \phi(t_c, z) \quad \text{.....(5.35)}$$

can be passed according to

$$\eta_\phi(z_c) = \int_{-w_c(z_c)/2}^{+w_c(z_c)/2} \phi(t_c, z) dt \quad \text{,.....(5.36)}$$

$$\phi_b(z_c) = \frac{\eta_\phi(z_c)}{w_c(z_c)} \text{, ...(5.37)}$$

and

$$\phi_b(z_p) = \phi_b(z_c) \quad \text{.....(5.38)}$$

The 2D-to-3D coupling process is shown in Fig. 5.23.

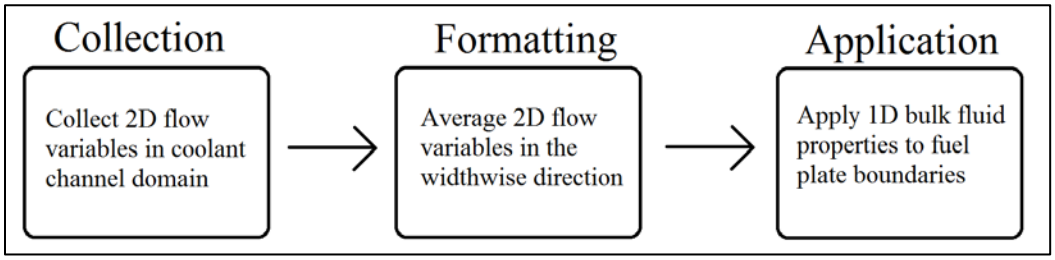

Fig. 5.23. 2D-to-3D coupling mechanism flow chart.

Unlike the 3D-to-2D coupling, the process of collecting and passing variables from the trailing edge in the coolant domain to the fuel plate domain is unchanged. Flow properties across both surfaces are still averaged in the *t*-direction and stored as a function of *z*. Therefore, a single value for each flow property is applied to the entire trailing edge.

The coupled flow properties are applied to the fuel plate surface via a simple convective boundary condition

$$q_n''(z_p) = h(T_{surf} - T_b) \quad \text{.....(5.39)}$$

where the heat transfer coefficient, *h*, is given as

$$h(z_p) = \mathrm{Nu}\frac{\lambda}{D_h} \quad \text{.....(5.40)}$$

where D_h is the hydraulic diameter and the Nusselt number, Nu, comes from a modified form of the Hausen correlation[114].

$$\mathrm{Nu}_{bz} = 0.116\,\mathrm{Pr}_{bz}^{1/3}\left(\frac{\mu_{bz}}{\mu_{wz}}\right)^{0.14}\left(\mathrm{Re}_{bz}^{2/3} - 125\right)\left[1 + \frac{1}{3}\left(\frac{D_h}{z}\right)^{2/3}\right] \quad \text{.....(5.41)}$$

where D_h is the hydraulic diameter of the full 3D coolant channel, not the channel width of the 2D coolant slice, a subscript *z* denotes a local value, and a subscript *w* denotes a wall value. The original Hausen correlation is valid in both the turbulent and transition flow regimes. The modified Hausen correlation was derived by Gambill and Bundy[32] as a result of experimental work performed in the study of turbulent flow in thin rectangular channels. The range of conditions over which Gambill and Bundy experimentally verified the applicability of the modified Hausen correlation is shown in Table 5.6. The range of nominal HFIR operating conditions are also shown for comparison.

Table 5.6. Modified Hausen correlation validation range

	Experimental conditions	Nominal HFIR conditions
q'' (W/cm^2)	32 - 2334	50 – 500
D_h (cm)	0.191 - 0.267	0.249
u (m/s)	3.1 - 26.0	7.8 - 18.0
Re_z	$9\text{x}10^3$ - $2.7\text{x}10^5$	$6.9\text{x}10^4$ - $1.0\text{x}10^5$
p (MPa)	0.11 - 3.91	2.51 - 3.17
L_h (cm)	30.5-45.7	50.8

The only criteria in which nominal HFIR operating conditions fall outside of the experimentally verified range is in the heated length. But even then the disparity is only 10% of the maximum verified heated length.

Values for Pr_{bz} and μ_{bz} are provided directly from the coupled variables for both. Values for Re_{bz} are calculated using coupled values for ρ_{bz} and μ_{bz} according to

$$\mathrm{Re}_{bz} = \frac{\rho_{bz} u_{bm} D_h}{\mu_{bz}} \quad \text{.....(5.42)}$$

where u_{bm} is bulk, mean axial velocity. The mean axial velocity is used, in lieu of an axially-dependent velocity, because the convective boundary condition requires a constant value for the external flow magnitude. Attempts to input velocity as a function of z failed after a single iteration. While an axially-dependent bulk flow velocity would be able to account for developing flow in the hydrodynamic entrance region, its exclusion is required by the code itself. As would be expected for such a high aspect ratio channel, the hydrodynamic entrance region turns out to be small, as will be shown in the results section of this chapter. Given this necessary simplification, u_{bm} was set to twice the inlet velocity. The wall viscosity, μ_{wz}, is calculated based on wall-adjacent flow conditions.

A key component in the successful implementation of the interdimensional model coupling mechanism is the exclusion of all of the coupling variables from the Jacobian solution matrix. Failure to do so increases the computation time by more than a factor of two. The exclusion of any coupling variable can be forced through the use of a *nojac* operator in its definition. As would be expected, the loss of such information in the Jacobian can lead to solution instabilities, sometimes severe. This is not an issue with the coupled model given the nature of the coupling variables in which they serve only as adaptive boundary conditions with which to drive internal domain solutions.

The coupling mechanisms are created in COMSOL using general projection model couplings. The general projection function allows for the selection of source domains in up to three dimensions and destination domains in up to two. In specifying the dimensions of the source domain, the last dimension is the one in which the integration is performed. The remaining dimensions (if applicable) are used to store the remaining information. The dimensionality of the information to be applied to the destination domain must necessarily be of one fewer dimensions than the source due to the integration process. Once a general projection has been defined a variable can be created from it. This variable can then be applied to boundary nodes the same as any number or predefined boundary condition.

The implementation of both coupling mechanisms creates a looped dependency between the models which, like the solutions of the internal domains, can converge to an equilibrium value through an iterative process. The complete coupling loop is shown in Fig. 5.24.

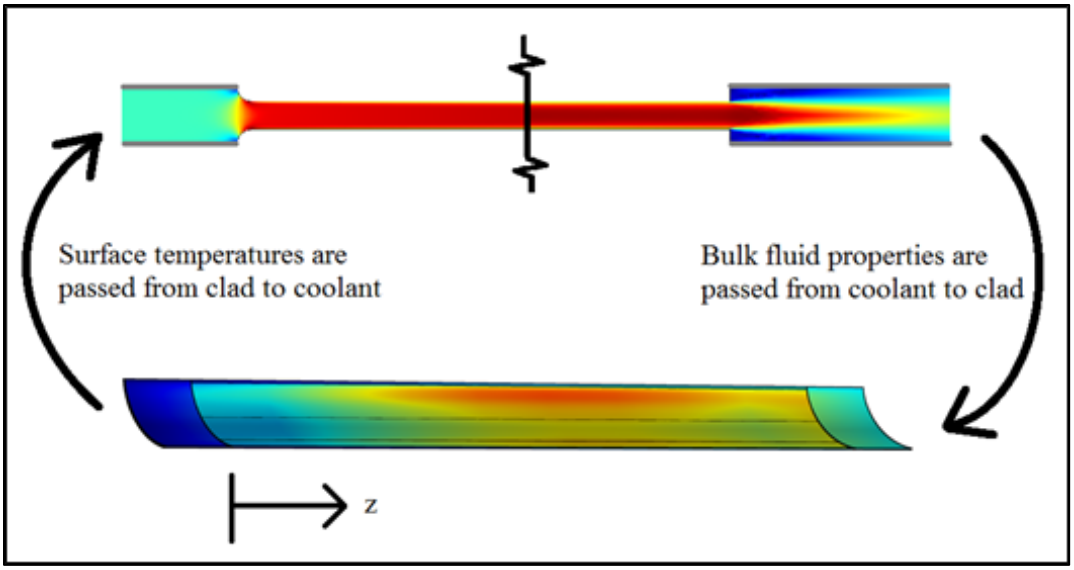

Fig. 5.24. Model Coupling Interdependency Loop. Flow is in the +z-direction.

The full iterative solution process implemented in the coupled model is shown in Fig. 5.25.

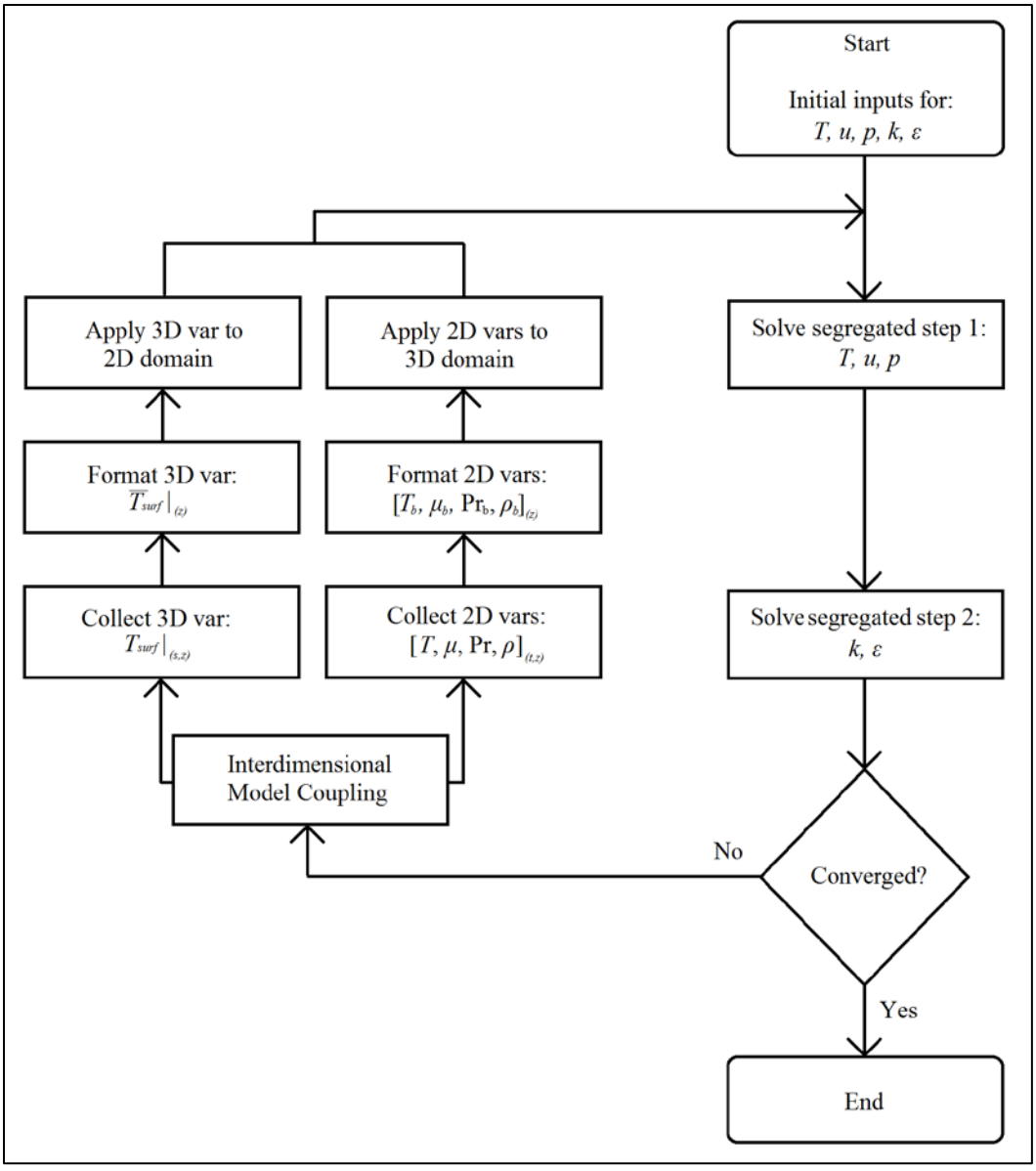

Fig. 5.25. Coupled Model solution process flow chart.

5.3.4 Physics

The same physics govern the coupled model that govern the 3D model. The only difference is in the application of boundary conditions. The coolant has the same inlet and outlet conditions. The axial boundary edges above and below the fuel plate coincide with the plate midpoint and are governed by periodic mass and heat flow conditions. The fuel plate boundary edges are modeled as no-slip, impermeable walls with imposed coupled heat flow conditions.

In the fuel plate, every coolant-adjacent surface is specified using the previously detailed convective boundary condition. The two surfaces that would mate with the side plates in the 3D model are modeled as thermally insulated boundaries. Given the extremely high-aspect ratio in the plate, heat conduction tends to occur predominantly in the *t*-direction. Heat conduction, as will be shown in the results section

of this chapter, is minimal in the *s*-direction. As such, stopping off the heat outlet that traditionally exists via the fuel plate-side plate shared surface has a negligible effect on the model.

5.3.5 Meshing

An important feature of the coupled model is the separation of its two solution domains, solid and liquid. This separation allows for separate basis functions to be used in each domain. Namely, the solid domain, in which the heat generation-resultant quadratic temperature profile is found, is able to use quadratic functions while the coolant can still use linear functions. The solid domain mesh has the same structure as in the 3D model. Meshes are mapped to *s*-*t* faces, where applicable, and extruded using the 2X MCNP axial mesh distribution. The maps in the fuel meat and the unfueled plate are structured meshes while the plate surrounding the meat is mapped using a free-triangular mesh. The rounded leading edge is meshed using free-tetrahedral elements. The mesh resolution in all of these domains is lower than in the 3D model, however, given the ability of the quadratic basis functions to provide a more accurate approximation using fewer elements.

As previously mentioned, the Coolant domain is split into three sections: upstream, fuel plate, and downstream. The upstream and downstream sections are mapped using unstructured triangular meshes. The fuel plate section was originally meshed using the same triangular elements. This proved extremely inefficient, however, given the high-aspect ratio of the channel. A second mesh was created consisting of a structured rectangular mesh. The mesh was extruded axially using both constant-width cells and the 2X MCNP distribution. A boundary layer was added to all three fuel plate section meshes along the wall boundaries. The two mesh types, free-triangular and structured, are shown in Fig. 5.26.

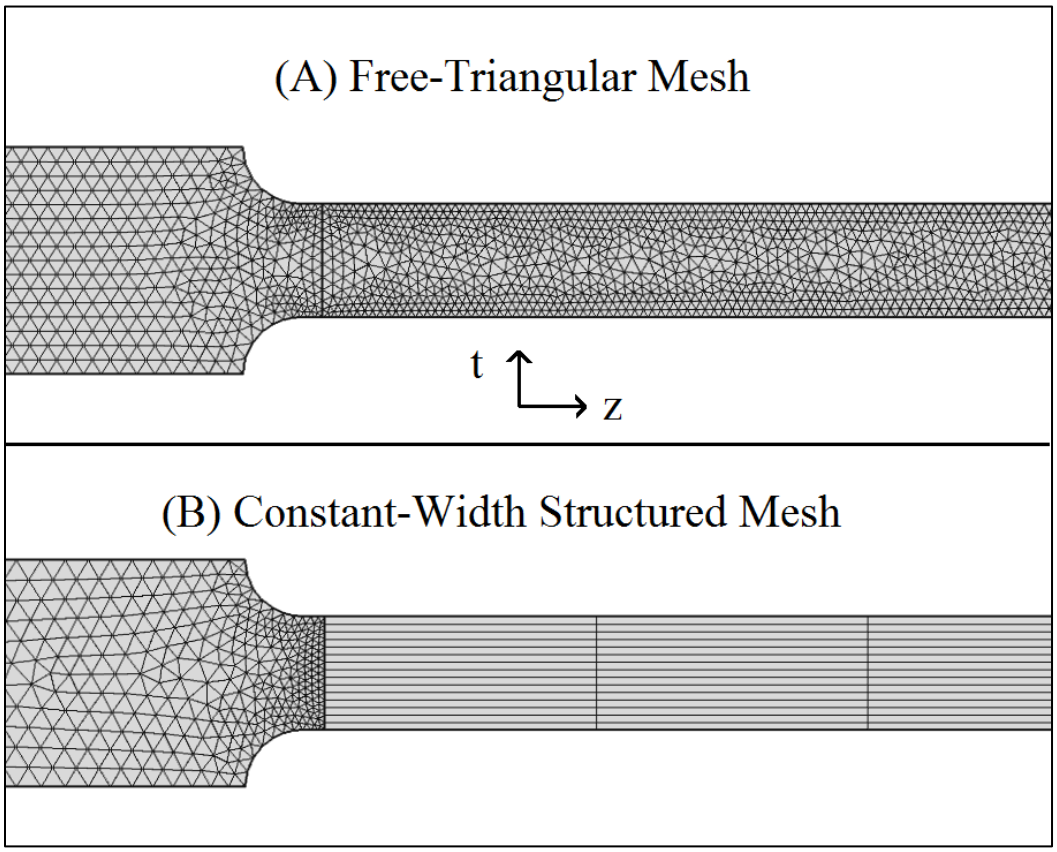

Fig. 5.26. Coupled model coolant mesh comparison.

An interesting limitation of the coupling mechanism is that it is incompatible with non-triangular mesh elements. This means it cannot be used on a surface that contains rectangular mesh elements. In the coolant, this requires the insertion of diagonal mesh walls to divide a single rectangular element into two triangular elements. In the solid domain, 3D volume mesh elements must be cut in half. A detailed view of a converted boundary-layer mesh is shown in Fig. 5.27.

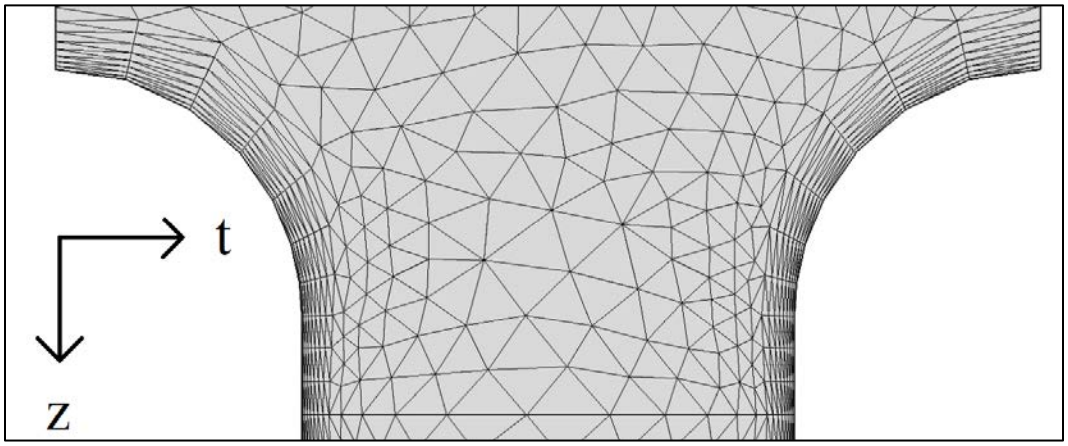

Fig. 5.27. Coupled model converted boundary layer detail.

5.3.6 Paneling

The biggest drawback of the coupled model is the homogenizing effect the coolant channel slice has on the fuel plate temperature profile. Surface temperature values passed from the clad to the coolant must necessarily drop a dimension given the dimensional disparity between the two domains. The passed variable cannot have a dimensionality greater than either its source or destination. This is also true in reverse. The problem, however, is that in this latter case the passed variable has a lower dimensionality than the boundary it is being passed to. In essence, the boundary is capable of storing more information than the passed variable is able to provide it. The result is that an entire dimension's worth of information is wasted.

This means that the incoming bulk properties, especially bulk temperature, have a profile proportional to spanwise-averaged surface temperature rather than local surface temperature. Thus, at any point where the local surface temperature is greater than the spanwise-averaged surface temperature, the incoming bulk temperature is lower than it should be. Conversely, at any point where the local surface temperature is less than the spanwise average, the incoming bulk temperature is higher than it should be. This has a smoothing effect on the surface temperature profile, blunting its maxima and minima. This smoothing effect propagates into the interior of the fuel plate and fuel meat as well. Given the model's primary intent of predicting maximum temperatures, this is an undesirable consequence of the model's construction.

An attempt was made to reintroduce a certain level of spanwise fidelity that the coupled model's construction had erased. In this model, the paneled model, the surface of the fuel plate is split into a finite number of axial strips as shown in Fig. 5.28.

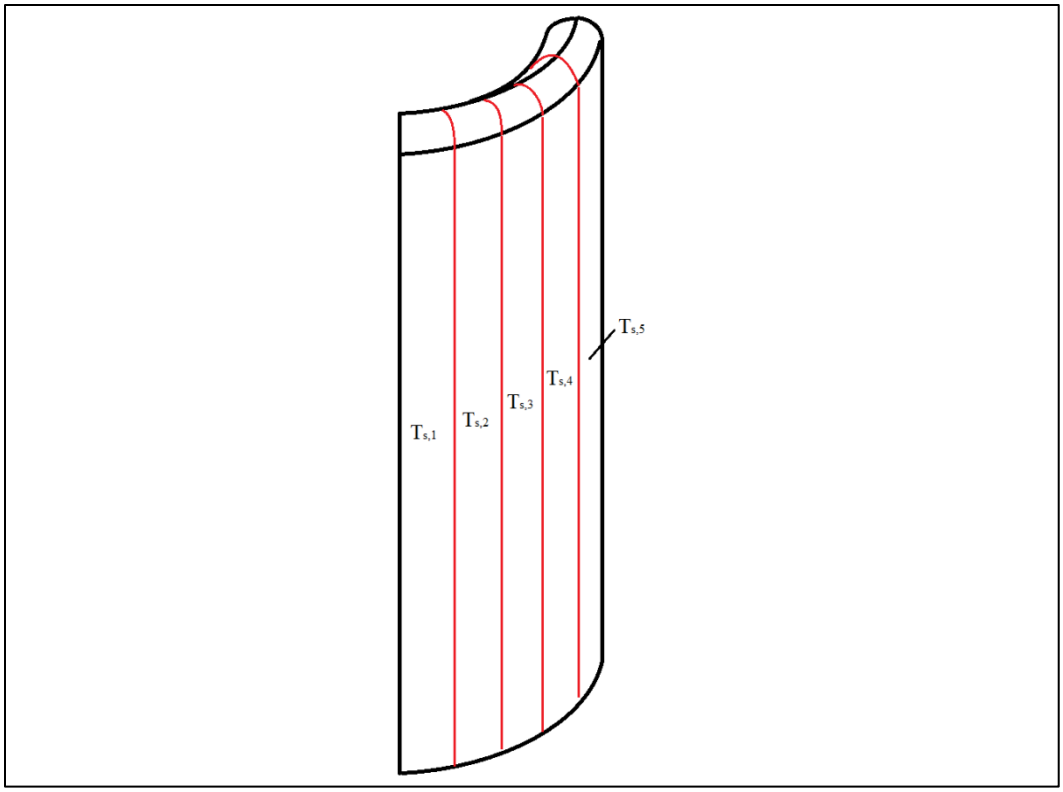

Fig. 5.28. Fuel plate paneling. Depicted is a five-panel decomposition. Figure is not to scale.

Each plate surface strip, along with its counterpart on the opposite side of the fuel plate, is paired with its own coolant channel slice. Plate surface temperatures are averaged across each strip and passed to their respective slice. Bulk flow properties are then passed back from slice to strip. Instead of relying on a single spanwise bulk flow, the model is split into a finite number of bulk flows. If the number of panels were increased to infinity one would essentially recreate the original 3D channel. By creating a small number of slices, however, a measure of that spanwise variation in flow and plate surface properties is allowed to manifest itself without the burden of solving the entire flow channel.

The dependency loop for a two-panel model is shown in Fig. 5.29. Ultimately, the design proved infeasible due to two factors. Firstly, increasing the number of panels beyond two increases the model's computational cost to a degree that it is no longer a viable improvement over the 3D model. This is due to the fact that every additional panel precipitates the need for an entire new coolant channel slice, thus doubling the degrees of freedom from that half of the model. While the coolant channel slice is the simpler of the two domains, from a geometry standpoint, the fact that it must solve the N-S equations means that the additional degrees of freedom are significant. Secondly, as will be shown in greater detail in the results section of this chapter, even a two-panel configuration does not produce the desired results due to the high-aspect ratio of the geometry.

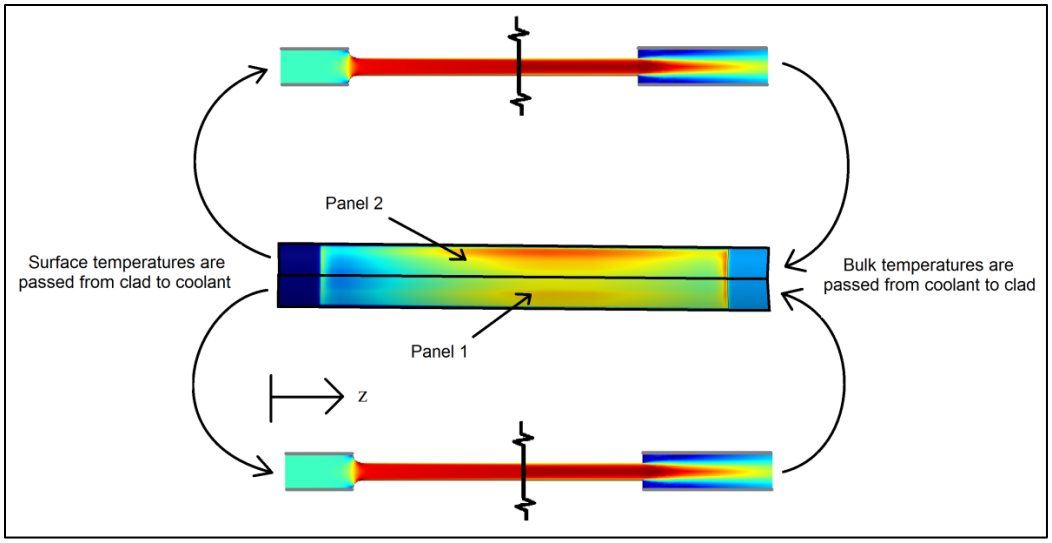

Fig. 5.29. Fuel plate paneling diagram.

5.4 SIMPLIFIED *S-Z* PLANE MODEL (BULK MODEL)

5.4.1 Construction

The bulk model is most like the 3D model in its construction in that all domains are modeled explicitly including the side plates and coolant. There are only two differences. The first is with regards to the model's widthwise (*t*-direction) span. Rather than encompassing one fuel plate and two half coolant channels it includes one fuel plate and two full coolant channels. The second is with regards to the exit region coolant subdomains. Whereas the 3D model split this region up into three subdomains—one to encapsulate the trailing edge of the fuel plate, one to correspond with the bottom of the inner side plate, and one to correspond to the bottom of the outer side plate—the bulk model removes the trailing edge cap. Instead, the fuel plate subdomain and the inner side plate subdomains extend to the fuel plate trailing edge where they meet. This new *t-z* plane cross-section is shown in Fig. 5.30. Widthwise boundaries in the fuel plate and exit regions correspond to the wall boundaries of the two adjacent fuel plates. The widthwise boundary in the entrance region corresponds to the midplate of the two adjacent fuel plates.

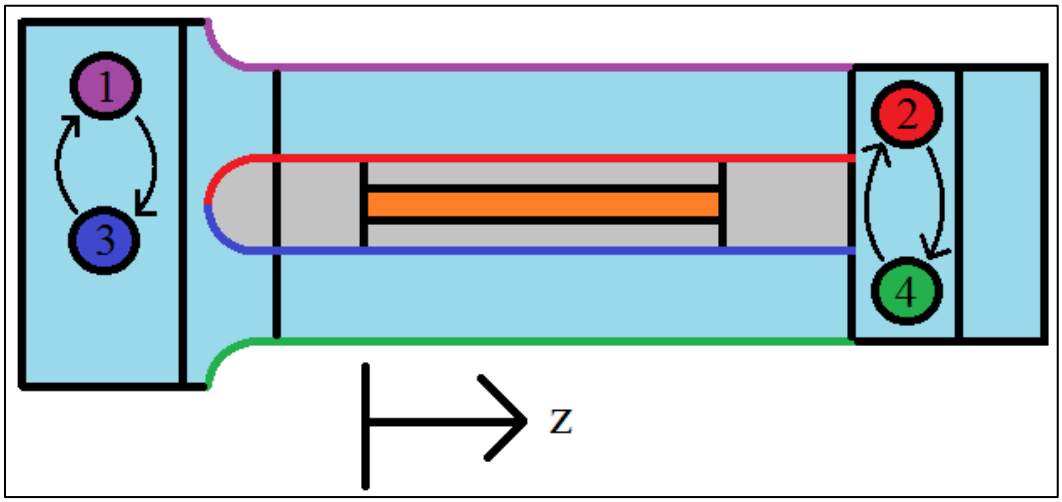

Fig. 5.30. Bulk model *t-z* plane cross-section. Not to scale.

Identity mapping functions are used to couple the model's periodic boundaries. The four identity mapped surfaces in the bulk model are highlighted in Fig. 5.30 for reference. There are two pairs of mapped boundaries. The concave surface of the fuel plate communicates with the outer boundary of the convex coolant channel (3-to-1). The convex surface of the fuel plate communicates with the outer boundary of the concave coolant channel (2-to-4). Communication also occurs through each pairing in reverse.

The identity mapping function is similar to the general projection function used to create the interdimensional model couplings in the previous chapter. The primary difference is that here, instead of using the coupling to remove one dimension's worth of information from the passed variables, variables are passed from one boundary to an identical boundary in a one-to-one map. In this capacity the identity map is essentially recreating the periodic boundary condition function.

5.4.2 Inputs

Inputs for the bulk model are identical to previous inputs in the first two models. Initial and inlet/outlet conditions (as appropriate) for pressure, temperature, and velocity are unchanged. As is the nuclear heat generation profile and the involute coordinate system.

5.4.3 Physics

The same governing physics apply in the fuel plate domain as in previous models. The coolant channels are modeled using laminar flow instead of turbulent. Additionally, all coolant wall boundaries are modeled as slip walls. Despite the model's explicit construction, however, the two domains do not interact directly for the most part but are instead coupled via the identity maps. Surface temperatures from the fuel plate are applied to the outer coolant channels by the couplings outlined in Section B. The only direct interaction between the two is in the application of temperature and heat flux across the two shared solid-liquid boundaries 2 and 3.

Bulk coolant properties are then passed back to the fuel plate via the same convective boundary condition from the coupled model. Bulk properties are obtained by averaging the wall values for each coupled flow variable across a given coolant channel. Given the asymmetric placement of the fuel meat within the fuel plate there is traditionally a "hot" side and a "cold" side. Since the model excludes no-slip wall effects

and the formation of a boundary layer, the average of these two points is assumed to represent the bulk state of the coolant. The process of collecting bulk temperature values for the coolant-to-fuel plate coupling is illustrated in Fig. 5.31.

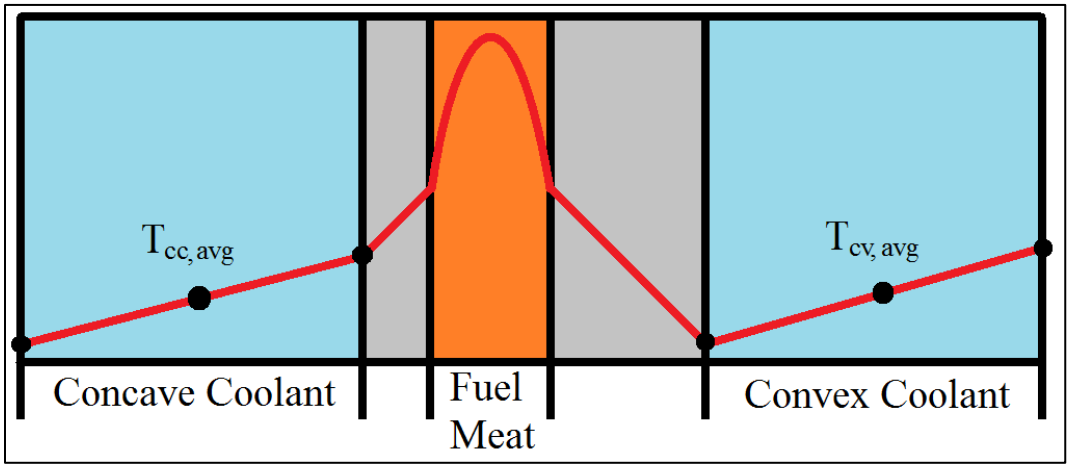

Fig. 5.31. Bulk model widthwise temperature profile.

5.4.4 Meshing

Meshing in the fuel plate and fuel meat is unaltered from the previous two models. The solid domains can be meshed with any level of mesh resolution deemed appropriate for the model. The coolant domains adjacent to the fuel plate, however, must be meshed a specific way. The spanwise resolution (*s*-direction) can be set to according to desired resolution within the fuel meat and plate. The widthwise resolution, however, must be set to one for each domain as shown in Fig. 5.32. This ensures a linear temperature profile in the coolant domains for bulk averaging.

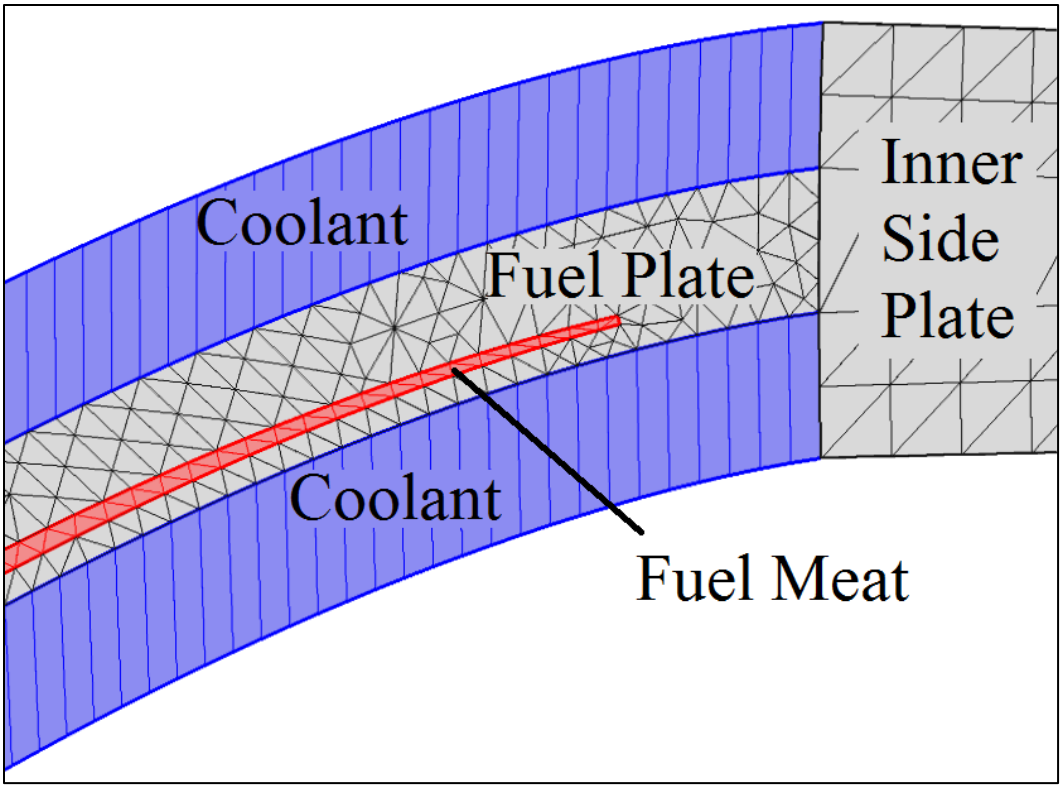

Fig. 5.32. Bulk Model fueled section *s-t* plane mesh cross section.

5.5 RESULTS

5.5.1 Error Evaluation

Before model results are presented, the means and methods of evaluating the validity of a given model configuration must be specified. This is achieved primarily through the assessment of a model's energy balance. For steady-state models such as those under consideration here this means that the conservation of energy takes on the form

$$\dot{E}_{in} + \dot{E}_{gen} - \dot{E}_{out} = 0 \quad \text{.....(5.43)}$$

where $\dot{E}$ is actually energy-per-unit-time and has units of power (W) and all terms are assumed to be positive. In order to break the model down further so as to trace energy imbalances to a specific domain—fuel plate or coolant—this simple energy balance can be evaluated individually for each domain. The fuel plate has no incoming energy term but does have an energy generation term due to the nuclear heat production in the fuel meat. This generation term, $\dot{E}_{p,gen}$, is given by

$$\dot{E}_{p,gen} = \iiint_V Q dV \quad \text{.....(5.44)}$$

The outgoing energy for the fuel plate, $\dot{E}_{p,out}$, is the total heat transfer through the surface of the fuel plate given by

$$\dot{E}_{p,out} = \iint_{A_p} (\boldsymbol{q}'' \cdot \hat{\boldsymbol{n}}_p) dA \quad \text{.....(5.45)}$$

where $\hat{\boldsymbol{n}}_p$ is the local outward surface normal vector for the fuel plate geometry and A_p is the surface area of the fuel plate. This $\dot{E}_{out}$ term for the fuel plate becomes part of the $\dot{E}_{in}$ term for the coolant (the side plates are considered part of the coolant domain for energy balance purposes in the 3D model). The other $\dot{E}_{in}$ components come from the inlet enthalpy in the coolant and inlet heat transfer in the side plates. The total term is given in the 3D model by

$$\dot{E}_{c,in}\big|_{3D} = -\left[\iint_{A_p} (\boldsymbol{q}'' \cdot \hat{\boldsymbol{n}}_c) dA + \iint_{A_{inlet}} (\boldsymbol{u} \cdot \hat{\boldsymbol{n}}_{inlet}) \rho c_p T dA + \iint_{A_{sp,inlet}} (\boldsymbol{q}'' \cdot \hat{\boldsymbol{n}}_{sp,inlet}) dA \right] \quad \text{.....(5.46)}$$

where $\hat{\boldsymbol{n}}_c$ is the outward surface normal vector of the coolant channel geometry in contact with the fuel plate and is the opposite of $\hat{\boldsymbol{n}}_p$. The coolant domain does not possess an $\dot{E}_{gen}$ term. $\dot{E}_{out}$ in the 3D model's coolant is given by

$$\dot{E}_{c,out}\big|_{3D} = \iint_{A_{outlet}} (\boldsymbol{u} \cdot \hat{\boldsymbol{n}}_{outlet}) \rho c_p T dA + \iint_{A_{open}} (\boldsymbol{u} \cdot \hat{\boldsymbol{n}}_{open}) \rho c_p T dA + \iint_{A_{sp,outlet}} (\boldsymbol{q}'' \cdot \hat{\boldsymbol{n}}_{sp,outlet}) dA \quad \text{.....(5.47)}$$

where the middle term is the outlet enthalpy along the open axial boundary beneath the inner side plate. Another way of looking at the energy balance in the coolant domain is to consider energy added to the system via the fuel plate and the change in enthalpy in the coolant and side plates between inlet and outlet. Ideally

$$\dot{E}_{c,in(plate)} - \Delta\dot{H}_c = 0 \quad \text{.....(5.48)}$$

where $\Delta\dot{H}_c$ is the change in enthalpy-per-unit-time in the coolant domain and the terms are given by

$$\dot{E}_{c,in(plate)}\big|_{3D} = -\iint_{A_p} (\boldsymbol{q}'' \cdot \hat{\boldsymbol{n}}_c) dA = \dot{E}_{p,out} \quad \text{.....(5.49)}$$

and

$$\Delta\dot{H}_c\big|_{3D} = (\dot{E}_{c,outlet} - \dot{E}_{c,inlet}) + (\dot{E}_{sp,outlet} - \dot{E}_{sp,inlet}) + \dot{E}_{c,open} \quad \text{.....(5.50)}$$

Coolant energy values are formulated differently for the coupled model. Since the coolant is represented as a two-dimensional *t-z* slice, boundary integrals become line integrals. These quantities must be multiplied by the span of the fuel plate axial surface, Δs, in order to maintain dimensional parity. The energy-in and enthalpy change terms become

$$\dot{E}_{c,in(plate)}\big|_{coupled} = -\Delta s \int_{z_1}^{z_2} [(\mathrm{q}'' \cdot \hat{\mathrm{n}}_{concave}) + (\mathrm{q}'' \cdot \hat{\mathrm{n}}_{convex})] dz \quad \text{.....(5.51)}$$

and

$$\Delta \dot{H}_c\Big|_{coupled} = \Delta s \int_{-w_c(z_{inlet})/2}^{+w_c(z_{inlet})/2} \left[\left(\mathrm{u} \cdot \hat{\mathrm{n}}_{outlet} \right) \rho c_p T - \left(\mathrm{u} \cdot \hat{\mathrm{n}}_{inlet} \right) \rho c_p T \right] dt = \dot{E}_{c,outlet} - \dot{E}_{c,inlet} \quad \text{.....(5.52)}$$

where terms for the side plates and the open boundary beneath the inner side plate are neglected because such features are not present in the coupled model and z_1 and z_2 correspond to the axial coordinates for the top and bottom of the coupled boundary, respectively. The normal $\hat{\boldsymbol{n}}_{concave}$ is the outward facing normal vector for the coolant domain edge boundary corresponding to the concave surface of the fuel plate. The normal $\hat{\boldsymbol{n}}_{convex}$ corresponds to the opposite fuel plate edge boundary in the coolant domain. Whereas the energy leaving the fuel plate, $\dot{E}_{p,out}$, and the energy entering the coolant domain from the fuel plate, $\dot{E}_{c,in(plate)}$, are equal in the 3D model, the same assumption cannot be made in the coupled model. This is due to the fact that they are separated via the interdimensional model coupling mechanism in the coupled model.

Individual energy balances can be constructed for each domain such that

$$\%e_p = \frac{\left| \dot{E}_{p,out} - \dot{E}_{p,gen} \right|}{\dot{E}_{p,gen}} \times 100\% \quad \text{.....(5.53)}$$

and

$$\%e_c = \frac{\left| \Delta \dot{H}_c - \dot{E}_{p,out} \right|}{\dot{E}_{p,out}} \times 100\% \quad \text{.....(5.54)}$$

In both local energy balances, the incoming energy is assumed to represent the *true* energy. Any nonzero result from the energy balance is thus attributed to the outgoing term (loosely defined in the coolant domain). In the fuel plate, the nuclear heat generation term actually is the *true* energy since it is set at a fixed, predetermined value. Thus, in this region, both the relative local error and the total global error are the same. In the coolant, however, the incoming heat flow itself can be incorrect, thus e_c is only good for quantifying the relative local error. In order to understand the total error in the coolant, a global energy balance, e_g, is constructed to compare the nuclear heat generation against the change in coolant channel enthalpy

$$\%e_g = \frac{\left| \Delta \dot{H}_c - \dot{E}_{p,gen} \right|}{\dot{E}_{p,gen}} \times 100\% \quad \text{.....(5.55)}$$

An additional error evaluation can be defined in the coupled model for the interdimensional model coupling mechanism itself. The error of the 3D-to-2D coupling, e_{imc}, can be calculated according to

$$\%e_{imc} = \frac{\left| \dot{E}_{c,in(plate)} - \dot{E}_{p,out} \right|}{\dot{E}_{p,out}} \times 100\% \quad \text{.....(5.56)}$$

The reverse, an evaluation of error in the 2D-to-3D coupling, is not readily calculable. While the effects of the convective boundary condition in the fuel plate domain can be measured, there is no direct counterpart in the coolant domain with which to compare. The fact that the convective boundary is itself composed of values calculated in both domains makes any such error analysis all but impossible. Thus the 3D-to-2D error must be used to evaluate the entire model coupling mechanism.

Using $\dot{E}_{p,gen}$ as a reference value, the energy terms used in calculating error can be normalized to produce

$$\frac{\dot{E}_{p,gen}}{\dot{E}_{p,gen}} = E'_{p,gen} = 1 \quad \text{,} \qquad (5.57)$$

$$\frac{\dot{E}_{p,out}}{\dot{E}_{p,gen}} = E'_{p,out} \quad \text{,} \qquad (5.58)$$

$$\frac{\dot{E}_{c,in(plate)}}{\dot{E}_{p,gen}} = E'_{c,in(plate)} \quad \text{,} \qquad (5.59)$$

and

$$\frac{\Delta\dot{H}_c}{\dot{E}_{p,gen}} = \Delta H'_c \quad \text{.} \qquad (5.60)$$

Another means of model evaluation lies in fuel plate temperatures. Specifically, the maximum fuel meat temperature can be used as a rough guide to determine a model's validity. While the energy balance method provides an empirical means of comparing a given model's solution against a known quantity, the maximum temperature method is only useful for providing a relative comparison between models. Thus when considering two models there is no way to declare one superior to the other based purely on their maximum fuel meat temperatures (assuming they are both within reason). In the course of a mesh convergence study in which many similar models are compared against each other, however, it can provide a meaningful way with which to track convergence.

5.5.2 3D Model Mesh Convergence

Solutions presented in this section will be for the axially-consistent LEU fuel geometry only. The axially-graded LEU geometry is excluded sever hike in computational cost associated with solving the extra mesh elements in the axially-graded section of the fuel meat. Solutions are otherwise centered on the LEU, versus the HEU, geometry because the desire to model it was the initial impetus behind the thesis. The 3D model mesh convergence study is truncated in comparison to the coupled model's study. This is a result of the model's complexity and sensitivity. The axial mesh distribution was held constant for the mesh convergence study. The 2X MCNP axial mesh distribution was found to be adequate for all domains. Solutions for temperature along an axial cut line bisecting the point of maximum fuel meat temperature using both the 2X and 1X mesh distributions are shown in Fig. 5.33.

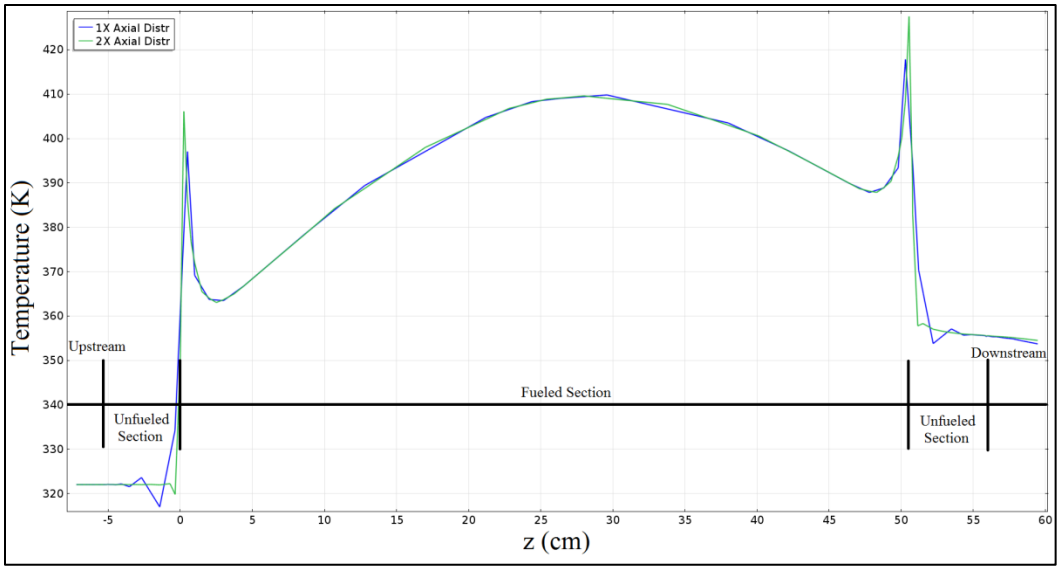

Fig. 5.33. Axial cut line temperature solution.

While the 1X MCNP axial mesh distribution clearly captures the overall contour of the temperature profile, it is insufficiently fine to accurately resolve abrupt shifts in the profile. The 2X distribution manages to resolve these shifts with greater clarity, especially with regards to the large temperature spikes at the top and bottom of the fuel meat. Additional refinements to the MCNP axial distribution could not be evaluated due to the increasing computational cost. Distribution refinements must necessarily double the previous distribution thus doubling the degrees of freedom in the model. With the 4X distribution the computational cost becomes too great to meet on available resources. It is doubtless that a 4X axial distribution would have further refined the profile in the vicinity of the temperature spikes. The agreement between the 1X and 2X distributions, combined with the diminishing returns to solution improvement that accompany mesh refinements, indicate that the 2X axial distribution can be assumed sufficient.

With the axial mesh distribution fixed the mesh convergence study dealt only with altering mesh densities in the s-t plane. The breadth of the study was limited due to model solution instabilities at lower mesh resolutions and meshing difficulties at higher mesh resolutions. What results were able to be obtained, however, show good convergence towards a state of minimal energy balance error. The results of the 3D model mesh convergence study are shown in Table 5.7. Mesh d2 was selected as the ideal 3D model mesh against which to base comparisons. This mesh is representative of current core modeling efforts at HFIR using COMSOL. The fact that the observed maximum temperature changed by only 0.3 K between the two meshes indicates that any increase in mesh resolution, and thus solution quality, would affect very little change to the overall temperature profile of the model. Given that temperature is dropping with increases in mesh resolution, however, indicates that, if anything, the reported maximum temperature could be slightly higher than a true converged value.

Table 5.7. 3D model mesh convergence study

Mesh	Mesh elements (in thousands)	$E'_{p,gen}$	$E'_{p,out}$	$\Delta H'_c$	e_p (%)	e_c (%)	e_g (%)	Max fuel meat T [K]
d1	1103	1.0000	1.0027	1.0021	0.267	0.060	0.207	432.1
d2	2311	1.0000	0.9997	0.9995	0.034	0.019	0.053	431.8

5.5.3 Coupled Model Mesh Convergence

The separation of the coupled model into two distinct domains permits a more detailed mesh convergence study to be performed. In fact, it permits two mesh convergence studies to be performed—one for the coolant and one for the fuel plate. Using the previously defined local error quantities, this permits the mesh in each domain to be optimized individually, thus ensuring adequate mesh resolution to capture physics while precluding the risk of unnecessary refinement. The coolant domain mesh convergence was performed first. For that, the fuel plate domain mesh was held constant and the coolant domain successively refined until a mesh-converged solution was achieved. The fuel mesh chosen was of a sufficient resolution that e_p equaled zero for all cases. Similarly, e_{imc} was found to be zero at all times, not just in the coolant mesh convergence study but in every solution obtained over the duration of thesis-related work. Thus it can be said that

$$\%e_{imc} = 0 \quad \text{.....(5.61)}$$

is true at all times. Coolant meshes were judged based on e_c which, with $e_p = e_{imc} = 0$, equals e_g in these cases. The results of the coolant mesh convergence study are shown in Table 5.8. The data in columns four, five, and six are plotted in Figs. 5.34, 5.35, and 5.36, respectively, as functions of the number of coolant mesh elements in each model. The plot of e_c is presented in logarithmic format to demonstrate that the error is decreasing near-logarithmically in accordance with finite element analysis theory.

Table 5.8. Coupled model coolant domain mesh convergence study

Mesh	Coolant mesh elements (in thousands)	$E'_{c,in(plate)}$	$\Delta H'_c$	e_c (%)	Max fuel meat T (K)
c1	163	1.0000	0.8493	15.07	425.1
c2	301	1.0000	0.9301	6.99	427.2
c3	456	1.0000	0.9686	3.14	428.2
c4	717	1.0000	0.9900	1.00	428.7
c5	1,035	1.0000	0.9971	0.29	428.9
c6	1,429	1.0000	1.0006	0.06	429.0

*Fuel plate domain mesh elements (in thousands) = 454
**Residual tolerance = 1.00×10^{-2}

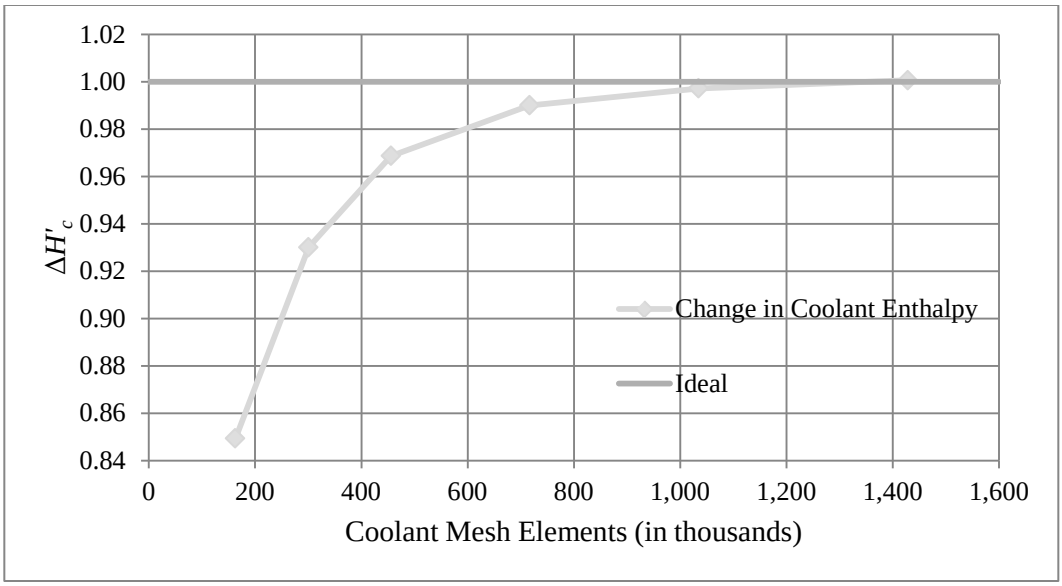

Fig. 34. Coupled model coolant mesh convergence—coolant channel enthalpy. The normalized nuclear heat generation, 1.00, is marked with a red line to show the coolant channel's convergence towards the correct value.

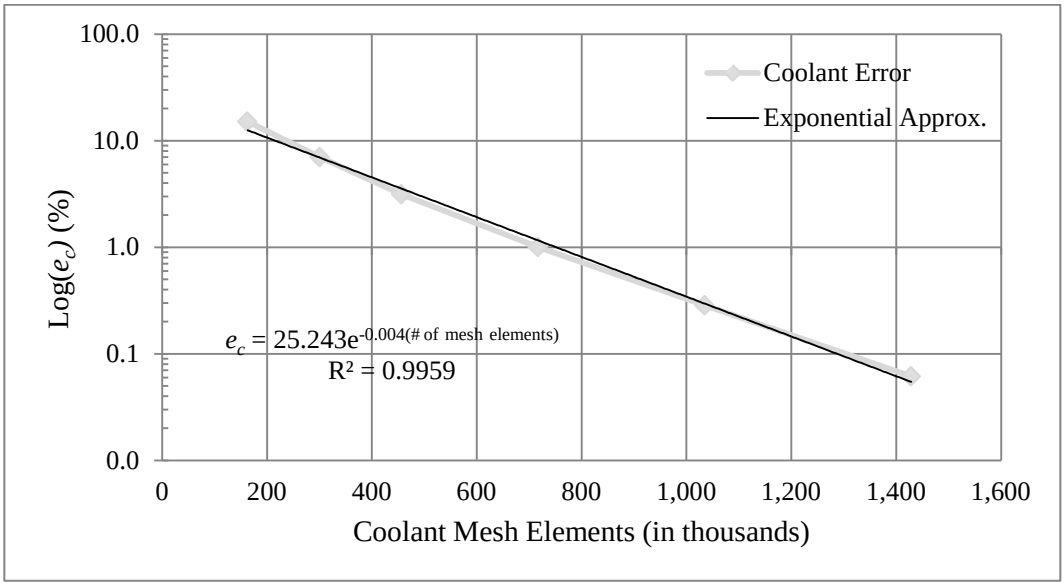

Fig. 5.35. Coupled model coolant mesh convergence—logarithmic coolant error.

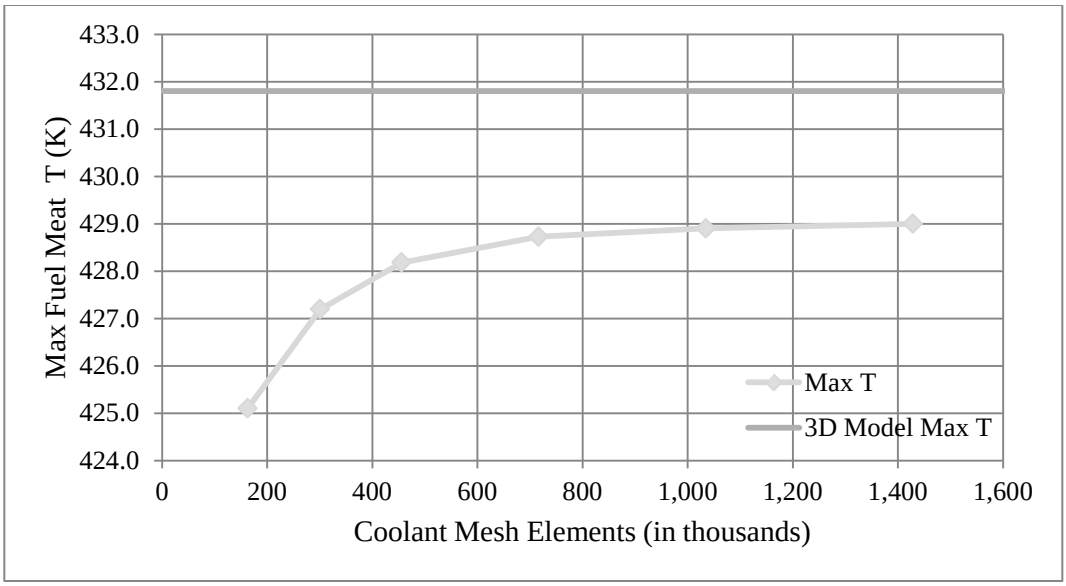

Fig. 5.36. Coupled model coolant mesh convergence—max fuel meat temperature. The 3D model's maximum fuel meat temperature is marked with a red line to demonstrate the offset between the two models' converged states.

The coolant mesh convergence study shows not only good convergence but also that the model is converging to a state very similar to that of the converged 3D model. The converged temperature is only 2.8 K below that of the 3D model. With the goal of balancing the efficiency and accuracy of the model, a total error of $e_g \approx 5\%$ was chosen as an acceptable margin. Given the relative difficulty of modeling the RANS equations in the coolant versus modeling heat transfer in the fuel plate, the majority of this error should be expected to come from the coolant. Thus mesh c3 was chosen as the ideal coolant mesh resolution. With only 456,000 mesh elements it has one-third the number of mesh elements as the "converged" mesh. Even still it has an energy balance error of only 3% and its maximum fuel meat temperature is still within 1 K of the converged value.

With the coolant mesh held constant at mesh c3, a mesh convergence study was then performed on the fuel plate domain. All meshes considered utilized quadratic basis functions. The results of the fuel plate mesh convergence study are shown in Table 5.9.. The data in columns six, eight, and nine are plotted in Figs. 5.37, 5.38, and 5.39, respectively.

Table 5.9. Coupled model fuel plate domain mesh convergence study

Mesh	Fuel plate mesh elements (in thousands)	$E'_{p,gen}$	$E'_{p,out}$	$\Delta H'_c$	e_p (%)	e_c (%)	e_g (%)	Max fuel meat t (K)
p1	24	1.0000	1.0036	0.9665	0.356	3.689	3.346	426.9
p2	35	1.0000	1.0003	0.9676	0.033	3.269	3.237	427.6
p3	51	1.0000	1.0002	0.9681	0.020	3.209	3.190	427.9
p4	84	1.0000	1.0002	0.9682	0.016	3.195	3.180	428.2
p5	110	1.0000	1.0001	0.9683	0.009	3.177	3.168	428.1
p6 (c3)	454	1.0000	1.0001	0.9686	0.008	3.146	3.138	428.2

*Coolant channel domain mesh elements (in thousands) = 456
**Residual tolerance = 1.00×10^{-2}

The convergence data for the fuel plate mesh study does not follow the same orderly exponential convergence rate that the coolant mesh study did. In looking at the fuel plate error for cases p6 and p5 it is apparent that the study reaches machine accuracy prior to case p6. The difference in solution in case p6 is attributable only to round-off error.

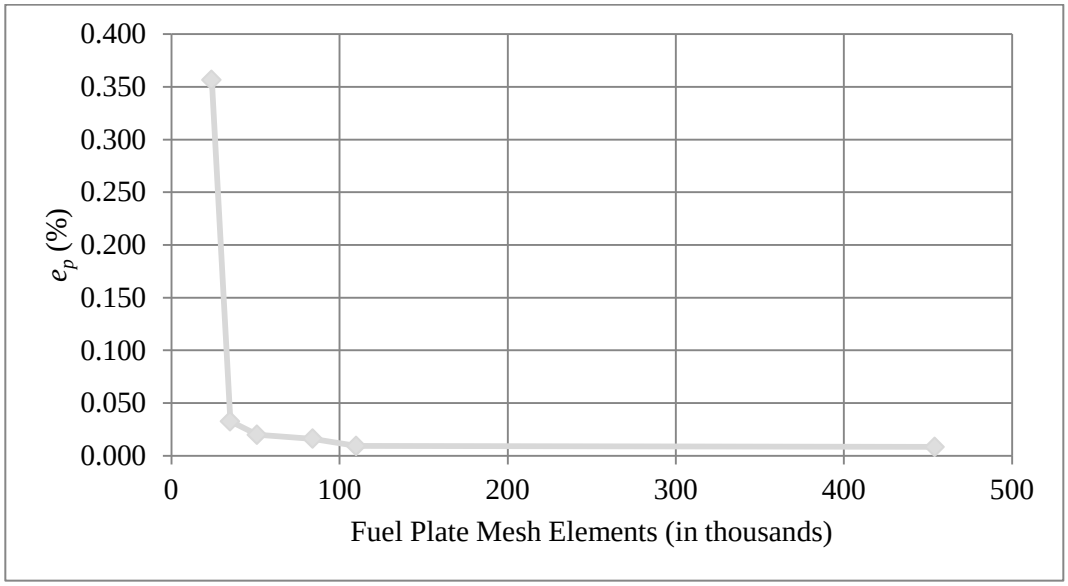

Fig. 5.37. Coupled Model Fuel Plate Mesh Convergence—Fuel Plate Error.

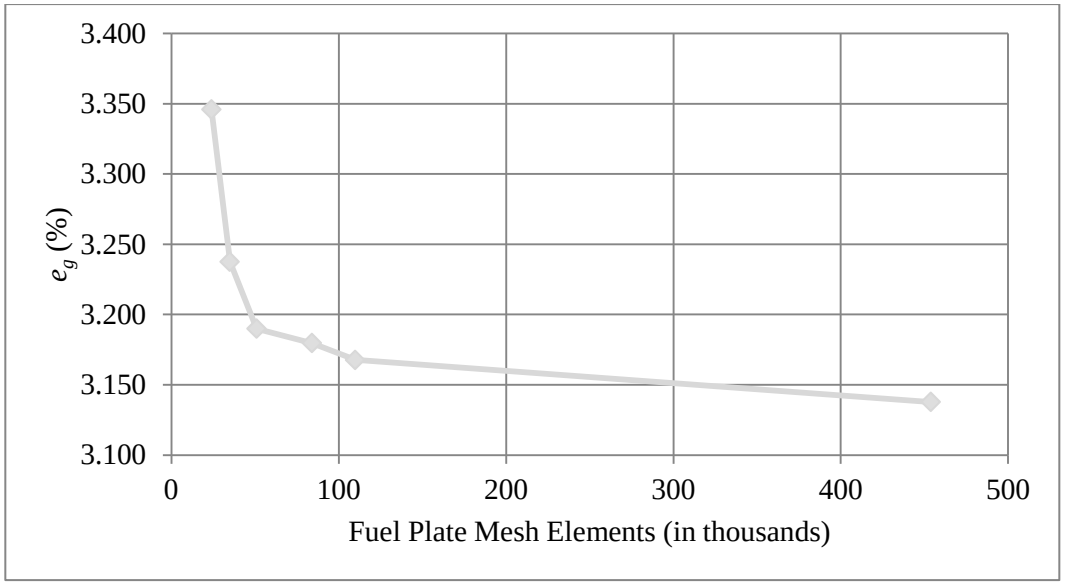

Fig.5.38. Coupled model fuel plate mesh convergence—global error.

The fuel plate domain stays in a near-constant state, at least from the perspective of the energy balance, from mesh p2 to mesh p6. It is only once the mesh count passes below 35,000 that the local fuel plate error, e_p, begins to increase drastically. Even then, "drastically" amounts to a 0.3% increase in local error. The local energy balance data would indicate that the mesh convergence study was focused on over-refined meshes in which increases to mesh resolution do not yield commensurate increases in solution

quality. Mesh p1 is rapidly approaching the coarsest possible mesh. As shown in Fig. 5.40, mesh p1 already spans the width of the fuel meat with only two mesh elements and, in some places, the surrounding fuel plate with only one. Further mesh reduction could be achieved only by decreasing the mesh resolution along the span of the plate.

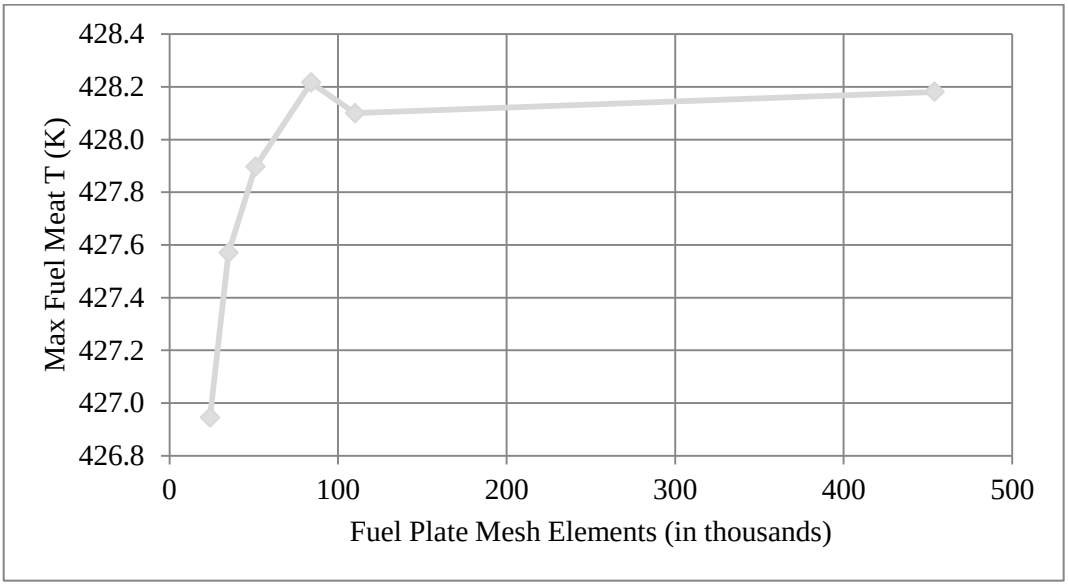

Fig.5.39. Coupled model fuel plate mesh convergence—max fuel meat temperature.

The global error data suggests that further mesh reduction is unnecessary. Its convergence shows a steady increase on return with decreasing mesh resolution throughout the study. The same is true of the maximum fuel meat temperature data which increases rapidly between meshes p1 and p4 before leveling out. In analyzing the global error for the fuel plate mesh convergence study it is apparent that the imposed 5% limit was never reached. The maximum fuel meat temperature becomes the limiting factor instead due its higher sensitivity to fuel plate mesh resolution. An ad hoc temperature "error" can be formulated using the maximum fuel meat temperature from mesh d2 as the ideal. This difference, e_T, is given by

$$\%e_T = \left| \frac{T_{\max} - T_{\max,d2}}{T_{\max,d3} - 273.15} \right| \times 100\% \quad \text{. .....(5.62)}$$

where all temperature values are in Kelvin. Note that the temperature "error" value is not a true error as the reference value, $T_{\max, d2}$, is not known to be correct. It is merely a reference value with which to compare deviations in subsequent model variants. The plot of temperature error is shown in Fig. 5.41.

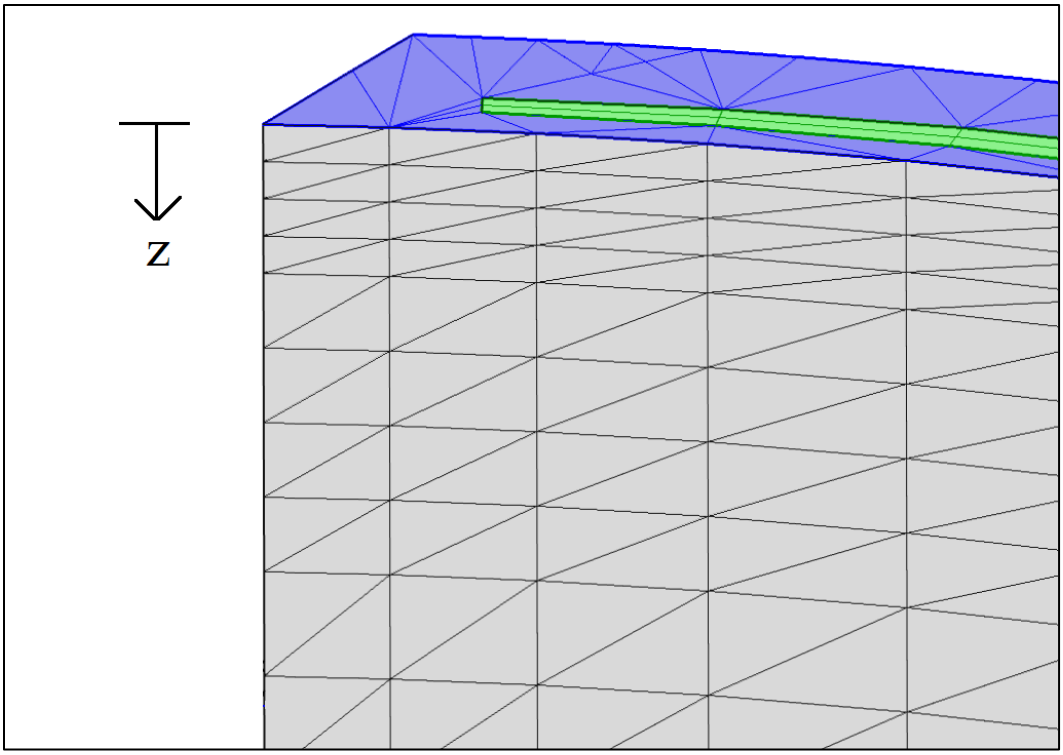

Fig. 5.40. Coupled model fuel plate mesh p1. Fuel plate *s-t* face is highlighted in blue, fuel meat face in green.

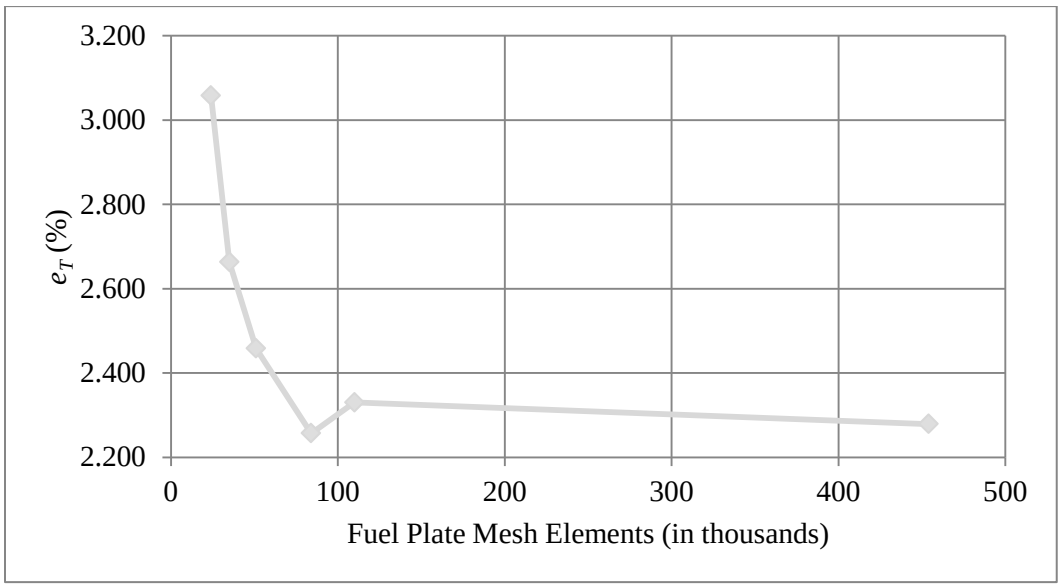

Fig. 5.41. Coupled model fuel plate mesh convergence—max fuel meat t error.

Mesh p3, with a maximum temperature of 427.9 K and a temperature error of 2.46%, was chosen as the ideal mesh. With ideal meshes selected for each domain and associated solution characteristics with which to evaluate alterations to the configuration, attention was turned once again to the coolant domain. Rather than seeking to alter the solution through either mesh reduction or refinement, simplifying mesh

alternatives were sought that affected the solution as little as possible. Such meshes were variants of the constant-width extruded mesh detailed in Section 5.2.

The results of the alternate coolant mesh study are shown in Table 5.10. The constant-width mesh distributions, meshes alt1-alt6, showed promising results. Meshes of this type with sufficient axial distributions allowed the overall number of mesh elements in the coolant to be greatly decreased without a serious effect on the solution. Mesh alt7 was included only to show that with sufficient mesh resolution the constant-width structured meshes converged to a sufficiently small global error. Interestingly, the 2X MCNP distribution, mesh alt9, failed to produce good results. The reason for this is unclear. Its use in the 3D model, as well as the fuel plate domain of the coupled model, has no ill effect on the solution. Its use in the coupled coolant domain, however, causes the model to converge to a much hotter state. The data for meshes alt1-alt6 from columns 8 and 9 are plotted in Figs. 5.42 and 5.43, respectively. Mesh alt7 was excluded because it skewed the scale of the convergence plots, making the inter-mesh behavior between coarser meshes harder to analyze. Reference quantities for meshes p3 and d2 are included where appropriate.

Table 5.10. Coupled model alternate coolant mesh study

Mesh	Coolant mesh elements (in thousands)	Structured mesh?	Axial mesh distr	$E'_{p,out}$	$\Delta H'_c$	e_c (%)	e_g (%)	Max fuel meat T (K)
alt1	12	Y	*l*/50	1.0002	1.0253	2.512	2.533	429.3
alt2	15	Y	*l*/100	1.0002	1.0351	3.488	3.509	429.6
alt3	21	Y	*l*/200	1.0002	1.0392	3.904	3.925	429.7
alt4	28	Y	*l*/300	1.0002	1.0389	3.870	3.890	429.7
alt5	46	Y	*l*/600	1.0002	1.0374	3.718	3.739	429.7
alt6	71	Y	*l*/1000	1.0002	1.0341	3.385	3.406	429.6
alt7	319	Y	*l*/5000	1.0002	1.0111	1.086	1.106	429.1
alt8 (p3)	456	N	N/A	1.0002	0.9681	3.209	3.190	427.9
alt9	14	Y	2X MCNP	1.0002	1.5189	51.860	51.891	442.8

*Constant-width axial mesh distributions are given as functions of plate length, *l*, divided by number of axial elements.
**Fuel plate domain mesh elements (in thousands) = 454
***Residual tolerance = 1.00×10^{-2}

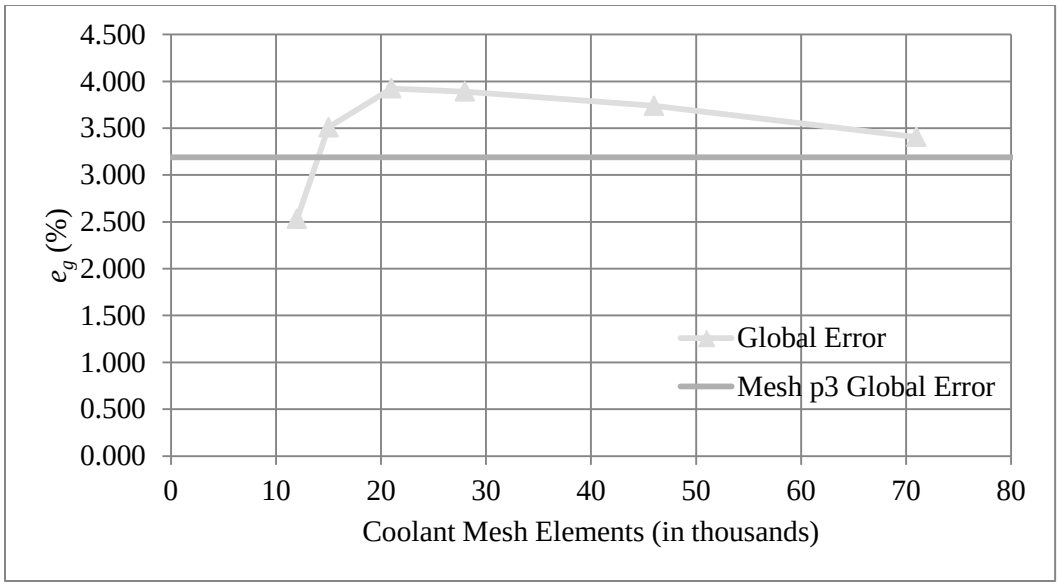

Fig. 5.42. Coupled model alternate coolant mesh study—global error.

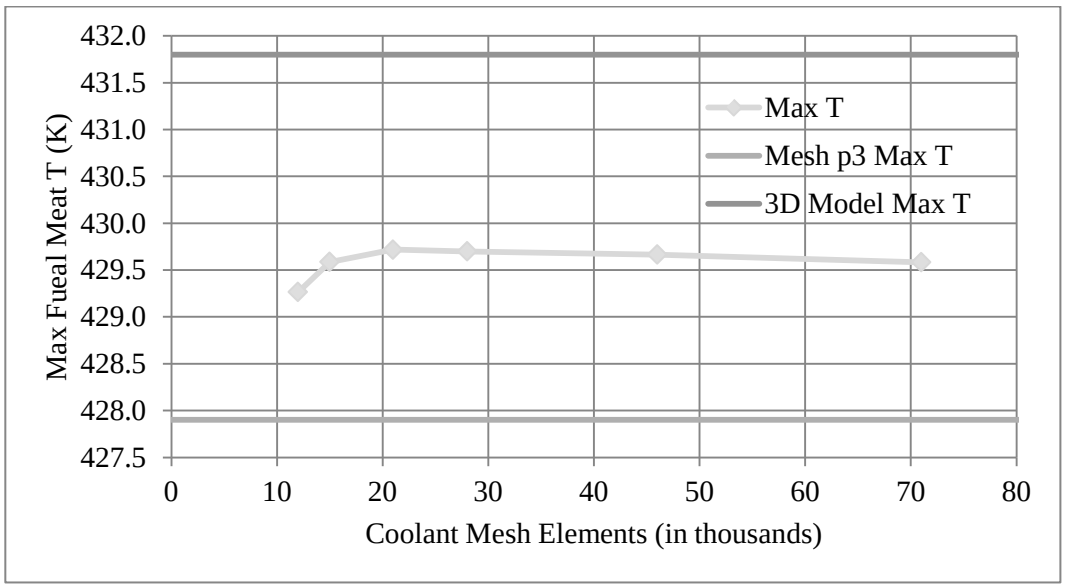

Fig. 5.43. Coupled model alternate coolant mesh study—max fuel meat T.

The fuel plate error, e_p, is constant at 0.02% for each case and was thus not plotted. The coolant error, e_c, is offset from the global error by this amount making the two nearly identical. From the temperature plot it is clear that the alternate coolant mesh variant of the coupled model is converging to a state somewhere between the 3D model and the initial converged coupled model. In both plots it is clear that meshes alt3 through alt6 show solid convergence while meshes alt1 and alt2 begin to diverge significantly with decreases to mesh resolution. The fact that these coarse meshes momentarily reproduce a model state close to the converged state is not to be taken as a positive attribute but merely a coincidence that rather than continuing to diverge upwards they change direction and diverge towards a lower energy state. Interestingly, meshes alt3 through alt6 are approach a converged state from higher energy states. The opposite was true with the original unstructured coolant mesh in which both temperature and coolant

channel enthalpy change approached their respective values from below. This behavior, coupled with the fact that the alternate coolant mesh model is converging towards a higher state than the original model, reintroduces a small measure of conservatism into the model that was removed, dually, by the smoothing effects of the coolant channel dimensional reduction and the convergence characteristics of the original coupled model.

In looking at the global energy balance errors it is clear that mesh alt3 is the coarsest alternate coolant mesh to sufficiently approximate the original converged solution. The fact that its maximum temperature is also closest to the 3D model's maximum temperature, while appealing, is really arbitrary in this instance. The only meaningful comparison is to the alternate model's converged temperature which mesh alt3 does a sufficient job of approximating.

One final tweak is made to this model. The alternate mesh study was performed using constant-width cells throughout the length of the fuel plate section of the channel. While this facilitated a faster mesh study it also created a large mesh size disparity on the mesh boundary separating the structured mesh from the unstructured mesh upstream and downstream of the fuel plate. In order to smooth over this transition, the first and last structured mesh elements in mesh alt3 were replaced with successively smaller transition mesh elements as shown in Fig. 5.44. This has a minimal, yet positive, effect on the solution as shown in Table 5.11.

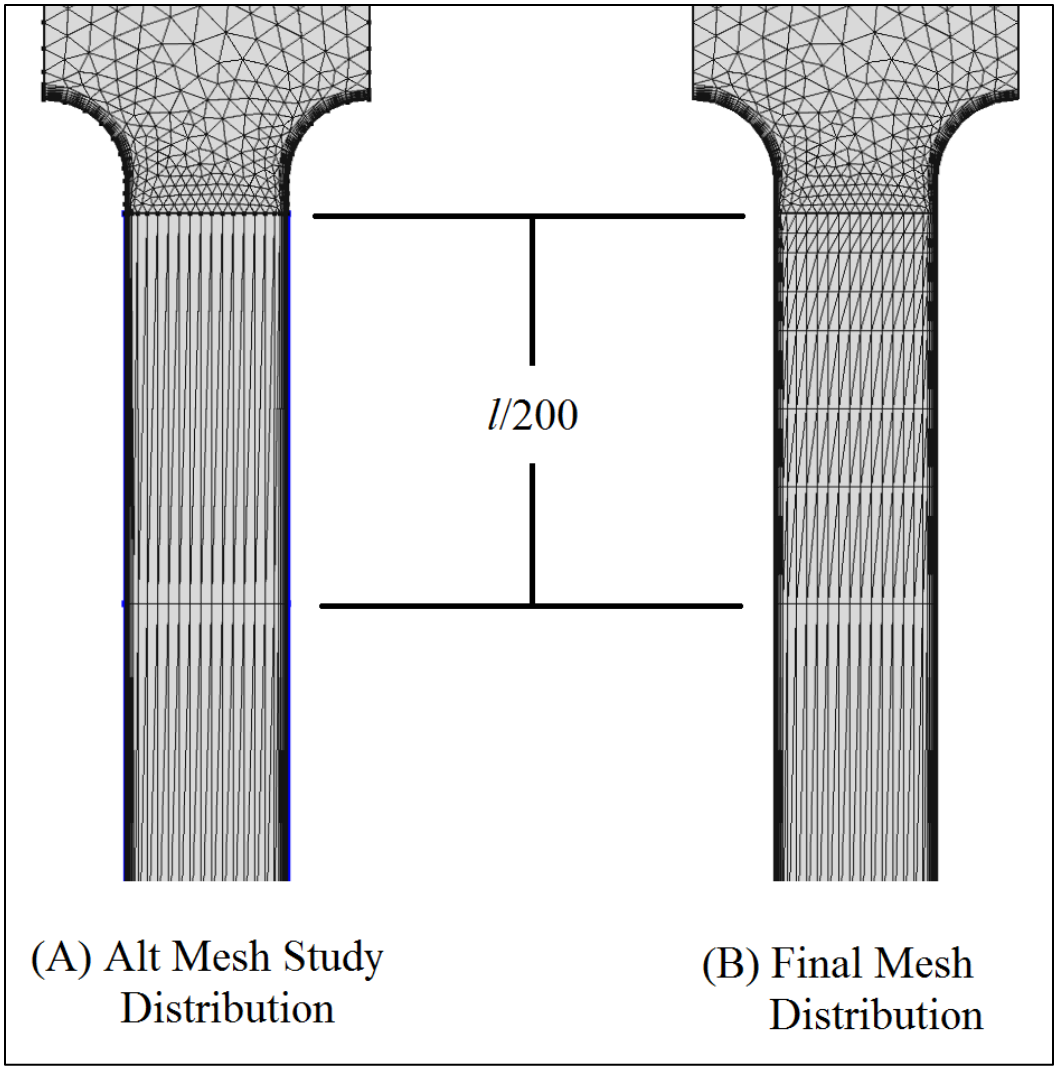

Fig. 5.44. Mesh alt3 distribution comparison.

Table 5.11. Mesh alt3 comparison solutions

Mesh	Coolant mesh elements (in thousands)	Structured mesh?	Axial mesh distribution	$E'_{p,out}$	$\Delta H'_c$	e_c (%)	e_g (%)	Max fuel meat T [K]
alt3	21	Y	*l*/200	1.0002	1.0392	3.904	3.925	429.7
alt3b	22	Y	~*l*/200	1.0002	1.0358	3.557	3.577	429.6

5.5.4 Validation of Simplifying Coupled Model Assumptions

As mentioned previously, the exclusion of the side plates from the coupled model is due in large part to their incompatibility with the 2D coolant domain. Their exclusion is justified by results from the 3D model which show that heat flow into the side plates is minimal compared to that in the fuel plate and coolant channel. Local heat flux into the inner side plate is shown in Fig. 5.45. Across the boundary with the fuel plate heat flow is predominantly into the side plate. Across the boundary with the coolant channel heat flow is predominantly outward. A surface integral of heat flux through the fuel plate boundary shows that the total inward heat flow is only 578 W. The total outward heat flow through the

coolant common boundary is only 227 W. Both of these are three orders of magnitude smaller than the total nuclear heat generation production. It is worth noting that replacing the thermally insulated boundary on the outer walls of the side plates in the 3D model would most likely increase these heat flow values significantly. Since this was not accounted for in the 3D model, however, the effect on the solution from removing them in the coupled model is minimal

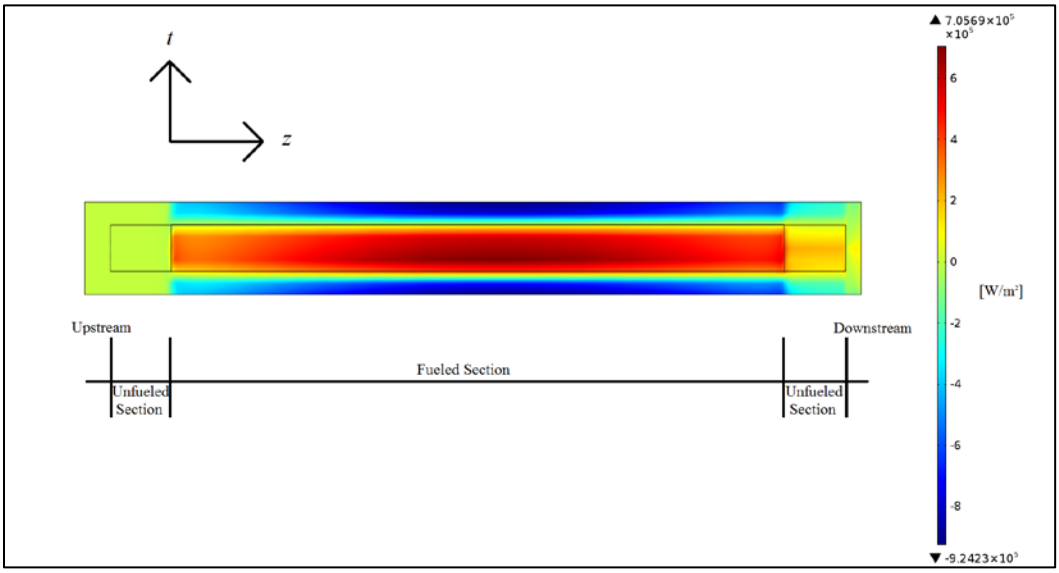

Fig. 5.45. 3D model inner side plate inward heat flux. Figure is not to scale. The *t*-direction has been stretched by a factor of 20 for ease of viewing. The fuel plate is outlined in three parts with the coolant channel surrounding it.

Additional simplifications can be made to the coupled model through observation of preliminary solutions to the model itself. The use of a single bulk velocity value along the length of the plate is validated by the short length of the hydrodynamic entrance region, as shown in Fig. 5.46. For reference, the leading edge of the fuel plate is situated at -5.08 cm. Within 2 cm, and still well before the top of the fuel section, the flow is fully developed. Similarly, the onset of turbulence is extremely rapid as shown in Fig. 5.47, validating both the assumption of turbulent flow throughout as well as verifying that the model remains within the limits of the modified Hausen correlation as experimentally verified by Gambill and Bundy. The thermal entrance region, shown in in Fig. 5.48, is also extremely short. The onset of thermally developed flow is delayed until just upstream of the fueled section. This gives the flow adequate space to become both fully developed and fully turbulent before interacting significantly with the fuel. The distance from onset to fully developed thermal flow occurs in less than 4 cm.

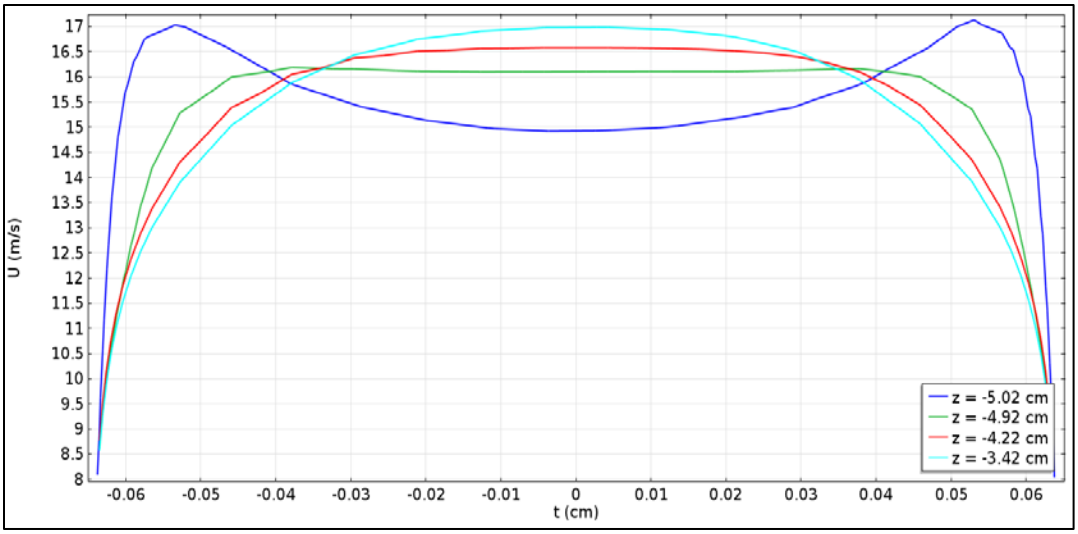

Fig. 5.46. Coupled model hydrodynamic entrance region velocity profiles.

Performing a surface integral of heat flux on the leading and trailing edge surfaces shows the total heat flow through each to be less than 1 W. This is a completely trivial quantity with respect to the magnitude of the nuclear heat generation. The coupling mechanisms attached to these surfaces can therefore be removed without affecting any noticeable change in the model's solution. With the coupling boundaries dropped, both surfaces—in both domains—are treated as insulated boundaries. Although a trivial quantity compared to the millions of degrees of freedom in the model, this allows a few hundred unnecessary coupling variables to be removed from the model. The greatest gain is in the increased simplicity of the coupling mechanism which is now active only on axial faces.

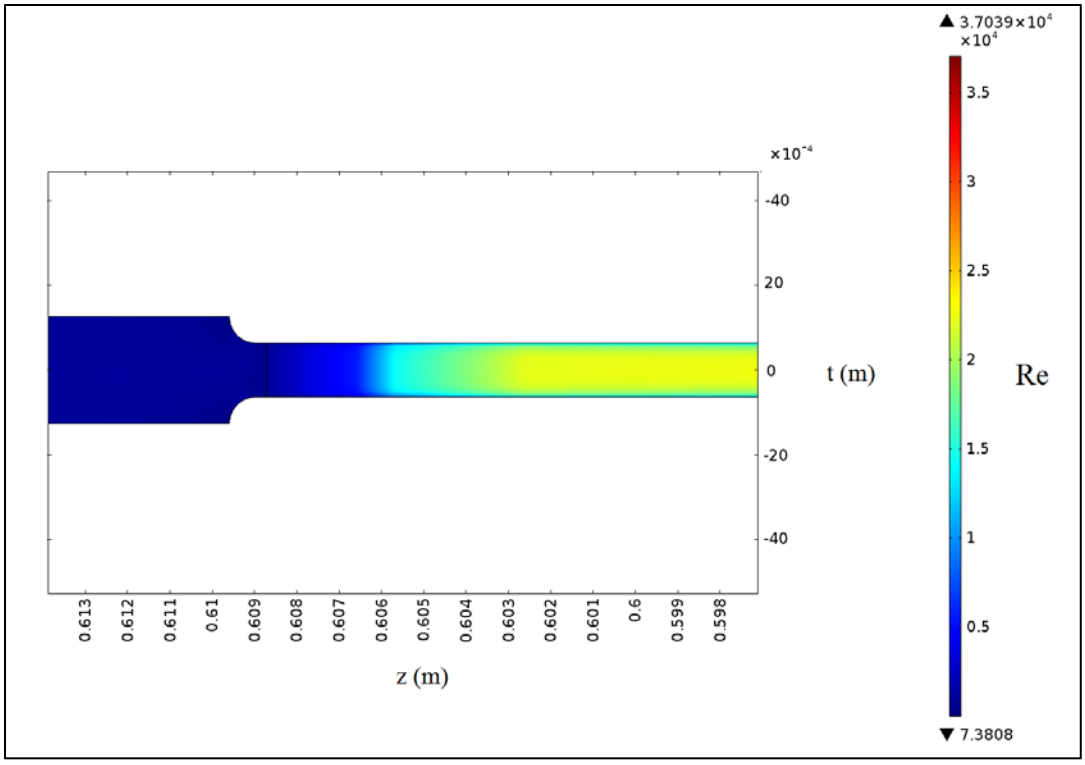

Fig. 5.47. Coupled model entrance region Reynolds number profile.

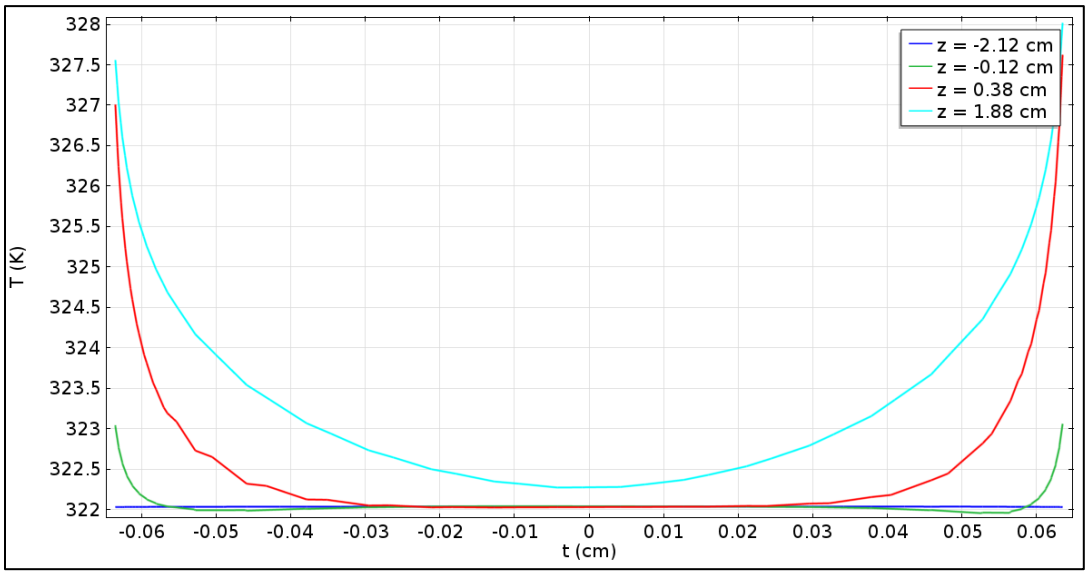

Fig.5.48. Coupled model thermal entrance region temperature profiles.

5.5.5 Paneling

The concept of paneling was first tested using a conceptual model. This model substituted the high-aspect ratio fuel plate with a simple block with two opposing faces cut in half and coupled to 2D coolant channel slices. Heat flow was triggered in the system by a specified midplane temperature profile. The interactions of the conceptual model are shown in Fig. 5.49.

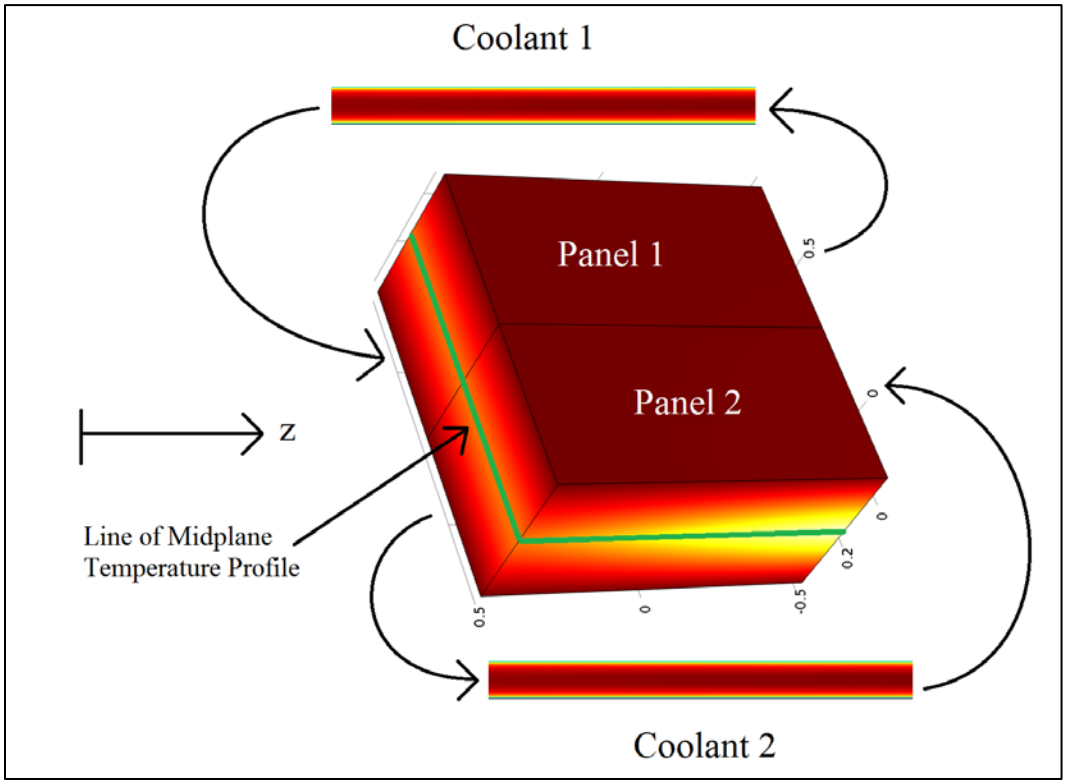

Fig. 5.49. Conceptual paneling model diagram.

The model performed exceedingly well, providing validation for the paneling concept. The bifurcated bulk temperature profile that the model yielded, as projected onto the panels themselves, is shown in Fig. 5.50. The gain of the model was that instead of imposing a single bulk temperature across the span of the heated body, a two-part discontinuous temperature profile could be imposed. Despite the discontinuity in the bulk temperature profile the conceptual model produced a smooth surface temperature, as shown in Fig. 5.51. The imposed midplane temperature profile is included for reference.

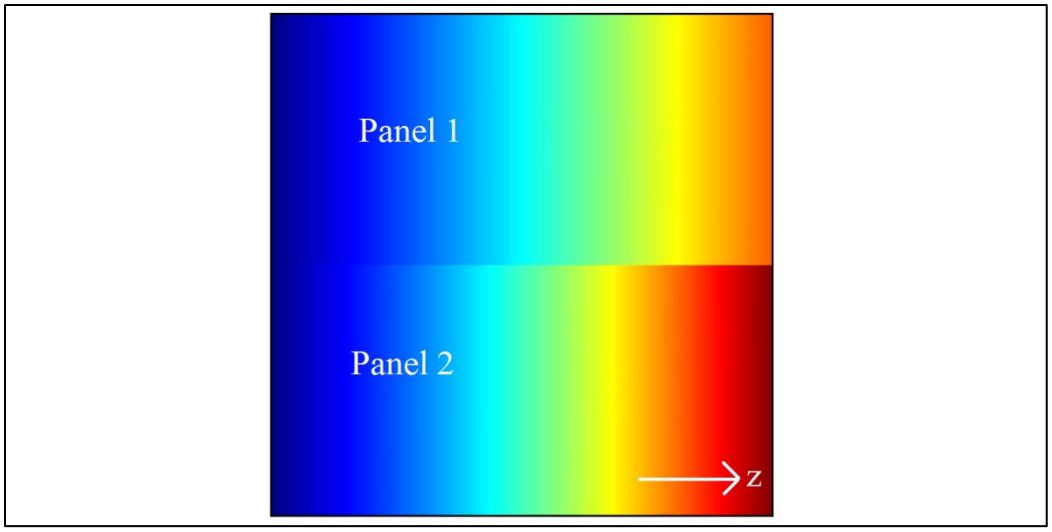

Fig. 5.50. Conceptual paneling model bulk temperature projections.

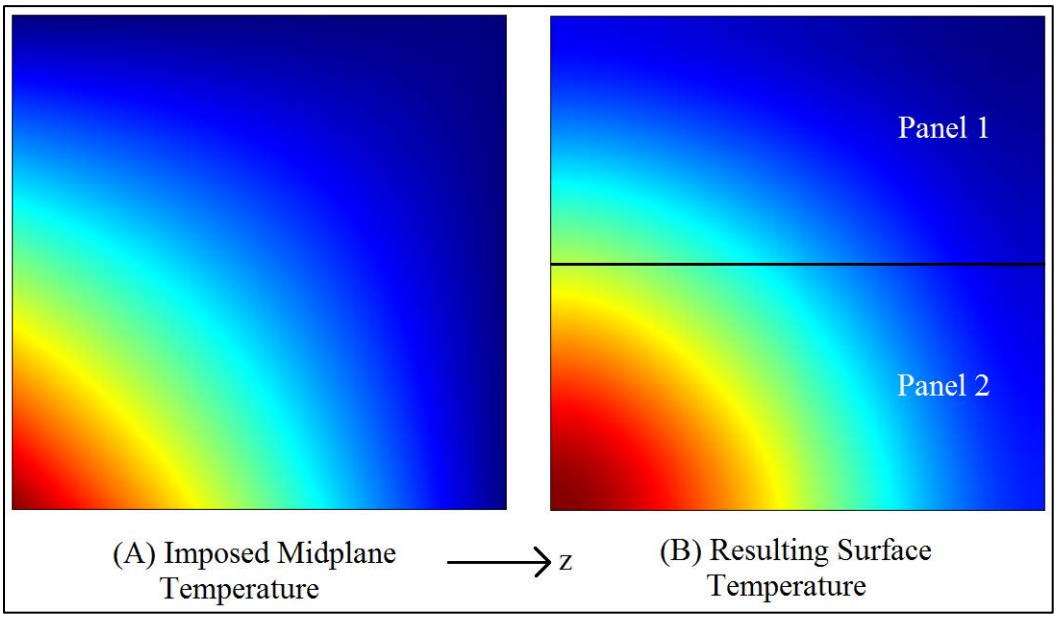

Fig. 5.51. Conceptual paneling model surface and midplane temperature profiles. Temperature profiles are not on the same color scale. They are merely intended to provide a qualitative comparison.

The paneling concept failed to transition successfully to the coupled model. The issue arises from the high aspect ratio of the fuel plate. The coolant creates a path of least resistance, so to speak, for heat flowing out of the fuel meat. Given the extremely short distance between the two, compared to both the length and the span of the fuel plate, heat flow occurs almost exclusively in the *t*-direction, parallel to the normal of the fuel plate's surface. Any diffusion occurring within the fuel plate in the *s*- or *z*-directions is miniscule in comparison. As a result, the surface temperature profile that this yields contains an artifact of the bifurcated bulk temperature profile. This surface temperature profile is shown in Fig. 5.52. There is a "kink" visible running down the axial midline of the temperature profile. It is likely that with an increasing number of panels the severity of the kinks between each would decrease. Eventually they would decrease to the point that they became trivial. The requisite number of panels would likely over-

encumber the model, however, and negate the benefit of its lowered computational expense. As such, the paneling concept was not pursued further, it being deemed incompatible with the fuel plate geometry.

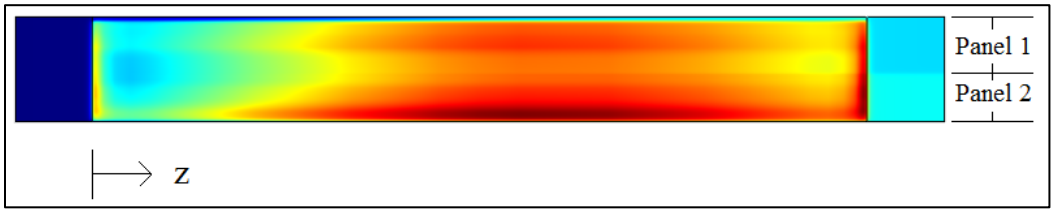

Fig. 5.52. Coupled paneled model concave fuel plate surface temperature profile.

5.5.6 Model Comparisons

Solution comparisons in the fuel plate are relatively straightforward given that the geometry itself is identical in both models. Coolant channel comparison are more difficult due to the dimensional disparity between the two models. While comparing profiles of surface variables provides the most information about the state of a given solution, it is less useful for quantifying differences between solutions. Consider, for example, Fig. 5.53 in which the temperature profile on the concave surface of the fuel meat in each model is shown. The surface profile comparison readily conveys the similarity in solution between the two models, showing similarly topographies and corresponding hot and cold patches. It does provide a clear understanding of the difference in magnitude between the solutions at any given point, however.

For this purpose, consider the 1D temperature data from Axial Lines 1 and 2 plotted in Fig. 5.54. Axial Lines 1 and 2 were placed such that they ran through sections of relatively high and low temperature, respectively. As was expected for the coupled model, in areas of higher temperature, Axial Line 1, the difference in observed temperatures between models is greatest. In areas of mid to lower temperature, Axial Line 2, the observed temperatures are in much closer agreement. This is a combination of the smoothing effect of the bulk coolant slice used in the coupled model which affects local minima and maxima as well as the sacrifice to accuracy made for the sake of computational cost associated with the final coupled model which lowers the temperature of the entire model by a few Kelvin.

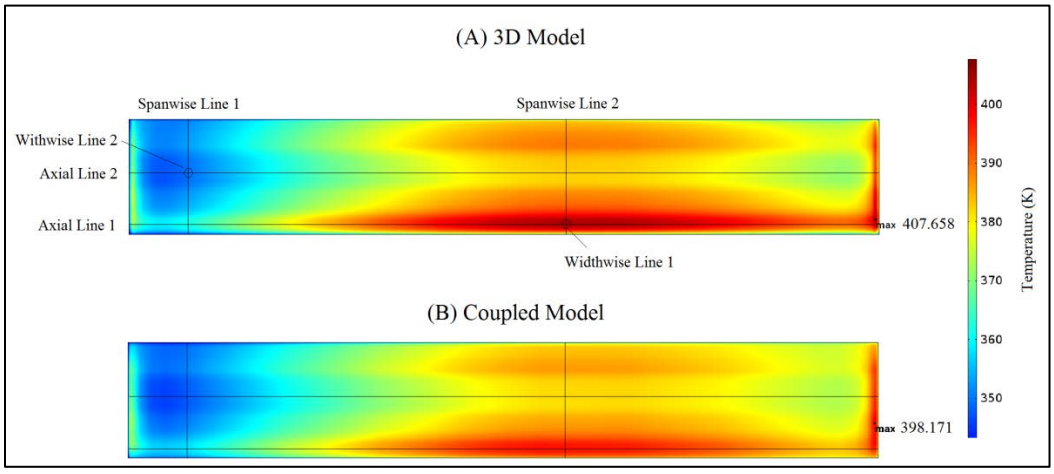

Fig.5.53. Fuel meat concave surface temperature profile comparison.

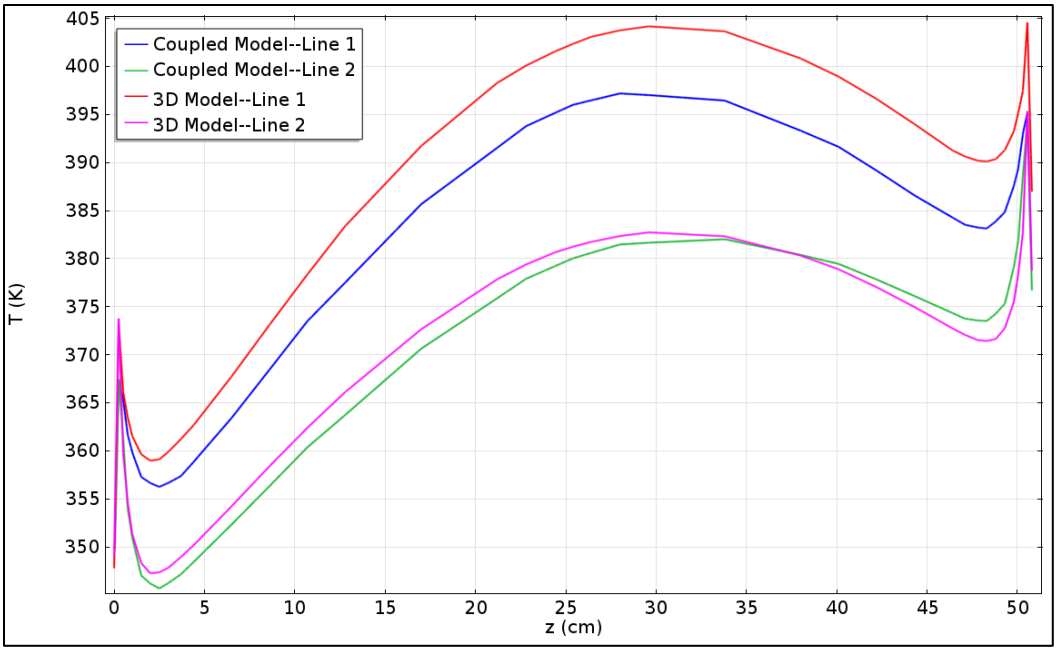

Fig. 5.54. Fuel meat concave surface axial 1D temperature profiles.

The 1D temperature comparison does a much better job of quantifying the difference between the two solutions than the 2D comparison does. The trade off with the 1D comparison is that it conveys much less information than the surface comparison, the former having one fewer dimension than the latter. For this reason, model comparisons, where appropriate, will be presented in two parts: one part to provide a qualitative comparison between models and another to quantify the difference between them.

The same quantitative comparison can be made in the spanwise direction using temperature data from Spanwise Lines 1 and 2, as shown in Fig. 5.55. Again, the hotter of the two lines, Spanwise Line 2, shows the greatest temperature disparity between the two models. In Spanwise Line 2's temperature profiles alone the effect that higher temperature has on differences between the models is also apparent. It is at the profile's lowest point, ignoring its outer edges, in which the two profiles are in the closest agreement. Performing a temperature average along Spanwise Line 2 in the coupled model shows that the average temperature is 385.8 K which is very close to the region in which the profiles are in the closest agreement.

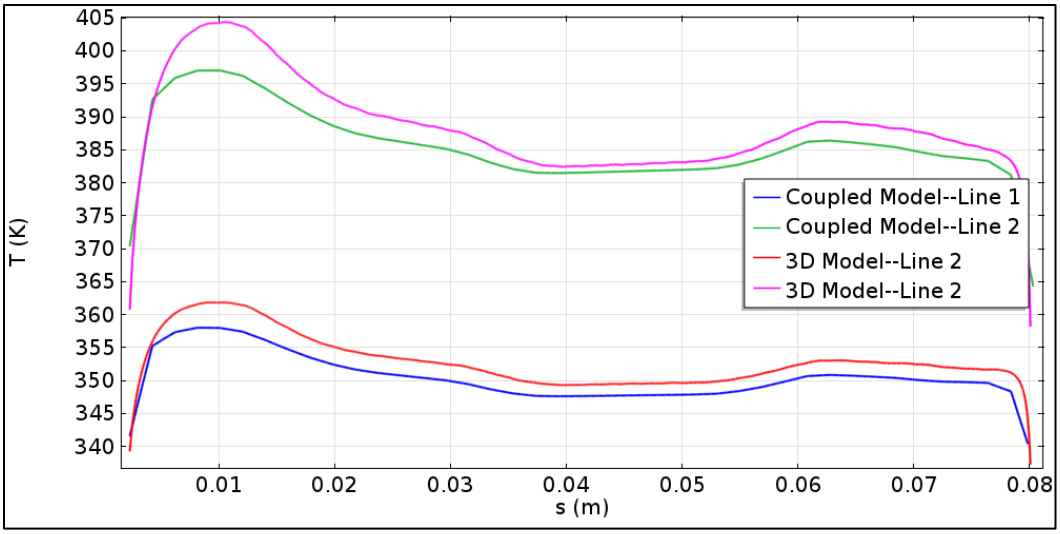

Fig. 5.55. Fuel meat concave surface spanwise 1D temperature profiles.

Looking at a cross-sectional plane cut through the entire model along Spanwise Line 2, a topographical comparison can be made in the *s-t* plane as well. This comparison is shown in Fig. 5.56. Both models show the same general topography with the coupled model showing slightly higher temperatures along the inner side plate border at top left than the 3D model. This is likely due to the fact that local fuel plate temperatures fall below the spanwise average in this area and the bulk coolant is thus higher than it should be. A small part of it could also be the removal of the side plate. A more direct comparison can be made between the models by looking at the 1D temperature profiles along Widthwise Line 1 drawn on both plots. Temperature data is plotted along Widthwise Line 1 in Fig. 5.57. The widthwise line corresponds roughly to the intersection of Axial Line 1 and Spanwise Line 2 in Fig .5.53 and serves as a high temperature comparison. A low temperature comparison is made with Widthwise Line 2 near the intersection of Axial Line 2 and Spanwise Line 1, as shown in Fig. 5.58. As with the 1D axial and spanwise temperature comparisons, the higher the local temperature the greater the temperature disparity between the two models. In the cold widthwise comparison the coolant temperatures are nearly aligned.

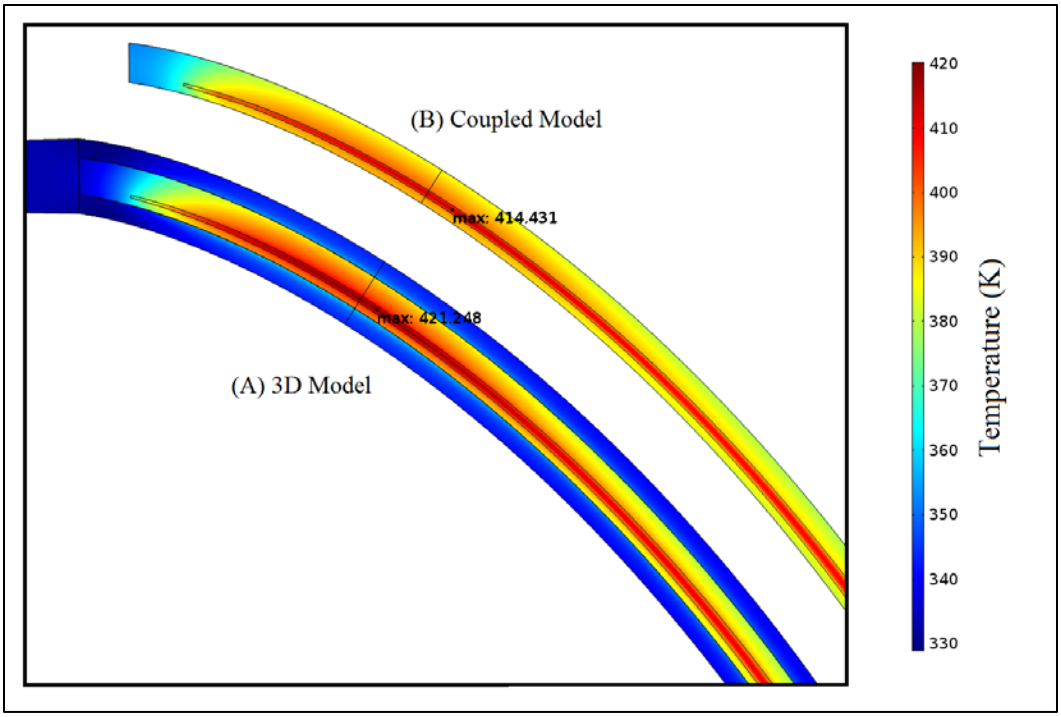

Fig. 5.56. Cross-Sectional Cut-Out Temperature Profile Comparison. The 3D model cross-section is shown with all geometry elements present including the fuel meat, fuel plate, coolant channels, and inner side plate. Given the dimensional disparity across the coupling interface in the coupled model, only the fuel meat and fuel plate are shown.

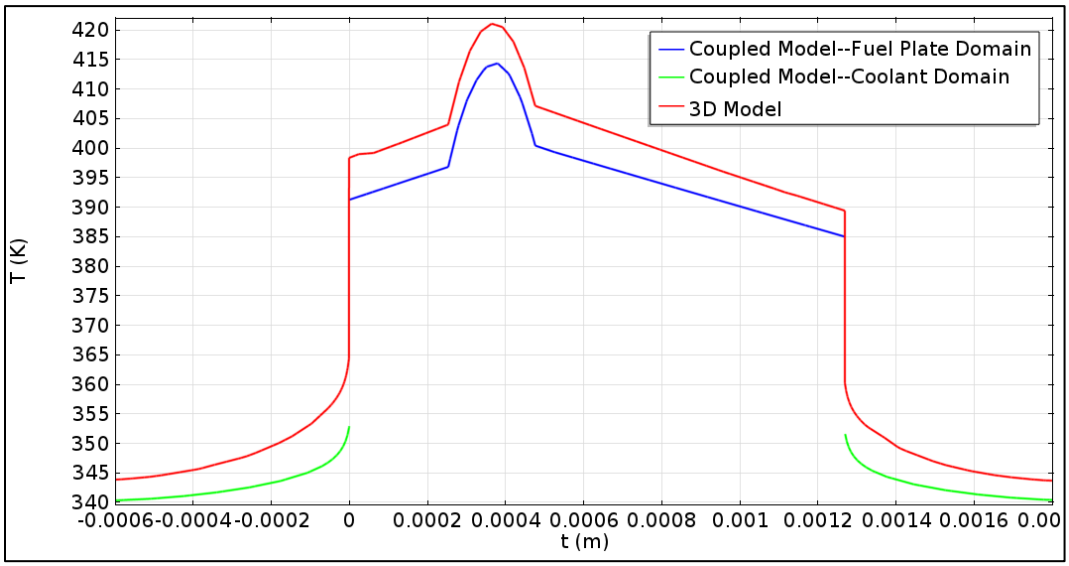

Fig. 5.57. Cross-Sectional cut-out widthwise line 1 1D Temperature profiles. While the 3D profile is plotted as a single entity, the coupling interface in the coupled model necessitates that the fuel plate and coolant temperature profiles be plotted separately.

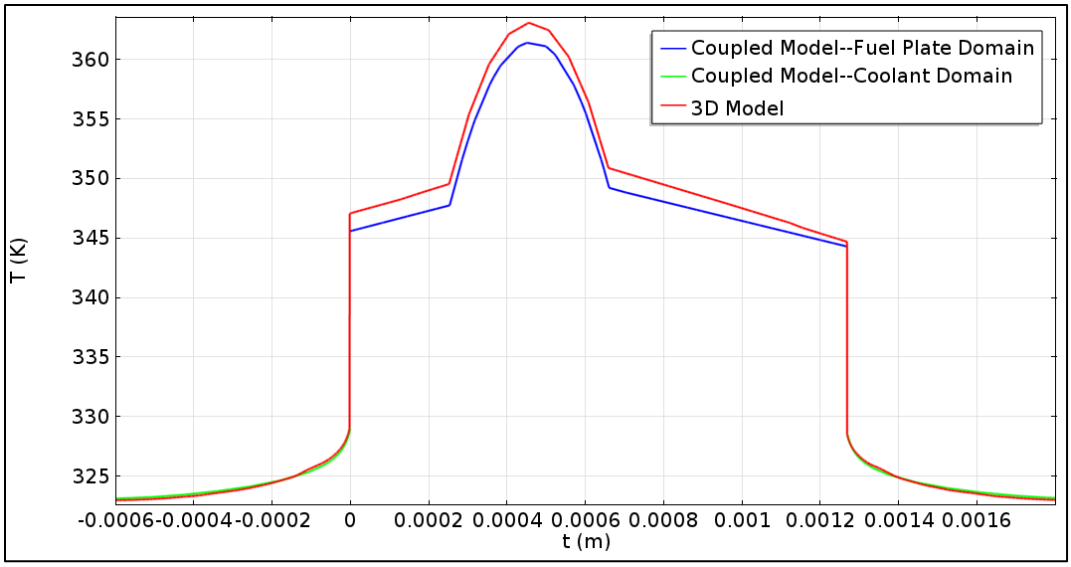

Fig. 5.58. Cross-sectional cut-out widthwise line 2 1D Temperature profiles. While the 3D profile is plotted as a single entity, the coupling interface in the coupled model necessitates that the fuel plate and coolant temperature profiles be plotted separately.

Qualitative comparisons can be made between the coolant channels using a *t*-*z* plane oriented along the same widthwise lines in Fig. 5.56. Given the extremely high aspect ratio of the coolant channel in the *t*-direction, two magnified velocity contours are presented which focus on the leading and trailing edge in Figs. 5.59 and 5.60, respectively. Both models' leading edge velocity contours look very similar from the effects of the mid-plate stagnation point to the rapid of flow acceleration leading from the rounded leading edge to the constant-width fuel plate. The effects of the boundary layer are more pronounced in the 3D model's solution.

The topography at the trailing edge is dominated by "cores" of high- and low-velocity coolant that persist downstream of the coolant channel and the fuel plate, respectively. Both high- and low-velocity cores appear to persist farther downstream in the coupled model than in the 3D model. This is to be expected as the coupled cores can only diffuse in the *t*-direction while the 3D cores experience a lesser diffusion in the *s*-direction as well. When considering these differences, however, it is important to note that the 3D model velocity contour is a local dissection of an explicit coolant channel while the coupled model profile is a homogenization of the entire span of the channel. The difference in exit core lengths could simply be attributed to a variation in upstream fuel plate temperatures.

Both models capture the slight misalignment in coolant channel exit core velocity caused by the nonsymmetric placement of the fuel meat inside the fuel plate. This yields a hot side (the concave side) and a cold side (the convex side). In the velocity profiles the hot side is on the right-hand side of the coolant channel. More energy enters the coolant channel from this, creating a slight non-uniformity in pressure across the width of the channel. At the trailing edge, this non-uniform pressure, higher on the right-hand side, pushes the flow slightly to the left. This non-symmetric pressure profile is shown in Fig. 5.61. In both models, the velocity field reaches a uniform profile well before the outlet, located roughly another 2 cm below the bottom cut-off of the figures, indicating that the exit region is sufficiently long enough to justify the use of a uniform pressure boundary condition.

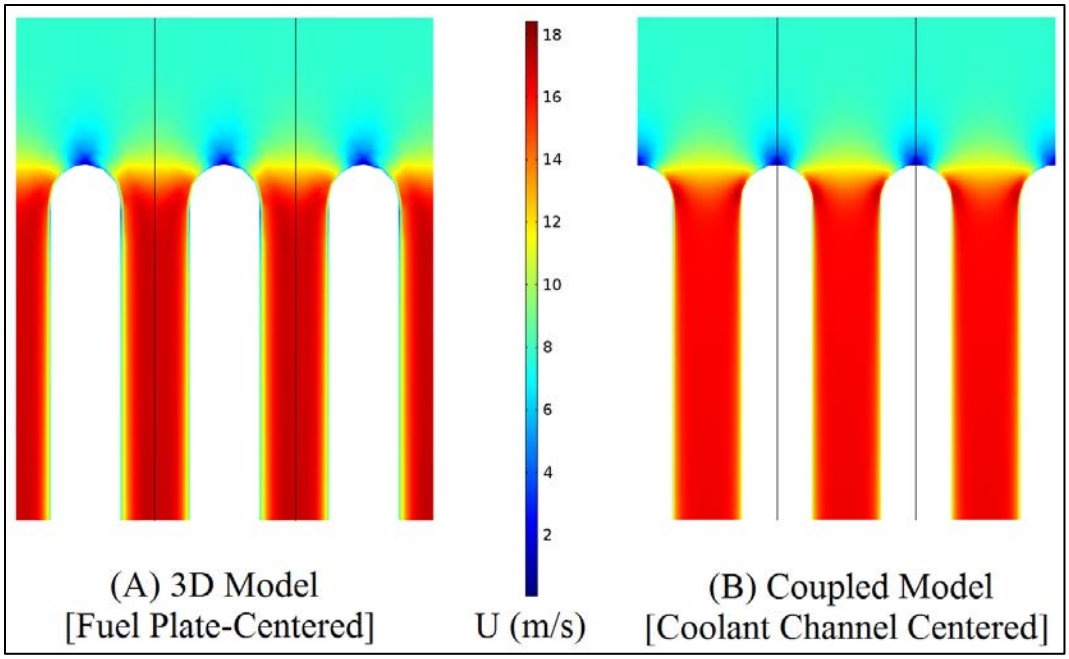

Fig. 5.59. Coolant channel leading edge total velocity contour comparison. Note that the coolant domain in each model consists of only a single channel. Three channels are presented side-by-side in order to better show the profile continuity across the periodic boundaries.

The smoothing effect of the coolant channel slice in the coupled model decreases with increasing distance from the coolant-fuel plate boundary. This diminishing effect with increasing distance can be illustrated by comparing maximum temperature values at varying distance from the coolant-fuel plate boundary. The effect's propagation is shown in Table 5.12. The ad hoc temperature error, e_T, from the coupled model fuel plate mesh convergence study can be reapplied here with the 3D model's temperature at each point serving as the reference value. Not only does the difference in maximum temperature decrease as the points move inward but the percent error decreases as well. The coolant slice's smoothing effect has very nearly worn off by the point it has propagated into the interior of the fuel meat.

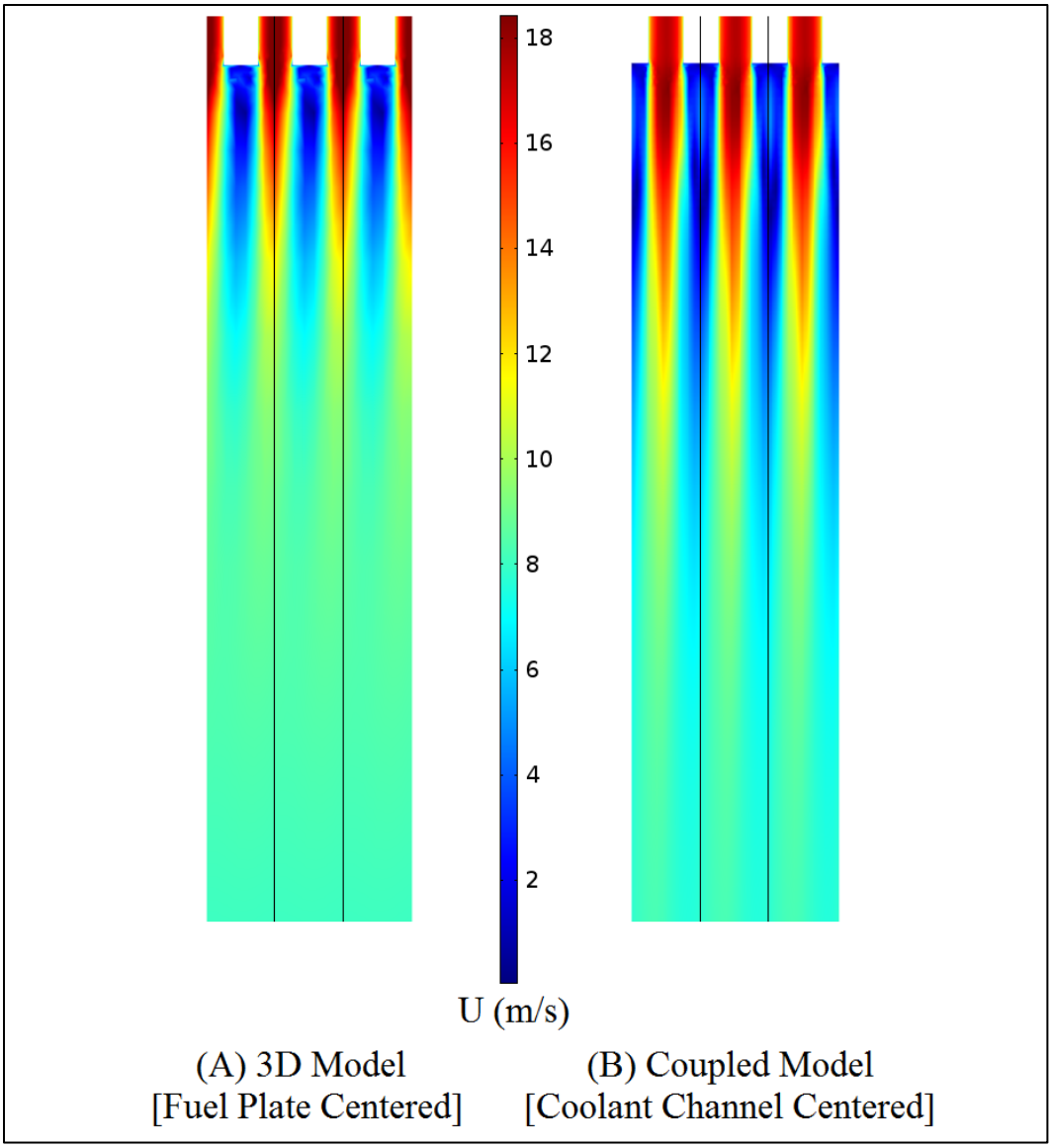

Fig. 5.60. Coolant channel trailing edge total velocity contour comparison. Note that the coolant domain in each model consists of only a single channel. Three channels are presented side-by-side in order to better show the profile continuity across the periodic boundaries.

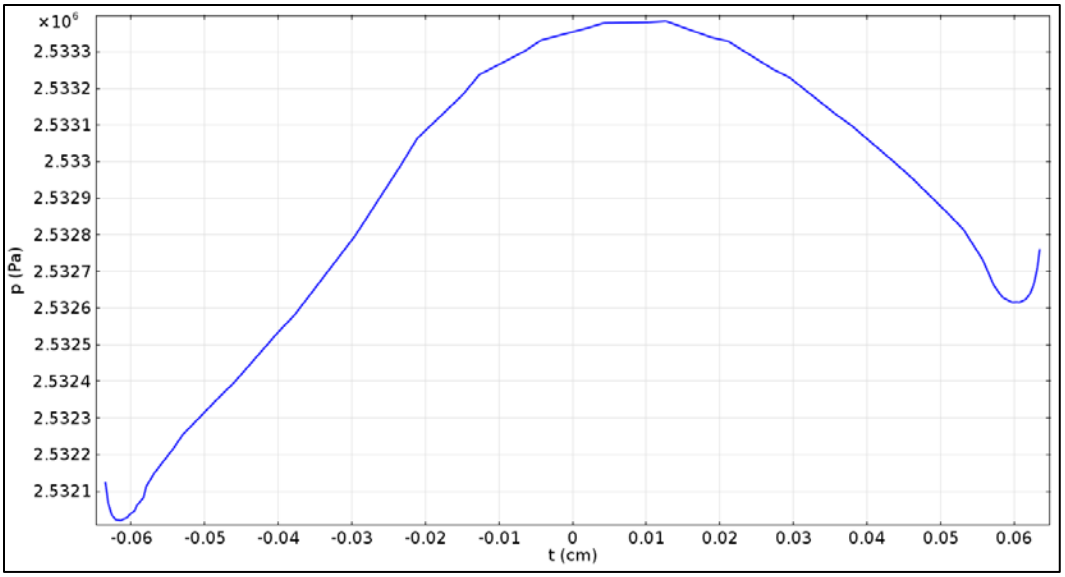

Fig. 5.61. Coupled model non-symmetric trailing edge pressure profile. The trailing edge pressure profile was taken from a widthwise line located at *z* = 55.78 cm, 0.1 cm above the trailing edge itself.

Table 5.12: Propagation of coolant smoothing effect into fuel plate

Domain	Max domain T (K)		ΔT (K)	e_T (%)
	3D	Coupled		
Coolant	375.3	364.6	10.7	10.5
Fuel Plate Surface	403.0	393.7	9.3	7.2
Fuel Meat Surface	409.1	400.7	8.4	6.2
Fuel Meat Internal	431.8	429.6	2.2	1.4

5.5.7 Computational Efficiency

It is indisputable that the coupled model trades a small measure of accuracy for the ability to replicate core conditions much faster and with fewer computational resources. While the former sacrifice is small, the latter gain is considerable. The solution times for both models are given in Table 5.13, along with the computational resources required to obtain the solution. All runs were performed on the computer cluster Betty at ORNL. Eight of the nodes on Betty are reserved for COMSOL use. Each node possesses two AMD Opteron 6128 processors, 16 cores, and 128 GB of RAM. For a small trade in accuracy, the coupled model can be run in ~1/23rd the time of the 3D model using 1/3rd of the computational resources. The true decrease in required computational resources is even greater. A single run of the coupled model requires less than half of the available resources on a single Betty node.

Table 5.13. Coupled vs. 3D speed-up

Model	Computation time (hrs)	Mesh elements (in thousands)	Degrees of freedom (in thousands)	Betty nodes
3D	69	2311	6465	3
Coupled	3	21	288	1

5.5.8 Justification of Selected Residual Tolerance

All solutions presented in this section were performed using a relative residual of $1.00x10^{-2}$ which was deemed sufficient to ensure adequate convergence. To demonstrate this point, the final coupled model was run using a relative residual of $1.00x10^{-5}$. A comparison of the two solutions is shown in Table 5.14. Any change in solution in the fuel plate fails to register with five significant digits. A slight drop in the change in coolant enthalpy is measured by the higher tolerance case but its effect is so minimal that it doesn't register a change in the maximum temperature to four significant digits. The only truly non-trivial effect that increasing the tolerance had was to increase the solution time substantially.

Table 5.14. Relative tolerance

Tolerance	Solution time (hrs)	$E'_{p,out}$	$\Delta H'_c$	e_c (%)	e_g (%)	Max fuel meat T [K]
$1.00x10^{-2}$	3	1.0002	1.0358	3.557	3.577	429.6
$1.00x10^{-5}$	27	1.0002	1.0304	3.011	3.035	429.6

6.0 SUPPORTING DEVELOPMENTS

6.1 MATERIAL PROPERTY LIBRARIES

The LEU Materials library is utilized by the COMSOL users in order to accurately model the properties of the fuel meat. This database, originally compiled by Kirk Lowe, contains all of the relevant thermal-physical properties of the U-10MO fuel. The material properties for the LEU fuel are taken from two sources provided to the HFIR facility from the Reduced Enrichment for Research and Test Reactors (RERTR) website. Because there are two sources released at different times, the newest source[15] takes precedence over the older source[115]. This procedure will be the same for any future updates to the library and the updates should be completed as new data becomes available. The only material property that did not change from the previous material library was the Young's Modulus.

The majority of the U-10MO material properties changed to a curve fit definition. Table 6.1 provides the new values:

Table 6.1. The updated U-10MO materials library values

Property	Equation	Units	Range
Specific Heat, C_p	$\mathbf{0.137} + \left(\mathbf{5.12 \times 10^{-5}}\right) \cdot \boldsymbol{T} + (\mathbf{1.99 \times 10^{-8}}) \cdot \boldsymbol{T^2}$	J g^{-1}°C^{-1}	100 – 1000 ˚C
Thermal Expansion, α	$\mathbf{11.2} + (\mathbf{8.07 \times 10^{-3}}) \cdot \boldsymbol{T}$	X 10^{-6} ˚C^{-1}	100 – 800 ˚C
Density, ρ	$\mathbf{17.15} - (\mathbf{8.63 \times 10^{-4}}) \cdot (\boldsymbol{T} + \mathbf{20})$	g cm^{-3}	20 – 700 ˚C
Thermal Conductivity, k	$\mathbf{10.2} + (\mathbf{3.51 \times 10^{-2}}) \cdot \boldsymbol{T}$	W m^{-1} ˚C^{-1}	20 – 800 ˚C
Elastic Modulus, E	83,000	MPa	Room temp

Of the five properties listed in Table 6.1, only the Elastic Modulus remained unchanged from the previous materials. Note that all curve fitting was done for temperatures given in Celsius, and thus were converted in COMSOL to Kelvin by subtracting 273.15 from the temperature value in COMSOL.

It is also suggested that a new naming scheme should be implemented into the materials library with the phrase "Updated_*date*" included at the end of the file name in order to keep track of the relevance of the material library. A README file has also been created that details the updates made and the references used in the updating process.

In order to verify the new material properties implemented in COMSOL, a test case was created. The test case utilized the Thermal-Stress module of COMOSL and was set up as a 2-D problem. This model consisted of a long, rectangular rod with the LEU fuel properties imposed with aspect ratio of 1:100. The long sides of the rod were set as insulated boundaries which created a 1-D problem. Each smaller side was set to a constant temperature of 20 ◦C and 1200 ◦C. The simulation consisted of 25,000 elements and was run to single precision convergence. The figures below present the experimental data taken from an Idaho National Lab report and from the data created in COMSOL.

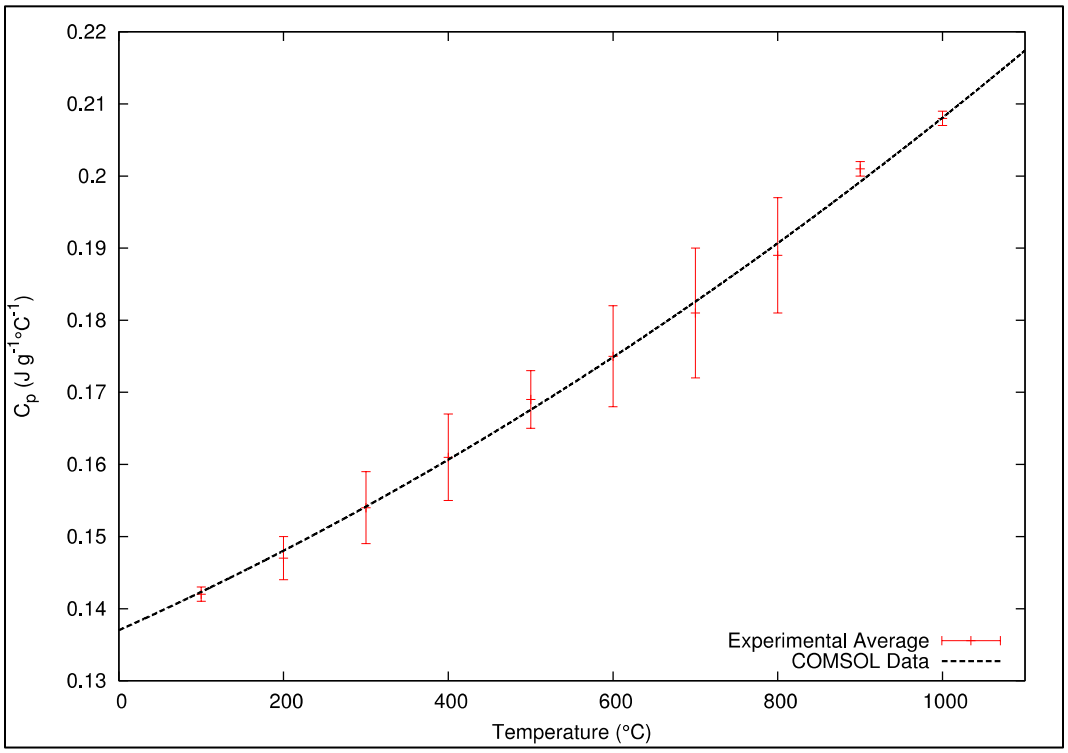

Fig. 6.1. The specific heat capacity as a function of temperature.

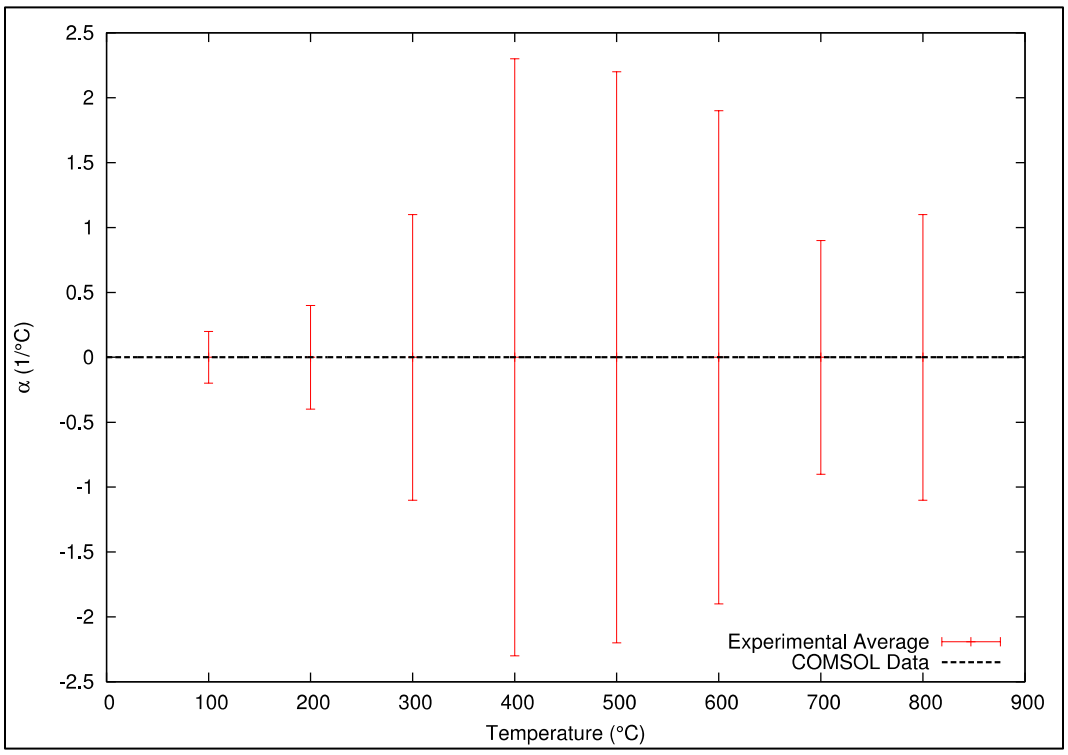

Fig. 6.2. The thermal expansion coefficient as a function of temperature.

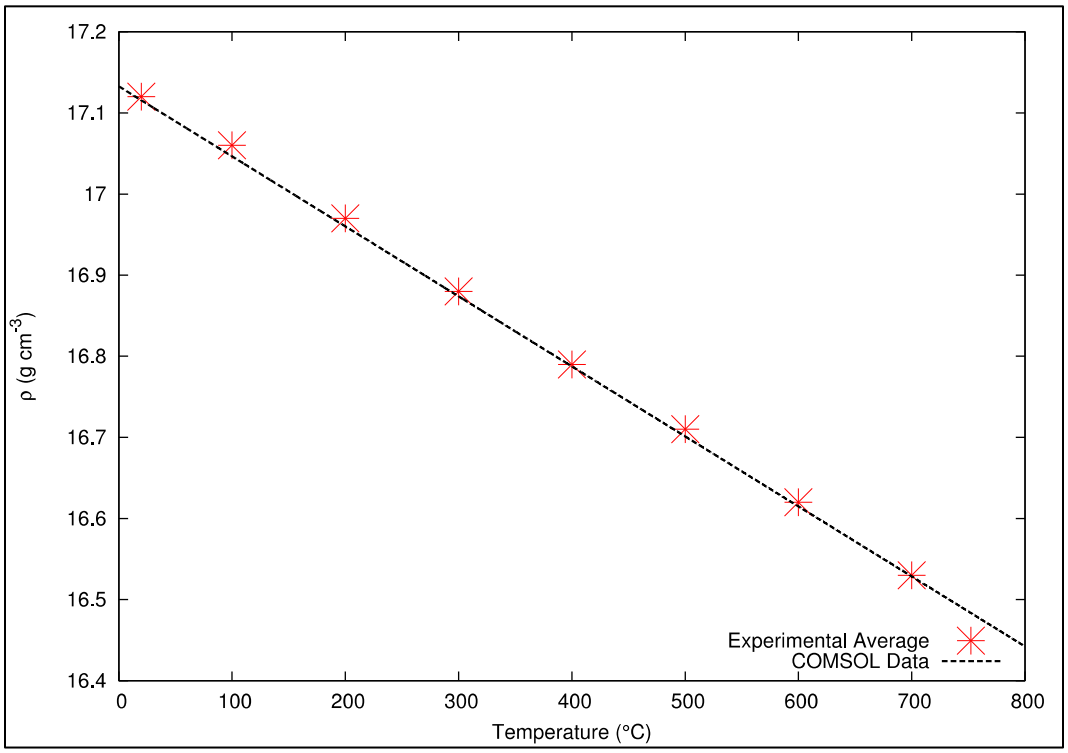

Fig. 6.3. The density as a function of temperature.

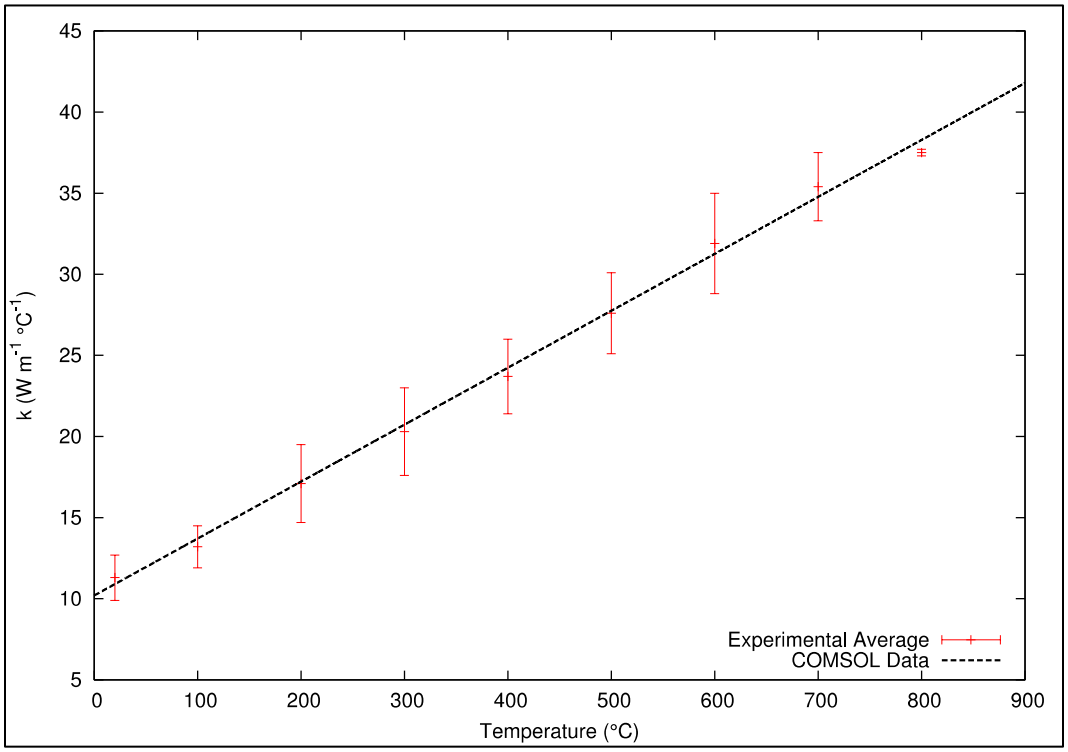

Fig. 6.4. The thermal conductivity as a function of temperature.

The COMSOL simulation data follows the data provided by the INL report. The extreme high temperature range for the thermal conductivity, seen in Fig. 6.4, contains the only outlier for the simulation. As new data becomes available, the materials library needs to be updated to stay current with the standards used for the LEU conversion.

6.2 MATERIAL PROPERTY LIBRARIES

COMSOL contains access to a built-in materials library that allows for the direct implementation of a large selection of material properties for multiphysics simulations. Because COMSOL will be used to verify the safety basis for the conversion to LEU fuel, it is desired to include the best materials properties available. As already demonstrated, the material properties for the U-10MO have been implemented and verified in Section 6.1. In order to ensure the most reliable properties for the coolant for the fuel plates, it is desired to include the water properties from the NIST Steam Tables.

The National Institute of Standards and Technology (NIST) has taken over the task of maintaining the Steam tables formerly maintained by the American Society of Mechanical Engineers (ASME). The NIST steam tables are derived from the "official international formulations for water properties developed and maintained by the International Association for the Properties of Water and Steam (IAPWS)." NIST has taken these formulations and implemented them into a FORTRAN code capable of providing 43 properties of water. The list of outputs is available in the NIST documentation. The majority of steam tables are derived from this formulation.

In order to implement the NIST Steam Tables into COMSOL, the MATLAB interface for COMSOL will be used. This interface facilitates the use of a MATLAB function inside of the COMSOL code. COMSOL sends a list of user-defined parameters, in matrix form, to MATLAB to be input into the function. The results of the function are then returned to COMSOL, in matrix form, and the data is used for the simulation. The MATLAB function can be used at any point in the COMSOL code: it can be used for initial conditions, during computation, or in post processing.

6.2.1 FORTRAN Compilation in MATLAB

COMSOL does not provide a direct way to call FORTRAN codes but can allow the user to create a custom function utilizing a function created in MATLAB. MATLAB in turn has a built in compiler, called the MEX-function, that allows the user to create a function from C++ or FORTRAN codes. This link will allow COMSOL to directly call the FORTRAN subroutines in the NIST Tables.

As an initial step, a fundamental understanding of the workings of the MEX-function in MATLAB is desired and MATLAB provides many examples of simple C++ and FORTRAN codes ready for compilation. Because the NIST Tables are FORTRAN subroutines, only the FORTRAN example codes are of interest. When compiling the FORTRAN code in MATLAB, one simply types "mex code.F" in the Command Window and MATLAB generates a file named "code.mexa64," which doubles as a MATLAB function of the name "code()" where the parenthesis includes any arguments fed to the FORTRAN code.

Using the examples provided in the MATLAB directory proved to be difficult as any of the FORTRAN examples would cause MATLAB to crash during the compilation process. As a test, the same examples, written in C++, were compiled using the MEX-function without any difficulty thus proving the MEX-function was not broken in this MATLAB release. A help request was sent to MATLAB and a response was given for the compilation problems encountered: "*Although FORTRAN does not generally use pointers, the MEX interface has "pointer" variables, it should be declared as INTEGER*4 on the 32 bit machine, and declared as INTEGER*8 on the 64 bit machine.*" The FORTRAN examples provided by

MATLAB were written for 32 bit machines and the machine being used for compilation at ORNL was a 64 bit machine and thus MATLAB would crash on every compilation attempt. The difference in coding can be seen in this example for the sample code called timestwo.F. The 32 bit code is written as:

```
C       Gateway routine
        subroutine mexFunction(nlhs, plhs, nrhs, prhs)
C       Declarations
        implicit none
C       mexFunction arguments:
        mwPointer plhs(*), prhs(*)
        integer nlhs, nrhs
C       Function declarations:
        mwPointer mxGetPr
        mwPointer mxCreateDoubleMatrix
        integer mxIsNumeric
        mwPointer mxGetM, mxGetN
C       Pointers to input/output mxArrays:
         mwPointer x_ptr, y_ptr
C       Array information:
        mwPointer mrows, ncols
        mwSize size
C       Arguments for computational routine:
        real*8  x_input, y_output
```

Whereas the 64 bit code is written as:

```
C       Gateway routine
        subroutine mexFunction(nlhs, plhs, nrhs, prhs)
C       Declarations
        implicit none
C       mexFunction arguments:
        integer*8 plhs(*), prhs(*)
        integer nlhs, nrhs
C       Function declarations:
        integer*8 mxGetPr
        integer*8 mxCreateDoubleMatrix
        integer mxIsNumeric
        integer*8 mxGetM, mxGetN
C       Pointers to input/output mxArrays:
        integer*8 x_ptr, y_ptr
C       Array information:
        integer*8 mrows, ncols
        mwSize size
C       Arguments for computational routine:
        real*8  x_input, y_output
```

Notice that for each declaration of mwPointer in the 32 bit code, it is replaced by integer*8 for the 64 bit code. Upon replacing this pointer, all of the MATLAB examples could be successfully compiled.

6.2.2 MATLAB Function Implementation

The compiled code has been compared to the steam tables available in *Thermodynamics: An engineering Approach*[116,117] with great accuracy. This code has been implemented into the COMOSL GUI by creating a MATLAB function that calls the mex-function. This implementation was made possible after several discussions with the COMSOL support group. It was revealed that COMSOL sends it variables as vector arrays of 1xN while the mex-function was created to only accept a scalar variable, that is a 1x1 variable. In using the NIST code implemented in MATLAB, the mex-function was called as follows:

```
output = input(press,temp)
```

where output is the desired output from the mex-function (density, thermal conductivity, etc.) and input is the mex-function. The mex-function only accepts one value for press and temp where COMSOL gives an array of variables. Using this knowledge allowed the creation of the following MATLAB function to call the mex-function:

```
function output = COMSOL_function(press,temp)
for ii = 1:length(press)
output(ii) = mex_function(press(ii),temp(ii))
end
return
```

The above MATLAB function has allowed the implementation of the NIST steam tables into COMSOL.

6.3 DERIVATION OF THE INVOLUTE COORDINATE SYSTEM

6.3.1 The Basic Involute

The basic circular involute shown in Fig. 6.5 is represented by the parametric relation

$$x = r_b\left[\cos(\theta) + \theta\sin(\theta)\right], \quad \theta \geq 0 \qquad \text{.....(6.1a)}$$

$$y = r_b\left[\sin(\theta) - \theta\cos(\theta)\right], \quad \theta \geq 0 \qquad \text{.....(6.1b)}$$

where r_b is the radius of the base involute, assumed to be positive, and θ is measured in radians[117]. For the purpose of brevity, the basic circular involute will be called the basic involute herein. The fact that it is a circular involute will be implied as this is the only involute curve detailed explicitly.

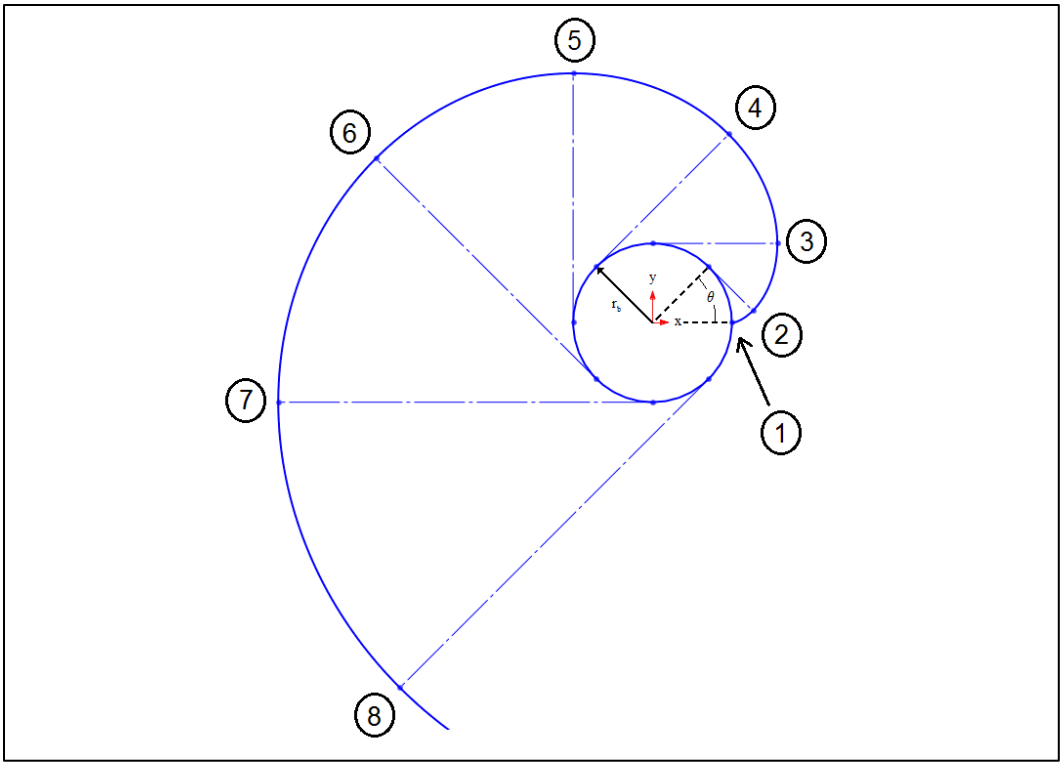

Fig. 6.5. Basic circular involute. The involute curve is shown along with its base circle. Tangent guidelines are represented by dashed lines. The numbers indicate the direction of progression of the involute in the direction deemed "positive."

While this is considered the basic involute equation, in truth however, this is a simplification of a more generalized form. In this more general form there are two variables, θ and α, where one is a linear function of the other. This generalized form is given by the parametric equation

$$x = r_b[\cos(\theta) + \alpha \sin(\theta)], \quad \alpha \geq 0 \qquad \text{.....(6.2a)}$$

$$y = r_b[\sin(\theta) - \alpha \cos(\theta)], \quad \alpha \geq 0 \qquad \text{.....(6.2b)}$$

$$\alpha = \Im(\theta) \qquad \text{.....(6.2c)}$$

where the $\Im$ operator denotes that α is a linear function of θ. In this generalized form, the variable θ specifies the angular position of the tangent line emanating from the perimeter of the base circle. The variable α specifies the angular position along the length of the involute curve itself. This is illustrated in Fig. 6.6.

Using this generalized form of the parametric equation, an entire array of involute curves can be created by varying θ_o. The process of incrementally increasing the angular offset of each successive curve can be repeated *n* times for *n* number of curves.

$$x_i = r_b\left[\cos(\theta_i) + \alpha\sin(\theta_i)\right], \quad \alpha \geq 0, \quad i = 1, \quad 2, \quad 3,..., n \qquad (6.3a)$$

$$y_i = r_b\left[\sin(\theta_i) - \alpha\cos(\theta_i)\right], \quad \alpha \geq 0, \quad i = 1, \quad 2, \quad 3,..., n \qquad (6.3b)$$

$$\theta_i = \alpha + 2\pi\frac{i-1}{n}, \quad \alpha \geq 0, \quad i = 1, \quad 2, \quad 3,..., n \qquad (6.3c)$$

The HFIR core consists of 540 basic involute fuel plates, 171 of which are arrayed in the inner element. The HFIR inner core can be recreated with n = 342. This is twice the number of fuel plates since each plate is separated by a coolant channel. This produces 171 constant-width fuel plates and 171 constant-width coolant channels. A magnified slice of the geometry that this produces is shown in Fig. 6.6.

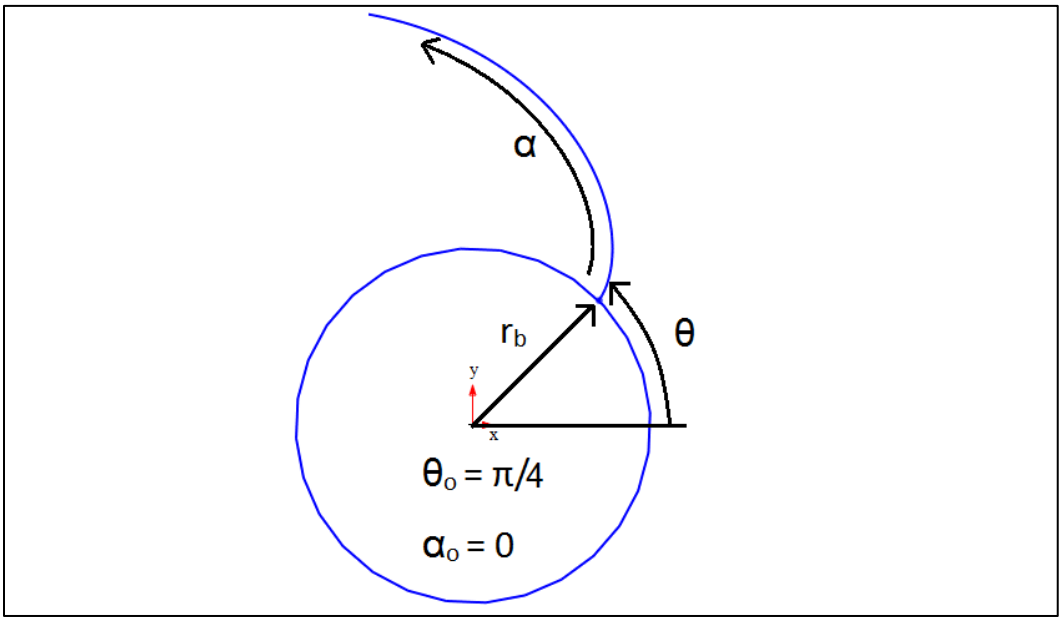

Fig. 6.6. Angular parameters. In this example α = θ – π/4. Instances in which α does not start at zero are also possible. These will, however, have some angular offset separating them from contact with the base circle.

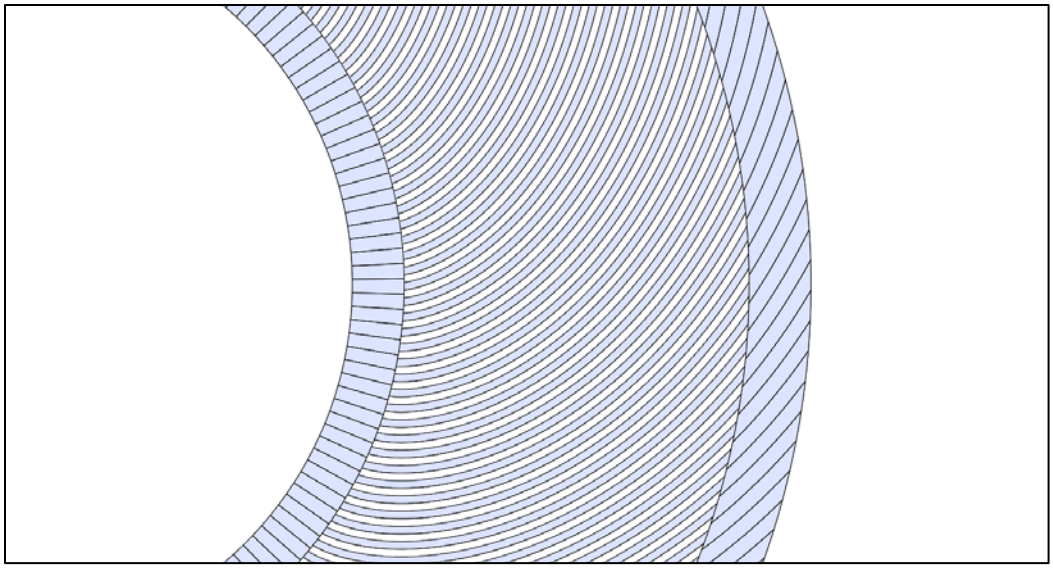

Fig. 6.7. HFIR core inner element fuel plate configuration. Inner element involute fuel plates are shown in grey with inner and outer side plates capping each end. The alternating white spaces between fuel plates are coolant channels.

6.3.2 Select Alterations to the Basic Involute

While Equation 6.2 adequately describes any general involute curve, it is not sufficient for describing the internal fuel geometries of the plates nor does it lend itself to a practical reference frame. For these purposes, Equation 6.2 can be rewritten in terms of two involute coordinates, θ and t. The new involute variable t is the perpendicular offset distance from a base involute curve. It takes the place of α such that

$$\alpha(\theta) = \theta + \frac{t}{r_b}, \quad \alpha \geq 0 \qquad \text{.....(6.4)}$$

where t is measured positive extending out from the convex side of the curve and negative out from the concave side. A pair of curves in which t is set to equal 0 and r_b such that θ equals α and $\alpha + 1$, respectively, is shown in Fig. 6.8. Both the arc length along the circumference of the base circle, a, and the perpendicular offset distance, t, between the two involute curves equals r_b. Thus it can be said that

$$\frac{a}{r_b} = \frac{t}{r_b} = \theta_o \qquad \text{.....(6.5)}$$

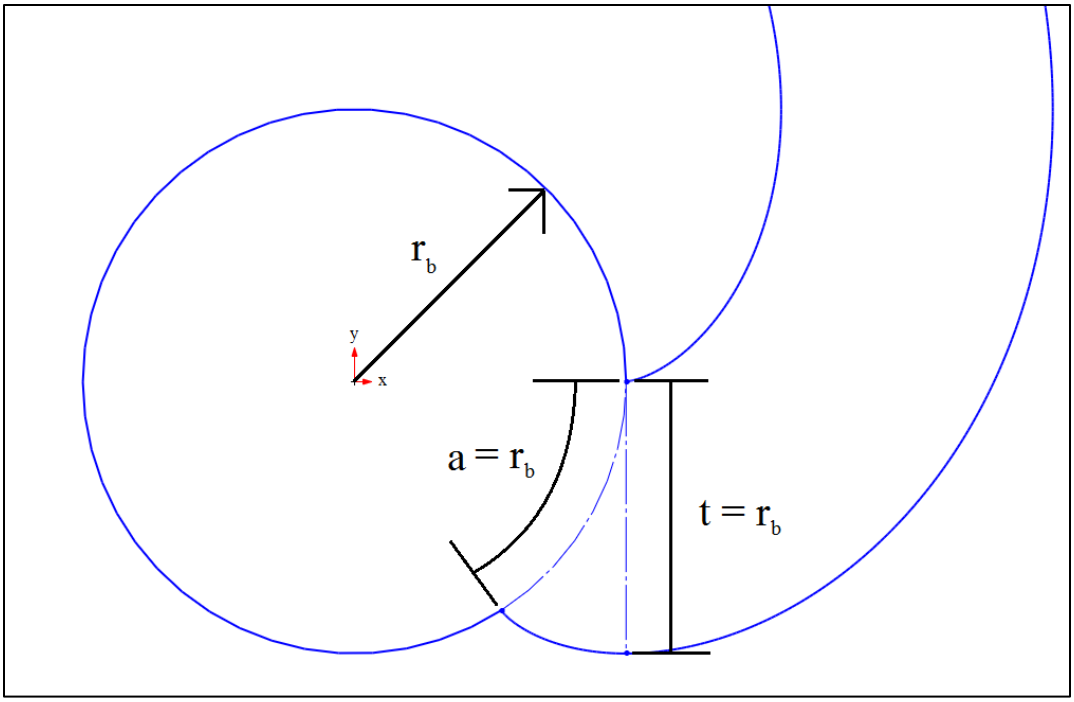

Fig. 6.8. Perpendicular involute offset. The top involute curve has $\theta = \alpha$. The bottom involute curve has $\theta = \alpha + 1$ which corresponds to a θ_o of 1 radian (CW positive).

In this new reference frame, adjacent involute curves are generated by specifying *t*, the linear offset distance between them, rather than the angular offset between their origin points. Equation 6.4 is valid for any involute with a constant offset. For involute curves with non-constant offset, *t* can be specified as a function of θ. If *t* varies linearly with θ, the offset can be determined using point-slope form such that

$$\alpha(\theta) = \theta + \frac{t(\theta)}{r_b}, \quad \alpha \geq 0, \quad t << r_b \qquad \text{.....(6.6a)}$$

$$t(\theta) = \frac{t_2 - t_1}{\theta_2 - \theta_1}\left(\theta - \theta_1\right) + t_1 \qquad \text{.....(6.6b)}$$

where θ_1 and θ_2 are the start and end points of the sloped line, respectively, and $t_1 = t(\theta_1)$, $t_2 = t(\theta_2)$. If *t* is given as a smooth, continuous function of θ then Equation 6.6a can be used independently.

In the same way that *t* is a more readily accessible substitute for θ_o, the angular coordinate θ can be converted into arc length along the involute curve, *s*. The variable *t* will be assumed constant in the following relations. First, consider the basic definition of arc length

$$s_{a \to b} = \int_a^b ds \qquad \text{.....(6.7)}$$

For the parametric equation given by Equations 6.2 and 6.4, the quantity *ds* is represented by

$$ds = \sqrt{\left(\frac{dx}{d\theta}\right)^2 + \left(\frac{dy}{d\theta}\right)^2}\, d\theta \quad \text{.....(6.8)}$$

Differentiating Eqations 6.2 and 6.4 with respect to θ and substituting into Equation 6.8) produces

$$ds = \sqrt{\left(r_b\theta + t\right)^2 \left(\cos^2\theta + \sin^2\theta\right)}\, d\theta \quad \text{.....(6.9)}$$

Simplifying via the Pythagorean identity and substituting into Equation 6.7 yields

$$s_{a\to b} = \int_a^b \left(r_b\theta + t\right) d\theta \quad \text{.....(6.10)}$$

Integrating and assuming $\theta_a = s_a = 0$ as a universal point of reference produces

$$s(\theta) = \frac{r_b\theta^2}{2} + t\theta, \quad \theta \geq 0 \quad \text{.....(.611)}$$

Arc length is considered a superior alternative to θ due to the fact that it increases linearly along the span of the fuel plate whereas θ increases at a rate proportional to the square root of *s*. In addition to *s* and θ there is a third coordinate, radius, *r*, that is frequently used to define positions along the span of the fuel plate. As various inputs and references use a mixture of all three coordinates, it is important to be able to easily and readily convert between the three. Radial position, *r*, can easily be determined as a function of θ by starting with

$$r = \sqrt{x^2 + y^2} \quad \text{.....(6.12)}$$

Substituting Equations 6.2 and 6.4 into Equation 6.12 yields

$$r = \sqrt{r_b^2\left[\cos\theta + \left(\theta + \frac{t}{r_b}\right)\sin\theta\right]^2 + \left[\sin\theta - \left(\theta + \frac{t}{r_b}\right)\cos\theta\right]^2}, \quad \theta \geq 0 \quad \text{.....(6.13)}$$

Squaring the quantities allows for the grouping of like terms

$$r = r_b\sqrt{\left(\cos^2\theta + \sin^2\theta\right) + \left(\theta + \frac{t}{r_b}\right)^2\left(\cos^2\theta + \sin^2\theta\right) + 2\left(\theta + \frac{t}{r_b}\right)\left(\cos\theta\sin\theta - \cos\theta\sin\theta\right)}, \quad \text{.....6.14)}$$

$$\theta \geq 0.$$

Again using the Pythagorean identity and cancelling like terms produces *r* as a function of θ

$$r(\theta) = r_b\sqrt{\left(\theta + \frac{t}{r_b}\right)^2 + 1}, \quad \theta \geq 0 \quad \text{.....(6.15)}$$

To bring the reference frame relations full circle, *s* can also be solved as a function of *r*. To start, Equation 6.15 is solved for θ

$$\theta(r)=\sqrt{\left(\frac{r}{r_b}\right)^2-1}-\frac{t}{r_b},\quad r\geq r_b \qquad (6.16)$$

The result is then substituted into Equation 6.11 to produce

$$s=\frac{r_b}{2}\left[\sqrt{\left(\frac{r}{r_b}\right)^2-1}-\frac{t}{r_b}\right]^2+t\left[\sqrt{\left(\frac{r}{r_b}\right)^2-1}-\frac{t}{r_b}\right],\quad r\geq r_b \qquad (6.17)$$

Squaring the first term and grouping like terms yields

$$s=\frac{r^2}{2r_b}-\frac{r_b}{2}+(t-t)\sqrt{\left(\frac{r}{r_b}\right)^2-1}+\frac{t^2}{r_b}\left(\frac{1}{2}-1\right),\quad r\geq r_b \qquad (6.18)$$

which reduces to

$$s=\frac{r^2}{2r_b}-\frac{r_b}{2}-\frac{t^2}{2r_b},\quad r\geq r_b \qquad (6.19)$$

Simplifying yields

$$s(r)=\frac{1}{2r_b}\left[r^2-r_b^2-t^2\right],\quad r\geq r_b \qquad (6.20)$$

With Equations 6.11, 6.15, and 6.20, it is possible to quickly cycle among all three coordinate systems. The relations for $s(r)$, $r(\theta)$, and $s(\theta)$ can readily be solved in reverse, allowing for quick conversions between any of the three primary involute coordinates.

The final alteration to the basic involute equation that is required in order to recreate specific HFIR fuel configurations is the out-of-plane alteration for involute curves with an axial component. The basic involute curve, referred to, in this context, as the in-plane involute, and all of its alterations presented thus far, exists solely in a two-dimensional *s*-*t* plane that is perpendicular to the axis of the core. The question arises of how to most appropriately extend the involute into the axial dimension to create an out-of-plane involute. There are many choices for defining the out-of-plane involute's axial position. Primarily, one could define the axial position as a function of θ, *r*, or *s*. One could also envision the out-of-plane involute as the hypotenuse of an involute triangle with the in-plane involute and the axial line connecting their two ends completing the perimeter of the triangle.

The most physically appropriate answer to this question comes from the fabrication process used to create the plates. The fuel plates, consisting of aluminum cladding and enriched uranium fuel powder, are assembled in a flat, rectangular geometry. The involute curve is introduced by pressing the flattened

assembly against an involute mold. In envisioning this process, it is easy to understand that the fuel plate is bent as a function of arc length along the in-plane involute curve. In the same way, the extension of the involute curve into the axial direction should be a function of arc length in order to realistically approximate the effects of this real-world bending process.

The introduction of an axial component into an involute curve in this manner turns out to be fairly simple. Consider again Equations 6.2 and 6.4. Let them represent a generic in-plane involute curve. A third equation to represent the curve's axial position as a function of the variable θ must be added to this set. The new parametric set then becomes Equations 6.2 and 6.4., and

$$z(\theta) = \frac{z_2 - z_1}{s_2 - s_1}\left(s(\theta) - s_1\right) + z_1 \qquad \text{.....(6.21)}$$

where $s(\theta)$ is given by Equation 6.11. The resultant out-of-plane involute curve that this produces is shown in Fig. 6.9.

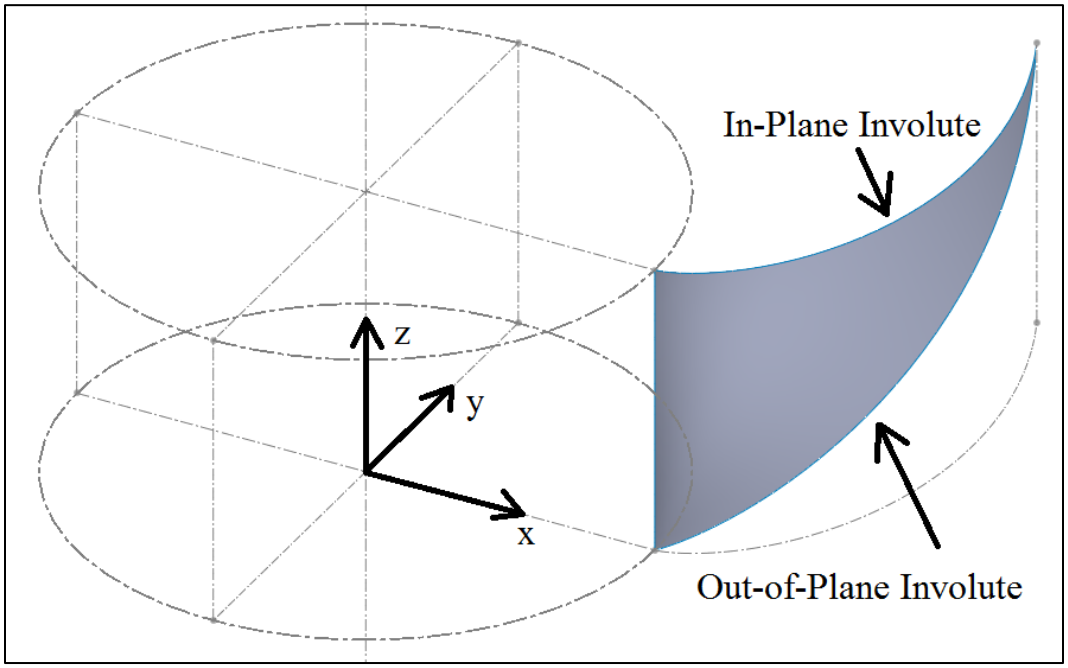

Fig. 6.9. Out-of-plane involute curve. The *z*-direction denotes the direction of the axis. As viewed down the axis, the out-of-plane involute has the same footprint as its in-plane involute.

6.4 CONSTRUCTING CAD GEOMETRIES IN SOLIDWORKS

6.4.1 Defining the Geometries

Only inner element geometries will be considered in this section. The most basic involute geometry in the core is that of the aluminum fuel plate. Its basic dimensions are shown in Fig. 6.10. The fuel plate's primary distinguishing features are a rounded leading edge and a chamfered inner corner. Given that this second feature is obscured from the coolant channel during operation, however, it can be removed from the CAD construction. In models in which the side plates are included for the purpose of analyzing heat transfer into them from the coolant and fuel plate, the fuel plate itself is cut off at this overlap boundary.

Anything beyond this line is assumed to be side plate—a trivial distinction given the uniformity of material used to construct both the fuel plates and the side plates.

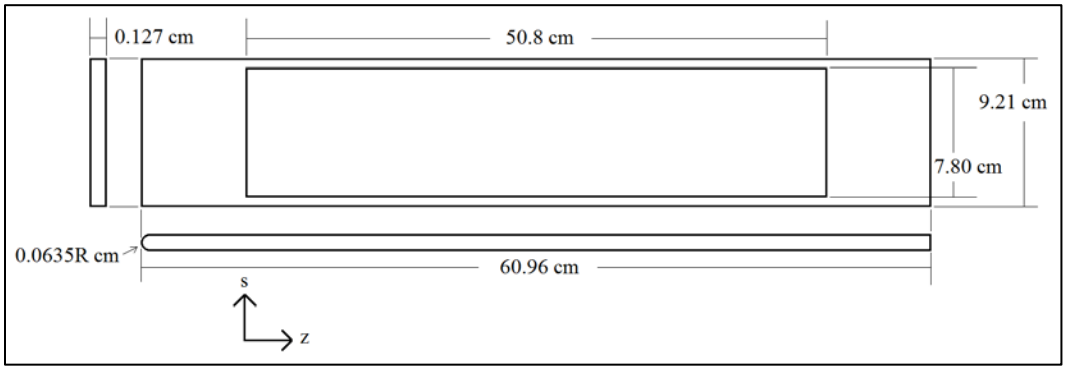

Fig. 6.10. Inner element fuel plate dimensions.

In considering the "basic" fuel plate, one is considering only the external dimensions. In actuality, the fuel plate has an internal cavity in which the fuel meat is placed. This cavity can be created through a Boolean subtraction of the fuel meat geometry from the solid fuel plate geometry, however, rather than through manual CAD construction. For the fuel meat itself, three geometries will be considered in this thesis. The first is the existing HEU fuel meat. The HEU fuel has a thickness that varies as a smooth function of *s*. The HEU fuel is axially consistent, meaning that its profile in the *s*-*t* plane remains constant for all axial positions. All of the fuel meats are non-symmetric such that one side forms a datum at t=0. The contour of the other side thus varies directly with the thickness of the fuel meat. The HEU fuel meat thickness profile is shown in Fig. 6.11. The profile is shown in linearized form in which the *s*-*t* plane has been mapped to an *x*-*y* Cartesian grid using a 1:1 mapping.

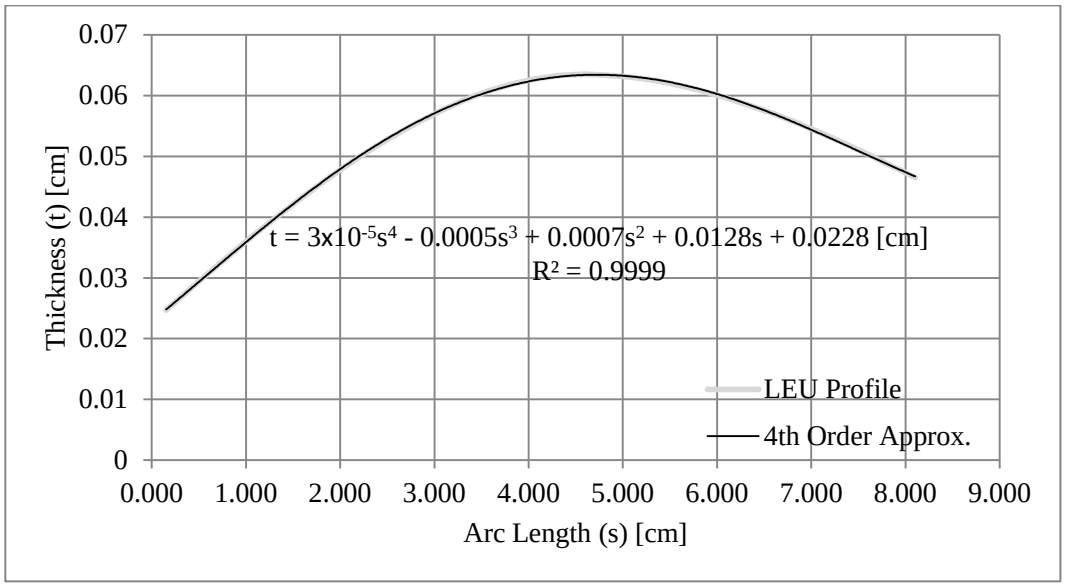

Fig. 6.11. Linearized HEU fuel thickness profile.
The curve fit is generated from 35 unevenly distributed points.

The HEU thickness is given as a collection of points that can be represented in cm by the 4th order polynomial

$$t(s) = \left(3s^4 - 50s^3 + 70s^2 + 1280s + 2280\right)\times 10^{-5}, \quad 0.152 \le s \le 8.103 \qquad (6.22)$$

with a coefficient of determination, R^2, of 0.9999 indicating a close approximation of the actual HEU thickness profile. The coefficient of determination is given by[94].

$$R^2 = 1 - \frac{\sum_{i=1}^{35}\left(t_i - f\left(s_i\right)\right)^2}{\sum_{i=1}^{35}\left(t_i - \bar{t}\right)^2} \qquad (6.23)$$

where t_i is the collection of points used to define the HEU thickness profile, $f(s_i)$ is the value of the approximation at those points, and $\bar{t}$ is the average of the defining points.

The second geometry is an intermediate LEU fuel meat. The intermediate LEU fuel has a thickness that varies piecewise linearly with *s* and is also axially consistent. The linearized LEU thickness profile is shown in Fig. 6.12.

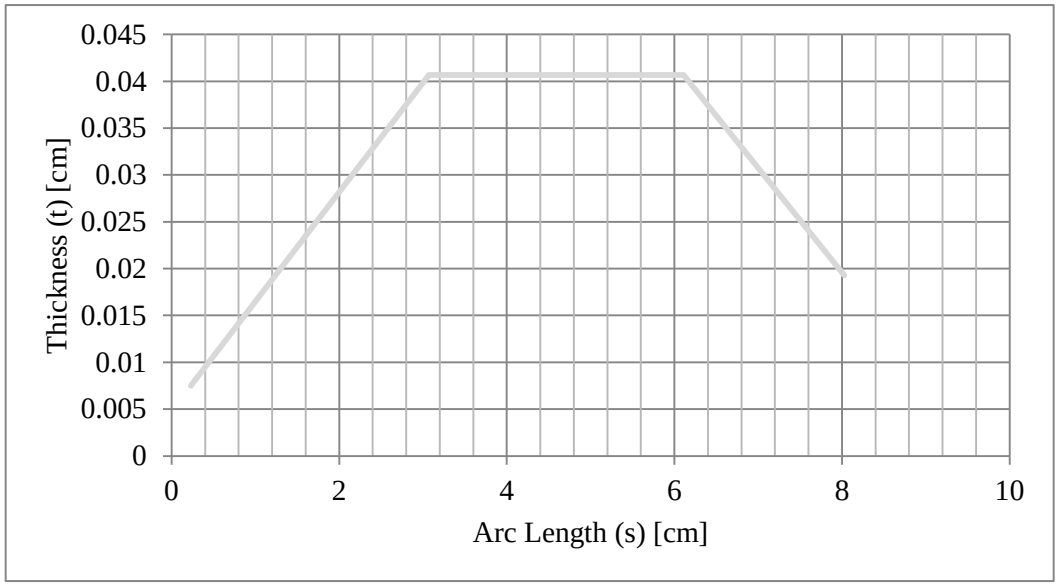

Fig. 6.12. Linearized LEU fuel thickness profile. Overall, the LEU fuel profile is thinner than the HEU profile. Even though the LEU fuel has less U^{235} per weight than the HEU fuel, it has a higher density.

The LEU thickness in cm can be represented by the piecewise function

$$t(s)=\begin{cases} 0.1168s+0.0102, & \text{if} \quad 0.2309 \le s \le 3.0270 \\ 0.0407, & \text{if} \quad 3.0720 \le s \le 6.1100 \\ -0.0112s+0.1027, & \text{if} \quad 6.1100 \le s \le 8.0270 \end{cases} \qquad \text{.....(6.24)}$$

The third geometry is another LEU fuel meat with the same starting profile as the first, but with the inclusion of axial grading. This geometry tapers towards its trailing edge in an effort to prevent a sharp spike in nuclear heat energy output in the tail of the fuel meat. This third geometry was, at the onset of this study, the geometry proposed for production. Since that time, however, more viable alternative fuel geometries have been proposed. The intermediate LEU fuel is included only because of the relative simplicity and ease of modeling that accompanies the change to an axially-consistent geometry. The axially-graded LEU geometry is shown alongside the intermediate geometry in Fig. 6.13.

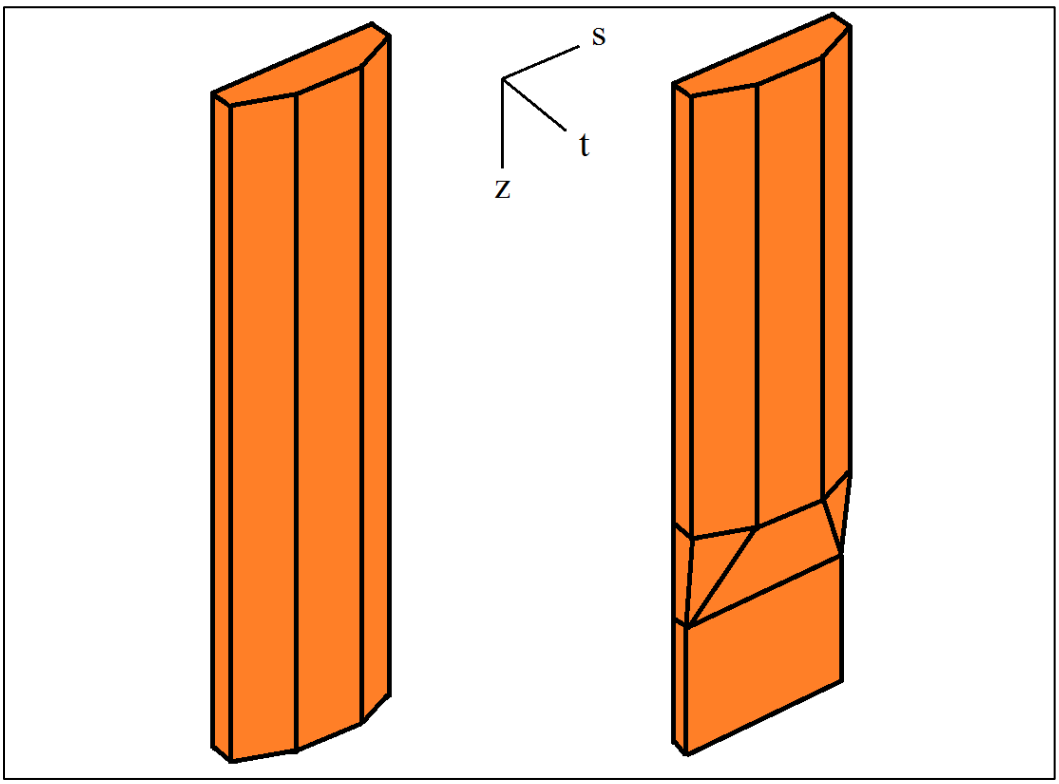

Fig.. 6.13. Linearized LEU fuel geometries. The axially-consistent intermediate LEU geometry is shown on the left. The axially-graded LEU geometry is shown on the right. Figures not to scale.

In the process of manufacturing the HEU plate, the cavity in the plate is filled with fuel powder to create the necessary profile. The remainder of the void is then filled with a radioactively inert composition of "filler" powder. In the outer fuel element, the filler is all aluminum powder. In the inner fuel element, the filler is composed by weight of ~99.9% aluminum powder and ~0.01% boron poison[16]. Since the poison constitutes such a small percentage of the overall filler material it can be disregarded with respect to its thermal properties. The filler can thus be assumed to have the thermal properties of aluminum. Furthermore, since the powder is primarily aluminum, this entire filler region can be assumed to be a part of the fuel plate itself. The only loss is in the modeling of the contact resistance between the two as well

as within the powder itself. The final method of manufacturing LEU plates has not been set. Therefore, the same assumptions are used in the LEU model. Under these assumptions, the process of creating the finalized fuel plate geometry through a Boolean subtraction of the fuel meat geometry is valid.

The last major geometry component is that of the coolant. The coolant is, like the fuel plate itself, fairly simple to construct. It encapsulates the fuel plate on the top and bottom as well as the concave and convex sides. An entry region approximately 2.0 cm in length, corresponding to the top of the side plates, is inserted upstream of the leading edge. This allows the inlet flow to be specified using the conditions under which it enters the reactor core. The flow then naturally develops as a result of the impingement of the rounded leading edge. A similar Region 3.5 cm in length, corresponding to the bottom of the outer side plate, is inserted downstream of the trailing edge. This region allows the flow to homogenize downstream of the fuel plate before being bounded by outlet flow conditions. The coolant is bounded in the *t*-direction by lines of periodicity.

6.4.2 SolidWorks Construction Techniques

SolidWorks was chosen to construct CAD geometries due to its inclusion of an equation-driven-curve function. Operating in a 3D sketch, the equation-driven-curve function can create a curve from three-dimensional Cartesian parametric equations. Namely, the involute parametric equation set derived in the preceding section can be used to directly generate involute geometries as a function of the angular coordinate θ. Steps for accessing the tool are outlined in Fig. 6.14.

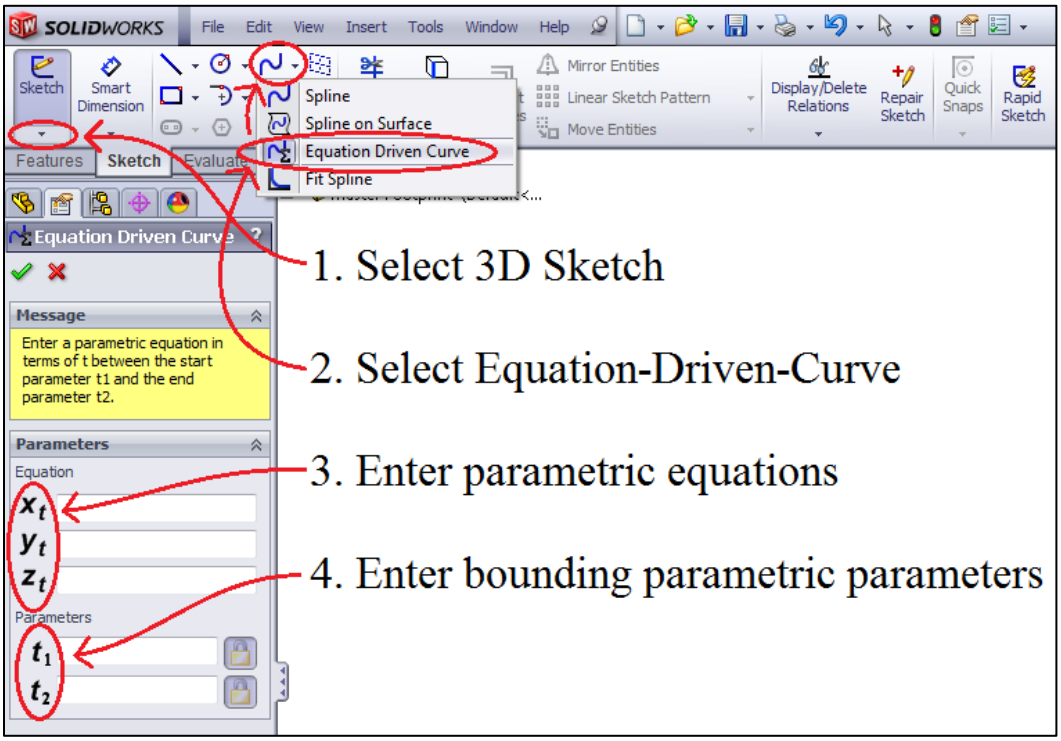

Fig. 6.14. Accessing the equation-driven-curve tool in solidworks. SolidWorks refers to the parametric parameter as *t*. For an involute curve this traditionally represents the angular coordinate θ although any coordinate can be used is the parametric equations are given as a function of it.

Constructing CAD geometries in a 3D sketch allows not only for the creation of in-plane involute curves—such as those used to create the contours for the fuel meat, fuel plate, side plates, and coolant—but also for out-of-plane curves like those necessary to create the axial grading in the LEU geometry. For axially-constant geometries a sketch plane can be used in order to work in a simplified 2D *x*-*y* plane in which only the coordinates θ and t are defined. For all of these geometries it is easiest to create a 2D "footprint" and then extrude in the axial direction. An example of a basic one-plate two-channel domain is shown in Fig. 6.15.

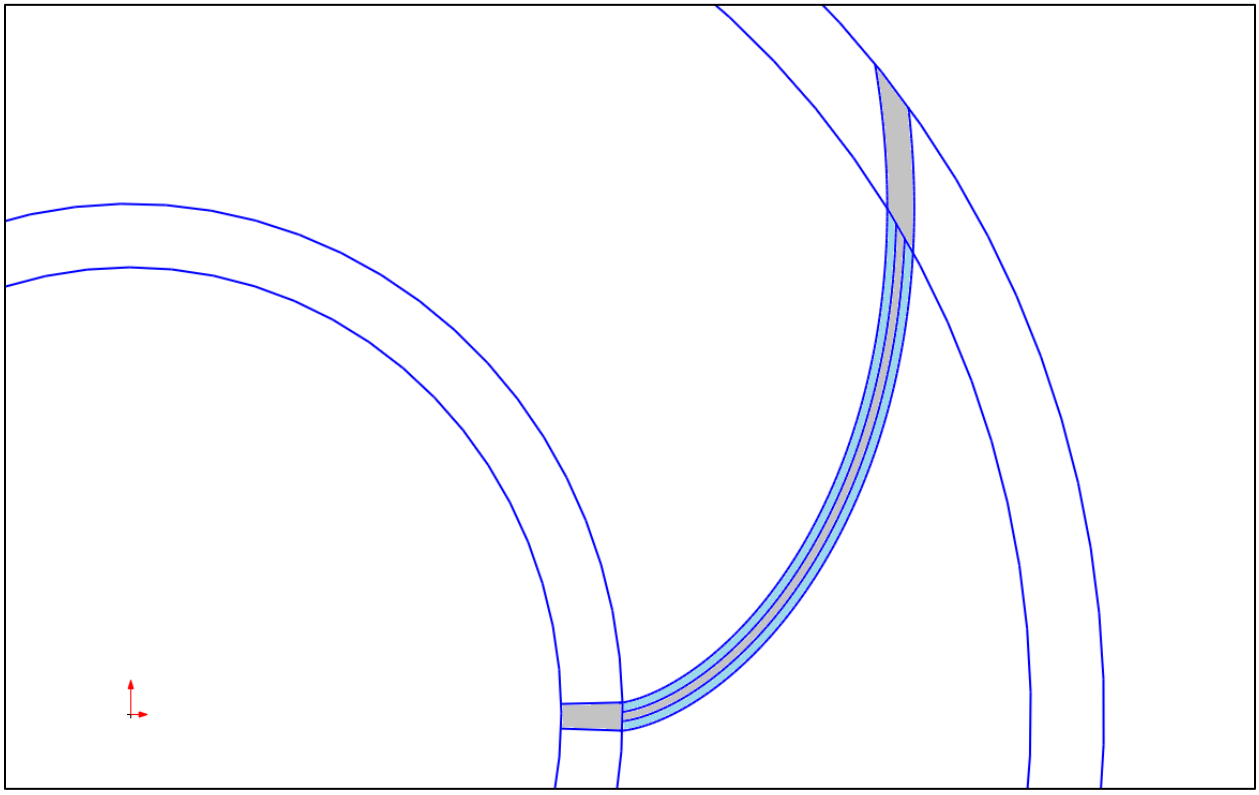

Fig. 6.15. 2D *x*-*y* Plane SolidWorks footprint. Only the curves are created in SolidWorks. The shading of specific areas was done purely as a means of orientation. The two full coolant channels are shaded in blue. The fuel plate and both side plates are shaded in grey. The fuel meat contour is not depicted.

7.0 CONCLUSIONS, RECOMMENDATIONS AND LESSONS LEARNED

This chapter summarizes the major results of this work and makes recommendations regarding further work associated with the thermal-hydraulic, fluid-structure interaction, and thermal-structure interaction modeling of the High Flux Isotope Reactor.

7.1 RESULTS FROM 2-D CONJUGATE HEAT TRANSFER MODELS

It was shown that for the constant heat flux situation with both constant and variable fluid properties, the Seider-Tate correlation provided convection coefficient results very close to the COMSOL model results for the transfer of heat from a solid surface by the use of the low Reynold number k-ε turbulent flow model. The Seider-Tate correlation produced a relative difference with the model Nusselt number of 1.2% to 4.4%. As a result, the temperature of the surface of the generating solid was also closely matched by the Seider-Tate Nusselt modulus.

In the case of constant heat flux with constant fluid properties, the model produces surface temperature results that are higher than those produced by the other correlations (i.e., Gnielinski, Seider-Tate, and Hausen). This trend is inverted, however, with the use of variable fluid properties where the model surface temperature distribution is lowest in magnitude relative to the surface temperature distributions produced by the other correlations. It was found that the Gnielinski correlation produced the highest estimate of the surface temperature for the constant heat flux case with variable fluid properties.

For a surface exhibiting constant heat flux into a fluid where the material properties vary negligibly over the temperature range of interest, the Seider-Tate correlation produces estimates of the convection coefficient which translate into higher surface temperature distributions than the other correlations considered in this work. On the other hand, if the fluid properties vary significantly over the temperature range of interest with a constant surface heat flux, then the Gnielinski correlation will provide higher surface temperature results than the other correlations investigated herein. It should be borne in mind, however, that the use of constant fluid properties actually produced higher surface temperatures than the use of variable fluid properties. It was discussed that the use of constant fluid properties greatly reduces the amount of computational effort associated with the developed computational model. This reduction in effort is associated with the removal of the interpolation steps taken for the material properties at subsequent thermodynamic states.

Similar results were found for the distributed heat flux model. In the constant fluid property model, the surface temperature results associated with the model were larger in magnitude than the surface temperature results found from the correlations. It was observed that one could use either the Seider-Tate correlation or the Hausen correlation to closely reproduce the model surface temperature results in the constant fluid property case. Also, the Gnielinski correlation produced the lowest estimate for the surface temperature distribution. As a result, to provide higher estimates of the surface temperature, one should use either the Hausen correlation or the Seider-Tate correlation.

It was observed that the variable fluid property case produced the opposite trend (i.e., the Gnielinski correlation produced higher surface temperature results than the other correlations and the model). Also, the model associated with the variable fluid property case produced the lowest magnitude surface temperatures. For the variable fluid property case in conjunction with the distributed heat flux, the Hausen correlation most closely matched the model results over most of the range of the Reynolds numbers investigated here (i.e., $\mathbf{80,000} \leq \boldsymbol{Re_D} \leq \mathbf{112,000}$). On the higher end of the Reynolds number range, the Seider-Tate correlation was a better fit. The combination of a distributed power density in the generating material and variable fluid properties most closely matches the physics of the

HFIR core system. As a result, it is recommended that the Gnielinski correlation be used to produce high estimates of the clad surface temperatures where conservative estimates are necessary.

7.2 RESULTS FROM THE 3-D CONJUGATE HEAT TRANSFER MODELS

Both the Advanced Neutron Source Reactor Thermal Hydraulic Test Loop model results and the results from the fuel defect models are summarized in the following sections.

7.2.1 Advanced Neutron Source Reactor Thermal Hydraulic Test Loop

As part of the validation effort of the COMSOL code, experimental data collected from the Advanced Neutron Source Reactor Thermal Hydraulic Test Loop (ANSR THTL) was used. In Chapter 5 it was demonstrated that the model of the ANSR THTL could reproduce the results of the experiment data considered in this work relatively well. This exercise with the ANSR THTL should instill confidence in the ability of the code to produce quality results within the parameters established for the ANSR THTL (i.e., high heat flux and large flow rates through long, narrow channels).

The ANSR THTL presents a unique experimental data set that has similar characteristics to that of the flow channels in the HFIR core (i.e., high surface heat flux and a long narrow coolant channel). The aspect ratio of the THTL coolant channel, length to thickness, is 399, which is only 16.9% less than that of the HFIR. Flow velocities through the THTL range from 62.34 fps (19.00 m/s) to 88.58 fps (27.00 m/s) which are also comparable to, albeit larger than, the flow velocity characteristic of the HFIR which, as previously stated, is approximately 52.00 fps (15.85 m/s) at steady state operation. The average and peak heat fluxes produced in the THTL are stated to be 6 MW/m^2 and 12 MW/m^2, respectively[39,40]. The average heat flux through the HFIR core is calculated to be 2.13 MW/m^2. Therefore, with higher flow velocities and higher average heat fluxes, the THTL provides extreme cases, relative to HFIR conditions, with which to validate the commercial code COMSOL.

7.2.2 Fuel Defect Analysis

Two types of fuel plate defects were investigated, a lack of metallurgical bond (i.e., blister defect) and a segregation defect. The blister defect is physically characterized by a region with relatively low thermal conductivity (i.e., fission gas). The blister defect was incorporated into the model as an adiabatic disc located between the fuel and clad domains. The segregation defect is physically characterized as a local region with excess ^{235}U loading. The segregation defect was incorporated into the simulation environment as a cylinder coincident with the fuel meat with an increased thermal generation rate per unit volume relative to the surrounding fuel material.

These defect models were compared with a nominal base case model in which no defects were incorporated. The location of the maximum surface temperature for the nominal case was used as the location for the defects. The logic of this strategy follows. The defects act to increase surface heat flux. The blister defect increases heat flux on the side of the plate opposite the defect geometry (i.e., the defect geometry was placed on the fuel contour side of the fuel plate and the heat flux was increased due to the defect on the uncontoured side of the fuel plate). The segregation defect increases the surface heat flux by a local increase in thermal generation rate per unit volume. An increase in surface heat flux results in an increase in surface temperatures, given that all other parameters remain unchanged (i.e., flow velocity, material properties, etc.). The purpose of the fuel defect model is to investigate whether the surface temperature is comparable with the saturation temperature of the liquid which could result in a transition to two-phase flow. It was shown that the segregation defect resulted in the highest surface temperatures with a magnitude of 219.24˚F (377.17 K), however, the probability of either defect resulting in a local change of fluid phase is very low.

7.3 RESULTS FROM FLUID-STRUCTURE INTERACTION MODELS

The fluid-structure interaction modeling capabilities of COMSOL were tested for a number of cases. First, an oscillating cylinder with prescribed displacement was considered. The results follow the experimental setup quite well. Only one simulation was found to not follow the experimental results presented by Koopman at a plunge amplitude of 0.2 and a frequency ratio of 1.2. This “extreme” case is an outlier in all of the other lock-on cases, and based upon the success of the other simulations does not negate the solver. For instance, the simulations around the “fork” of the experimental results follow the lock-on/non lock-on progression as expected. The most reasonable explanation for this outlier is the fact that experiments, by their nature, have error involved and thus the “fork” may be in a different place.

Next, we considered a cylinder, which was allowed to freely oscillate in the transverse direction due to the fluid forces acting on the body. COMSOL’s fluid solver was used to compute the flowfield and the structural dynamics were modeled as a mass-damper-spring system using the ODE solution module of COMSOL. The results provided insight into the capabilities of the FSI solver to capture the physics of the phenomena. The exploration of the three different solving techniques available in the code for the 2-D case allowed for an assessment of the applicability of the methods for the FSI cases. It was shown that the fastest solution can be obtained using the one-way coupling. While the one-way coupled solver produced oscillating frequencies similar to the fully-coupled solver, the maximum deflections were smaller than the fully-coupled case. The segregated solver was not able to capture the physics correctly resulting in an unstable solution in which the residual would diverge.

The 2-D, free displacement case revealed the need for the perfectly symmetric mesh. The need for this new meshing technique was discovered by observing the displacement of the cylinder once it reached its limit cycle. Assuming a perfectly round cylinder, the displacement should oscillate around the original position of the cylinder but when the mesh was not symmetric, the cylinder would initially drift up and begin to oscillate about another mean position.

The 3-D case, which included the linear-elastic structural model, was able to capture the physics as well. For each run, the maximum displacement was smaller than the 2-D cases since a relatively stiff cantilever cylinder was used in the simulations. Taking these assumptions into account, the displacements obtained from the simulations appear to be reasonable.

As the next case, we considered a stationary cylinder with a moving elastic tail, which provides a context to explore large deflections produced by the fluid. In particular, the FSI2 case produced results for which the deflection at the tail was approximately 8 times larger than the thickness of the plate. This large deflection tests the code’s ability to resolve the large stresses in the linear-structural model, to adapt the mesh as the structure deforms, and to capture the change in fluid characteristics, especially around the end of the tail. The final solution of FSI2 demonstrating these attributes matched the test cases provided by Turek and Hron very well and also produces deflections for a much stiffer plate as shown in the steel tail case.

Having gained confidence in COMSOL capabilities for simpler problems, next we turned our attention in modeling fluid-structure interaction phenomena in flat plates typically used in nuclear reactors. The first three-dimensional case was based on the experimental setup studied by Smissaert in late 1960s. The large aspect ratio of the Smissaert experimental setup (180 length to channel thickness ratio) presented a difficult computational problem when it comes to balancing computational time, size and stability. The long, thin flow channels required a large number of elements in order to properly capture the flow field. For the flow field, a free tetrahedral mesh was used with a mapped quadrilateral mesh along the no-slip boundaries of the side wall and plate. The final mesh consisted of approximately 750,000 elements.

As seen in Section 4.2.3, FSI simulations with strong fluid and structure coupling must be run using a fully coupled solver. In order to obtain a reasonable initial condition, one-way coupling is used to establish the initial condition for the fully coupled solver. Without this step, the solution process is not stable and no solution was obtained. A segregated approach was tried with too little success[79]. In order to obtain an FSI solution for high-aspect ratio fuel plates, the following solution process should be followed:

Use the one-way coupled FSI solver to obtain a fluid solution and solid mechanics solution with a coarse mesh.

Use the one-way coupled solution as an initial condition for the fully coupled solver using the same mesh that was used for the one-way coupling.

Refine the mesh using the previous solution as an initial condition for the fully coupled solver until the solution is mesh converged.

As the final test case related to fluid-structure interaction modeling, curved plates were considered. Similar to flat plate simulations, a one-way coupled solver should be used to obtain a "good" initial flow and deflection solution, which must be provided to the fully coupled solver. This has proven to be the most stable approach for strongly coupled FSI simulations. The HFIR SAR predicts, using an eigenfrequency analysis, that the first mode of the involute plates will have an 'S' shape near the leading edge[7]. This behavior was confirmed through the fully coupled FSI solutions that captured 'S' shaped leading edge deflections.

It must be noted that, UTK's efforts in this area are still ongoing as Mr. Curtis continues to pursue his PhD in Mechanical Engineering. We plan to provide ORNL new results in the future as they become available.

7.4 RESULTS FROM THERMAL-HYDRAULIC INTERDIMENSIONAL COUPLING MODELS

Without experimentally verified data against which to compare the coupled model, it is impossible to say definitively that it is a sufficiently accurate tool with which to model HFIR core thermal-hydraulics. The close agreement between the coupled model and the more complete 3D model, however, is a strong indicator that both provide good approximations of core conditions. In this regard, the coupled model has proven itself to be an exceedingly more efficient and less time-consuming alternative to the 3D model capable of producing results of a comparable quality.

This thesis was begun with the intent to create a simplified model that could eventually be expanded to model the entire core. It is doubtful that the coupled model is such a model. It does, however, greatly expand the computational range possible for a single model. The 3D model, with its gratuitous DOF, would be hard-pressed to encapsulate even two adjacent fuel plates and their surrounding coolant channels in a single model. It is most likely possible with the available resources on Betty, but only just. The coupled mode, by contrast, could be expanded to encapsulate 22 fuel plates and coolant channels for the same DOF as the 3D model, assuming a linear expansion of DOF with added domains. If the doubling of the 3D model is assumed plausible then so would be the creation of a 44 plate coupled expansion. Additional improvements need to be made to the model before all 540 fuel plates in the reactor core, both inner fuel elements and outer fuel elements, can be modeled together. Forty-four plates constitutes over a quarter of the 171 inner fuel elements, however, and would thus be sufficient to provide quarter-turn axial symmetry to a simulation of non-uniform core operation.

There are additional improvements that could be made to the coupled model to further increase its efficiency. Chiefly, more advanced meshing techniques, some of them unavailable at the onset of thesis-related work, would permit an even greater decrease in the DOF for the coupled model. Mapped meshes could be inserted into the entrance and exit coolant channel regions above and below the fuel plate region, respectively, to replace the computationally inefficient free-triangular mesh that exists there now. Virtual mesh elements could be used to replace the free-triangular *s-t* face mesh extruded down the length of the fueled section of the fuel plate with a neater, more evenly-spaced mapped mesh. CAD repairing features could be used to remove the free-tetrahedral mesh in the rounded leading edge of the fuel plate with a similarly neat mapped mesh extruded down the span of the leading edge.

The greatest advancement to be made in the coupled model, however, is finding the means to further separate the current segregated solution variable groups. As was mentioned earlier, the coupled model currently requires that temperature in both the fuel plate domain and the coolant domain be solved in the same segregated step. Otherwise the model fails. This would indicate that an expansion of the model to include additional fuel plates and coolant channels would also require that the flow variables for every channel, u and p, be solved in a single step. The same would be true for k and ε. The means to break this limitation and create segregated steps capable of solving manageable chunks of the solution domain would permit the model to encapsulate the entire core without fear of memory limitations. The only remaining concern would be computation time, which could become significant. Still, this is more of an inconvenience than a true limitation.

The coupled model might not be the definitive answer to the question first posed in this thesis but it is a confident step in the right direction.

This page intentionally blank.

8.0 REFERENCES

(1) D. Chandler, R. T. Primm III, and G. I. Maldonado, "Validating MCNP for LEU Fuel Design via Power Distribution Comparisons," Oak Ridge, TN., ORNL/TM-20091126, 008.

(2) K. S. Krane, *Introductory Nuclear Physics.:* Wiley & Sons, 1988.

(3) National Nuclear Security Administration. [Online]. http://tmsa.energy.gov.

(4) Reduced Enrichment for Research and Test Reactors. [Online]. http://www.rertr.anl.gov.

(5) http://nnsa.energy.gov/aboutus/ourprograms/dtm!gtri.

(6) National Nuclear Security Administration. [Online]. http://nnsa.energy.gov/mediaroom/ factsheets/reactorconversion.

(7) "High Flux Isotope Reactor Safety Analysis Report," ORNL, Tech. Rep. ORNL/HFIR/SAR/2344 2013.

(8) H. A. McLain, "HFIR Fuel Element Steady State Heat Transfer Analysis Revised Edition," Oak Ridge, TN., ORNL-TM-1904, 1967.

(9) D. G. Morris and M. W. Wendel, "High Flux Isotope Reactor System RELAP5 Input Model," Oak Ridge, TN, ORNL/TM-11647, 1993.

(10) David Renfro and David Chandler, "Preliminary Evaluation of Alternate Designs For HFIR Low-enriched Uranium Fuel," ORNL, Tech. Rep. ORNL/TM2014/154 2014.

(11) Neutron Sciences. [Online]. http://neutrons.ornl.gov/facilities/HFIR/history/

(12) N. Xoubi and R. T. Primm III, "Modeling of the High Flux Isotope Reactor Cycle 400," ORNL, Tech. Rep. ORNL/TM-2004/251 2005.

(13) R. C. Juvinall, *Fundamentals of Machine Component Design.:* John Wiley & Sons, Ltd, 1983.

(14) G Ilas and R T Primm III, "Low Enriched Uranium Fuel Design with Two-Dimensional Grading for the High Flux Isotope Reactor," ORNL, Tech. Rep. ORNL/TM-2010/318 2010.

(15) DE Burkes and G. S. Mickum, "Thermophysical Properties ofU-10Mo Alloy," Idaho National Lab, Tech. Rep. INL/EXT-10-19373 2010.

(16) L. Tschaepe, A. E. Ruggles, J. D. Freels, and R. T. Primm III, "Evaluation of HFIR LEU Fuel Using the COMSOL Multiphysics Platform," ORNL, Tech. Rep. ORNL/TM-2008/188 2008.

(17) J. D. Freels, I. T. Bodey, R. V. Arimilli, and K. T. Lowe, "Two-Dimensional Thermal Hydraulic Analysis and Benchmark in Support of HFIR LEU Conversion using COMSOL," ORNL, Tech. Rep. ORNL/TM-2010/018 2010.

(18) D. G. Renfro et al., "Low-Enriched Uranium Fuel Conversion Activities for the High Flux Isotope Reactor, Annual Report for FY 2011," ORNL, Tech. Rep. ORNL/TM-2011/507 2011.

(19) I. T. Bodey, R. V. Arimilli, and J. D. Freels, "Complex Geometry Creation and Turbulent Conjugate Heat Transfer Modeling," in *COMSOL Conference: Boston,* 2011.

(20) J.D. Freels and P. K. Jain, "Multiphysics Simulations of the Complex 3D Geometry of the High Flux Isotope Reactor Fuel Elements Using COMSOL," in *COMSOL Conference: Boston,* 2011.

(21) V. B. Khane, P. K. Jain, and J. D. Freels, "COMSOL Simulations for Steady State Thermal Hydraulics Analyses ofORNL's High Flux Isotope Reactor," in *COMSOL Conference: Boston,* 2012.

(22) V. B. Khane, P. K. Jain, and J.D. Freels, "Development of CFD Models to Support LEU Conversion of ORNL's High Flux Isotope Reactor," in *COMSOL Conference: Boston,* 2012.

(23) A. R. Travis, K. Ekici, and J.D. Freels, "Simulating HFIR Core Thermal Hydraulics Using 3D-2D Model Coupling," in *COMSOL Conference: Boston,* 2013.

(24) D. Wang, P. K. Jain, and J. D. Freels, "Application of COMSOL Pipe Flow Module To Develop a High Flux Isotope Reactor System Loop Model," in *COMSOL Conference: Boston,* 2013.

(25) A. R. Travis, "Simulating High Flux Isotope Reactor Core Thermal-Hydraulics via Interdimensional Model Coupling," Mechanical, Aerospace and Biomedical Engineering, University of Tennessee-Knoxville, Master's Thesis 2014.

(26) F. Curtis, K. Ekici, and J. Freels, "Fluid-Structure Interaction for Coolant Flow in Research-type Nuclear Reactors," in *COMSOL Users' Conference,* Boston, MA.

(27) Franklin G. Curtis, Kivanc Ekici, and James D Freels, "Fluid-Structure Interaction Modeling of High-Aspect Ratio Nuclear Fuel Plates Using COMSOL," in *COMSOL Conference: Boston*, 2013.
(28) P. K. Jain, J. D. Freels, and D. H. Cook, "3D COMSOL Simulations for Thermal Deflection of HFIR Fuel Plate in the "Cheverton-Kelley" Experiments," ORNL, Tech. Rep. ORNL/TM-20121138, 2012.
(29) David Chandler, "Neutronic Modeling of the High Flux Isotope Reactor using COMSOL," Anals of Nuclear Energy, Volume 38, Issue 11, November 2011, pages 2594-260511.
(30) I. T. Bodey, "Thermal Hydraulic Characteristics of Fuel Defects in Plate Type Nuclear Research Reactors," Mechanical, Aerospace, and Biomedical Engineering, University of Tennessee Knoxville, Ph.D. Dissertation, May 2015, ORNL/TM-2014/273.
(31) W. R. Gambill and R. D. Bundy, "HFIR Heat-Transfer Studies ofTurbulent Water Flow in Thin Rectangular Channels," Oak Ridge, TN, ORNL-3079, 1961.
(32) R. D. Cheverton and T. M. Sims, "HFIR Core Nuclear Design," Reactor Technology, Oak Ridge, TN., ORNL-4621 UC-80, 1971.
(33) R. D. Cheverton and W. H. Kelley, "Experimental Investigation ofHFIR Fuel Plate Deflections Induced by Temperature and Pressure Differentials," Oak Ridge, TN., ORNL-TM-2325, 1968.
(34) N. Hilvety and T. G. Chapman, "HFIR Fuel Element Steady State Heat Transfer Analysis," Oak Ridge, TN., ORNL-TM-1903, 1967.
(35) W. E. Thomas, "Bases for the Scram Setpoints, Limiting Safety System Settings, and Safety Limits of the HFIR for Mode 1 Operation at 85 MW(th)," ORNL/RRD/INT-22, December 22, 1987.
(36) COMSOL Help File - Turbulence Modeling.
(37) NIST/ASME Steam Properties, Version 2.21, May 2004.
(38) F. P. Incropera, D.P. DeWitt, T. L. Bergman, and A. S. Lavine, *Fundamentals of Heat and Mass Transfer*. Hoboken, NJ.: Wiley & Sons, 2007.
(39) D. K. Felde and et al., "Advanced Neutron Source Reactor Thermal-Hydraulic Test Loop Facility Description," Oak Ridge, TN., ORNL/TM-12397, 1994.
(40) M. Siman-Tov and et. al., Static Flow Instability in Subcooled Flow Boiling in Parallel Channels, 1995.
(41) Ismail B. Celik and et.al., "Procedure for Estimation and Reporting of Uncertainty Due to Discretization in CFD Applications," *Journal of Fluids Engineering*, vol. 130, pp. 078001-1 to 078001-4, 2008.
(42) William Kays and et al., *Convective Heat and Mass Transfer*. New York, NY: McGraw-Hill, 2005.
(43) Frank M. White, *Vsicous Fluid Flow*, 3rd ed.: McHraw-Hill Book Company, 2006.
(44) J. R. Kirkpatrick, "Calculations for HFIR Fuel Plate Non-Bonding and Fuel Segregation Uncertainty Factors," Oak Ridge, TN., K/CSD/TM-79, 1990.
(45) G. E. Giles, "Advanced Neutron Source Reactor Thermal Analysis of Fuel Plate Defects," Oak Ridge, TN., ORNL/TM-13072, 1995.
(46) Giovanni Pastore and et. al., "Physica-based modelling of fission gas swelling and release in UO_2 applied to integral fuel rod analysis," *Nuclear Engineering and Design*, vol. 256, pp. 75-86, 2012.
(47) A. Boulore, C. Struzik, and F. Gaudier, "Uncertainty and Sensitivity Analysis of the Nuclear Fuel Thermal Behavior," *Nuclear Engineering and Design*, vol. 253, pp. 200-210, 2012.
(48) G. Khvostov, K. Mikityuk, and M. A. Zimmermann, "A model for fission gas release and gaseous swelling of the uranium dioxide fuel coupled with the FALCON code," *Nuclear Engineering and Design*, vol. 241, no. 8, pp. 2983-3007,2011.
(49) D.H. Locke, "The Behavior of Defective Reactor Fuel," *Nuclear Engineering and Design*, vol. 21, no. 2, pp. 318-330, 1971.
(50) HFIR Inner Fuel Element Fuel Plate Loading Details, HFIR Drawing D-42114, Revision J, 2005.

(51) G. S. Chang and R. G. Ambrosek, "Advanced Test Reactor LEU Fuel Conversion Feasibility Study," Idaho National Lab, Tech. Rep. INL/CON-05-00921 2005.
(52) Idaho National Lab. [Online]. https://atmsuf.inl.gov
(53) The MIT Nuclear Reactor Laboratory. [Online]. http://web.mit.edu/nrllwww/reactor/core description.htm
(54) W. K. Stromquist and O. Sisman, "High Flux Reactor Fuel Assemblies Vibration and Water Flow," ORNL, Tech. Rep. ORNL-50 1948.
(55) D. R. Miller, "Critical Flow Velocities for Collapse of Reactor Parallel-Plate Fuel Assemblies," Knolls Atomic Power Lab, Tech. Rep. KAPL-1954 1960.
(56) R. D. Groninger and J. J. Kane, "Flow Induced Deflections of Parallel Flat Plates," *Nuclear Science and Engineering*, vol. 16, pp. 218-226, 1963.
(57) G. S. Smissaert, "Static and Dynamic Hydroelastic Instabilities in MTR-type Fuel Elements Part 1. Introduction and Experimental Investigation," *Nuclear Engineering and Design* , vol. 7, pp. 535-546, 1968.
(58) J. C. Kennedy and C. J. Jesse, "Fluid-Structure Interaction Modeling and Experimental Benchmarking," University of Missouri, Tech. Rep. TDR-MU-CALC-201210-005A 2012.
(59) W. F. Swinson, R. L. Battiste, C. R. Luttrell, and G. T. Yahr, "Follow-up Fuel Plate Stability Experiments and Analysis for the Advanced Neutron Source," ORNL, Tech. Rep. ORNL/TM-12629 1993.
(60) M. Ho and G. Hong, "Experimental Investigation of Flow-induced Vibration in a Parallel Plate Reactor Fuel Assembly," in *15th Australasian Fluid Mechanics Conference* , 2004, pp. 13-17.
(61) W R Marcum and B G Woods, "Predicting the Onset of Dynamic Instability of a Cylindrical Plate Under Axial Flow Conditions," *Nuclear Engineering and Design*, vol. 250, pp. 81-100, 2012.
(62) T. Ha and W J Garland, "Hydraulic Study of Turbulent Flow in MTR-type Nuclear Fuel Assembly," *Nuclear Engineering and Design*, vol. 236, pp. 975-984, 2006.
(63) W. F. Swinson, R. L. Battiste, C. R. Luttrell, and G. T. Yahr, "Fuel-Plate Stability Experiments and Analysis for the Advanced Neutron Source," *Symposium on Flow-Induced Vibration and Noise*, vol. 5, pp. 133-143, 1992.
(64) E B Johansson, "Hydraulic Instability of Reactor Parallel-Plate Fuel Assemblies," General Electric Company, tech. Rep. 1958.
(65) J. J. Kane, "The Effect of Inlet Spacing Deviations on the Flow-Induced Deflections of Flat Plates," *Nuclear Science and Engineering*, vol. 15, pp. 305-308, 1962.
(66) R. J. Scavuzzo, "Hydraulic Instability of Flat Parallel-Plate Assemblies," *Nuclear Science and Engineering*, vol. 21, pp. 463-472, 1965.
(67) M. W. Wambsganss Jr, "Second Order Effects as Related to Critical Coolant Flow Velocities and Reactor Parallel Plate Fuel Assemblies," *Nuclear Engineering and Design* , vol. 5, pp. 268-276, 1967.
(68) R. S. Wick, "Hydro-elastic Behavior of Multiple-plate Fuel-assemblies- I: Pressure Wave Propagation," *Journal of Nuclear Energy*, vol. 23, pp. 387-405, 1969.
(69) R. S. Wick, "Hydro-elastic Behavior of Multiple-Plate Fuel-assemblies- II: Hydro- static Divergence," *Journal of Nuclear Energy*, vol. 23, pp. 407-418, 1969.
(70) Y. T. Kim and H A Scarton, "Flow Induced Bending of Rectangular Plates," *Journal of Applied Mechanics*, vol. 44, pp. 207-212, 1977.
(71) H. M. Cekirge and E. Ural, "Critical Coolant Flow Velocities in Reactors Having Parallel Fuel Plates," *Camp. and Math with Appls.*, vol. 4, pp. 153-156, 1978.
(72) S. J. Pavone and H. A. Scarton, "Laminar Flow Induced Deflections of Stacked Plates," *Nuclear Engineering and Design*, vol. 74, no. 1, pp. 79-89, 1983.
(73) Y. Kerbuoa and A. A. Lakis, "Modelling of Plates Subjected to Flowing Fluid Under Various Boundary Conditions," *Engineering Applications of Computational Fluid Mechanics*, vol. 2, pp. 525-539, 2008.

(74) C. Guo and M. Paidossis, "Analysis of Hydroelastic Instabilities of Rectangular Parallel-Plate Assemblies," *Journal of Pressure Vessel Technology,* vol. 122, no. 4, pp. 502-508, 2000.
(75) G. Kim and G. Davis, "Hydrodynamic Instabilities in Flat-plate-type Fuel Assemblies," *Nuclear Engineering and Design,* vol. 158, no. 1, pp. 1-17, 1995.
(76) Z-D Cui and T-Q Tang, "Flow-induced Vibration and Stability of an Element Model for Parallel-plate Fuel Assemblies," *Nuclear Engineering and Design,* vol. 238, pp. 1629-1635, 2008.
(77) S. Michelin and S. G. Llewellyn Smith, "Linear Stability Analysis of Coupled Parallel Flexible Plates in an Axial Flow," *Journal of Fluids and Structures,* vol. 25, pp. 1136-1157, 2009.
(78) G. D. Roth, "CFD Analysis of Pressure Differentials in a Plate-Type Fuel Assembly," Oregon State University, Master's Thesis 2012.
(79) J. C. Kennedy and G. L. Solbrekken, "Coupled Fluid Structure Interaction (PSI) Modelling of Parallel Plate Assemblies," in *Proceedings of the ASME 2011 International Mechanical Engineering Congress & Exposition,* 2011.
(80) K. Billah and R. H. Scanlan, "Resonance, Tacoma Narrows Bridge Failure, and Undergraduate Physics Textbooks," *American Journal of Physics,* vol. 51, pp. 118-121, 1991.
(81) A. Roshko, "On the Development of Turbulent Wakes from Vortex Streets," National Advisory Committee for Aeronautics, Tech. Rep. # 1191 1954.
(82) G. H. Koopman, "The Vortex Wakes of Vibrating Cylinders at Low Reynolds Numbers," *Journal of Fluid Mechanics,* vol. 28, pp. 501-512, 1967.
(83) M. Schafer and S. Turek, Benchmark Computations of Laminar Flow Around a Cylinder: Springer, 1996.
(84) H. M. Blackburn and R. D. Henderson, "A Study of Two-dimensional Flow Past an Oscillating Cylinder," *Journal of Fluid Mechanics,* vol. 385, pp. 255-286, 1999.
(85) C. Evangelinos and G. E. Kaniadakis, "Dynamics and Flow Structures in the Turbulent Wake of Rigid and Flexible Cylinders Subject to Vortex-induced Vibrations," *Journal of Fluid Mechanics,* vol. 400, pp. 91-124, December 1999.
(86) M. S. McMullen, "The Application of Non-linear Frequency Domain Methods to the Euler and Navier-Stokes Equations," School of Aeronautics and Astronautics, Stanford University, Ph.D. thesis 2003.
(87) G. Pedro and A. Suleman, "A Numerical Study of the Propulsive Efficiency of a Flapping Hydrofoil," *International Journal for Numerical Methods in Fluids,* vol. 42, no. 5, pp. 493-526, 2003.
(88) S. Turek and J. Hron, Proposal for Numerical Benchmarking of Fluid- structure Interaction Between an Elastic Object and Laminar Incompressible Flow.: Springer, 2006.
(89) M. A. Spiker, "Development of an Efficient Design Method for Non-synchronous vibrations," Mechanical Engineering and Materials Science, Duke University, Ph.D. thesis 2008.
(90) A. Placzek and J-F Sigrist, "Numerical Simulation of an Oscillating Cylinder in a Cross-flow at Low Reynolds Number: Forced and Free Oscillations," *Computers and Fluids,* vol. 38, no. 1, pp. 80-100, 2009.
(91) J. N .Reddy and D. K. Gartling, The Finite Element Method in Heat Transfer and Fluid Dynamics, 3rd ed.: CRC Press, 2010.
(92) W. Cochran and J. W. Cooley, "What is the fast Fourier transform?," in *Proceedings of the IEEE,* vol. 55, 1967,pp. 1664-1674.
(93) C. H. K. Williamson, "Defining the Universal and Continuous Strouhal-Reynolds Number Relationship for the Laminar Vortex Shedding of a Circular Cylinder," *Physics of Fluids,* 1988.
(94) R. S Figliola and D. E. Beasley, *Theory and Design for Mechanical Measurements,* 3rd ed.: J. Wiley & Sons, 2000.
(95) W. R. Buell and B. A. Bush, "Mesh Generation-A Survey," *American Society of Mechanical Engineers Publication,* vol. 95, no. 1, pp. 332-338, 1973.
(96) D. A. Field, "Laplacian Smoothing and Delaunay Triangulations," *Communications in Applied Numerical Methods,* vol. 4, no. 6, pp. 709-712, 1988.

(97) A. M. Winslow, "Numerical Solution of the Quasilinear Poisson Equation in a Non-uniform Triangle Mesh," *Journal of Computational Physics,* vol. 1, no. 2, pp. 149-172, 1966.
(98) S. L. Karman, "Virtual Control Volumes for Two-Dimensional Unstructured Elliptic Smoothing," in *Proceedings of the 19th International Meshing Roundtable,* Chattanooga, TN, 2010, pp. 121-142.
(99) H. Askes and E. Kuhl, "An ALE Formulation Based on Spatial And Material Settings of Continuum Mechanics. Part 2: Classification and Applications," *Computer Methods in Applied Mechanics andEngineering,* vol. 193, no. 39-41, pp. 4223-4234, 2004.
(100) J. M .Gere and S. P. Timoshenko, *Mechanics of Materials.:* PWS-Kent Publishing Company, 1990.
(101) W K Sartory, "Analysis of Hydraulic Instabilities of ANS Involute Fuel Plates," ORNL, Tech. Rep. ORNL/TM-11580, 1991.
(102) W. K. Sartory, "Nonlinear Analysis of Hydraulic Buckling Instability of ANS Involute Fuel Plates," ORNL, Tech. Rep. ORNL/TM-12319 1993.
(103) W. F. Swinson, R. L. Battiste, C. R. Luttrell, and G. T. Yahr, "Fuel Plate Stability Experiments and Analysis for the Advanced Neutron Source," ORNL, Tech Rep. ORNL/TM-12353 1993.
(104) M. Siman-Tov, "Thermal Hydraulic Correlations for the Advanced Neutron Source Reactor Fuel Element Design and Analysis," in *Proceeding 1991 ASME Winter Annual Meeting,* Atlanta, 1991.
(105) D. K. Felde, "The Advanced Neutron Source Thermal Hydraulic Test Loop," in *Proceedings 8th Power Plant Dynamics, Control and Testing Symposium,* Knoxville, 1992.
(106) G. L. Yoder, et al., "Steady-State Thermal-Hydraulic Design and Analysis of the Advanced Neutron Source Reactor," ORNL, Tech. Rep. ORNL/TM-12398 1994.
(107) M. Siman-Tov, et al., "FY 1995 Progress Report on the ANS Thermal-Hydraulic Test Loop Operation and Results," ORNL, Tech. Rep. ORNL/TM-12972, 1997.
(108) W. F. Swinson and C. R. & Yahr, G. T. Luttrell, "An Examination of the Elastic Structural Response of the Advanced Neutron Source Fuel Plates," ORNL, Tech. Rep. ORNL/TM-12712, 1994.
(109) C. R. Luttrell, "Finite Element Analysis of Advanced Neutron Source Fuel Plates," ORNL, Tech. Rep. ORNL/TM-4600, 1995.
(110) J. W. Swinson, R. Battiste, L. Luttrell, and G. Yahr, "An Experimental Investigation of the Structural Response of Reactor Fuel Plates," *Experimental Mechanics,* vol. 35, pp. 212-215, 1995.
(111) W. V. Titow, *PVC Technology.:* Elsevier Applied Science, 1984.
(112) X-5 Monte Carlo Team, "MCNP-A General Monte Carlo N-Particle Transport Code, Version 5," Los Alamos National Laboratory, LA-CP-03-0245 2003.
(113) D. C. Wilcox, *Turbulence Modeling/or CFD.* La Canada, CA: DCW Industries, 2006.
(114) E G Eckert and R M Drake Jr, *Fundamentals of Mass and Heat Transfer.:* McGraw-Hill, 2006.
(115) J Rest, Y SKim, G L Hofman, M K Meyer, and S L Hayes, "U_Mo Fuels Handbook: Version 1.0," Argonne National Lab, Tech Rep. W-31-109-ENG-38 2006.
(116) Y. Aa Cenge1 and M. A. Boles, *Thermodynamics: An Engineering Approach,* 5th ed.: McGraw hill, 2006.
(117) X. Jingzhou and X-C Zhang, "Circular Involute Stage," *Optics Letters,* vol. 29, no. 17, pp. 2082-2084,2004.

INTERNAL DISTRIBUTION

1. D. H. Cook (dhc@ornl.gov)
2. J. D. Freels (freelsjd@ornl.gov)
3. G. Ilas (ilasg@ornl.gov)
4. P. K. Jain (jainpk@ornl.gov
5. D. G. Renfro (renfrodg@ornl.gov)
6. K. A. Smith (smithka@ornl.gov)
7. G. L. Yoder Jr. (yodergljr@ornl.gov)
8. D. Chandler (chandlerd@ornl.gov)
9. E. L. Popov (popove@ornl.gov)
10. M. W. Crowell (crowellmw@ornl.gov)
11. F. P. Griffin (griffinfp@ornl.gov)
12. C. R. Hyman III (hymancriii@ornl.gov)
13. J. R. Valentine (valentinejr@ornl.gov)
14. R. E. Hale (halere1@ornl.gov)
15. B. R. Betzler (betzlerbr@ornl.gov)
16. E. E. Sunny (sunnyee@ornl.gov)
17. F. G. Curtis (curtisfg@ornl.gov)
18. D. L. Green (greendl1@ornl.gov)
19. C. D. Bryan (bryancd@ornl.gov)
20. M. N. Gussev (gussevmn@ornl.gov)
21. R. W. Hobbs (hobbsrw@ornl.gov)
22. C. J. Hurt (hurtcj@ornl.gov)
23. C. H. Lau (lauch@ornl.gov)
24. K. J. Leonard (leonardk@ornl.gov)
25. S. L. Hogle (hoglesl@ornl.gov)
26. ORNL/RRD Document Control (phillipsth@ornl.gov)

EXTERNAL DISTRIBUTION

27. I. T. Bodey, Savannah River Remediation, LLC., DWPF Mechanical Engineering Building: 704-27S Room 2 (Isaac.Bodey@srs.gov)
28. R. V. Arimilli, Professor, Mechanical, Aerospace and Biomedical Engineering Department, 414 Dougherty Engineering Building, The University of Tennessee, Knoxville, Tennessee 37996-2210 (arimilli@utk.edu)
29. E. Fontes, COMSOL AB, Tegnergatan 23, SE-111 40, Stockholm, Sweden (ed@comsol.com)
30. W. F. Jones, Idaho National Laboratory, P.O. Box 1625, Idaho Falls, ID 83415-3750 (warren.jones@inl.gov)
31. K. T. Lowe, Bettis Atomic Power Laboratory, Bechtel Bettis, Inc, Mail Stop 36E, P. O. Box 79, West Mifflin, PA, 15122 (lowekt@bettis.gov)
32. A. E. Ruggles, Department of Nuclear Engineering, 315 Pasqua Engineering Building, Knoxville, TN 37996 2300 (aruggles@utk.edu)
33. B. Sjodin, COMSOL, Inc., New England Executive Park, Suite 350, Burlington, MA 01803 (bjorn@comsol.com)
34. P. L. Angelo, Y-12 National Security Complex, P.O. Box 2009, Oak Ridge, TN, 37831-8245 (Peter.Angelo@cns.doe.gov)
35. W. R. Marcum, Assistant Professor, Nuclear Engineering & Radiation Health Physics, Oregon State University (marcumw@engr.orst.edu)

36. G. L. Solbrekken, Assistant Professor, Mechanical and Aerospace Engineering, E2411A Lafferre Hall,
Columbia, MO, 65211 (SolbrekkenG@missouri.edu)
37. A. M. Tentner, Nuclear Engineering Division, Argonne National Laboratory, 9700 S Cass Avenue, Bldg 208, Argonne, IL 60439 (tentner@anl.gov)
38. K. Ekici, Assistant Professor, Graduate Program Director, Mechanical, Aerospace and Biomedical Engineering Department, 315 Perkins Hall, 415 Dougherty Engineering Building, The University of Tennessee, Knoxville, Tennessee 37996-2030 (ekici@utk.edu)
39. A. Elzawawy, Assistant Professor, Vaughn College of Aeronautics and Technology, Engineering and Technology Department, Rm F-128 (amir.elzawawy@vaughn.edu)
40. Vincent Lamberti, Y-12 National Security Complex, P.O. Box 2009, Oak Ridge, TN, 37831-8245 (Vincent.Lamberti@cns.doe.gov)
41. A. R. Travis, Alcoa Corporate Center, 201 Isabella St., Pittsburgh, PA 15212 (atravis6@vols.utk.edu)